

# Next-Generation Energy Storage Materials Explored by Advanced Scanning Techniques

Lead Guest Editor: Huaiyu Shao

Guest Editors: Hai-Wen Li, Yajun Cheng, Huaijun Lin, and Liqing He





---

**Next-Generation Energy Storage Materials  
Explored by Advanced Scanning Techniques**

Scanning

---

# **Next-Generation Energy Storage Materials Explored by Advanced Scanning Techniques**

Lead Guest Editor: Huaiyu Shao

Guest Editors: Hai-Wen Li, Yajun Cheng, Huaijun Lin,  
and Liqing He



---

Copyright © 2018 Hindawi. All rights reserved.

This is a special issue published in "Scanning." All articles are open access articles distributed under the Creative Commons Attribution License, which permits unrestricted use, distribution, and reproduction in any medium, provided the original work is properly cited.

---

## Editorial Board

Masayuki Abe, Japan  
David Alsteens, Belgium  
Igor Altfeder, USA  
Jose Alvarez, France  
Richard Arinero, France  
Renato Buzio, Italy  
Antonio Checco, USA  
Ovidiu Cretu, Japan  
Nicolas Delorme, France  
Hendrix Demers, Canada  
John R. Dutcher, Canada

Jonathan R. Felts, USA  
Marina I. Giannotti, Spain  
Sacha Gómez, Spain  
Federico Grillo, UK  
Anton V. Ievlev, USA  
Berndt Koslowski, Germany  
Jessem Landoulsi, France  
Emanuela Margapoti, Brazil  
Alessio Morelli, UK  
Daniele Passeri, Italy  
Andrea Picone, Italy

Jason L. Pitters, Canada  
Michela Relucenti, Italy  
Damien Riedel, France  
Francesco Ruffino, Italy  
Steven R. Schofield, UK  
Christian Teichert, Austria  
Marilena Vivona, UK  
Kislon Voitchovsky, UK  
Masamichi Yoshimura, Japan

## Contents

### Next-Generation Energy Storage Materials Explored by Advanced Scanning Techniques

Huaiyu Shao , Hai-Wen Li , Ya-Jun Cheng, Huaijun Lin , and Liqing He 

Editorial (3 pages), Article ID 3280283, Volume 2018 (2018)

### Flexible Freestanding Carbon Nanofiber-Embedded TiO<sub>2</sub> Nanoparticles as Anode Material for Sodium-Ion Batteries

Xuzi Zhang, Zhihong Chen , Lingling Shui, Chaoqun Shang , Hua Liao, Ming Li , Xin Wang , and Guofu Zhou 

Research Article (7 pages), Article ID 4725328, Volume 2018 (2018)

### Evaluation of A-Site Ba<sup>2+</sup>-Deficient Ba<sub>1-x</sub>Co<sub>0.4</sub>Fe<sub>0.4</sub>Zr<sub>0.1</sub>Y<sub>0.1</sub>O<sub>3-δ</sub> Oxides as Electrocatalysts for Efficient Hydrogen Evolution Reaction

Xiangnan Li, Liqing He, Xiongwei Zhong, Jie Zhang, Shijing Luo, Wendi Yi, Luozheng Zhang, Manman Hu, Jun Tang, Xianyong Zhou, Xingzhong Zhao, and Baomin Xu 

Research Article (10 pages), Article ID 1341608, Volume 2018 (2018)

### L-Leucine Templated Biomimetic Assembly of SnO<sub>2</sub> Nanoparticles and Their Lithium Storage Properties

Peng Yu, Mili Liu, Haixiong Gong, Fangfang Wu, Zili Yi, and Hui Liu 

Research Article (8 pages), Article ID 4314561, Volume 2018 (2018)

### Anomalously Faster Deterioration of LiNi<sub>0.8</sub>Co<sub>0.15</sub>Al<sub>0.05</sub>O<sub>2</sub>/Graphite High-Energy 18650 Cells at 1.5 C than 2.0 C

Dawei Cui , Jinlong Wang , Ailing Sun , Hongmei Song , and Wenqing Wei 

Research Article (7 pages), Article ID 2593780, Volume 2018 (2018)

### Surface Characteristic Effect of Ag/TiO<sub>2</sub> Nanoarray Composite Structure on Supercapacitor Electrode Properties

Jie Cui, Lin Cao, Dahai Zeng, Xiaojian Wang, Wei Li, Zhidan Lin , and Peng Zhang 

Research Article (10 pages), Article ID 2464981, Volume 2018 (2018)

### Advanced SEM and TEM Techniques Applied in Mg-Based Hydrogen Storage Research

Jianding Li, Jincheng Xu, Bo Li, Liqing He , Huaijun Lin , Hai-Wen Li , and Huaiyu Shao 

Review Article (12 pages), Article ID 6057496, Volume 2018 (2018)

### Effective Removal of Congo Red by Triarrhena Biochar Loading with TiO<sub>2</sub> Nanoparticles

Peng Yu, Tao Hu, Hong Hui Chen, Fangfang Wu, and Hui Liu 

Research Article (7 pages), Article ID 7670929, Volume 2018 (2018)

### Synthesis, Morphology, and Hydrogen Absorption Properties of TiVMn and TiCrMn Nanoalloys with a FCC Structure

Bo Li, Jianding Li, Huaiyu Shao , Wei Li, and Huaijun Lin 

Research Article (9 pages), Article ID 5906473, Volume 2018 (2018)

**Structural and Kinetic Hydrogen Sorption Properties of  $Zr_{0.8}Ti_{0.2}Co$  Alloy Prepared by Ball Milling**

Hui He, Huaqin Kou , Wenhua Luo , Tao Tang, Zhiyong Huang, Ge Sang, Guanghui Zhang, Jingwen Ba, and Meng Liu

Research Article (13 pages), Article ID 5736742, Volume 2018 (2018)

**A Novel Open-Framework Cu-Ge-Based Chalcogenide Anode Material for Sodium-Ion Battery**

Quan Sun, Lin Fu, and Chaoqun Shang

Research Article (6 pages), Article ID 3876525, Volume 2017 (2018)

**Facile Synthesis of Indium Sulfide/Flexible Electrospun Carbon Nanofiber for Enhanced Photocatalytic Efficiency and Its Application**

Liu Han, Haohao Dong, Dong Mao, Baolv Hua, Qinyu Li, and Dong Fang

Research Article (10 pages), Article ID 6513903, Volume 2017 (2018)

## Editorial

# Next-Generation Energy Storage Materials Explored by Advanced Scanning Techniques

Huaiyu Shao <sup>1</sup>, Hai-Wen Li <sup>2</sup>, Ya-Jun Cheng,<sup>3,4</sup> Huaijun Lin <sup>5</sup> and Liqing He <sup>6</sup>

<sup>1</sup>*Institute of Applied Physics and Materials Engineering (IAPME), University of Macau, Macau*

<sup>2</sup>*Kyushu University, Fukuoka, Japan*

<sup>3</sup>*Ningbo Institute of Materials Technology and Engineering, Chinese Academy of Sciences, Ningbo, China*

<sup>4</sup>*University of Oxford, Oxford, UK*

<sup>5</sup>*Jinan University, Guangzhou, China*

<sup>6</sup>*Southern University of Science and Technology, Shenzhen, China*

Correspondence should be addressed to Huaiyu Shao; [hshao@umac.mo](mailto:hshao@umac.mo) and Huaijun Lin; [hjlin@jnu.edu.cn](mailto:hjlin@jnu.edu.cn)

Received 8 August 2018; Accepted 8 August 2018; Published 3 December 2018

Copyright © 2018 Huaiyu Shao et al. This is an open access article distributed under the Creative Commons Attribution License, which permits unrestricted use, distribution, and reproduction in any medium, provided the original work is properly cited.

Energy storage, which is capturing and storing energy produced at one time and/or at a certain place for use at a later time and/or other locations, is one of the most critical issues for human society to realize sustainability. Development of next-generation energy storage materials is one of the hottest research topics in the materials science field. In recent decades, advanced scanning techniques including SEM, TEM, AFM, STMs, and Raman spectroscopy have been abundantly employed in observing morphologies, characterizing microstructures, and identifying specific physical and chemical properties in order to design innovative materials with controllable structures, understand the formation mechanisms, clarify the catalytic mechanisms, and elucidate the effect of designed parameters on energy storage properties [1]. The aim of this special issue is to publish high-quality research papers as well as provide a comprehensive review addressing the latest and state-of-the-art topics from active researchers in the field of energy storage materials. This special issue contains 10 research papers and 1 review paper representing some of the latest research in energy storage materials explored by advanced scanning techniques.

Hydrogen storage materials are one of the main research topics in this special issue. Mg-based materials have attracted great attention because of the interest in high-capacity hydrogen storage applications in the past decades [2, 3]. J. Li et al. reviewed the advanced SEM

and TEM techniques applied in Mg-based hydrogen storage research. The reviewed literature implies that the applications of advanced SEM and TEM play significantly important roles in the research and development of next-generation hydrogen storage materials. H. He et al. reported the structural and hydrogenation kinetic properties of a  $Zr_{0.8}Ti_{0.2}Co$  alloy prepared by ball milling. High-resolution- (HR-) TEM studies revealed that a large number of disordered microstructures including amorphous regions and defects existed after ball milling, and these played an important role in improving the hydrogenation performances. B. Li et al. synthesized FCC-structure TiVMn-based and TiCrMn-based nanoalloys with a mean particle size of around a few tens of  $\mu m$  and with an average crystallite size of just 10 to 13 nm. The microstructures of the alloys were carefully studied by SEM and XRD, while hydrogen storage properties were studied by high-pressure DSC under a  $H_2$  atmosphere. It showed that the absorption reaction was much stronger, and it started at a much lower temperature ( $210^\circ C$ ) in the TiVMn nanoalloy than that in the TiCrMn one.

Studies on rechargeable lithium-ion batteries (LIBs) [4] and sodium-ion batteries (SIBs) [5] have become one of the most widely investigated research directions all over the world, and they are also the main topics included in this special issue. LIBs currently have governed the worldwide rechargeable battery markets due to their outstanding energy and power capability. In recent days, research interest in SIBs

has been resurrected, driven by new applications with requirements different from those in portable electronics and the need to address the concern of low Li abundance in the Earth's crust.  $\text{SnO}_2$  has been considered as an outstanding alternative to graphite as an anode for LIBs [6]. P. Yu et al. synthesized  $\text{SnO}_2$  nanoparticles by a novel route of the sol-gel method assisted with biomimetic assembly using L-leucine as a biotemplate. The results demonstrated that the growth of  $\text{SnO}_2$  nanoparticles could be regulated by L-leucine at a high calcination temperature. D. Cui et al. reported that the  $\text{LiNi}_{0.8}\text{Co}_{0.15}\text{Al}_{0.05}\text{O}_2/\text{graphite}$  LIBs showed better cycle lives at a 2.0 C discharge rate than that at a 1.5 C discharge rate, which was due to the reason that the negative electrodes contributed more than the positive electrodes. Q. Sun et al. reported a novel open-framework Cu-Ge-based chalcogenide,  $[\text{Cu}_8\text{Ge}_6\text{Se}_{19}](\text{C}_5\text{H}_{12}\text{N})_6$  (CGSe), as an anode material for SIBs. As a result, the CGSe anode exhibited good electrochemical performances such as high reversible capacity ( $463.3 \text{ mAh g}^{-1}$ ), excellent rate performance, and considerable cycling stability. X. Zhang et al. synthesized flexible freestanding carbon nanofiber-embedded  $\text{TiO}_2$  nanoparticles (CNF- $\text{TiO}_2$ ) and then applied it directly as the anode in SIBs without a binder or current collector. The anode exhibited a high reversible capacity of  $614 \text{ mAh g}^{-1}$  ( $0.27 \text{ mAh cm}^{-2}$ ) after almost 400 cycles and an excellent capacity retention ability of  $\sim 100\%$ .

Supercapacitors have drawn great attention due to their high power, energy density and long lifecycle [7]. J. Cui et al. designed and fabricated Ag-ion-modified titanium nanotube (Ag/ $\text{TiO}_2$ -NT) arrays as the electrode material of supercapacitors for electrochemical energy storage. The modified electrode showed a high capacitance of  $9324.6 \text{ mF}\cdot\text{cm}^{-3}$  ( $86.9 \text{ mF}\cdot\text{g}$ ,  $1.2 \text{ mF}\cdot\text{cm}^{-2}$ ), energy density of  $82.8 \mu\text{Wh}\cdot\text{cm}^{-3}$  ( $0.8 \mu\text{Wh}\cdot\text{g}$ ,  $0.0103 \mu\text{Wh}\cdot\text{cm}^{-2}$ ), and power density of  $161.0 \text{ mW}\cdot\text{cm}^{-3}$  ( $150.4 \mu\text{W}\cdot\text{g}$ ,  $2.00 \mu\text{W}\cdot\text{cm}^{-2}$ ) at the current density of 0.05 mA.

Exploring earth-abundant and cost-effective catalysts with high activity and stability for hydrogen evolution reaction (HER) is of great importance to practical applications of alkaline water electrolysis [8]. X. Li et al. reported on A-site  $\text{Ba}^{2+}$ -deficiency doping as an effective strategy to enhance the electrochemical activity of  $\text{BaCo}_{0.4}\text{Fe}_{0.4}\text{Zr}_{0.1}\text{Y}_{0.1}\text{O}_{3-\delta}$  for HER, which was related to the formation of oxygen vacancies around active Co/Fe ions.

The heterojunction system has been proven to be one of the best architectures for photocatalysts [9]. L. Han et al. reported the facile synthesis of indium sulfide/flexible electrospun carbon nanofiber ( $\text{In}_2\text{S}_3/\text{CNF}$ ) for enhanced photocatalytic efficiency. The prepared  $\text{In}_2\text{S}_3/\text{CNF}$  photocatalysts exhibited greatly enhanced photocatalytic activity compared to pure  $\text{In}_2\text{S}_3$ . In addition, the formation mechanism of the one-dimensional heterojunction  $\text{In}_2\text{S}_3/\text{CNF}$  photocatalyst was discussed.

Congo red 1-naphthalenesulfonic acid is the critical source of contamination of wastewater [10]. P. Yu et al. reported a composite of pyrolytic Triarrhena biochar loading with  $\text{TiO}_2$  nanoparticles synthesized by a sol-gel method. When used as an absorbent to remove Congo red from an aqueous solution, it was found that the as-prepared

composite performed better absorption capacity than a single biochar or  $\text{TiO}_2$ .

In summary, the contributed papers in this special issue cover several general aspects of energy storage materials, which are explored by scanning techniques, including SEM, TEM, AFM, STMs, and Raman spectroscopy. The advancement of scanning technologies requires deeply understanding the microstructures of energy materials and elucidating the mechanisms of material properties with various structures. It may then bring possible breakthroughs in the development of next-generation energy storage materials. We tried our best to present the latest cutting-edge applications of scanning techniques in this field and hope that our endeavor may shed light on future research on energy storage technologies.

## Conflicts of Interest

The authors declare that there is no conflict of interest regarding the publication of this article.

## Acknowledgments

We appreciate all the authors for submitting their original work to this special issue, and we also thank all the reviewers for their important suggestions and comments to improve the quality of the accepted submissions.

Huaiyu Shao  
Hai-Wen Li  
Ya-Jun Cheng  
Huaijun Lin  
Liqing He

## References

- [1] H.-J. Lin, J.-J. Tang, Q. Yu et al., "Symbiotic  $\text{CeH}_{2.73}/\text{CeO}_2$  catalyst: a novel hydrogen pump," *Nano Energy*, vol. 9, pp. 80–87, 2014.
- [2] H. Shao, L. He, H. Lin, and H.-W. Li, "Progress and trends in magnesium-based materials for energy-storage research: a review," *Energy Technology*, vol. 6, no. 3, pp. 445–458, 2018.
- [3] H. Shao, G. Xin, J. Zheng, X. Li, and E. Akiba, "Nanotechnology in Mg-based materials for hydrogen storage," *Nano Energy*, vol. 1, no. 4, pp. 590–601, 2012.
- [4] J. W. Choi and D. Aurbach, "Promise and reality of post-lithium-ion batteries with high energy densities," *Nature Reviews Materials*, vol. 1, no. 4, article 16013, 2016.
- [5] M. D. Slater, D. Kim, E. Lee, and C. S. Johnson, "Sodium-ion batteries," *Advanced Functional Materials*, vol. 23, no. 8, pp. 947–958, 2013.
- [6] R. Hu, D. Chen, G. Waller et al., "Dramatically enhanced reversibility of  $\text{Li}_2\text{O}$  in  $\text{SnO}_2$ -based electrodes: the effect of nanostructure on high initial reversible capacity," *Energy Environmental Science*, vol. 9, no. 2, pp. 595–603, 2016.
- [7] G. Wang, L. Zhang, and J. Zhang, "A review of electrode materials for electrochemical supercapacitors," *Chemical Society Reviews*, vol. 41, no. 2, pp. 797–828, 2012.
- [8] Y. Shi and B. Zhang, "Recent advances in transition metal phosphide nanomaterials: synthesis and applications in

- hydrogen evolution reaction,” *Chemical Society Reviews*, vol. 45, no. 6, pp. 1529–1541, 2016.
- [9] H. Wang, L. Zhang, Z. Chen et al., “Semiconductor hetero-junction photocatalysts: design, construction, and photocat-alytic performances,” *Chemical Society Reviews*, vol. 43, no. 15, pp. 5234–5244, 2014.
- [10] M. T. Yagub, T. K. Sen, S. Afroze, and H. M. Ang, “Dye and its removal from aqueous solution by adsorption: a review,” *Advances in Colloid and Interface Science*, vol. 209, pp. 172–184, 2014.

## Research Article

# Flexible Freestanding Carbon Nanofiber-Embedded TiO<sub>2</sub> Nanoparticles as Anode Material for Sodium-Ion Batteries

Xuzi Zhang,<sup>1</sup> Zhihong Chen ,<sup>2</sup> Lingling Shui,<sup>1</sup> Chaoqun Shang ,<sup>1</sup> Hua Liao,<sup>3</sup> Ming Li ,<sup>3</sup> Xin Wang ,<sup>1,4</sup> and Guofu Zhou ,<sup>1,4</sup>

<sup>1</sup>National Center for International Research on Green Optoelectronics, South China Normal University, Guangzhou, China

<sup>2</sup>Shenyang Institute of Automation, Chinese Academy of Sciences, Guangzhou, China

<sup>3</sup>Institute of Solar Energy, Yunnan Normal University, Kunming, China

<sup>4</sup>International Academy of Optoelectronics at Zhaoqing, South China Normal University, Guangdong, China

Correspondence should be addressed to Chaoqun Shang; [chaoqun.shang@ecs-scnu.org](mailto:chaoqun.shang@ecs-scnu.org) and Xin Wang; [wangxin@scnu.edu.cn](mailto:wangxin@scnu.edu.cn)

Received 31 May 2018; Accepted 30 July 2018; Published 4 November 2018

Academic Editor: Huaiyu Shao

Copyright © 2018 Xuzi Zhang et al. This is an open access article distributed under the Creative Commons Attribution License, which permits unrestricted use, distribution, and reproduction in any medium, provided the original work is properly cited.

Sodium-ion batteries (SIBs), owing to the low cost, abundant resources, and similar physicochemical properties with lithium-ion batteries (LIBs), have earned much attention for large-scale energy storage systems. In this article, we successfully synthesize flexible freestanding carbon nanofiber-embedded TiO<sub>2</sub> nanoparticles (CNF-TiO<sub>2</sub>) and then apply it directly as anode in SIBs without binder or current collector. Taking the advantage of flexible CNF and high structural stability, this anode exhibits high reversible capacity of 614 mAh·g<sup>-1</sup> (0.27 mAh·cm<sup>-2</sup>) after almost 400 cycles and excellent capacity retention ability of ~100%

## 1. Introduction

Sodium-ion batteries (SIBs) have earned much attention as a candidate substitution for lithium-ion batteries (LIBs) in the area of large-scale energy storage [1, 2], which is ascribed to the earth's abundance of sodium resource and similar physicochemical properties with LIBs [3–5]. Until now, many efforts have been made to solve the slow sodiation/desodiation kinetics and large-volume expansion caused by a large radius of Na<sup>+</sup> (1.02 Å versus 0.76 Å of Li<sup>+</sup>) [6–8]. Furthermore, the capacity and cycling stability also need to be improved to satisfy the practical application. It is essential to select and design proper anode materials for SIBs to realize fast Na<sup>+</sup> insertion/extraction with high capacity and cycling stability [9, 10].

Among numerous anode material candidates, TiO<sub>2</sub> with anatase phase has been explored as a promising anode material for SIBs with low cost, abundance, environmental benignity, and excellent structural stability [11–13]. However, the undesirable electrical conductivity and sluggish ionic diffusivity restrict its further applications [14]. Many efforts have been cost to improve the ion/electron transportation for SIBs.

Zhu and coworkers [15] synthesized TiO<sub>2</sub> nanoparticles coated by multiwalled carbon nanotubes and carbon nanorods as anode, exhibiting excellent rate capability and cycling stability. He and coworkers [16] prepared a hierarchical rod-in-tube structure TiO<sub>2</sub> modified with a conductive carbon layer as anode, which delivered fast ion diffusion and high conductivity. Therefore, the efficient strategy to enhance the electrochemical performance is nanosizing TiO<sub>2</sub> and then incorporating with the conductive matrix [16–22]. Despite the progresses, the rational design nanostructure of TiO<sub>2</sub>-based anode is still of great demand.

Herein, we proposed freestanding flexible wrinkled carbon nanofiber-embedded anatase TiO<sub>2</sub> nanoparticles (CNF-TiO<sub>2</sub>) as anode of SIBs directly without binder and current collector, which can not only increase the energy density but also explore the potential application in flexible devices. The long-range continuous carbon nanofibers can improve the conductivity of nanosized anatase TiO<sub>2</sub>, and the thin fibers can shorten the diffusion path of Na<sup>+</sup>, which can promote the electrochemical kinetics in Na<sup>+</sup> insertion/extraction. The freestanding flexible 3D carbon structure and embedded TiO<sub>2</sub> nanoparticles can improve structural

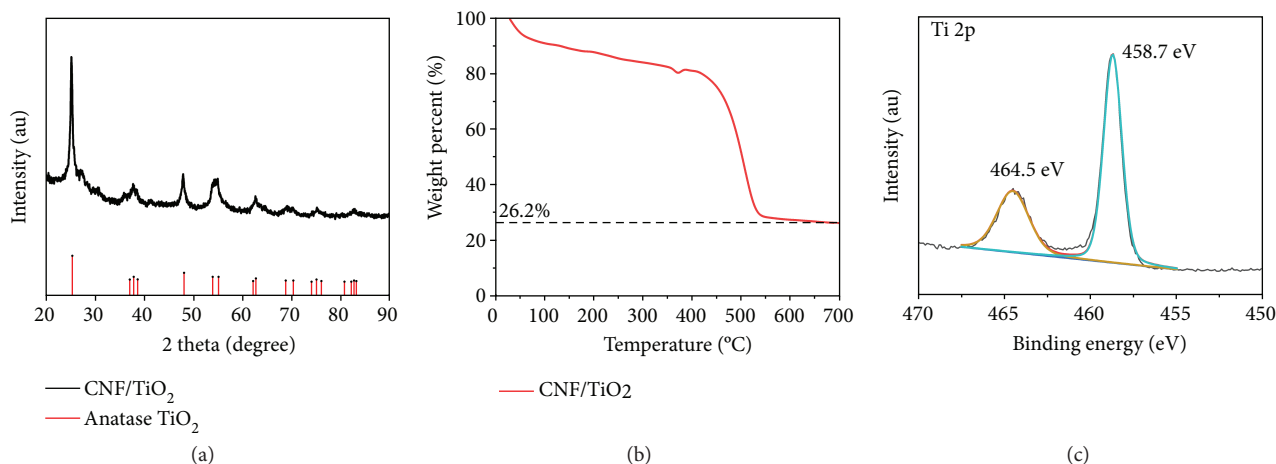


FIGURE 1: (a) The XRD pattern of CNF-TiO<sub>2</sub> after pyrolysis at 700°C; (b) TG pattern of CNF-TiO<sub>2</sub> under air atmosphere; (c) XPS of Ti 2p in CNF-TiO<sub>2</sub>.

stability to alleviate the volume change during Na<sup>+</sup> insertion/extraction. In addition, the rough surface of CNFs increases the electrode-electrolyte contact points and lowers the charge transfer resistance. High specific capacity of 614 mAh·g<sup>-1</sup> (0.27 mAh·cm<sup>-2</sup>) was obtained after almost 400 cycles with capacity retention of ~100%, confirming the potential of CNF-TiO<sub>2</sub> as anode for SIBs.

## 2. Experimental Section

**2.1. Synthesis of the Freestanding CNF-TiO<sub>2</sub>.** The electrospinning precursor solution was prepared firstly by dissolving 1.48 g polyacrylonitrile (PAN, Mw = 150,000, Sigma-Aldrich) in 18 ml *N,N*-dimethylformamide (DMF) under magnetic stirring overnight. Then, 2.5 ml tetrabutyl titanate (Ti(OC<sub>4</sub>H<sub>9</sub>)<sub>4</sub>) was added into this solution and stirring was continued for 10 min to obtain homogeneous white turbid solution. The distance between the needle and Al foil was 15 cm, and the voltage was maintained at 25 kV. Then the obtained precursor nanofibers were stabilized at 280°C for 2 h with a heating rate of 5°C·min<sup>-1</sup> and carbonized at 700°C with 1°C·min<sup>-1</sup> for 2 h under argon atmosphere.

**2.2. Structure Characterizations.** The morphologies and size of CNF/TiO<sub>2</sub> were characterized by scanning electron microscopy (SEM, ZEISS Ultra 55). Transmission electron microscopy (TEM) and EDS mapping were both carried out by JEM-2100 HR. The crystalline property of CNF-TiO<sub>2</sub> was recorded by Bruker D8 Advance. The thermal gravity analysis TG test was performed to evaluate the content of TiO<sub>2</sub> by Netzsch STA 449. The 250Xi X-ray photoelectron spectroscopy (XPS) was obtained from ESCALAB.

**2.3. Electrochemical Tests.** The CR2016-type coin cells were assembled with sodium metal as the reference electrode, glass fiber membrane as the separator, and the as-prepared CNF-TiO<sub>2</sub> directly as the anode. The above procedures were all carried out in an Ar-filled glove box (O<sub>2</sub> < 0.1 ppm, H<sub>2</sub>O < 0.1 ppm). The electrolyte was 1 M NaClO<sub>4</sub> in propylene carbonate (PC)/ethylene carbonate (EC) (PC : EC = 1 : 1,

in volume). The cyclic voltammetry (CV) and electrochemical impedance spectroscopy (EIS) results were obtained from an electrochemical workstation (CHI660E, Shanghai Chen Hua Instruments Ltd). Also, the galvanostatic discharge-charge tests were conducted in a Neware battery testing system.

## 3. Results and Discussion

The structure and morphology of CNF-TiO<sub>2</sub> are detected by XRD, TG, XPS, SEM, and TEM. As shown in Figure 1(a), all the diffraction peaks matched well with anatase TiO<sub>2</sub> (JCPDS number 021-1272), which confirms that the pyrolysis temperature is appropriate to gain high-purity anatase TiO<sub>2</sub>. Furthermore, the slightly weak intensity of these diffraction peaks suggests that the TiO<sub>2</sub> nanoparticles were well embedded in the carbon nanofibers. In the thermogravimetry measurement (Figure 1(b)) of CNF-TiO<sub>2</sub>, the content of TiO<sub>2</sub> is 26.2%. The Ti in CNF-TiO<sub>2</sub> is clarified by X-ray photoelectron spectroscopy (XPS) as shown in Figure 1(c), which indicates two peaks of 464.6 eV and 458.7 eV, corresponding to the orbits of 2p 3/2 and 2p 1/2 of Ti<sup>4+</sup>, respectively. The Ti 2p XPS result also confirms the formation of anatase TiO<sub>2</sub>.

Figures 2(a)–2(f) perform the morphologies of CNF-TiO<sub>2</sub>. SEM images (Figures 2(a)–2(c)) show an extremely rough surface of the as-synthesized nanofibers with diameter of ~300 nm. Many wrinkles appear after 700°C pyrolysis treatment for the crystallization of TiO<sub>2</sub> nanoparticles and decomposition of the polymer fibers, which may provide active sites for Na<sup>+</sup> insertion/extraction. In addition, the long-range continuous carbon nanofiber matrix with high conductivity will lead to fast electron transmission. As for the TEM images with different magnification (Figures 2(d)–2(f)), the well-distributed TiO<sub>2</sub> nanoparticles can be clearly observed with sizes between 100 nm and 200 nm and they are all coated with amorphous carbon. A lattice spacing of 0.363 nm, corresponding to (101) planes of anatase TiO<sub>2</sub>, can be clearly detected in the high-resolution TEM image (Figure 2(f)), which means the high degree of crystallinity of anatase TiO<sub>2</sub>. The TiO<sub>2</sub> larger lattice spacing of 0.363 nm

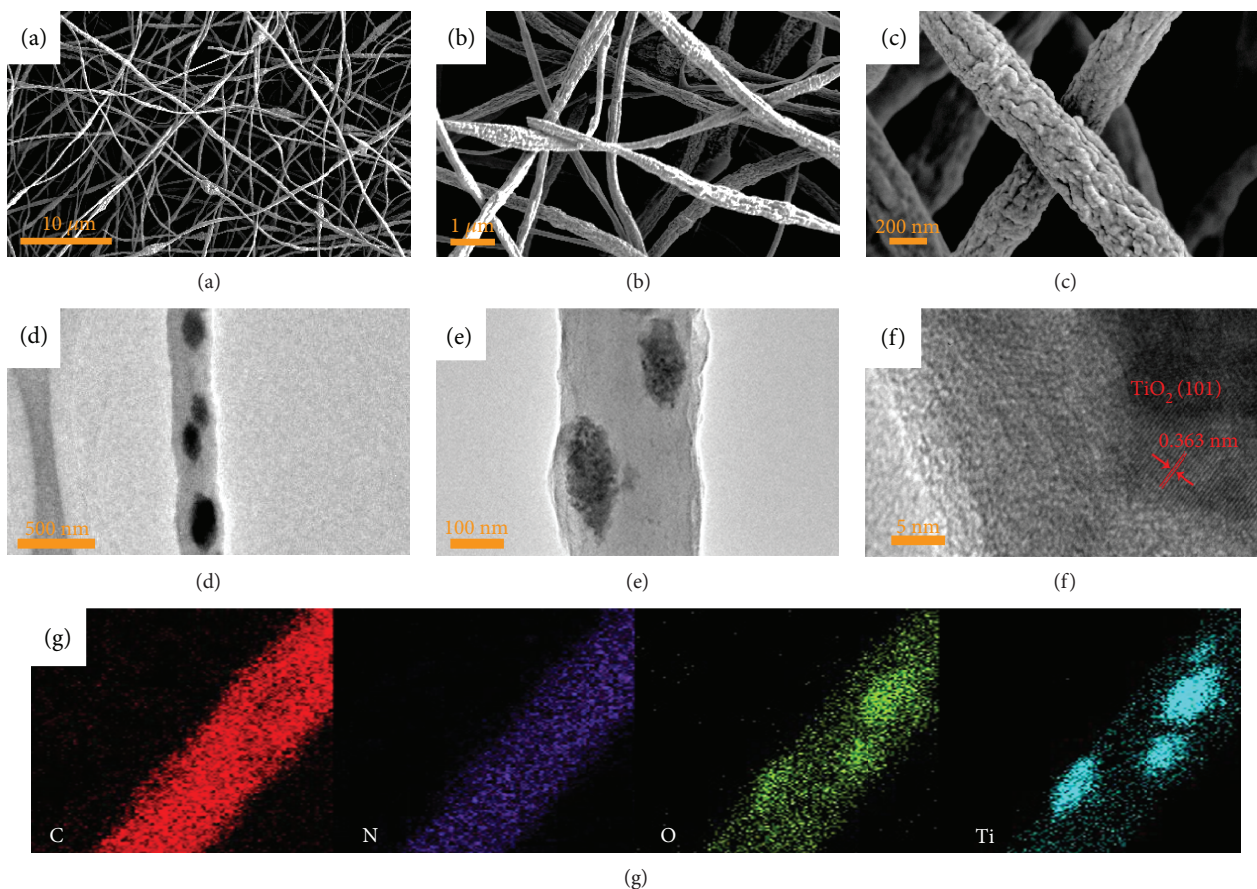


FIGURE 2: SEM images (a–c), TEM images (d–f), and EDS mapping (g) of CNF-TiO<sub>2</sub>.

than 0.102 nm of Na<sup>+</sup> and the specific space group of  $I4_1/amd$  ( $a = 3.785 \text{ \AA}$ , and  $c = 9.514 \text{ \AA}$ ) can ensure the fast insertion/extraction of Na<sup>+</sup> [23, 24], in which Na<sup>+</sup> is inserted/extracted in the interspace of anatase TiO<sub>2</sub> [23]. Furthermore, it can stabilize the structure of CNF-TiO<sub>2</sub> cooperated with amorphous carbon through enduring the volume change in the battery reaction.

The electrochemical performance of CNF-TiO<sub>2</sub> anode for SIBs is investigated by cyclic voltammetry (CV) between 0.01 V and 3 V with a scan rate of  $0.1 \text{ mV}\cdot\text{s}^{-1}$  and galvanostatic charge-discharge techniques at  $200 \text{ mA}\cdot\text{g}^{-1}$ . As depicted in Figure 3(a), a strong cathodic peak between 0 and 0.5 V appears in the first cycle of SIB and disappears in the following four cycles, which demonstrates the decomposition of electrolyte and the formation of solid electrolyte interphase (SEI) film. The benign overlapped CV curves of the next four scans indicate excellent cycle stability and reversibility for Na<sup>+</sup> insertion/extraction. Figure 3(b) shows the charge/discharge curves of CNF-TiO<sub>2</sub> as anode for SIBs with constant current of  $200 \text{ mA}\cdot\text{g}^{-1}$ . In the initial cycle, there exists a large irreversible capacity compared to the following curves, which is in agreement with the CV tests. The charge/discharge curves without obvious plateaus demonstrate the fluent insertion/extraction of Na<sup>+</sup> into the amorphous carbon and crystalline TiO<sub>2</sub> lattice. The initial discharge capacity is  $792 \text{ mAh}\cdot\text{g}^{-1}$  ( $0.35 \text{ mAh}\cdot\text{cm}^{-2}$ ) with a coulombic efficiency of 35.5%, and the discharge capacities increase slightly during

the subsequent cycles, showing the continuous reduced resistance of CNF-TiO<sub>2</sub> by the activation of this material, which is also confirmed in electrochemical impedance spectroscopy (EIS, Figure 3(d)). The EIS results show the slight decrease in charge transfer resistance before 10 cycles and then a gradual increase until 80 cycles, which is the consequence of activation and slight structural damage of CNF-TiO<sub>2</sub>, respectively.

The rate performance of CNF-TiO<sub>2</sub> is further investigated at various constant currents from  $100 \text{ mA}\cdot\text{g}^{-1}$  to  $5000 \text{ mA}\cdot\text{g}^{-1}$ . As shown in Figure 3(c), the capacity can still retain  $378 \text{ mAh}\cdot\text{g}^{-1}$ ,  $309 \text{ mAh}\cdot\text{g}^{-1}$ , and  $133 \text{ mAh}\cdot\text{g}^{-1}$  at the current densities of  $1000 \text{ mA}\cdot\text{g}^{-1}$ ,  $2000 \text{ mA}\cdot\text{g}^{-1}$ , and  $5000 \text{ mA}\cdot\text{g}^{-1}$ , indicating the rapid process of the insertion/extraction of Na<sup>+</sup>. Moreover, when the current density recovers to  $100 \text{ mA}\cdot\text{g}^{-1}$ , the capacities can retain to the initial level, showing the outstanding rate performance of CNF-TiO<sub>2</sub> as anode for SIB. CNF-TiO<sub>2</sub> also exhibits remarkable long-term cycling stability (Figure 3(e)). It can deliver a high initial capacity of  $792 \text{ mAh}\cdot\text{g}^{-1}$  with a coulombic efficiency of 35.5% and stability at  $614 \text{ mAh}\cdot\text{g}^{-1}$  after almost 400 cycles, indicating the excellent cycling performance and structural stability of CNF-TiO<sub>2</sub> anode. On the one hand, the large length-to-volume ratio of CNFs-TiO<sub>2</sub> provides more active sites for Na ion adsorption on the surface of 1D nanofibers, which offers additional capacity contribution. On the other hand, the specific capacity of CNFs-TiO<sub>2</sub> is based on the

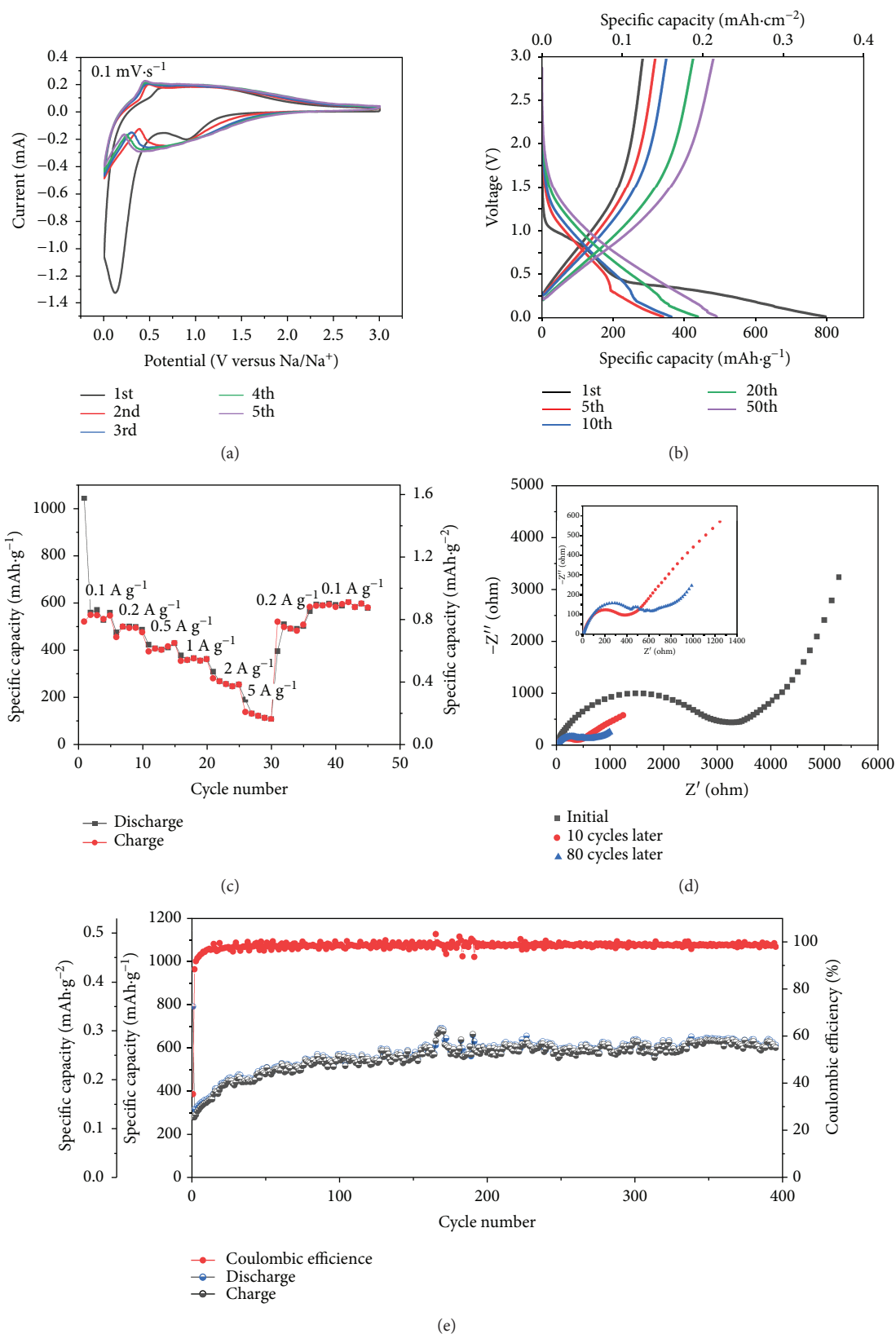


FIGURE 3: (a) CV tests at 0.1 mV·s<sup>-1</sup>. (b) Galvanostatic charge-discharge curves of CNF-TiO<sub>2</sub> recorded at 200 mA·g<sup>-1</sup>; (c) rate performance of CNF-TiO<sub>2</sub>; (d) EIS of CNF-TiO<sub>2</sub> before and after cycles; (e) cycling stability of CNF-TiO<sub>2</sub> as anode for SIBs at 200 mA·g<sup>-1</sup>.

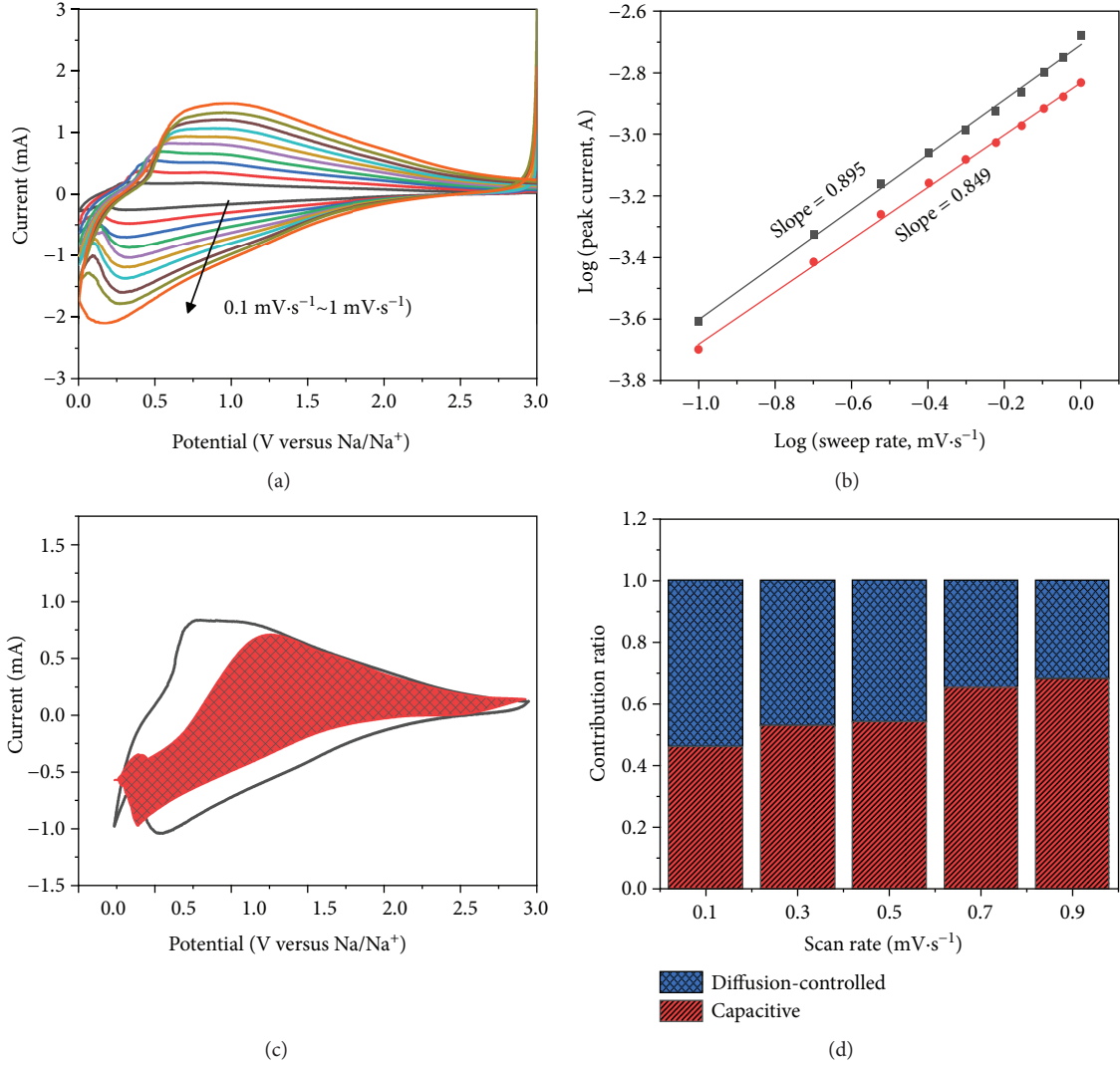


FIGURE 4: (a) CV curves of CNF-TiO<sub>2</sub> at different scan rates from 0.1 mV·s<sup>-1</sup> to 1 mV·s<sup>-1</sup>. (b) The relationship between peak current ( $i$ ) and scan rates ( $v$ ). (c) The contribution of capacitive (red) and battery (blank) reaction at 0.5 mV·s<sup>-1</sup>. (d) The ratio of capacitive and battery contribution at different scan rates.

mass of TiO<sub>2</sub>, while the carbon substrate may contribute partial capacity. It should be noted that the capacity increases during the initial cycles, which might be attributed to the active process owing to the 3D interconnected nanostructure of CNF-TiO<sub>2</sub> [16].

To further unravel the electrochemical kinetic properties of CNF-TiO<sub>2</sub> as anode in SIBs, CV tests at different scan rates from 0.1 mV·s<sup>-1</sup> to 1 mV·s<sup>-1</sup> are performed in Figure 4(a). All the CV cycles have a similar shape of broad peaks for Na<sup>+</sup> insertion/extraction. Also, the small peak shift with different scan rates indicates the smaller polarization of CNF-TiO<sub>2</sub>. The peak current ( $i$ ) of curves can be separated into two mechanism parts: diffusion-controlled and surface-controlled, which corresponds to battery and capacitive reaction, respectively.

In order to figure out the contribution of each part, the equation of  $i = a \cdot v^b$  [25, 26] linked peak current ( $i$ , mA) and scan rate ( $v$ , mV·s<sup>-1</sup>) is performed to qualitatively analyze the kinetics, which can also express as  $\log i = \log a +$

$b \cdot \log v$ .  $a$  and  $b$  are constants which are obtained from the experiments. The  $b$  value is represented by the slope of  $\log v - \log i$  plots. There are two limit cases: that  $b = 0.5$  means a diffusion-controlled mechanism (battery) and that  $b = 1$  represents a surface-controlled process (capacitive). As shown in Figure 4(b), the cathodic peaks show the estimated  $b$  value of 0.895 and anodic peaks of 0.849 from 0.1 mV·s<sup>-1</sup> to 1 mV·s<sup>-1</sup>, which means the electrochemical kinetic of CNF-TiO<sub>2</sub> as anode is the combined mechanism of diffusion control and surface control (dominant).

Furthermore, the capacitive contribution and battery contribution can be separately quantitatively analyzed by the equation  $i = k_1 v + k_2 v^{1/2}$  [20], where  $i$  is the current at a fixed voltage with different scan rates, and  $k_1 v$  and  $k_2 v^{1/2}$  originated from the contribution of surface-controlled and diffusion-controlled reaction, respectively. In order to easily calculate, this formula can be transformed to  $i/v^{1/2} = k_1 v^{1/2} + k_2$ . Then,  $k_1$  and  $k_2$  can be obtained from the fitting plot of  $v^{1/2} - i/v^{1/2}$ . Figure 4(c) shows that the current is derived

from two parts with the obvious red shadow area and blank space representing capacitive and battery reaction, respectively, which indicates that the contribution of capacitive effect is 54.3%. Figure 4(d) exhibits the capacity contribution increasing with the rising scan rates, 46.2% ( $0.1 \text{ mV}\cdot\text{s}^{-1}$ ), 53% ( $0.3 \text{ mV}\cdot\text{s}^{-1}$ ), 54.3% ( $0.5 \text{ mV}\cdot\text{s}^{-1}$ ), 65.4% ( $0.7 \text{ mV}\cdot\text{s}^{-1}$ ), and 68.4% ( $0.9 \text{ mV}\cdot\text{s}^{-1}$ ). These capacitive contributions reveal that CNF-TiO<sub>2</sub> as anode can shorten the electron transfer path and decrease the barrier of Na<sup>+</sup> insertion/extraction.

#### 4. Conclusion

In summary, this flexible freestanding CNF-TiO<sub>2</sub> can be successfully synthesized by a facile electrospinning method followed by pyrolysis treatment at 700°C. This material as anode exhibits high specific reversible capacity of  $614 \text{ mAh}\cdot\text{g}^{-1}$  ( $0.27 \text{ mAh}\cdot\text{cm}^{-2}$ ), excellent rate performance, and long-cycle stability at  $200 \text{ mA}\cdot\text{g}^{-1}$ , which can be ascribed to the long-range continuous conductive carbon nanofibers and TiO<sub>2</sub> nanoparticles with excellent structural stability and larger lattice of 0.363 nm than the radius of Na<sup>+</sup>. After almost 400 cycles, the capacity retention keeps ~100%, which indicates the high reversible performance and excellent tolerance of volume change in the process of Na<sup>+</sup> insertion/extraction.

#### Data Availability

The data used to support the findings of this study are included within the article.

#### Conflicts of Interest

The authors declare that they have no conflicts of interest.

#### Acknowledgments

The authors acknowledge the financial support from the National Natural Science Foundation of China Program (no. 51602111), Cultivation project of National Engineering and Technology Center (2017B090903008), Xijiang R&D Team (Xin Wang), Guangdong Provincial Grant (2015A030310196 and 2017A050506009), Special Fund Project of Science and Technology Application in Guangdong (2017B020240002), and 111 project.

#### References

- [1] H. Hou, X. Qiu, W. Wei, Y. Zhang, and X. Ji, "Carbon anode materials for advanced sodium-ion batteries," *Advanced Energy Materials*, vol. 7, no. 24, article 1602898, 2017.
- [2] Y. J. Zhu, X. G. Han, Y. H. Xu et al., "Electrospun Sb/C fibers for a stable and fast sodium-ion battery anode," *ACS Nano*, vol. 7, no. 7, pp. 6378–6386, 2013.
- [3] H. Park, J. Kwon, H. Choi, D. Shin, T. Song, and X. W. D. Lou, "Unusual Na<sup>+</sup> ion intercalation/deintercalation in metal-rich Cu<sub>1.8</sub>S for Na-ion batteries," *ACS Nano*, vol. 12, no. 3, pp. 2827–2837, 2018.
- [4] Q. Sun, L. Fu, and C. Shang, "A novel open-framework Cu-Ge-based chalcogenide anode material for sodium-ion battery," *Scanning*, vol. 2017, Article ID 3876525, 6 pages, 2017.
- [5] L. Fu, X. Wang, J. Ma et al., "Graphene-encapsulated copper tin sulfide submicron spheres as high-capacity binder-free anode for lithium-ion batteries," *ChemElectroChem*, vol. 4, no. 5, pp. 1124–1129, 2017.
- [6] S. Tan, Y. Jiang, Q. Wei et al., "Multidimensional synergistic nanoarchitecture exhibiting highly stable and ultrafast sodium-ion storage," *Advanced materials*, vol. 30, no. 18, article e1707122, 2018.
- [7] Q. Chen, S. Sun, T. Zhai, M. Yang, X. Zhao, and H. Xia, "Yolk-shell NiS<sub>2</sub> nanoparticle-embedded carbon fibers for flexible fiber-shaped sodium battery," *Advanced Energy Materials*, vol. 8, no. 19, article 1800054, 2018.
- [8] P. Hu, X. Wang, T. Wang et al., "Boron substituted Na<sub>3</sub>V<sub>2</sub>(P<sub>1-x</sub>B<sub>x</sub>O<sub>4</sub>)<sub>3</sub> cathode materials with enhanced performance for sodium-ion batteries," *Advanced science*, vol. 3, no. 12, article 1600112, 2016.
- [9] X. Wang, C. Niu, J. Meng et al., "Novel K<sub>3</sub>V<sub>2</sub>(PO<sub>4</sub>)<sub>3</sub>/C bundled nanowires as superior sodium-ion battery electrode with ultra-high cycling stability," *Advanced Energy Materials*, vol. 5, no. 17, article 1500716, 2015.
- [10] C. Xu, Y. Xu, C. Tang et al., "Carbon-coated hierarchical NaTi<sub>2</sub>(PO<sub>4</sub>)<sub>3</sub> mesoporous microflowers with superior sodium storage performance," *Nano Energy*, vol. 28, pp. 224–231, 2016.
- [11] M. L. Mao, F. L. Yan, C. Y. Cui et al., "Pipe-wire TiO<sub>2</sub>-Sn@carbon nanofibers paper anodes for lithium and sodium ion batteries," *Nano Letters*, vol. 17, no. 6, pp. 3830–3836, 2017.
- [12] Y. Wu, Y. Jiang, J. Shi, L. Gu, and Y. Yu, "Multichannel porous TiO<sub>2</sub> hollow nanofibers with rich oxygen vacancies and high grain boundary density enabling superior sodium storage performance," *Small*, vol. 13, no. 22, p. 8, 2017.
- [13] Y. Zhang, C. W. Wang, H. S. Hou, G. Q. Zou, and X. B. Ji, "Nitrogen doped/carbon tuning yolk-like TiO<sub>2</sub> and its remarkable impact on sodium storage performances," *Advanced Energy Materials*, vol. 7, no. 4, p. 12, 2017.
- [14] D. Guan, Q. Yu, C. Xu et al., "Aerosol synthesis of trivalent titanium doped titania/carbon composite microspheres with superior sodium storage performance," *Nano Research*, vol. 10, no. 12, pp. 4351–4359, 2017.
- [15] Y.-E. Zhu, L. Yang, J. Sheng et al., "Fast sodium storage in TiO<sub>2</sub>@CNT@C nanorods for high-performance Na-ion capacitors," *Advanced Energy Materials*, vol. 7, no. 22, article 1701222, 2017.
- [16] H. He, Q. Gan, H. Wang et al., "Structure-dependent performance of TiO<sub>2</sub>/C as anode material for Na-ion batteries," *Nano Energy*, vol. 44, pp. 217–227, 2018.
- [17] X. Ma, J.-L. Tian, F. Zhao, J. Yang, and B.-F. Wang, "Conductive TiN thin layer-coated nitrogen-doped anatase TiO<sub>2</sub> as high-performance anode materials for sodium-ion batteries," *Ionics*, pp. 1–9, 2018.
- [18] J. Wang, G. Liu, K. Fan et al., "N-doped carbon coated anatase TiO<sub>2</sub> nanoparticles as superior Na-ion battery anodes," *Journal of Colloid and Interface Science*, vol. 517, pp. 134–143, 2018.
- [19] Y. L. Dingtao Ma, H. Mi, S. Luo et al., "Robust SnO<sub>2-x</sub> nanoparticle-impregnated carbon nanofibers with outstanding electrochemical performance for advanced sodium-ion batteries," *Angewandte Chemie International Edition*, vol. 57, no. 29, pp. 8901–8905, 2018.

- [20] B. Li, B. Xi, Z. Feng et al., "Hierarchical porous nanosheets constructed by graphene-coated, interconnected  $\text{TiO}_2$  nanoparticles for ultrafast sodium storage," *Advanced materials*, vol. 30, no. 10, 2018.
- [21] P. He, Y. Fang, X. Y. Yu, and X. W. D. Lou, "Hierarchical nanotubes constructed by carbon-coated ultrathin SnS nanosheets for fast capacitive sodium storage," *Angewandte Chemie International Edition*, vol. 56, no. 40, pp. 12202–12205, 2017.
- [22] Q. Gan, H. He, K. Zhao, Z. He, S. Liu, and S. Yang, "Plasma-induced oxygen vacancies in urchin-like anatase titania coated by carbon for excellent sodium-ion battery anodes," *ACS Applied Materials & Interfaces*, vol. 10, no. 8, pp. 7031–7042, 2018.
- [23] J. Chen, G. Zou, H. Hou, Y. Zhang, Z. Huang, and X. Ji, "Pinecone-like hierarchical anatase  $\text{TiO}_2$  bonded with carbon enabling ultrahigh cycling rates for sodium storage," *Journal of Materials Chemistry A*, vol. 4, no. 32, pp. 12591–12601, 2016.
- [24] Y. Xiong, J. Qian, Y. Cao, X. Ai, and H. Yang, "Electrospun  $\text{TiO}_2/\text{C}$  nanofibers as a high-capacity and cycle-stable anode for sodium-ion batteries," *ACS Applied Materials & Interfaces*, vol. 8, no. 26, pp. 16684–16689, 2016.
- [25] X. Xu, J. Liu, J. Liu et al., "A general metal-organic framework (MOF)-derived selenidation strategy for in situ carbon-encapsulated metal selenides as high-rate anodes for Na-ion batteries," *Advanced Functional Materials*, vol. 28, no. 16, article 1707573, 2018.
- [26] P. Hu, X. Wang, J. Ma et al., " $\text{NaV}_3(\text{PO}_4)_3/\text{C}$  nanocomposite as novel anode material for Na-ion batteries with high stability," *Nano Energy*, vol. 26, pp. 382–391, 2016.

## Research Article

# Evaluation of A-Site Ba<sup>2+</sup>-Deficient Ba<sub>1-x</sub>Co<sub>0.4</sub>Fe<sub>0.4</sub>Zr<sub>0.1</sub>Y<sub>0.1</sub>O<sub>3-δ</sub> Oxides as Electrocatalysts for Efficient Hydrogen Evolution Reaction

Xiangnan Li,<sup>1,2</sup> Liqing He,<sup>1</sup> Xiongwei Zhong,<sup>1</sup> Jie Zhang,<sup>1</sup> Shijing Luo,<sup>1</sup> Wendi Yi,<sup>1</sup> Luozheng Zhang,<sup>1</sup> Manman Hu,<sup>1</sup> Jun Tang,<sup>1</sup> Xianyong Zhou,<sup>1</sup> Xingzhong Zhao,<sup>2</sup> and Baomin Xu <sup>1</sup>

<sup>1</sup>Department of Materials Science and Engineering, Southern University of Science and Technology, Shenzhen, Guangdong 518055, China

<sup>2</sup>Department of Physics, Wuhan University, Wuhan, Hubei 430072, China

Correspondence should be addressed to Baomin Xu; xubm@sustc.edu.cn

Received 28 March 2018; Revised 6 July 2018; Accepted 22 July 2018; Published 12 September 2018

Academic Editor: Masamichi Yoshimura

Copyright © 2018 Xiangnan Li et al. This is an open access article distributed under the Creative Commons Attribution License, which permits unrestricted use, distribution, and reproduction in any medium, provided the original work is properly cited.

Exploring earth-abundant and cost-effective catalysts with high activity and stability for a hydrogen evolution reaction (HER) is of great importance to practical applications of alkaline water electrolysis. Here, we report on A-site Ba<sup>2+</sup>-deficiency doping as an effective strategy to enhance the electrochemical activity of BaCo<sub>0.4</sub>Fe<sub>0.4</sub>Zr<sub>0.1</sub>Y<sub>0.1</sub>O<sub>3-δ</sub> for HER, which is related to the formation of oxygen vacancies around active Co/Fe ions. By comparison with the benchmarking Ba<sub>0.5</sub>Sr<sub>0.5</sub>Co<sub>0.8</sub>Fe<sub>0.2</sub>O<sub>3-δ</sub>, one of the most spotlighted perovskite oxides, the Ba<sub>0.95</sub>Co<sub>0.4</sub>Fe<sub>0.4</sub>Zr<sub>0.1</sub>Y<sub>0.1</sub>O<sub>3-δ</sub> oxide has lower overpotential and smaller Tafel slope. Furthermore, the Ba<sub>0.95</sub>Co<sub>0.4</sub>Fe<sub>0.4</sub>Zr<sub>0.1</sub>Y<sub>0.1</sub>O<sub>3-δ</sub> catalyst is ultrastable in an alkaline solution. The enhanced HER performance originated from the increased active atoms adjacent to oxygen vacancies on the surface of the Ba<sub>0.95</sub>Co<sub>0.4</sub>Fe<sub>0.4</sub>Zr<sub>0.1</sub>Y<sub>0.1</sub>O<sub>3-δ</sub> catalyst induced by Ba<sup>2+</sup>-deficiency doping. The low-coordinated active atoms and adjacent oxygen ions may play the role of heterojunctions that synergistically facilitate the Volmer process and thus render stimulated HER catalytic activity. The preliminary results suggest that Ba<sup>2+</sup>-deficiency doping is a feasible method to tailor the physical and electrochemical properties of perovskite, and that Ba<sub>0.95</sub>Co<sub>0.4</sub>Fe<sub>0.4</sub>Zr<sub>0.1</sub>Y<sub>0.1</sub>O<sub>3-δ</sub> is a potential catalyst for HER.

## 1. Introduction

The hydrogen fuel cell is considered as one of the most promising green solutions for new energy vehicles with the advantages of high working efficiency and zero emission [1–3]. Electrochemical water splitting is an efficient and promising energy storage technology to produce pure H<sub>2</sub>, benefiting from abundant water resources on the earth, via converting electrical energy generated from intermittent wind energy and solar energy into chemical energy [4, 5]. In the practical application of alkaline water electrolysis, it is still a great challenge to develop a highly efficient catalyst with low cost and good electrochemical stability for H<sub>2</sub> production. Though carbon-supported Pt (Pt/C) catalysts are reported to have

the highest activity toward hydrogen evolution reaction (HER), their widespread application is limited by their high cost, low crust abundance, and poor stability [6]. Therefore, the development of cost-effective and earth-abundant catalyst materials for HER with high activity and stability is of significant importance for realizing large-scale pure hydrogen production through alkaline water electrolysis.

Very recently, several nonnoble functional heterojunction-like-structured electrocatalysts, including metal/metal oxide/carbon hybrids [7, 8], transition-metal sulfides [9], and nitrides [5], have been reported to exhibit outstanding catalytic activities for HER. On these heterojunction-like-structured interfaces, positively-charged metal ion species could preferentially serve as an adsorption site for OH<sup>-</sup> (generated by H<sub>2</sub>O splitting) due

to the strong electrostatic affinity between each other, while a nearby metal or anion ion site would be kinetically beneficial for the adsorption of H. Consequently, these heterojunctions of metal cation/metal atom or anion are able to function synergistically in order to facilitate the Volmer process and thus render stimulated HER catalytic activity [7]. Benefiting from the advantage of flexibility in the oxidation states of transition metals and high tolerance of defective structures for oxygen vacancy or excess, the perovskite oxides with a general formula  $ABO_{3-\delta}$  (where A = rare earth or alkaline earth metal ions and B = transition-metal ions) can be engineered to fit a wide range of applications [10–12]. In a perovskite structure, the octahedral building containing a transition-metal cation and contiguous 6-fold coordinated oxygen anions could play the role of heterojunctions and possibly be reactive sites for HER. Very recently, the perovskite oxides  $Ba_{0.5}Sr_{0.5}Co_{0.8}Fe_{0.2}O_{3-\delta}$ ,  $Pr_{0.5}(Ba_{0.5}Sr_{0.5})_{0.5}Co_{0.8}Fe_{0.2}O_{3-\delta}$ , and  $SrNb_{0.1}Co_{0.7}Fe_{0.2}O_{3-\delta}$  were found to be highly active and stable for HER [13, 14], which demonstrate the remarkable effectiveness of perovskite oxides as candidates for the HER catalyst. However, up to now, studies on the activity of perovskite oxide for HER are scanty, due to the unclear HER mechanism on these materials. More works on perovskites are required for further study of the structure-activity correlation with respect to tunable electronic structures by doping modification, in order to optimize the activity for HER. In spite of the commonly used A-site and/or B-site partial substitution-doping modification, another effective way that is attracting increasing attention is to amend the surface redox chemistry and oxygen deficiency of perovskite oxides via getting A-site cationic deficiencies introduced into their lattice structure. As reported, a significantly improved electrochemical performance has been observed in oxygen reduction reaction with cationic-deficient perovskites (like  $Ba_{1-x}Co_{0.7}Fe_{0.2}Nb_{0.1}O_{3-\delta}$  ( $x = 0.00 - 0.15$ ) [15],  $La_{0.6}Sr_{0.4-x}Co_{0.2}Fe_{0.8}O_{3-\delta}$  ( $x = 0.0 - 0.2$ ) [16], and  $PrBa_{1-x}Co_{2}O_{5+\delta}$  ( $x = 0 - 0.08$ ) [16]) as electrocatalysts. However, there has been no reported work yet regarding the catalytic performance of a cation-deficient modification oxide in HER. In this study, the composition of  $BaCo_{0.4}Fe_{0.4}Zr_{0.1}Y_{0.1}O_{3-\delta}$  (BaCFZY) was chosen as the parent perovskite oxide for A-site  $Ba^{2+}$ -deficiency doping because BaCFZY was found to have a high ability for proton uptake by the incorporation of  $H_2O$  ( $H_2O + V_O^{\bullet\bullet} + O_O^{\times} \leftrightarrow 2OH^*$ ) and high structural stability in alkaline media, which would be favorable to HER [17]. Meanwhile, as a case study, we evaluated the HER activity of  $Ba_{0.5}Sr_{0.5}Co_{0.8}Fe_{0.2}O_{3-\delta}$  (BSCF), one of the most spotlighted perovskite oxides that is assumed to be a strong catalyst candidate for ORR/OER/HER given it is with high catalytic activity [10, 13, 18]. The effects of  $Ba^{2+}$  deficiency on the crystal structure, surface chemical properties, microstructure, electrochemical activity, and stability of BaCFZY for HER were carefully investigated. The results suggest that the additional negative charges introduced by an A-site  $Ba^{2+}$  deficiency are mainly compensated by the generation of oxygen vacancy. It is helpful to form the low-coordinated active Fe/Co cations which is beneficial to adsorb  $H_2O$  and  $OH^-$  and to promote the catalytic activity for HER.

## 2. Materials and Methods

**2.1. Synthesis of BCFZY and BSCF Oxides.**  $Ba_{1-x}Co_{0.4}Fe_{0.4}Zr_{0.1}Y_{0.1}O_{3-\delta}$  ( $Ba_{1-x}CFZY$ ,  $x = 0 - 0.05$ ) and BSCF oxides were synthesized by a combined EDTA-citrate complexing sol-gel method. Here, taking BaCFZY as an example, the stoichiometric amounts of Ba ( $NO_3$ )<sub>2</sub> (AR), Co( $NO_3$ )<sub>2</sub>·6H<sub>2</sub>O (AR), Fe( $NO_3$ )<sub>3</sub>·9H<sub>2</sub>O (AR), (Zr( $NO_3$ )<sub>4</sub>·5H<sub>2</sub>O (AR) and Y( $NO_3$ )<sub>3</sub>·6H<sub>2</sub>O (AR) were firstly dissolved in deionized water and added into an EDTA-NH<sub>3</sub>·H<sub>2</sub>O solution (pH ≈ 9) under heating and stirring to form an aqueous solution. Then, a certain amount of citric acid-NH<sub>3</sub>·H<sub>2</sub>O solution (pH ≈ 9) was introduced with a molar ratio of 1:1:2 for EDTA acid:total metal ions:citric acid. The resulting solution was evaporated at 80°C and 150°C in sequence to obtain a dark dry foam-structured precursor. The precursor was made to decompose on a hot plate followed by calcinations in a muffle furnace at 600°C for 5 h and 1050°C for 10 h to yield the desired oxide powders. The commercial catalysts Pt/C were purchased from SangLaiTe.

**2.2. Material Characterization.** Phase structures of as-synthesized  $Ba_{1-x}CFZY$  ( $x = 0.00 - 0.05$ ) and BSCF powders were characterized by X-ray diffraction measurement (XRD, D/max-2400 Rigaku, Tokyo) with a step size of 0.02° in  $2\theta$  using the scanning range of 20° to 80° at room temperature. To get more precise details of crystal structures, zero-point correction of XRD patterns was performed based on the X-ray diffraction theory. The morphologies of the catalysts were observed using a field-emission scanning electron microscope (SEM, TESCAN MIRA3). Energy dispersive X-ray spectroscopy (EDX) was carried out to analyze the contained elements in samples. The chemical compositions and surface element states were determined by X-ray photoelectron spectroscopy (XPS) (PHI 5000 VersaProbe II) with Al K $\alpha$  as an excitation source.

**2.3. Electrochemical Measurement.** The HER electrochemical activities of the investigated catalyst were evaluated in a three-electrode configuration with the aid of typical thin film rotating disk electrode systems (Pine Instrument Company, USA) on an electrochemical workstation (CHI 760). A standard Hg|HgO (1 M KOH) electrode and a graphite rod electrode were used as the reference and counter electrodes, respectively. The Hg|HgO (1 M KOH) electrode was calibrated with respect to the reversible hydrogen electrode (RHE) according to the Nernst equation ( $E$  versus RHE =  $E$  (Hg|HgO) + 0.098 + 0.0592 × pH) in 1 M KOH. The electrolyte was a 1 M KOH aqueous solution (Acros, 99.98%), which was saturated by N<sub>2</sub> by bubbling N<sub>2</sub> into it for more than 30 min prior to the test and maintained under a N<sub>2</sub> atmosphere throughout. The ink of the working electrodes was prepared by the ultrasonic dispersion of 5.0 mg of catalyst, 1.0 mg of acetylene black (AB) carbon, and 33  $\mu$ L of K<sup>+</sup>-exchanged Nafion solution into the mixture of 500  $\mu$ L of 2-methoxyl ethanol and 467  $\mu$ L of tetrahydrofuran for 1 h. Then, 10  $\mu$ L of the catalyst ink was dropped on the glassy carbon RDE (0.196 cm<sup>2</sup>, area) polished by 50 nm alumina slurry and rinsed by sonicating in pure water. Then, the RDE was

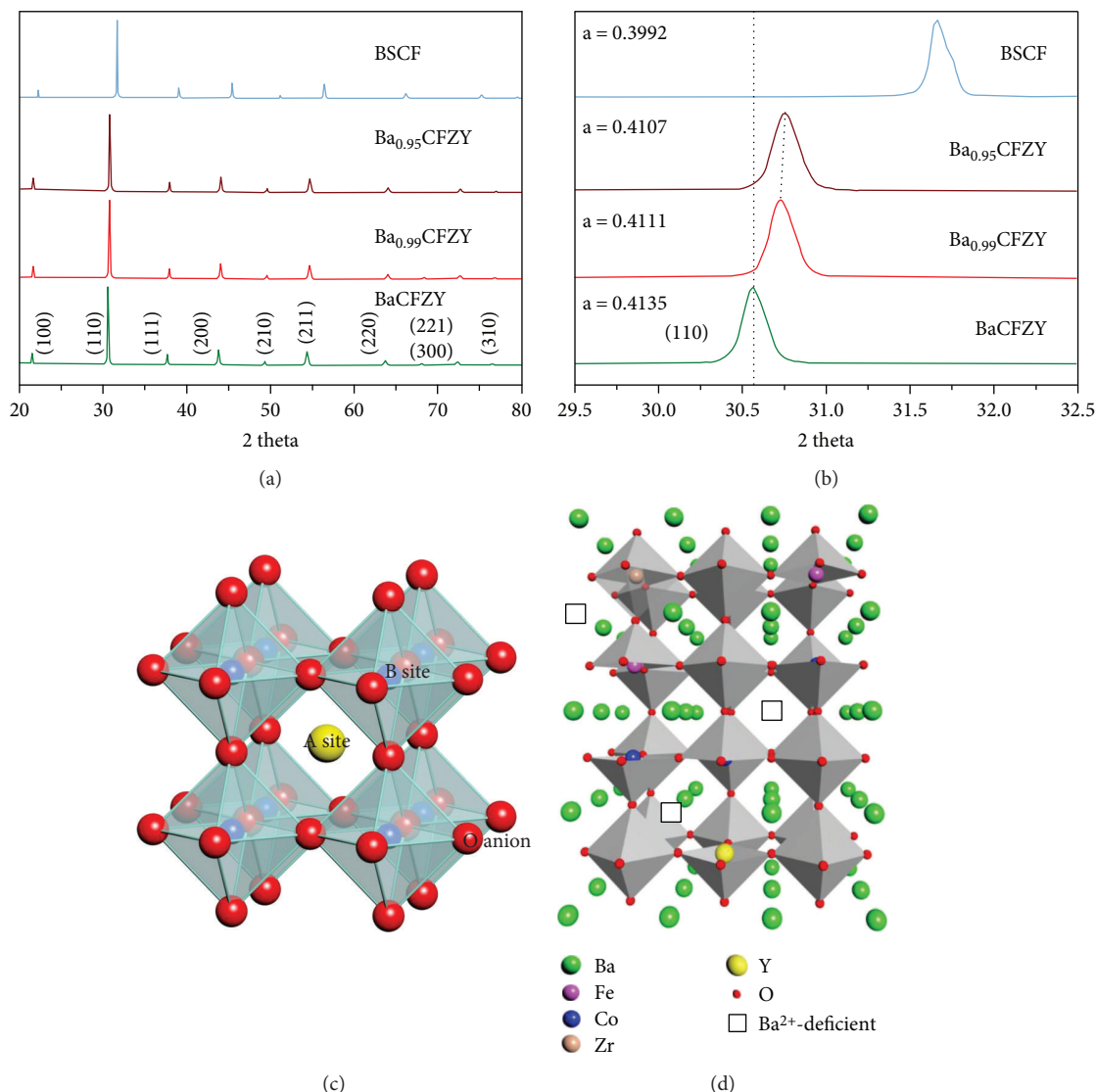


FIGURE 1: (a) XRD patterns and (b) magnified parts of the as-synthesized BSCF and Ba<sub>1-x</sub>CFZY ( $x = 0 - 0.05$ ) powders calcined at 1050°C for 10 h; (c) crystal structure schematic of a cubic perovskite oxide with the formula of ABO<sub>3</sub>; (d) crystal structure schematic of the Ba<sup>2+</sup>-deficient Ba<sub>1-x</sub>CFZY perovskite oxides.

rotated at 700 rpm until the film was dry (about 30 min), yielding a catalyst mass loading of  $0.255 \text{ mg}_{\text{oxide}} \text{ cm}_{\text{disk}}^{-2}$ . Before all the measurements, the catalyst was electrochemically activated via cyclic voltammetry in the potential range of  $-0.9$  to  $-1.65 \text{ V}$  (versus Hg|HgO) at  $100 \text{ mV s}^{-1}$  for 80 cycles with a rotating rate of 1600 rpm. The cyclic voltammetry measurement of HER activity was performed at  $10 \text{ mV s}^{-1}$  and 1600 rpm. The CV curve was capacity corrected by averaging the forward and reverse currents, and ohmic resistance was corrected according to the following equation:  $E_{iR\text{-corrected}} = E - iR$ , where  $i$  is the current, and  $R$  ( $\sim 0.5 \Omega$ ) is the ohmic resistance from an electrolyte measured via electrochemical impedance spectroscopy. The chronopotentiometry was carried out at  $20 \text{ mA cm}_{\text{disk}}^{-2}$  and 1600 rpm for 2 h. Electrochemical impedance spectroscopy measurement was performed at  $-0.9 \text{ V}$  and  $-1.6 \text{ V}$  versus Hg|HgO between 100 kHz and 10 Hz with an amplitude of 20 mV.

### 3. Results and Discussion

**3.1. Phase Structure and Micromorphology.** Figure 1 shows XRD patterns of BSCF and Ba<sub>1-x</sub>CFZY oxides with various Ba<sup>2+</sup> deficiencies ( $x = 0 - 0.05$ ) after calcination at 1050°C for 10 h. All the diffraction peaks could be indexed by a cubic  $Pm\text{-}3m$  space group without a detectable amount of impurities, indicating that the as-synthesized Ba<sub>1-x</sub>CFZY and BSCF powders are single phased and well crystallized. As we know, BSCF is a well-known perovskite oxide with the general formula ABO<sub>3</sub>. Figure 1(c) illustrates a typical crystal structure schematic of a cubic perovskite oxide. Thereunto, for BSCF Ba<sup>2+</sup>/Sr<sup>2+</sup> ions are at the A site and Co/Fe ions are situated at the B site (the center of the oxygen octahedron). While in the Ba<sub>1-x</sub>CFZY perovskite structure Figure 1(d), the A site is occupied by 12-fold coordinated Ba<sup>2+</sup> cations with a larger ionic radius, while the B site is occupied by smaller Co/Fe/Zr/

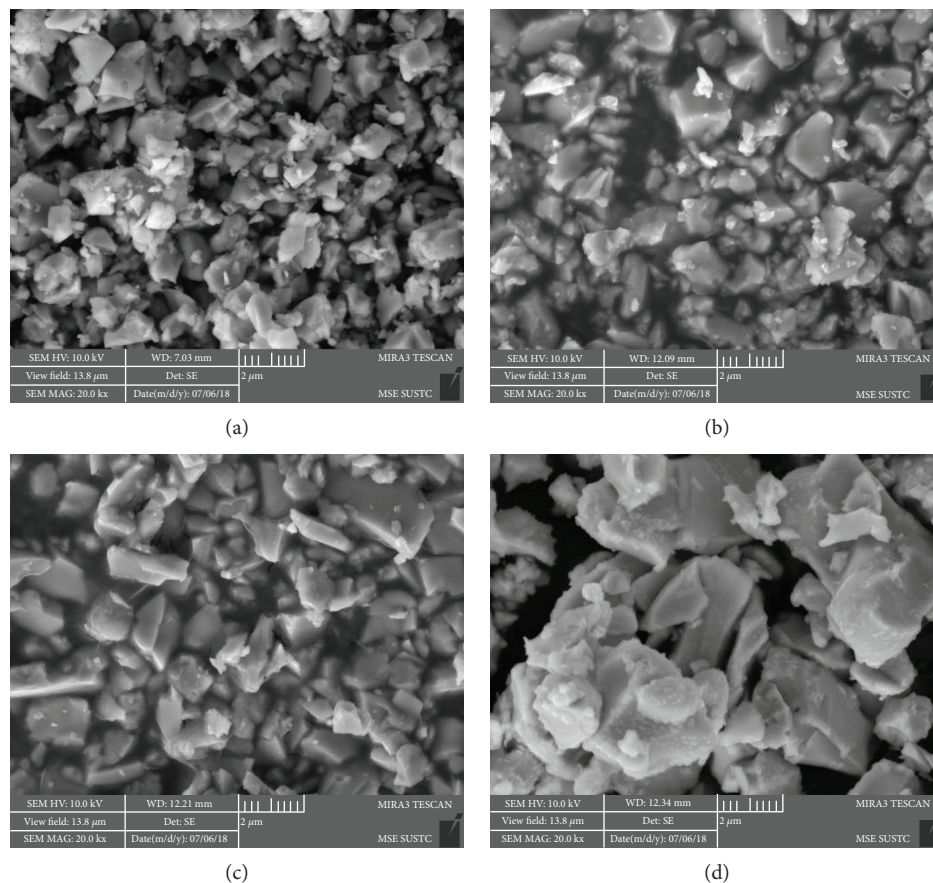


FIGURE 2: Typical SEM image of as-synthesized (a) BaCFZY, (b) Ba<sub>0.99</sub>CFZY, (c) Ba<sub>0.95</sub>CFZY, and (d) BSCF.

Y ions in 6-fold coordination to the oxygen anions (that is to say Co/Fe/Zr/Y ions are at the center of the oxygen octahedron). Moreover, from the magnified parts of the XRD patterns depicted in Figure 1(b), in comparison with BSCF, the diffraction peaks of Ba<sub>1-x</sub>CFZY ( $x = 0 - 0.05$ ) all shifted to lower  $2\theta$  angles, indicating an expansion in the perovskite lattice as a result of the introduction of the larger Zr<sup>4+</sup> (0.72 Å) and Y<sup>3+</sup> (0.9 Å) ions. In contrast, the diffraction peaks (110) for Ba<sub>1-x</sub>CFZY shift slightly to higher angles with the increase of Ba<sup>2+</sup> deficiency, indicating a lattice shrinkage probably from the increased electrostatic attraction [19]. Besides, the crystal lattice parameter could be obtained by the Bragg diffraction equation and be marked in Figure 1(b). The results indicate that with a higher Ba<sup>2+</sup> deficiency introduced from  $x = 0$  to  $x = 0.05$ , the lattice constant of Ba<sub>1-x</sub>CFZY is decreased slightly from 4.135 Å to 4.107 Å, but it is still larger than that of BSCF (0.399 Å). Figures 2(a) and 3(a) present typical SEM images for Ba<sub>1-x</sub>CFZY and BSCF. Unlike the classical perovskite powders of BSCF with an irregularly and aggregate shape [20], BaCFZY presents a uniformly distributed blocky appearance with more edge-like surfaces, which would provide more active sites for HER than that of BSCF. Besides, the corresponding energy-dispersive X-ray elemental (EDX) mapping as shown in Figures 2(c)-2(h) and 3(c)-3(g) suggests the homogeneous

distribution of Ba, Co, Fe, Zr, Y, and O for BCFZY as well as Ba, Sr, Co, Fe, and O for BSCF.

**3.2. X-Ray Photoelectron Spectroscopy Analysis.** To analyze the influence of the surface properties of BSCF and Ba<sub>1-x</sub>CFZY ( $x = 0 - 0.05$ ) on HER, the chemical states of the active elements of Co and Fe were measured by XPS and normalized with a C 1s peak to 284.6 eV. Via the narrow spectra of high-resolution XPS as shown in Figure 4, the peaks of Fe 2p<sub>3/2</sub>, Fe 2p<sub>1/2</sub>, and Co 2p<sub>1/2</sub> can be clearly identified in all samples, while it is difficult to separate out the Co 2p<sub>2/3</sub> peaks due to the overlap between Co 2p<sub>3/2</sub> and Ba 3d<sub>5/2</sub> main lines [14]. Meanwhile, the negative shift of the characteristic peaks of Fe 2p<sub>3/2</sub>, Fe 2p<sub>1/2</sub>, and Co 2p<sub>1/2</sub> together with Co 2p<sub>3/2</sub> @Ba3d<sub>2/5</sub> can be observed, indicating that the reduction of both Co and Fe cations in Ba<sub>1-x</sub>CFZY as compared to BSCF [13, 21]. Additionally, both of the Co 2p and Fe 2p peak positions of Ba<sub>1-x</sub>CFZY ( $x = 0 - 0.05$ ) are almost invariant, and only a slight increment shift (~0.1 eV for Co and ~0.06 eV for Fe) from BaCFZY to Ba<sub>0.95</sub>CFZY was detected. The little change of peak position implies that the additional negative charges introduced by the A-site Ba<sup>2+</sup> deficiency are barely compensated by the oxidation of B-site Co/Fe ions to a higher valence state in Ba<sub>1-x</sub>CFZY ( $x = 0 - 0.05$ ), but mainly by the generation of oxygen vacancy. Namely, the

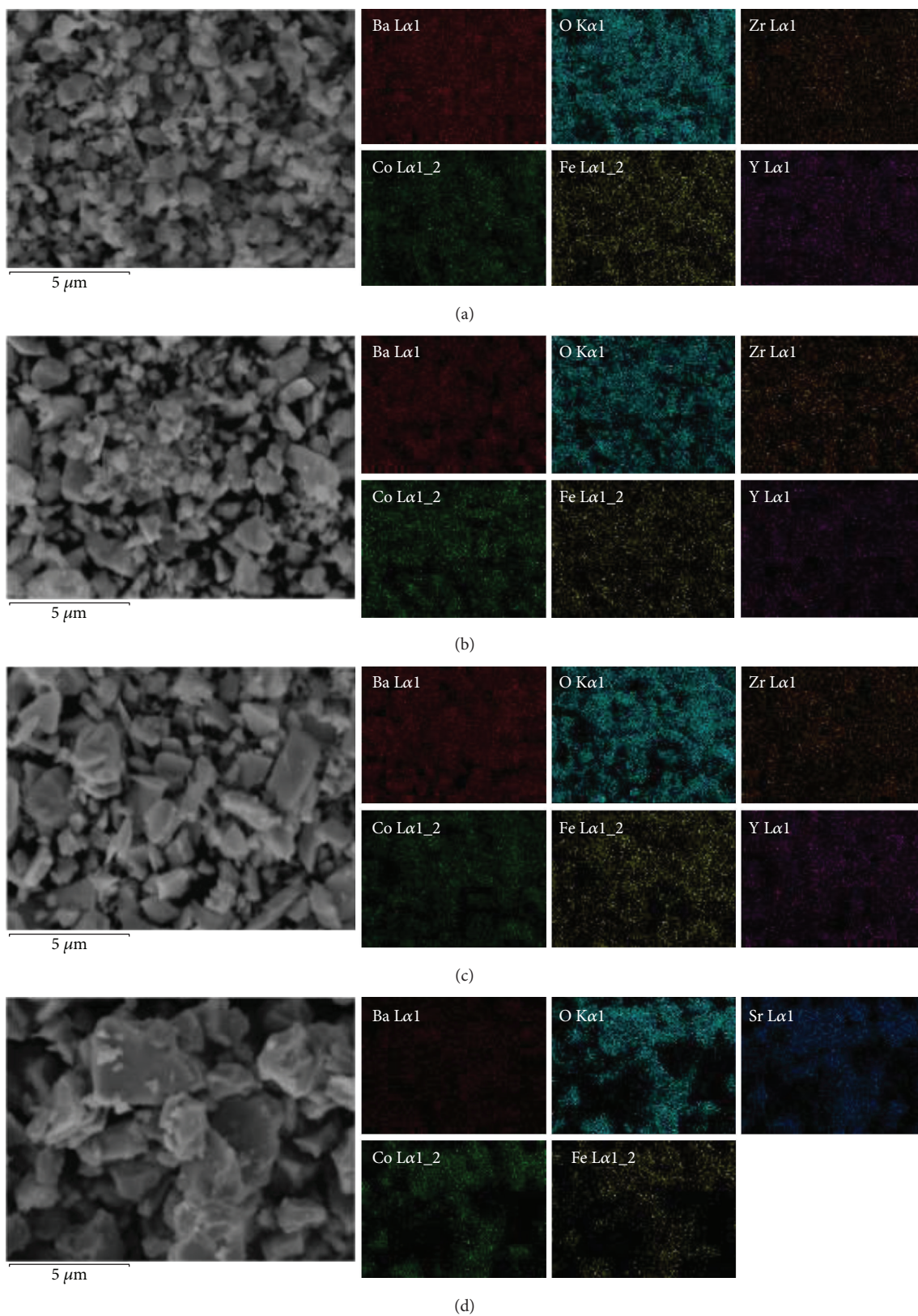


FIGURE 3: High-resolution SEM image and the corresponding EDX element mapping of (a) BaCFZY, (b) Ba<sub>0.99</sub>CFZY, (c) Ba<sub>0.95</sub>CFZY, and (d) BSCF.

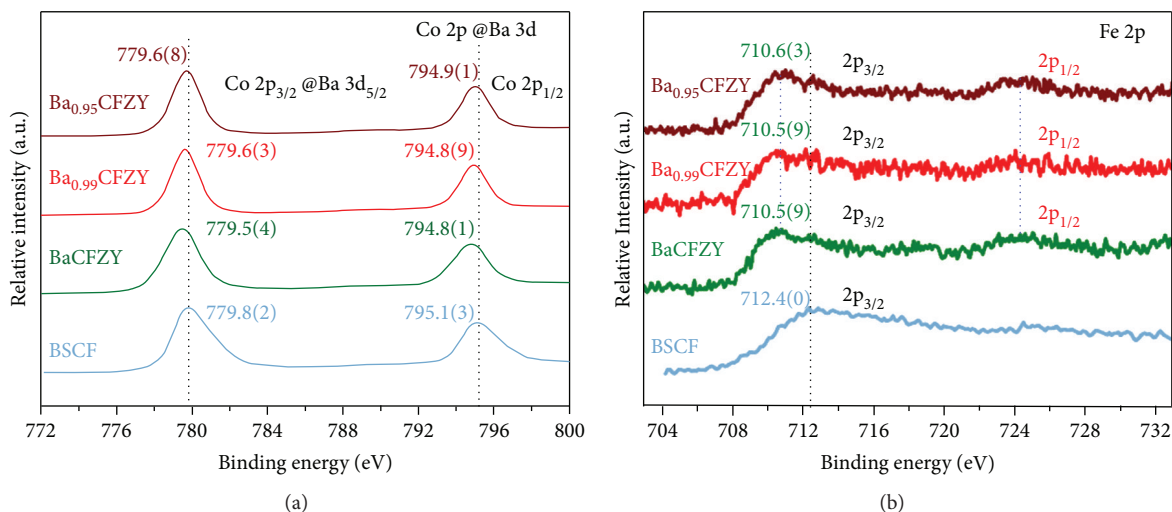


FIGURE 4: (a) Co 2p and Ba 3d core-level XPS results of BSCF and Ba<sub>1-x</sub>CFZY ( $x = 0 - 0.05$ ). (b) Fe 2p core-level XPS results of BSCF and Ba<sub>1-x</sub>CFZY ( $x = 0 - 0.05$ ).

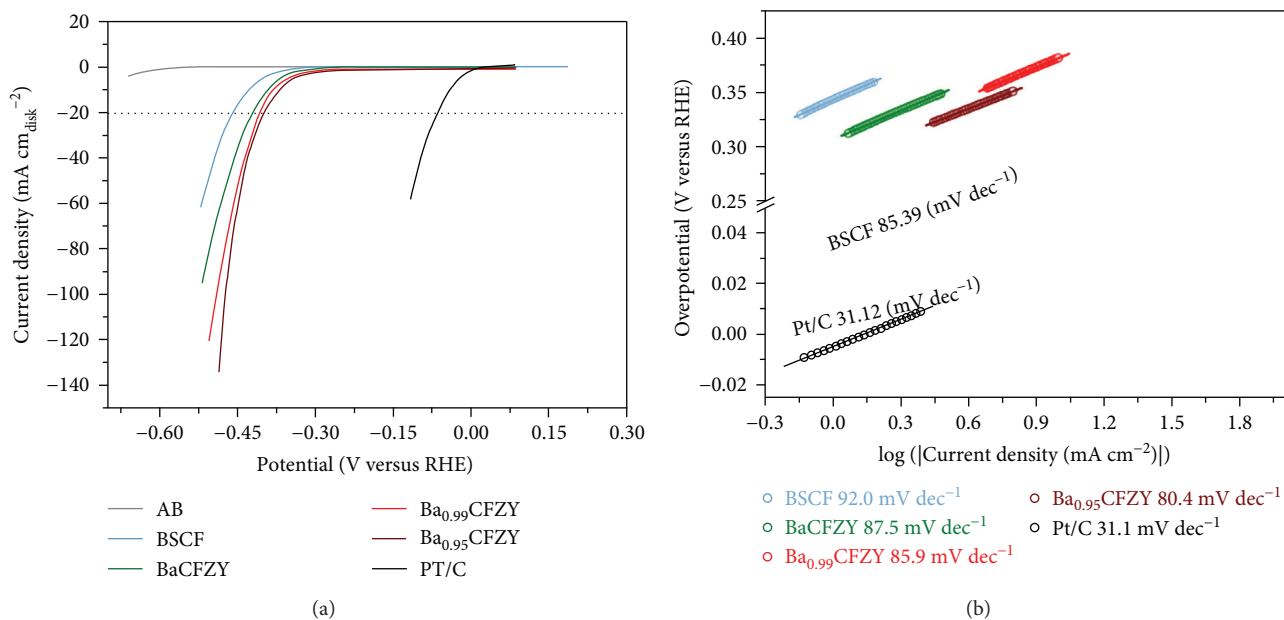


FIGURE 5: (a) Polarization curves and (b) the corresponding Tafel plots of BSCF, Ba<sub>1-x</sub>CFZY ( $x = 0 - 0.05$ ), and commercial Pt/C catalysts. The background HER activity of a conductive acetylene black- (AB-) supported GC electrode is shown for reference.

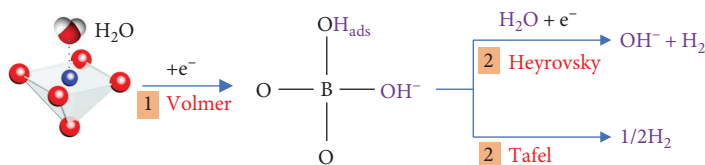


FIGURE 6: Schematic diagram of the HER reaction pathway on perovskite oxide.

introduction of Ba<sup>2+</sup> deficiency will create more oxygen vacancy in the lattice (like the case of (Ba<sub>0.5</sub>Sr<sub>0.5</sub>)<sub>1-x</sub>Co<sub>0.8</sub>Fe<sub>0.2</sub>O<sub>3-δ</sub> [22], PrBa<sub>1-x</sub>Fe<sub>2</sub>O<sub>5+δ</sub> [23], and La<sub>0.6</sub>Sr<sub>0.4-x</sub>Co<sub>0.2</sub>Fe<sub>0.8</sub>O<sub>3-δ</sub> [16]) which is helpful to form the low-coordinated activity of Fe/Co cations which facilitates the

adsorption of H<sub>2</sub>O and OH<sup>-</sup>, and is expected to be beneficial to promote the catalytic activity for HER.

3.3. *Catalytic Activity for HER.* To evaluate the electrochemical catalytic activity of Ba<sub>1-x</sub>CFZY ( $x = 0 - 0.05$ ) for HER,

the catalytic performance of BSCF, commercial Pt/C, and acetylene black (AB) was measured simultaneously for comparison. All of the polarization curves described in Figure 5(a) were capacity corrected by averaging the forward and backward currents of the CV curves, and were normalized to the geometric area of the GC electrode. It can be seen that Pt/C exhibits superior HER activity in alkaline media with a near-zero onset overpotential, and the conductive acetylene black shows negligible HER activity in the investigated potential range. All  $\text{Ba}_{1-x}\text{CFZY}$  samples show much smaller onset potential than that of BSCF. (e.g., to achieve a current density of  $0.5 \text{ mA cm}^{-2}$  and  $1 \text{ mA cm}^{-2}$ , the overpotential needed is 27 mV and 254 mV for  $\text{Ba}_{0.95}\text{CFZY}$ , while for BSCF the overpotential is 270 mV and 306 mV, resp.). The HER performance of  $\text{Ba}_{1-x}\text{CFZY}$  was found to be enhanced by A-site  $\text{Ba}^{2+}$ -deficiency doping. The activity of perovskite oxides  $\text{Ba}_{1-x}\text{CFZY}$  in catalyzing HER was further evaluated using the overpotential required to deliver an electrode current density of  $10 \text{ mA cm}^{-2}$  ( $\eta_{10}$ )—a desirable current density on the basis of 10% solar-to-fuel conversion efficiency.  $\text{Ba}_{0.95}\text{CFZY}$  shows the lowest  $\eta_{10}$  of 360 mV in  $\text{Ba}_{1-x}\text{CFZY}$ , which is much lower than that of BSCF (430 mV). Although this value is larger than that of commercial Pt/C, it is comparable to many other homogenous-structured non-Pt catalysts (noble metal-free or transition-metal complex-based catalysts) for HER in alkaline medium, such as Ni [24], Co-NRCNTs [6], and  $\text{Mn}_1\text{Ni}_1$  [25]. Moreover, the Tafel plots depicted in Figure 5(b) were calculated to get an insight into the HER kinetic processes of the catalysts. The Pt/C catalyst shows a Tafel slope of  $31.2 \text{ mV dec}^{-1}$ , which is consistent with the reported values [11, 26]. The Tafel slope of  $\text{Ba}_{0.95}\text{CFZY}$  is  $80.4 \text{ mV dec}^{-1}$ , which is lower than those of  $\text{Ba}_{0.99}\text{CFZY}$  ( $85.9 \text{ mV dec}^{-1}$ ),  $\text{BaCFZY}$  ( $87.5 \text{ mV dec}^{-1}$ ), and BSCF ( $92.0 \text{ mV dec}^{-1}$ ). The substantially enhanced HER activity achieved by the introduction of  $\text{Ba}^{2+}$  deficiency into the A site is further confirmed by the gradually decreased Tafel slope, demonstrating that the  $\text{Ba}^{2+}$ -deficiency doping plays a positive role in facilitating the kinetics process of water splitting. Additionally, the rate-limited step of HER can be assessed from the Tafel slope (slopes of  $\approx 120$ , 40, and  $30 \text{ mV dec}^{-1}$  corresponding to the Volmer, Heyrovsky, and Tafel reaction limitations, respectively [5, 9, 27]). It can be seen that all the observed Tafel slopes for BSCF and  $\text{Ba}_{1-x}\text{CFZY}$  catalysts are between 40 and  $120 \text{ mV dec}^{-1}$ , suggesting that electrochemical desorption is the rate-limited step in the catalysts and the HER process possibly occurs via a Volmer-Heyrovsky mechanism.

As well known, electrocatalytic HER proceeds through two charge-transfer steps in alkaline media. The first step is a Volmer reaction ( $\text{H}_2\text{O} + \text{e}^- \rightarrow \text{H}_{\text{ads}} + \text{OH}^-$ ), in which the water molecule adsorbed on the catalyst surface is ionized and transferred to be  $\text{H}_{\text{ads}}$ . The second step is either a Heyrovsky reaction ( $\text{H}_2\text{O} + \text{H}_{\text{ads}} + \text{e}^- \rightarrow \text{H}_2 + \text{OH}^-$ ) or a Tafel reaction ( $\text{H}_{\text{ads}} + \text{H}_{\text{ads}} \rightarrow \text{H}_2$ ) [26]. Both of the HER pathways (Volmer-Heyrovsky or Volmer-Tafel pathway) involved the adsorption of water molecules on the active sites, electrochemical reduction of adsorbed water molecules into adsorbed hydroxyl ions ( $\text{OH}^-$ ) and  $\text{H}_{\text{ads}}$ , desorption of  $\text{OH}^-$  to refresh the catalyst surface, and formation of  $\text{H}_{\text{ads}}$  for  $\text{H}_2$  generation [7]. Therefore,

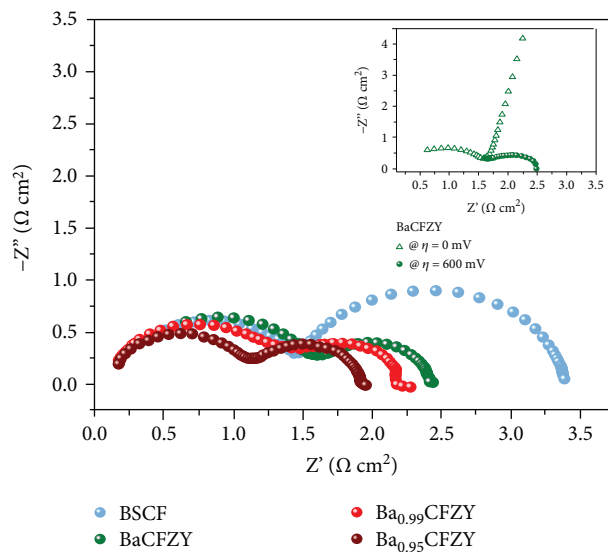


FIGURE 7: EIS Nyquist plots of BSCF and  $\text{Ba}_{1-x}\text{CFZY}$  ( $x = 0 - 0.05$ ) catalysts collected at HER overpotential of 600 mV. The inset in Figure 7 shows the EIS Nyquist plots of the  $\text{BaCFZY}$  catalyst at various overpotentials.

according to the HER mechanism, the highly efficient HER process means that the catalyst has good  $\text{H}_2\text{O}$  adsorption abilities, strong affinity to  $\text{H}_{\text{ads}}$ , and facile desorption of  $\text{OH}^-$  on the active site. More importantly, early fundamental studies suggested that, in alkaline medium,  $\text{OH}^-$  competes with  $\text{H}_{\text{ads}}$  for surface active sites of metal-based catalysts, seriously poisoning the electrode and reducing overall rates [6]. Thus, the water-splitting process may also be influenced by the  $\text{OH}_{\text{ads}}$  species on the electrode [12, 28]. It is reported that the low-coordinated active atoms on the surface can serve as active sites accessible to the  $\text{OH}_{\text{ads}}$  species [28, 29]. Consequently, the increase of active atoms adjacent to oxygen vacancies will be beneficial for  $\text{OH}^-$  adsorption (generated from  $\text{H}_2\text{O}$  splitting) and can leave alone a nearby anion ion ( $\text{O}^{2-}$ ) site for  $\text{H}_{\text{ads}}$  (Figure 6). These low-coordinated active atoms and adjacent oxygen ions may play the role of heterojunctions that synergistically facilitate the Volmer process and thus render stimulated HER catalytic activity.

As we can conclude from the XPS results in Figure 4, the enhanced activity of  $\text{Ba}_{0.99}\text{CFZY}$  could be assigned to the formation of oxygen vacancies around active ions Co/Fe. Moreover, as the charge transfer resistance ( $R_{ct}$ ) has a direct bearing on HER processes, electrochemical impedance spectroscopy was conducted at an overpotential of 600 mV to investigate the electrode kinetics of HER process for BSCF and  $\text{Ba}_{1-x}\text{CFZY}$  catalysts. As can be observed from Nyquist plots in Figure 7, the introduction of  $\text{Ba}^{2+}$  deficiency results in an obvious semicircle decrease in the low-frequency zone, signifying the smaller  $R_{ct}$  of  $\text{Ba}_{1-x}\text{CFZY}$  as a result of  $\text{Ba}^{2+}$ -deficiency doping. The truth that all  $R_{ct}$  of  $\text{Ba}_{1-x}\text{CFZY}$  are smaller than that of BSCF, indicates a faster electron transferring and more facile HER kinetics at the electrode/electrolyte interface of  $\text{Ba}_{1-x}\text{CFZY}$  [13]. Thus, the facile method of introducing A-site deficiency in perovskite lattice could be an effective way of promoting HER catalytic activity.

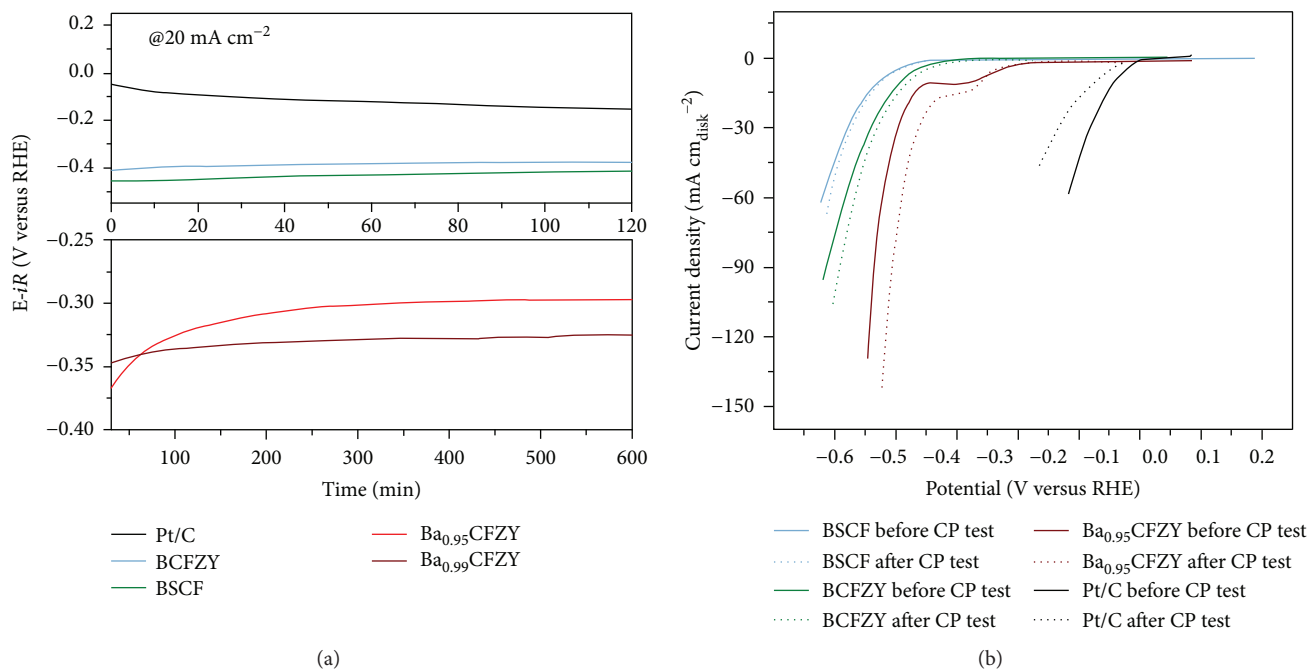


FIGURE 8: (a) Chronopotentiometry test curves of BSCF,  $\text{Ba}_{1-x}\text{CFZY}$ , and commercial Pt/C catalysts at a constant cathodic current density of  $20 \text{ mA cm}^{-2}$ . (b) Comparison of the HER activity curves of BSCF,  $\text{Ba}_{1-x}\text{CFZY}$ , and commercial Pt/C catalysts before and after chronopotentiometry measurement.

Stability is another important factor in the development of advanced electrocatalysts. To assess this, a chronopotentiometric (CP) test (Figure 8(a)) was carried out and the voltammograms (Figure 8(b)) before and after the CP test for 2 h at  $20 \text{ mA cm}^{-2}$  were compared. Pt/C exhibits the highest initial activity but undergoes a rapid degradation during the CP test, corresponding to its poor HER durability as reported [14]. In sharp contrast,  $\text{BaCFZY}$  even exhibits a decreasing operating overpotential over the same testing period, demonstrating its superior stability in the long-term electrochemical process. Meanwhile, the current density of the voltammogram of  $\text{BaCFZY}$  even increases slightly after 2 h of catalyzing HER, further indicating the stable HER electrocatalysis of  $\text{BaCFZY}$  in basic solutions. These results confirm the potentials of the  $\text{Ba}_{1-x}\text{CFZY}$  perovskite oxide as an efficient, stable, and economic HER catalyst.

In conclusion, A-site  $\text{Ba}^{2+}$ -deficiency doped  $\text{BaCo}_{0.4}\text{Fe}_{0.4}\text{Zr}_{0.1}\text{Y}_{0.1}\text{O}_{3-\delta}$  oxides,  $\text{Ba}_{1-x}\text{Co}_{0.4}\text{Fe}_{0.4}\text{Zr}_{0.1}\text{Y}_{0.1}\text{O}_{3-\delta}$  ( $\text{Ba}_{1-x}\text{CFZY}$ ,  $x = 0.00 - 0.05$ ) have been synthesized and evaluated as a kind of new electrocatalysts for HER in alkaline solutions. As a case study,  $\text{Ba}_{0.5}\text{Sr}_{0.5}\text{Co}_{0.8}\text{Fe}_{0.2}\text{O}_{3-\delta}$  (BSCF) oxides have also been synthesized and studied. The as-synthesized  $\text{Ba}_{1-x}\text{CFZY}$  and BSCF oxides are well-crystallized single phases, indexed with the cubic space group of  $Pm-3m$ . All  $\text{Ba}_{1-x}\text{CFZY}$  samples show a much lower onset potential and overpotential and smaller Tafel slope than that of BSCF. The HER performance of  $\text{BaCFZY}$  can be enhanced by simple A-site  $\text{Ba}^{2+}$ -deficiency doping. Electrochemical desorption is the rate-limited step on  $\text{Ba}_{1-x}\text{CFZY}$  catalyst surfaces and the HER process may occur via a Volmer-Heyrovsky mechanism. Furthermore,  $\text{Ba}_{1-x}\text{CFZY}$  exhibits superior stability in the long-term of the electrochemical process

compared with commercial Pt/C. The enhanced HER performance may originate from the increased oxygen vacancies around active Co/Fe ions on the surface of  $\text{Ba}_{1-x}\text{Co}_{0.4}\text{Fe}_{0.4}\text{Zr}_{0.1}\text{Y}_{0.1}\text{O}_{3-\delta}$  induced by  $\text{Ba}^{2+}$ -deficiency doping into the A site. These low-coordinated active atoms and contiguous oxygen ions may play the role of heterojunctions that synergistically facilitate the Volmer process and thus render stimulated HER catalytic activity, corresponding to a faster electron transfer and more facile HER kinetics at the electrode/electrolyte interface. The method of introducing A-site deficiency in perovskite lattice could be a facile and effective way to promote HER catalytic activity and this work sheds light on perovskite oxides as electrocatalysts for HER applications.

## Data Availability

The data used to support the findings of this study are available from the corresponding author upon request.

## Conflicts of Interest

The authors declare that they have no conflicts of interest.

## Authors' Contributions

Xiangnan Li and Liqing He contributed equally to this work.

## Acknowledgments

This work was supported by the Fundamental Research (Discipline Arrangement) project funded by the Shenzhen

Science and Technology Innovation Committee (Grant no. JCYJ20170412154554048), the Peacock Team Project funded by the Shenzhen Science and Technology Innovation Committee (Grant no. KQTD2015033110182370), and the National Key Research and Development Project funded by the Ministry of Science and Technology of China (Grant nos. 2016YFA0202400 and 2016YFA0202404).

## References

- [1] K. P. Gong, F. Du, Z. H. Xia, M. Durstock, and L. M. Dai, "Nitrogen-doped carbon nanotube arrays with high electrocatalytic activity for oxygen reduction," *Science*, vol. 323, no. 5915, pp. 760–764, 2009.
- [2] M. Shao, Q. Chang, J. P. Dodelet, and R. Chenitz, "Recent advances in electrocatalysts for oxygen reduction reaction," *Chemical Reviews*, vol. 116, no. 6, pp. 3594–3657, 2016.
- [3] J. Stacy, Y. N. Regmi, B. Leonard, and M. Fan, "The recent progress and future of oxygen reduction reaction catalysis: a review," *Renewable and Sustainable Energy Reviews*, vol. 69, pp. 401–414, 2017.
- [4] X. Zhao, X. Shang, Y. Quan et al., "Electrodeposition-solvothermal access to ternary mixed metal Ni-Co-Fe sulfides for highly efficient electrocatalytic water oxidation in alkaline media," *Electrochimica Acta*, vol. 230, pp. 151–159, 2017.
- [5] X. Zhong, L. Zhang, J. Tang et al., "Efficient coupling of a hierarchical  $V_2O_5@Ni_3S_2$  hybrid nanoarray for pseudocapacitors and hydrogen production," *Journal of Materials Chemistry A*, vol. 5, no. 34, pp. 17954–17962, 2017.
- [6] X. Zou, X. Huang, A. Goswami et al., "Cobalt-embedded nitrogen-rich carbon nanotubes efficiently catalyze hydrogen evolution reaction at all pH values," *Angewandte Chemie-International Edition*, vol. 53, no. 17, pp. 4372–4376, 2014.
- [7] M. Gong, W. Zhou, M. C. Tsai et al., "Nanoscale nickel oxide/nickel heterostructures for active hydrogen evolution electrocatalysis," *Nature Communications*, vol. 5, no. 1, p. 4695, 2014.
- [8] Y. Xie, X. Wang, K. Tang, Q. Li, and C. Yan, "Blending  $Fe_3O_4$  into a Ni/NiO composite for efficient and stable bifunctional electrocatalyst," *Electrochimica Acta*, vol. 264, pp. 225–232, 2018.
- [9] W. Zhou, D. Hou, Y. Sang et al., "MoO<sub>2</sub> nanobelts@nitrogen self-doped MoS<sub>2</sub> nanosheets as effective electrocatalysts for hydrogen evolution reaction," *Journal of Materials Chemistry A*, vol. 2, no. 29, p. 11358, 2014.
- [10] D. J. Chen, C. Chen, Z. M. Baiyee, Z. P. Shao, and F. Ciucci, "Nonstoichiometric oxides as low-cost and highly-efficient oxygen reduction/evolution catalysts for low-temperature electrochemical devices," *Chemical Reviews*, vol. 115, no. 18, pp. 9869–9921, 2015.
- [11] B. Hua, M. Li, Y.-Q. Zhang, Y.-F. Sun, and J.-L. Luo, "All-in-one perovskite catalyst: smart controls of architecture and composition toward enhanced oxygen/hydrogen evolution reactions," *Advanced Energy Materials*, vol. 7, no. 20, article 1700666, 2017.
- [12] J. Wang, Y. Gao, D. Chen et al., "Water splitting with an enhanced bifunctional double perovskite," *ACS Catalysis*, vol. 8, no. 1, pp. 364–371, 2017.
- [13] X. Xu, Y. Chen, W. Zhou et al., "A perovskite electrocatalyst for efficient hydrogen evolution reaction," *Advanced Materials*, vol. 28, no. 30, pp. 6442–6448, 2016.
- [14] Y. Zhu, W. Zhou, Y. Zhong et al., "A perovskite nanorod as bifunctional electrocatalyst for overall water splitting," *Advanced Energy Materials*, vol. 7, no. 8, article 1602122, 2017.
- [15] Z.-B. Yang, M.-F. Han, P. Zhu, F. Zhao, and F. Chen, " $Ba_{1-x}Co_{0.9-y}Fe_yNb_{0.1}O_{3-\delta}$  ( $x=0-0.15$ ,  $y=0-0.9$ ) as cathode materials for solid oxide fuel cells," *International Journal of Hydrogen Energy*, vol. 36, no. 15, pp. 9162–9168, 2011.
- [16] G. C. Kostoglouidis and C. Ftikos, "Properties of A-site-deficient  $La_{0.6}Sr_{0.4}Co_{0.2}Fe_{0.8}O_{3-\delta}$ -based perovskite oxides," *Solid State Ionics*, vol. 126, no. 1-2, pp. 143–151, 1999.
- [17] C. C. Duan, J. H. Tong, M. Shang et al., "Readily processed protonic ceramic fuel cells with high performance at low temperatures," *Science*, vol. 349, no. 6254, pp. 1321–1326, 2015.
- [18] B. Hua, M. Li, Y.-F. Sun et al., "A coupling for success: controlled growth of Co/CoO<sub>x</sub> nanoshoots on perovskite mesoporous nanofibres as high-performance trifunctional electrocatalysts in alkaline condition," *Nano Energy*, vol. 32, pp. 247–254, 2017.
- [19] S. Pang, X. Jiang, X. Li, Q. Wang, and Z. Su, "Characterization of Ba-deficient  $PrBa_{1-x}Co_2O_{5+\delta}$  as cathode material for intermediate temperature solid oxide fuel cells," *Journal of Power Sources*, vol. 204, pp. 53–59, 2012.
- [20] X. Xu, Y. Pan, W. Zhou, Y. Chen, Z. Zhang, and Z. Shao, "Toward enhanced oxygen evolution on perovskite oxides synthesized from different approaches: a case study of  $Ba_{0.5}Sr_{0.5}Co_{0.8}Fe_{0.2}O_{3-\delta}$ ," *Electrochimica Acta*, vol. 219, pp. 553–559, 2016.
- [21] J.-I. Jung and D. D. Edwards, "X-ray photoelectron study on  $Ba_{0.5}Sr_{0.5}Co_xFe_{1-x}O_{3-\delta}$  (BSCF:  $x=0.2$  and  $0.8$ ) ceramics annealed at different temperature and  $pO_2$ ," *Journal of Materials Science*, vol. 46, no. 23, pp. 7415–7422, 2011.
- [22] W. Zhou, R. Ran, Z. P. Shao, W. Q. Jin, and N. P. Xu, "Evaluation of A-site cation-deficient ( $Ba_{0.5}Sr_{0.5}Co_{0.8}Fe_{0.2}O_{3-\delta}$  ( $x>0$ )) perovskite as a solid-oxide fuel cell cathode," *Journal of Power Sources*, vol. 182, no. 1, pp. 24–31, 2008.
- [23] T. Chen, S. Pang, X. Shen, X. Jiang, and W. Wang, "Evaluation of Ba-deficient  $PrBa_{1-x}Fe_2O_{5+\delta}$  oxides as cathode materials for intermediate-temperature solid oxide fuel cells," *RSC Advances*, vol. 6, no. 17, pp. 13829–13836, 2016.
- [24] H. Vrabel and X. L. Hu, "Molybdenum boride and carbide catalyze hydrogen evolution in both acidic and basic solutions," *Angewandte Chemie-International Edition*, vol. 51, no. 51, pp. 12703–12706, 2012.
- [25] M. Ledendecker, G. Clavel, M. Antonietti, and M. Shalom, "Highly porous materials as tunable electrocatalysts for the hydrogen and oxygen evolution reaction," *Advanced Functional Materials*, vol. 25, no. 3, pp. 393–399, 2015.
- [26] M. Tavakkoli, T. Kallio, O. Reynaud et al., "Single-shell carbon-encapsulated iron nanoparticles: synthesis and high electrocatalytic activity for hydrogen evolution reaction," *Angewandte Chemie-International Edition*, vol. 54, no. 15, pp. 4535–4538, 2015.
- [27] J. Zhang, B. Xiao, X. Liu et al., "Copper dopants improved the hydrogen evolution activity of earth-abundant cobalt pyrite catalysts by activating the electrocatalytically inert sulfur sites," *Journal of Materials Chemistry A*, vol. 5, no. 33, pp. 17601–17608, 2017.

- [28] K.-L. Yan, X. Shang, Z.-Z. Liu et al., "A facile method for reduced  $\text{CoFe}_2\text{O}_4$  nanosheets with rich oxygen vacancies for efficient oxygen evolution reaction," *International Journal of Hydrogen Energy*, vol. 42, no. 38, pp. 24150–24158, 2017.
- [29] H. D. Yang, Y. Liu, S. Luo et al., "Lateral-size-mediated efficient oxygen evolution reaction: insights into the atomically thin quantum dot structure of  $\text{NiFe}_2\text{O}_4$ ," *ACS Catalysis*, vol. 7, no. 8, pp. 5557–5567, 2017.

## Research Article

# L-Leucine Templated Biomimetic Assembly of SnO<sub>2</sub> Nanoparticles and Their Lithium Storage Properties

Peng Yu,<sup>1</sup> Mili Liu,<sup>1</sup> Haixiong Gong,<sup>1</sup> Fangfang Wu,<sup>1</sup> Zili Yi,<sup>2</sup> and Hui Liu<sup>1</sup> 

<sup>1</sup>College of Science, Hunan Agricultural University, Changsha 410128, China

<sup>2</sup>College of Bioscience and Biotechnology, Hunan Agricultural University, Changsha 410128, China

Correspondence should be addressed to Hui Liu; [liu.hui@hunau.edu.cn](mailto:liu.hui@hunau.edu.cn)

Received 27 May 2018; Accepted 30 July 2018; Published 19 August 2018

Academic Editor: Liqing He

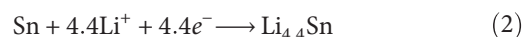
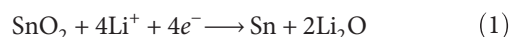
Copyright © 2018 Peng Yu et al. This is an open access article distributed under the Creative Commons Attribution License, which permits unrestricted use, distribution, and reproduction in any medium, provided the original work is properly cited.

SnO<sub>2</sub> nanoparticles have been synthesized by a novel route of a sol-gel method assisted with biomimetic assembly using L-leucine as a biotemplate. The microstructure of as-prepared SnO<sub>2</sub> nanoparticles was characterized by X-ray diffraction (XRD), scanning electron microscopy (SEM), Fourier transform infrared spectra (FT-IR), and Brunner–Emmet–Teller (BET) measurements. The results demonstrated that the growth of SnO<sub>2</sub> could be regulated by L-leucine at a high calcination temperature. The electrochemical performance of SnO<sub>2</sub> was also measured as anodes for lithium-ion battery. It is a guidance for the growth regulation of SnO<sub>2</sub> at high temperature to obtain SnO<sub>2</sub>/C with nanosized SnO<sub>2</sub> coated by a graphitic carbon.

## 1. Introduction

Lithium-ion batteries (LIBs) are the dominant power supply for portable electronics and also show promising applications for electric vehicles and power storage systems, due to their high specific energy, good cycling performance, high coulombic, and energy efficiency [1, 2]. In accordance with the increasing energy requirement for these industries, LIBs develop toward higher capacity, higher energy, and higher power. Therefore, it is of great significance to explore electrode materials with high capacity for the next generation LIBs. Graphite is the principal commercialized anode for LIBs since invented in 1991, but its explored capacity has been reached the theoretical limit (372 mAh/g) [3–10]. Metal oxides (Co<sub>3</sub>O<sub>4</sub>, Fe<sub>3</sub>O<sub>4</sub>, and SnO<sub>2</sub>) have been studied as anodes to enhance energy density of LIBs, for they can deliver higher capacity than graphite [11–13]. In this regard, SnO<sub>2</sub> has been considered as an outstanding alternative to graphite because of its high theoretical capacity of 782 mAh/g and moderate lithiation potential (~0.6 V vs. Li<sup>+</sup>/Li) [8, 14–17]. It is

commonly recognized that SnO<sub>2</sub> experiences a two-step lithiation process, namely,



The reaction shown in (1) is irreversible, which would induce low initial coulombic efficiency (CE) of ~50%. Additionally, SnO<sub>2</sub> electrode would suffer a large volume variation (~260%) resulted by the reaction of (2) as well as Sn, which would cause crack and collapse. And then, the capacity fading of SnO<sub>2</sub> is dramatical during cycling. To improve cycling performance for SnO<sub>2</sub>, tremendous investigations have indicated that SnO<sub>2</sub>/C composite anode with nanosized SnO<sub>2</sub>-coated carbon is the most effective strategy [15, 18–20]. In SnO<sub>2</sub>/C electrode, nanosized SnO<sub>2</sub> could sustain large volume change of Sn during lithiation and delithiation and carbon can buffer the volume change and also maintain the conductivity network for the whole electrode. Therefore, the cycling life

of SnO<sub>2</sub>/C would greatly be extended. However, most previous studies presented that SnO<sub>2</sub> was usually coated by amorphous carbon via the pyrolysis of carbonaceous organic material at 400~500°C, such as glucose. Unfortunately, amorphous carbon with a higher specific surface area might bring large amounts of side reactions with electrolyte, leading to a lower initial CE of SnO<sub>2</sub>. Besides, amorphous carbon usually shows higher average lithiation/delithiation voltage and larger voltage hysteresis, which would contribute little improvement in terms of energy density for LIBs in fact. Now, even since it has been reported that amorphous carbon can be catalytically graphitized at a lower temperature of about 600~700°C [21–23], SnO<sub>2</sub> particles would grow greatly large at this temperature and experience a rapid capacity fading as lithium-ion anodes. Accordingly, it is of importance to obtain nanosized SnO<sub>2</sub> and suppress its growth at 600~700°C for the application implementation of SnO<sub>2</sub>/C.

In this work, nanosized SnO<sub>2</sub> were synthesized by a sol-gel method assisted with biomimetic assembly. Biomimetic synthesis is a novel route to fabricate nanosized inorganic particles with organic templates. Investigations have identified that specific molecular interactions at inorganic-organic interfaces could result in the controlled nucleation and growth of inorganic crystals [24–26]. During the biomimetic assembly process, the organic template could promote self-assembly, recognize the reactant substrate, guide the nucleation, and limit the growth of inorganic particles by utilizing biological adsorption, hydrogen bond, van der Waals force, and so on. Considering that L-leucine could regulate the synthesis and the growth of organic particles and even enzymes, while no researches related to the regulation of inorganic materials by L-leucine could be found [27], we would like to control SnO<sub>2</sub> nucleation and growth by biomimetic assembly using L-leucine as a biomimetic template here. The regulated mechanism of SnO<sub>2</sub> synthesis and growth is studied for the first time in this work. Moreover, the electrochemical performance of as-prepared SnO<sub>2</sub> was also measured as lithium-ion anodes.

## 2. Experimental

**2.1. Preparation of Materials.** SnO<sub>2</sub> nanoparticles were synthesized by a sol-gel method assisted with biomimetic assembly using leucine as a biotemplate. Firstly, 9% of dilute aqua ammonia was dripped slowly into SnCl<sub>4</sub> (0.4 M/40 ml) including 0.001 mol L-leucine with continuous stirring in a water bath under 65°C. Secondly, the pH of the as-produced solution was adjusted to 3 and then kept stirring for 1 h to get white sol. Finally, the resulting sol was centrifuged, washed with ethanol and deionized water three times after keeping stand under 80°C for 24 h, respectively, and then dried at 80°C. The resultant was heated to 450°C, 550°C, and 650°C at a ramp rate of 10°C·min<sup>-1</sup> in the air for 4 h to get SnO<sub>2</sub>, named as L-SnO<sub>2</sub>-450°C, L-SnO<sub>2</sub>-550°C, and L-SnO<sub>2</sub>-650°C, respectively. For comparison, SnO<sub>2</sub> nanoparticles were also prepared using the same procedure without the L-leucine biotemplate, named as SnO<sub>2</sub>-450°C, SnO<sub>2</sub>-550°C, and SnO<sub>2</sub>-650°C.

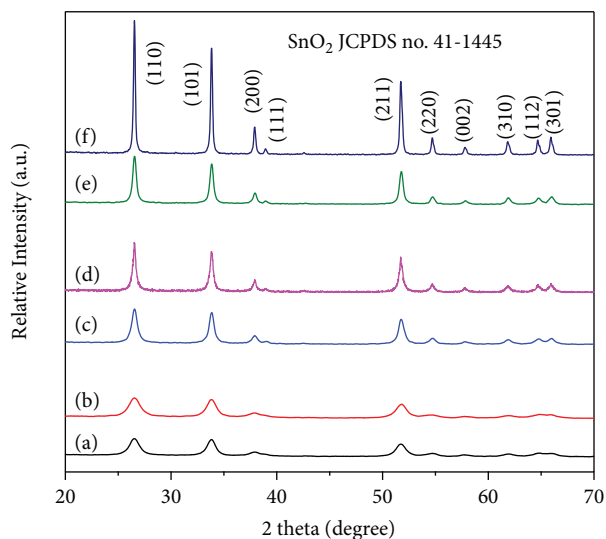


FIGURE 1: XRD patterns of as-prepared SnO<sub>2</sub> nanoparticles divided into three groups of (a) L-SnO<sub>2</sub>-450°C and (b) SnO<sub>2</sub>-450°C, (c) L-SnO<sub>2</sub>-550°C and (d) SnO<sub>2</sub>-550°C, and (e) L-SnO<sub>2</sub>-650°C and (f) SnO<sub>2</sub>-650°C.

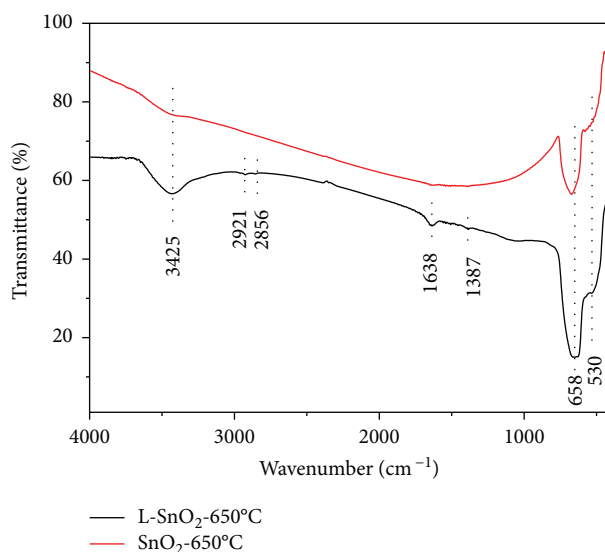


FIGURE 2: FT-IR spectrum of synthesized L-SnO<sub>2</sub>-650°C and SnO<sub>2</sub>-650°C.

**2.2. Material Characterization.** The microstructure of SnO<sub>2</sub> particles was carried out by a Shimadzu X-ray 6000 diffractometer (XRD) with CuK<sub>α</sub> radiation at 40 kV, 30 mA and a Quanta 250 FEG scanning electron microscope (SEM). Fourier transform infrared (FTIR) spectra were recorded using a Bruker Alpha spectrometer. Brunner–Emmet–Teller (BET) measurements were recorded using a QUADRASORB SI analyzer.

**2.3. Electrochemical Measurements.** The electrode slurry was prepared by mixing 90 wt% active material, 2 wt% super-p, and 8 wt% carboxymethyl cellulose (CMC). And then, the slurry was spread on Cu foil and dried at 120°C for 1 h. The electrochemical measurements of the electrodes were tested

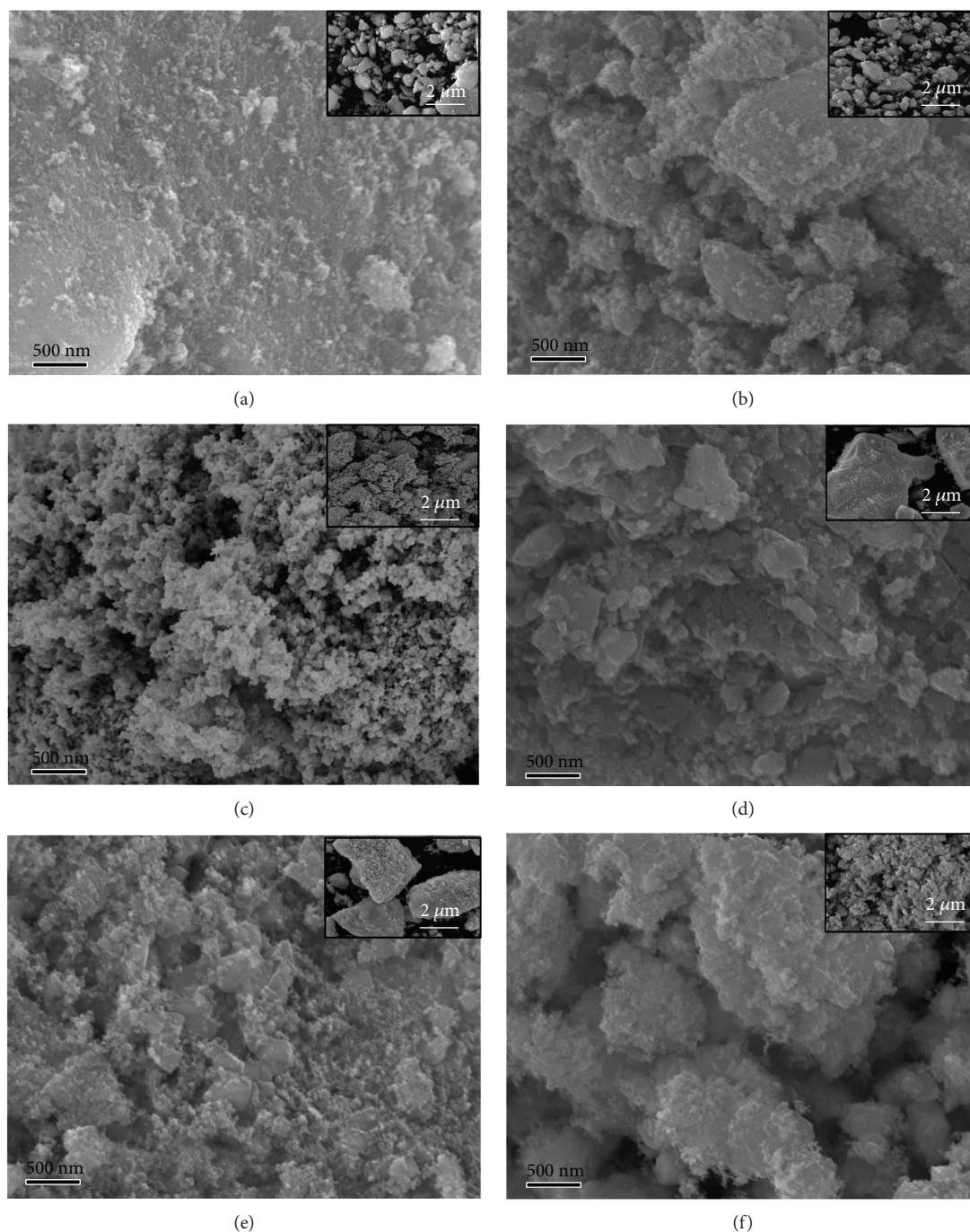


FIGURE 3: SEM images of (a) L-SnO<sub>2</sub>-450°C, (b) L-SnO<sub>2</sub>-550°C, (c) L-SnO<sub>2</sub>-650°C, (d) SnO<sub>2</sub>-450°C, (e) SnO<sub>2</sub>-550°C, and (f) SnO<sub>2</sub>-650°C.

using CR2032 coin cells assembled with Li foil as the counter and reference electrodes in an argon-filled glove box. The electrodes were separated by two layers of a Celgard separator. The electrolyte was 1 M LiPF<sub>6</sub> dissolved in a mixture of ethylene carbonate, ethyl methyl carbonate, and dimethyl carbonate (EC:EMC:DMC=1:1:1 in volume).

Cycle test was conducted with a system of LAND CT2001A from 0.005 to 2.5 V at a 0.1 C rate and trickle discharged at 0.005 V to a C/40 rate in the first three cycles. For subsequent cycles, cells were cycled from 0.005 to 2.5 V at a 0.2 C rate and trickle discharged at 0.005 V

to a C/20 rate. All electrochemical tests were carried out at ambient temperature.

### 3. Results and Discussion

Figure 1 compares the XRD patterns of as-prepared SnO<sub>2</sub> nanoparticles divided into three groups of (a) L-SnO<sub>2</sub>-450°C and (b) SnO<sub>2</sub>-450°C, (c) L-SnO<sub>2</sub>-550°C and (d) SnO<sub>2</sub>-550°C, and (e) L-SnO<sub>2</sub>-650°C and (f) SnO<sub>2</sub>-650°C. All patterns show obvious diffraction peaks at  $2\theta$  of 26.61°, 33.89°, 37.95°, 51.78°, and 65.94°, corresponding to (110),

(101), (200), (211), and (301) planes of rutile  $\text{SnO}_2$  (JCDF no. 41-1445), respectively. No peak corresponding to crystallographic impurities was observed, indicating the high purity of  $\text{SnO}_2$ . As the increase of calcination temperature from 450°C to 650°C, the diffraction peaks become sharp and the full width at half maximum (FWHM) narrows significantly for both L- $\text{SnO}_2$  and  $\text{SnO}_2$ , which is an indication that the grain size of  $\text{SnO}_2$  increases with an increase of calcination temperature. What is more, it could be observed that the grain size of  $\text{SnO}_2$  is finer in L- $\text{SnO}_2$  than that of  $\text{SnO}_2$  prepared without leucine templates under the same temperature. Moreover, such distinctions in  $\text{SnO}_2$  grain size get more evident as the calcination temperature increases.

Compared Figure 1(a) and (b), the FWHM of the  $\text{SnO}_2$  diffraction peak is very close for L- $\text{SnO}_2$ -450°C and  $\text{SnO}_2$ -450°C, while it is obviously wide in L- $\text{SnO}_2$ -550°C than  $\text{SnO}_2$ -550°C as shown in Figure 1(c) and (d). Especially in Figure 1(e) and (f), the diffraction peaks become much sharper in  $\text{SnO}_2$ -650°C than L- $\text{SnO}_2$ -650°C. Based on peak profile analysis using a Voigt function, it is confirmed that the grain size of  $\text{SnO}_2$  is calculated as 11.2, 16.7, and 20.5 nm for L- $\text{SnO}_2$ -450°C, L- $\text{SnO}_2$ -550°C, and L- $\text{SnO}_2$ -650°C, respectively, while 11.0, 23.0, and 39.2 nm for  $\text{SnO}_2$ -450°C,  $\text{SnO}_2$ -550°C, and  $\text{SnO}_2$ -650°C, respectively. It could be concluded that the  $\text{SnO}_2$  growth can be suppressed when synthesized by a sol-gel method assisted with biomimetic assembly using leucine as a biotemplate.

Figure 2 shows the FT-IR spectra of L- $\text{SnO}_2$ -650°C and  $\text{SnO}_2$ -650°C. The main peak of L- $\text{SnO}_2$ -650°C and  $\text{SnO}_2$ -650°C is at the same position of 658  $\text{cm}^{-1}$  attributed to the Sn-O-Sn asymmetric stretching mode of surface bridging oxide. It confirms  $\text{SnO}_2$  formation in L- $\text{SnO}_2$ -650°C and  $\text{SnO}_2$ -650°C. The weak peak is around 3425  $\text{cm}^{-1}$  in  $\text{SnO}_2$ -650°C corresponding to the stretching vibration of O-H bond, which may be due to the presence of water molecule on the surface of  $\text{SnO}_2$  nanoparticles and the stretching vibrations of Sn-OH groups [28, 29]. However, the peak of 530  $\text{cm}^{-1}$  assigned to Sn-O vibration of Sn-OH group is weak in  $\text{SnO}_2$ -650°C. Therefore, it could be considered that the peak around 3425  $\text{cm}^{-1}$  is mainly due to the vibration of absorbed water molecules. A stronger peak of 3425  $\text{cm}^{-1}$ , together with 1387  $\text{cm}^{-1}$  of  $-\text{CH}_3$  and 1638  $\text{cm}^{-1}$  of  $-\text{NH}_2$  in L- $\text{SnO}_2$ -650°C, is an indication of L-leucine residuum bonding with  $\text{SnO}_2$ , though  $\text{Sn}(\text{OH})_4$  precursor was washed by ethanol and deionized water before calcination.

It is predicted that the growth of  $\text{SnO}_2$  particles in L- $\text{SnO}_2$  gets suppressed for its direction and rate of interfacial migration between individual grains is regulated by L-leucine. This should maintain a block structure accompanied with wrinkled morphology and retain a smooth and dense surface structure for L- $\text{SnO}_2$ , while a large number of scattered particles and flakes increase to the surface of the control  $\text{SnO}_2$  group. When calcined at 650°C as shown in Figures 3(c) and 3(f), the block structure of L- $\text{SnO}_2$ -650°C and  $\text{SnO}_2$ -650°C has damaged at a certain degree, with  $\text{SnO}_2$  nanoparticles reuniting on the various surfaces and edges along the block. It should be noted that L- $\text{SnO}_2$ -650°C shows highly porous foam-like morphology.

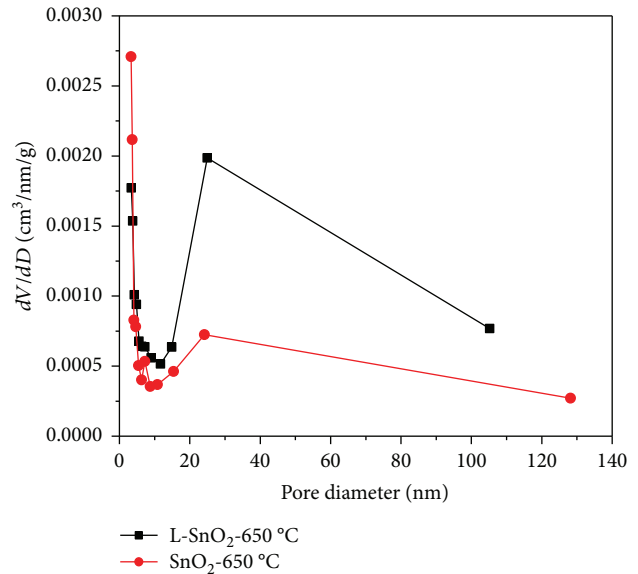


FIGURE 4: Pore size distribution of L- $\text{SnO}_2$ -650°C and  $\text{SnO}_2$ -650°C.

TABLE 1: The surface area, pore volume, and pore diameter of L- $\text{SnO}_2$ -650°C and  $\text{SnO}_2$ -650°C.

Sample	Surface area (m <sup>2</sup> /g)	Pore volume (cm <sup>3</sup> /g)	Pore diameter (nm)
L- $\text{SnO}_2$ -650°C	14.7	0.15	24.9
$\text{SnO}_2$ -650°C	7.8	0.07	3.3

To observe the porous structure of L- $\text{SnO}_2$ -650°C, Figure 4 shows the pore size distribution curves for L- $\text{SnO}_2$ -650°C and  $\text{SnO}_2$ -650°C and Table 1 shows the surface area, pore volume, and pore diameter of L- $\text{SnO}_2$ -650°C and  $\text{SnO}_2$ -650°C. Compared with  $\text{SnO}_2$ -650°C, L- $\text{SnO}_2$ -650°C possesses more mesopores of about 30 nm, the pore volume of 0.15  $\text{cm}^3/\text{g}$  is much bigger than 0.07  $\text{cm}^3/\text{g}$ , and the pore diameter of 24.9 nm is eight times than 3.3 nm. Therefore, the surface area of L- $\text{SnO}_2$ -650°C is nearly twice larger than that of  $\text{SnO}_2$ -650°C.

Based on above microstructure characterization, the mechanism of  $\text{SnO}_2$  synthesis by biomimetic assembly could be schematic in Figures 5 and 6. First,  $-\text{NH}_2$  of L-leucine accelerates the self-assembled process of  $\text{Sn}^{4+}$  and  $\text{OH}^-$  to form  $\text{Sn}(\text{OH})_4$ . And then,  $\text{Sn}(\text{OH})_4$  could be recognized and integrated with L-leucine. In addition,  $-\text{COOH}$  of L-leucine, an electron-withdrawing group, easily form a hydrogen bond with  $-\text{NH}_2$  of the next L-leucine molecule. Therefore, a “nanocage” with L-leucine molecules enclosed with  $\text{Sn}(\text{OH})_4$  would be created by the intermolecular hydrogen bonding of L-leucine. Lastly, a high-order nanocage group would be formed. When heating  $\text{Sn}(\text{OH})_4$ ,  $\text{SnO}_2$  nucleates in the “nanocage” and its growth would be restricted by the “nanocage.” Therefore, fine and high-order layered  $\text{SnO}_2$  particles could be obtained by biomimetic assembly using the L-leucine template. Figure 6 illustrates the formation mechanism of the porous foam-like surface for L- $\text{SnO}_2$ . L-Leucine has integrated with  $\text{Sn}(\text{OH})_4$  to form a “nanocage” group,

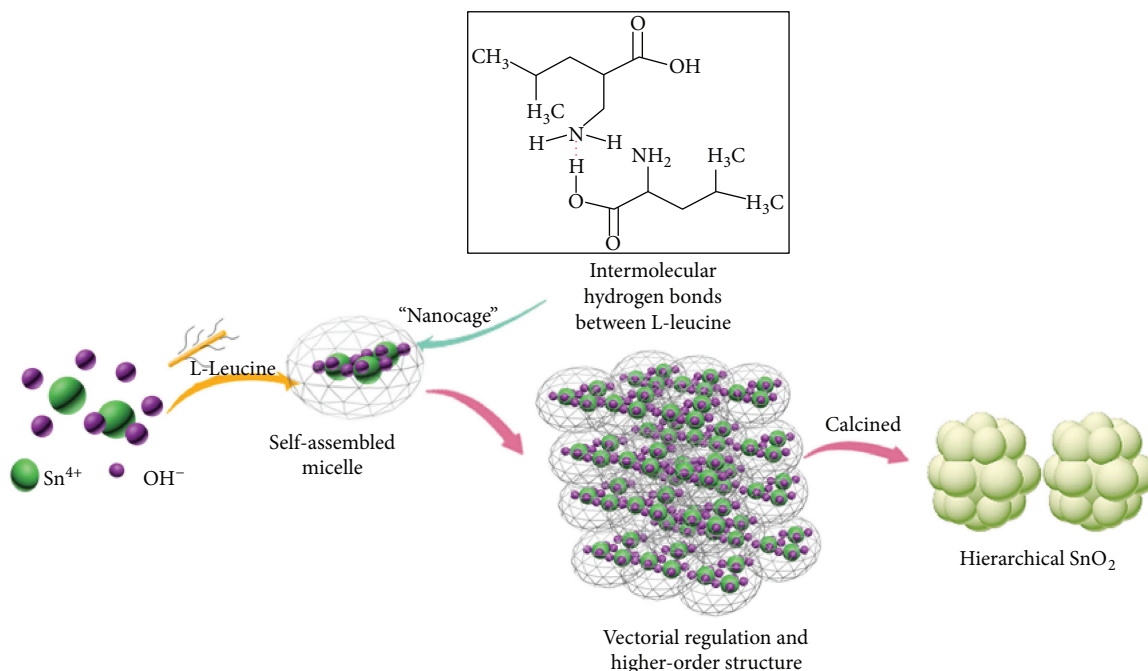


FIGURE 5: The formation of “nanocage” and intermolecular hydrogen bonds between L-leucines.

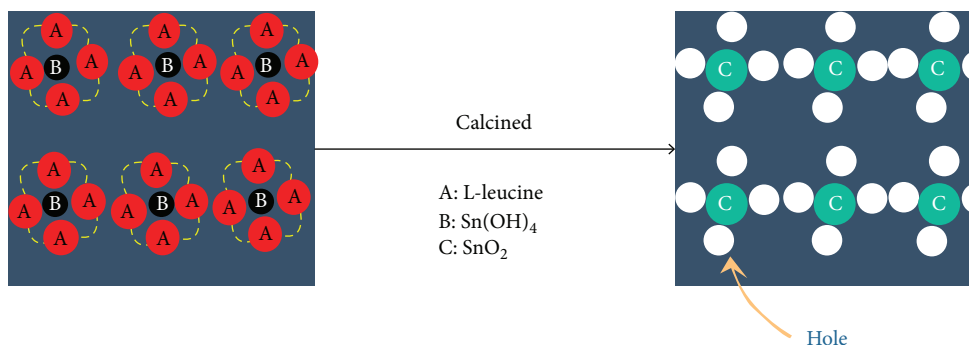


FIGURE 6: Schematic for the foam-like morphology of L-SnO<sub>2</sub>-650°C.

which would not be washed. When calcined at a high temperature, L-leucine would decompose into gaseous product such CO<sub>2</sub>, NH<sub>2</sub>, and CO as reported in [30]. Then, the escapement of these gases and the pyrolysis removal of the L-leucine template would leave holes around SnO<sub>2</sub> and promote the formation of porous morphology.

Figure 7 shows voltage-capacity curves of the 1st, 2nd, and 5th cycles for as-prepared SnO<sub>2</sub> electrodes cycled versus lithium metal from 0.005 to 2.5 V. All the voltage curves are characteristic of SnO<sub>2</sub> in appearance, having an initial discharge sloping above 1.0 V, a flat plateau about 0.8 V, and a sloping plateau during the subsequent lithiation and delithiation process. A large irreversible capacity at above 1.0 V during the first discharge could also be observed, corresponding to the irreversible reaction between SnO<sub>2</sub> and Li (1). The flat plateau about 0.8 V is consistent with the reaction between Li<sup>+</sup> and Sn. The L-SnO<sub>2</sub>-450°C, L-SnO<sub>2</sub>-550°C, and L-SnO<sub>2</sub>-650°C deliver the

initial discharge capacity of 1488.3 mAh/g, 1616.1 mAh/g, and 1408.9 mAh/g, respectively, which is higher than 1441.3 mAh/g, 1491.7 mAh/g, and 1370.0 mAh/g of SnO<sub>2</sub>-450°C, SnO<sub>2</sub>-550°C, and SnO<sub>2</sub>-650°C, respectively. And the initial charge capacity of L-SnO<sub>2</sub> is also higher than the latter, with 704.0 mAh/g, 914.9 mAh/g, and 824.8 mAh/g for L-SnO<sub>2</sub>-450°C, L-SnO<sub>2</sub>-550°C, and L-SnO<sub>2</sub>-650°C, respectively, while 655.1 mAh/g, 869.7 mAh/g, and 698.3 mAh/g for SnO<sub>2</sub>-450°C, SnO<sub>2</sub>-550°C, and SnO<sub>2</sub>-650°C, respectively. Additionally, the compacted density is 3.63 g/cm<sup>3</sup>, 3.74 g/cm<sup>3</sup>, and 3.38 g/cm<sup>3</sup> for L-SnO<sub>2</sub>-450°C, L-SnO<sub>2</sub>-550°C, and L-SnO<sub>2</sub>-650°C, respectively. So, the corresponding reversible volumetric capacity is 982.9 mAh/cm<sup>3</sup>, 1316.0 mAh/cm<sup>3</sup>, and 1072.2 mAh/cm<sup>3</sup>, respectively, which is higher than commercial graphite of 720 mAh/cm<sup>3</sup>. Moreover, the flat plateau of L-SnO<sub>2</sub> is a little higher than single SnO<sub>2</sub> calcined at the same temperature. This should be related to smaller SnO<sub>2</sub> in L-SnO<sub>2</sub>, so they could provide more passageways

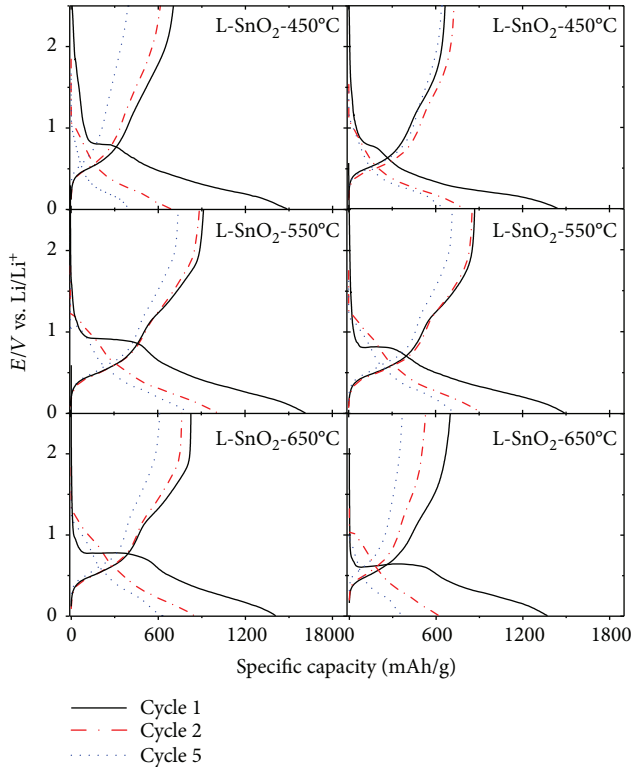


FIGURE 7: The 1st, 2nd, and 5th voltage-capacity profiles of as-prepared  $\text{SnO}_2$  electrodes.

for  $\text{Li}^+$  diffusion, deliver more capacity, and react with  $\text{Li}^+$  easily to form  $\text{Li}_2\text{Sn}$ . Additionally,  $\text{L-SnO}_2\text{-450}^\circ\text{C}$  and  $\text{L-SnO}_2\text{-550}^\circ\text{C}$  perform a coulombic efficiency of 47.3% and 56.6%, respectively, which is equal to 45.5% and 58.3% for  $\text{SnO}_2\text{-450}^\circ\text{C}$  and  $\text{SnO}_2\text{-550}^\circ\text{C}$ , respectively. This would be concluded that the functional groups in the surface of  $\text{SnO}_2$  have no irreversible capacity contribution.

Figure 8 shows the differential capacity versus potential curves for the 1st, 2nd, 5th, and 25th cycles for as-prepared  $\text{SnO}_2$  electrodes. The differential capacity refers to the calculated value of two adjacent points on the voltage-time curve ( $V(n)$ ,  $V(n+1)$ ,  $t(n)$ ,  $t(n+1)$ ), and the known charge, discharge current  $I$ , and the value of the active material mass  $m$  in the electrode according to  $dQ/dV = (I[t(n+1) - t(n)]) / (m[V(n+1) - V(n)])$ . Researchers have testified that the reversibility of lithiation and delithiation of  $\text{SnO}_2$  should be good while the differential capacity curve is broad. The peaks on the differential capacity curve correspond to the platform of the voltage-capacity curve. The change of the area is enclosed by the curve which reflects the attenuation degree of the capacity; the area changes larger, and capacity attenuates faster. As shown in Figure 8,  $\text{L-SnO}_2\text{-450}^\circ\text{C}$ ,  $\text{L-SnO}_2\text{-550}^\circ\text{C}$ , and  $\text{L-SnO}_2\text{-650}^\circ\text{C}$  show a sharp peak around 0.80 V, 0.90 V, and 0.77 V during the first discharge, respectively, which is higher than 0.78 V, 0.81 V, and 0.65 V of  $\text{SnO}_2\text{-450}^\circ\text{C}$ ,  $\text{SnO}_2\text{-550}^\circ\text{C}$ , and  $\text{SnO}_2\text{-650}^\circ\text{C}$ , respectively. This phenomenon would also exist during the 2nd and 5th discharges, with lithiation peaks at 0.20 V, 0.33 V, and 0.34 V for  $\text{L-SnO}_2\text{-450}^\circ\text{C}$ ,  $\text{L-SnO}_2\text{-550}^\circ\text{C}$ , and  $\text{L-SnO}_2\text{-650}^\circ\text{C}$ , respectively.

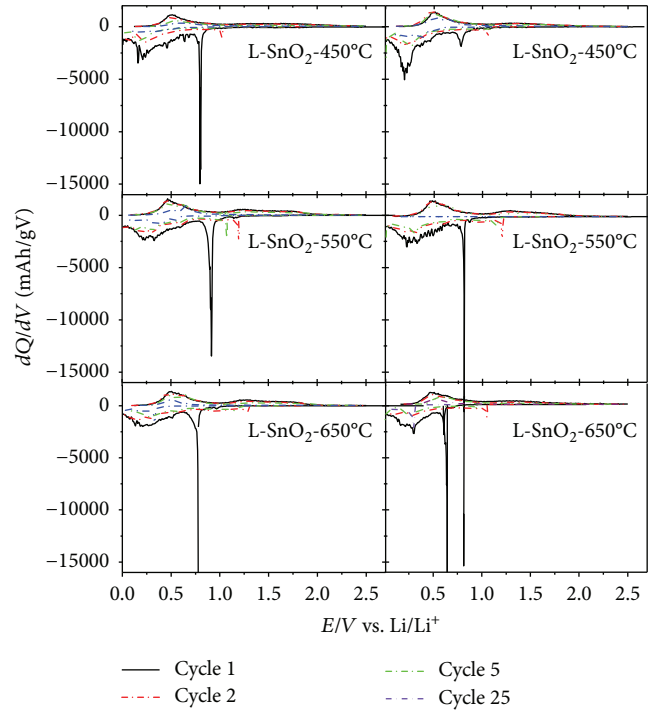


FIGURE 8: Differential capacity vs. potential curves of the 1st, 2nd, 5th, and 25th cycles for  $\text{L-SnO}_2$  electrodes and the control group of  $\text{SnO}_2$  electrodes.

$650^\circ\text{C}$ , respectively, while 0.20 V, 0.27 V, and 0.30 V for  $\text{SnO}_2\text{-450}^\circ\text{C}$ ,  $\text{SnO}_2\text{-550}^\circ\text{C}$ , and  $\text{SnO}_2\text{-650}^\circ\text{C}$ , respectively. This suggests that smaller  $\text{SnO}_2$  is easy to alloy with  $\text{Li}^+$ . No sharp peak could be observed after the first charge curves, which manifests that no 2-phase district exists. The reductive electric potentials around 0.3 V are also a featured platform of Sn corresponding to Sn and Li formed an alloy. The differential capacity curve of the 25th discharge process was basically a smooth state, and it proves that there is some irreversible oxidation-reduction reaction happened. This phenomenon was associated with electrolyte consumption of SEI on the fresh surface of electrodes. Sn would reunite and easily collapse in charge and discharge processes. Thus, SEI should reform on the exposed fresh surface of Sn. As for the smoothness of  $dQ-dV$  curves, peak of  $\text{L-SnO}_2$  is broader than single  $\text{SnO}_2$ , suggesting that  $\text{L-SnO}_2$  have preferable transmission property for lithiation and delithiation. Therefore, the reason that the capacity of  $\text{L-SnO}_2\text{-450}^\circ\text{C}$  was less than  $\text{SnO}_2\text{-450}^\circ\text{C}$  is due to the adsorption of functional groups on the surface of the material, thus blocked the passage of the electrons and led to a decrease in the lithium storage capacity of the material. As for  $\text{L-SnO}_2\text{-550}^\circ\text{C}$  and  $\text{L-SnO}_2\text{-650}^\circ\text{C}$ , their curves were also smoother as well as indicated advantageous performance than  $\text{SnO}_2\text{-550}^\circ\text{C}$  and  $\text{SnO}_2\text{-650}^\circ\text{C}$ .

Figure 9 shows the cycling performance for  $\text{L-SnO}_2$  electrodes and the control group of  $\text{SnO}_2$  electrodes. Compared  $\text{L-SnO}_2\text{-450}^\circ\text{C}$  with  $\text{SnO}_2\text{-450}^\circ\text{C}$ , the capacity retention of  $\text{L-SnO}_2\text{-450}^\circ\text{C}$  is inferior to that of  $\text{SnO}_2\text{-450}^\circ\text{C}$ . It should be mainly related to the larger specific surface area for  $\text{L-SnO}_2\text{-450}^\circ\text{C}$  while the particle size of  $\text{SnO}_2$  is close. The cyclic

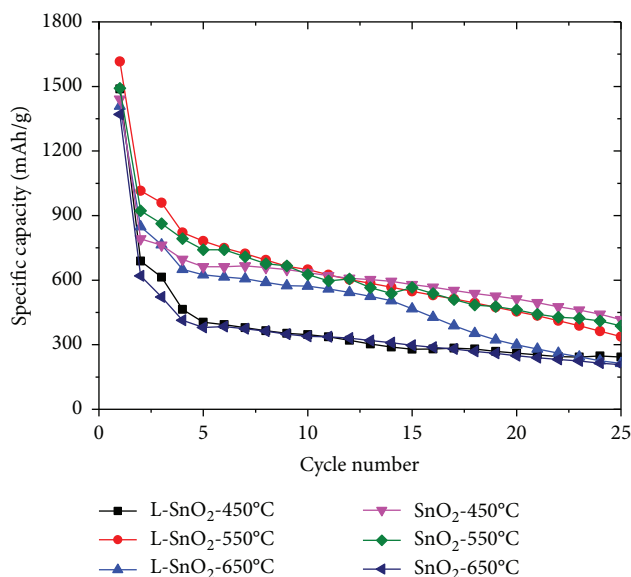


FIGURE 9: Cyclic performance of L-SnO<sub>2</sub> electrodes and the control group of SnO<sub>2</sub> electrodes.

performance of L-SnO<sub>2</sub>-550°C and L-SnO<sub>2</sub>-650°C is much better than the SnO<sub>2</sub>-550°C and SnO<sub>2</sub>-650°C, because the particle size of SnO<sub>2</sub> is much smaller in the former, which would experience less inner stress. Moreover, the porous structure of L-SnO<sub>2</sub> can provide more channels and place-holders for the embedding and deembedding of ions. This was helpful to reduce SnO<sub>2</sub> crushing and improve the stability of electrode materials. Even so, all SnO<sub>2</sub> electrodes do not show expected excellent cyclability as well as those reported previously. However, it is believed that nanosized SnO<sub>2</sub> coated by graphitic carbon at 600~700°C would perform better cyclability, which would be further studied.

#### 4. Conclusion

SnO<sub>2</sub> nanoparticles have been prepared by biomimetic synthesis combined with a sol-gel method using L-leucine as a biotemplate for the first time. L-Leucine could form a “nanocage” by its intermolecular hydrogen bond and accelerate the assembly of Sn<sup>4+</sup> and OH<sup>-</sup> in the nanocage during the preparation process. Therefore, SnO<sub>2</sub> growth could be regulated at a high temperature calcination of 650°C. As-prepared L-SnO<sub>2</sub> show a block and porous structure. As anodes for lithium-ion battery, L-SnO<sub>2</sub> perform better electrochemical performance than SnO<sub>2</sub>. This should give a promising route to produce enhanced SnO<sub>2</sub>/C electrodes with nanosized SnO<sub>2</sub> coated by graphitic carbon at high temperature for lithium-ion batteries.

#### Data Availability

All data generated or analyzed during this study are included in this published article (and its supplementary information files).

#### Conflicts of Interest

The authors declare that they have no conflicts of interest.

#### Acknowledgments

This work was supported by the NSFC under project no. 51701073 and the Youth Fund of Hunan Agricultural University no. 16QN13.

#### References

- [1] R. Schmich, R. Wagner, G. Hörpel, T. Placke, and M. Winter, “Performance and cost of materials for lithium-based rechargeable automotive batteries,” *Nature Energy*, vol. 3, no. 4, pp. 267–278, 2018.
- [2] E. A. Olivetti, G. Ceder, G. G. Gaustad, and X. Fu, “Lithium-ion battery supply chain considerations: analysis of potential bottlenecks in critical metals,” *Joule*, vol. 1, no. 2, pp. 229–243, 2017.
- [3] F. Ding, W. Xu, D. Choi et al., “Enhanced performance of graphite anode materials by AlF<sub>3</sub> coating for lithium-ion batteries,” *Journal of Materials Chemistry*, vol. 22, no. 25, pp. 12745–12751, 2012.
- [4] M.-T. F. Rodrigues, F. N. Sayed, H. Gullapalli, and P. M. Ajayan, “High-temperature solid electrolyte interphases (SEI) in graphite electrodes,” *Journal of Power Sources*, vol. 381, pp. 107–115, 2018.
- [5] L. Chen, M. Zhang, and W. Wei, “Graphene-based composites as cathode materials for lithium ion batteries,” *Journal of Nanomaterials*, vol. 2013, Article ID 940389, 8 pages, 2013.
- [6] Y. Chen, X. Zhang, Y. Tian, and X. Zhao, “Synthesis and characterization of silicon nanoparticles inserted into graphene sheets as high performance anode material for lithium ion batteries,” *Journal of Nanomaterials*, vol. 2014, Article ID 734751, 6 pages, 2014.
- [7] M. J. K. Reddy, S. H. Ryu, and A. M. Shanmugaraj, “Synthesis of SnO<sub>2</sub> pillared carbon using long chain alkylamine grafted graphene oxide: an efficient anode material for lithium ion batteries,” *Nanoscale*, vol. 8, no. 1, pp. 471–482, 2016.
- [8] M. Usman Hameed, S. Ullah Dar, S. Ali et al., “Facile synthesis of low-dimensional SnO<sub>2</sub> nanostructures: an investigation of their performance and mechanism of action as anode materials for lithium-ion batteries,” *Physica E: Low-dimensional Systems and Nanostructures*, vol. 91, pp. 119–127, 2017.
- [9] H. Zhang, R. Hu, H. Liu et al., “A spherical Sn-Fe<sub>3</sub>O<sub>4</sub>@graphite composite as a long-life and high-rate-capability anode for lithium ion batteries,” *Journal of Materials Chemistry A*, vol. 4, no. 26, pp. 10321–10328, 2016.
- [10] H. Zhang, R. Hu, Y. Liu, J. Liu, Z. Lu, and M. Zhu, “Origin of capacity increasing in a long-life ternary Sn-Fe<sub>3</sub>O<sub>4</sub>@graphite anode for Li-ion batteries,” *Advanced Materials Interfaces*, vol. 4, no. 12, article 1700113, 2017.
- [11] Z. Li, B. Li, L. Yin, and Y. Qi, “Prussian blue-supported annealing chemical reaction route synthesized double-shelled Fe<sub>2</sub>O<sub>3</sub>/Co<sub>3</sub>O<sub>4</sub> hollow microcubes as anode materials for lithium-ion battery,” *ACS Applied Materials & Interfaces*, vol. 6, no. 11, pp. 8098–8107, 2014.
- [12] J. Wang, Q. Zhang, X. Li et al., “Three-dimensional hierarchical Co<sub>3</sub>O<sub>4</sub>/CuO nanowire heterostructure arrays on nickel foam for high-performance lithium ion batteries,” *Nano Energy*, vol. 6, pp. 19–26, 2014.

- [13] J. Liu, X. Xu, R. Hu, L. Yang, and M. Zhu, "Uniform hierarchical  $\text{Fe}_3\text{O}_4$ @polypyrrole nanocages for superior lithium ion battery anodes," *Advanced Energy Materials*, vol. 6, no. 13, article 1600256, 2016.
- [14] H. Li, Q. Su, J. Kang et al., "Porous  $\text{SnO}_2$  hollow microspheres as anodes for high-performance lithium ion battery," *Materials Letters*, vol. 217, pp. 276–280, 2018.
- [15] M. He, L. Yuan, X. Hu, W. Zhang, J. Shu, and Y. Huang, "A  $\text{SnO}_2$ @carbon nanocluster anode material with superior cyclability and rate capability for lithium-ion batteries," *Nanoscale*, vol. 5, no. 8, pp. 3298–3305, 2013.
- [16] R. Liu, Y. Liu, Q. Kang et al., "Synergistic effect of graphene and polypyrrole to enhance the  $\text{SnO}_2$  anode performance in lithium-ion batteries," *RSC Advances*, vol. 6, no. 12, pp. 9402–9410, 2016.
- [17] M. Sumithra, P. R. Rao, A. Nagaratnam, and Y. Aparna, "Characterization of  $\text{SnO}_2$  nanoparticles in the traditionally prepared Ayurvedic medicine," *Materials Today: Proceedings*, vol. 2, no. 9, pp. 4636–4639, 2015.
- [18] M. Wu, J. Liu, M. Tan et al., "Facile hydrothermal synthesis of  $\text{SnO}_2$ /C microspheres and double layered core-shell  $\text{SnO}_2$  microspheres as anode materials for Li-ion secondary batteries," *RSC Advances*, vol. 4, no. 48, pp. 25189–25194, 2014.
- [19] L. Li, H. Zhang, Z. Li, W. Zhong, H. Liao, and Z. Li, "Rapid preparation of  $\text{SnO}_2$ /C nanospheres by using organotin as building blocks and their application in lithium-ion batteries," *RSC Advances*, vol. 7, no. 55, pp. 34442–34447, 2017.
- [20] B. Li, J. Zai, Y. Xiao, Q. Han, and X. Qian, " $\text{SnO}_2$ /C composites fabricated by a biotemplating method from cotton and their electrochemical performances," *CrystEngComm*, vol. 16, no. 16, pp. 3318–3322, 2014.
- [21] Y. Kodama, K. Sato, K. Suzuki, Y. Saito, T. Suzuki, and T. J. Konno, "Electron microscope study of the formation of graphitic nanostructures in nickel-loaded wood char," *Carbon*, vol. 50, no. 10, pp. 3486–3496, 2012.
- [22] G. P. Khokhlova, C. N. Barnakov, V. Y. Malysheva, A. N. Popova, and Z. R. Ismagilov, "Effect of heat treatment conditions on the catalytic graphitization of coal-tar pitch," *Solid Fuel Chemistry*, vol. 49, no. 2, pp. 66–72, 2015.
- [23] R. Anton, "On the reaction kinetics of Ni with amorphous carbon," *Carbon*, vol. 46, no. 4, pp. 656–662, 2008.
- [24] E. Gravel and E. Poupon, "Biosynthesis and biomimetic synthesis of alkaloids isolated from plants of the *Nitraria* and *Myrioneuron* genera: an unusual lysine-based metabolism," *Natural Product Reports*, vol. 27, no. 1, pp. 32–56, 2010.
- [25] R. James and C. T. Laurencin, "Musculoskeletal regenerative engineering: biomaterials, structures, and small molecules," *Advances in Biomaterials*, vol. 2014, Article ID 123070, 12 pages, 2014.
- [26] Z. Tong, Y. Jiang, D. Yang et al., "Biomimetic and bioinspired synthesis of titania and titania-based materials," *RSC Advances*, vol. 4, no. 24, pp. 12388–12403, 2014.
- [27] L. P. S. de Carvalho, A. Argyrou, and J. S. Blanchard, "Slow-onset feedback inhibition: inhibition of *Mycobacterium tuberculosis*  $\alpha$ -isopropylmalate synthase by L-leucine," *Journal of the American Chemical Society*, vol. 127, no. 28, pp. 10004–10005, 2005.
- [28] A. Bhattacharjee and M. Ahmaruzzaman, "Facile synthesis of  $\text{SnO}_2$  quantum dots and its photocatalytic activity in the degradation of eosin Y dye: a green approach," *Materials Letters*, vol. 139, pp. 418–421, 2015.
- [29] A. Bhattacharjee, M. Ahmaruzzaman, and T. Sinha, "A novel approach for the synthesis of  $\text{SnO}_2$  nanoparticles and its application as a catalyst in the reduction and photodegradation of organic compounds," *Spectrochimica Acta. Part A, Molecular and Biomolecular Spectroscopy*, vol. 136, pp. 751–760, 2015.
- [30] J. Li, Z. Wang, X. Yang, L. Hu, Y. Liu, and C. Wang, "Decomposing or subliming? An investigation of thermal behavior of L-leucine," *Thermochimica Acta*, vol. 447, no. 2, pp. 147–153, 2006.

## Research Article

# Anomalous Faster Deterioration of $\text{LiNi}_{0.8}\text{Co}_{0.15}\text{Al}_{0.05}\text{O}_2/\text{Graphite}$ High-Energy 18650 Cells at 1.5 C than 2.0 C

Dawei Cui , Jinlong Wang , Ailing Sun , Hongmei Song , and Wenqing Wei 

School of Mechanical-Electronic and Vehicle Engineering, Weifang University, Weifang 261061, China

Correspondence should be addressed to Dawei Cui; [wfxycdw@163.com](mailto:wfxycdw@163.com)

Received 2 May 2018; Accepted 25 June 2018; Published 31 July 2018

Academic Editor: Huaiyu Shao

Copyright © 2018 Dawei Cui et al. This is an open access article distributed under the Creative Commons Attribution License, which permits unrestricted use, distribution, and reproduction in any medium, provided the original work is properly cited.

Discharge rate is a key parameter affecting the cycle life of lithium-ion batteries (LIB). Normally, lithium-ion batteries deteriorate more severely at a higher discharge rate. In this paper, we report that the cycle performance of  $\text{LiNi}_{0.8}\text{Co}_{0.15}\text{Al}_{0.05}\text{O}_2/\text{graphite}$  high-energy 2.8 Ah 18650 cells is abnormally worse at a 1.5 C discharge rate than at a 2.0 C discharge rate. Combining macromethods with micromethods, the capacity/rate performance, electrochemical impedance spectroscopy (EIS), and scanning electron microscope (SEM) morphology of the electrodes are systematically investigated. We have found that the impedance of the negative electrodes after 2.0 C aged is smaller than that after 1.5 C aged, through EIS analysis, and the discharge rate performance of the negative electrodes after 2.0 C aged is better than that after 1.5 C aged through coin cell analysis. In addition, some special microcracks in the negative electrodes of aged cells are observed through SEM analysis, which can accelerate the side reaction between active and electrolyte and form the thicker SEI which will hinder the  $\text{Li}^+$  insertion and cause resistance increase. In short, the  $\text{LiNi}_{0.8}\text{Co}_{0.15}\text{Al}_{0.05}\text{O}_2/\text{graphite}$ -based lithium-ion batteries show better cycle life at a 2.0 C discharge rate than at a 1.5 C discharge rate which indicates that the negative electrodes contribute more than the positive electrodes.

## 1. Introduction

Lithium-ion batteries (LIB) used in electric vehicles (EV) need high energy density, high power capacity, long cycle life, and good security to achieve superior driving performance and better economic viability [1–4]. In recent years, the  $\text{LiNi}_{(1-x-y)}\text{Co}_x\text{M}_y\text{O}_2$  system (denoted as NCM, where M represents metal elements such as Mn and Al) has been widely reported as cathode materials due to its many advantages, such as high specific capacity, long lifespan, and low cost [5–9]. Among this family,  $\text{LiNi}_{(1-x-y)}\text{Co}_x\text{Al}_y\text{O}_2$  (NCA) is attracting much attention and becoming a promising candidate material for the positive electrode because of its highest capacity among the whole cathodes which have been used in mass [10–13].

There are many published studies on NCA-based LIB, focusing on the electrochemical characteristics [14–16], the storage performance [17, 18], the factors that affect the performance [19–21], and especially the capacity fading mechanism [22–25]. As reported, the main factor which deteriorated the cycle life at 100% depth of discharge

(DOD) for the NCA/graphite system was the microcracks in the positive electrode [23–25] and these micro-cracks were mainly induced by the shrink in volume under charge and discharge operations [12]. It has great difference with the  $\text{LiMn}_2\text{O}_4/\text{graphite}$  and NCM/graphite systems in which the main factors causing the capacity fading were considered to be the dissolution of Mn, the increase of the polarization, and the decrease of active  $\text{Li}^+$  [26–28].

Electric vehicles (EV) and plug-in hybrid electric vehicles (PHEV) usually require LIB to work at higher charge/discharge currents, and therefore, it is very important for LIB to understand the fading mechanism at high charge/discharge rates. Generally, the cycle life for LIB is deteriorated at higher charge/discharge rates: the higher the rates, the worse the cycle life [29]. Whether it has the same conclusion for the NCA/graphite system is the question. From the reported papers, we have learned that the pulse discharge current had the worse effect on cycle life than the constant current for 3 Ah 18650 cells with NCA [30]. However, few studies have examined the effect of constant current discharge rates on cycle life of NCA-based 18650 cells. In the

TABLE 1: Details for NCA-based 18650 cells from BPI.

Item	Specification
Nominal capacity (Ah)	2.75
Nominal voltage (V)	3.65
Mass/g	47.0
Energy density (Wh·kg <sup>-1</sup> )	210

present work, the basic fading mechanisms for NCA-based 18650 cells cycled at two different discharge rates (1.5 C and 2.0 C) were studied and their cycle performance including capacity and morphology was discussed through electrode analysis. The initial reasons which affect the cycle life for the NCA/graphite-based LIB were further explained.

## 2. Experimental

The NCA-based 18650 cells used are from an automotive battery manufacturer Boston-Power Incorporation (BPI), and the details of the cells are listed in Table 1. The nominal capacity of the cells was 2.75 Ah (charge/discharge at 0.2 C). The positive electrode of the cells is NCA, the negative electrode is artificial graphite with polyethylene-based ceramic separate, and the electrolyte is a mixture of ethylene carbonate (EC), ethyl methyl carbonate (EMC), and dimethyl carbonate (DMC) with lithium hexafluorophosphate (LiPF<sub>6</sub>).

The cycle tests were conducted at two different discharge rates, that is, 1.5 C (4125 mA) and 2.0 C (5500 mA), by using a battery tester LAND (5 V/5 A). The temperature was controlled to 25°C by a high-low temperature chamber (Hongzhan, 80 L). Note that the same charging protocols, that is, constant current (CC) (0.5 C) and constant voltage (CV) with an upper voltage limit of 4.2 V and a cutting-off current of 138 mA, were employed in all discharge cases. The cycle tests were continued until the capacity retention decreases to 80% of the initial capacity.

In order to gain insights into the aging origins, we disassembled the fresh cell and the cells aged at different rates after discharging these cells to 2.5 V in an Ar atmosphere glove box, in which the moisture content was less than 0.1 ppm. The positive and negative electrodes were rinsed by DMC. After that, we assembled these harvested electrodes into new coin cells with Li metal as the counter electrode in the Ar atmosphere glove box. In terms of these reassembled coin cells, the capacity and rate performance were examined using battery tester LAND (5 V/10 mA). The impedance changes were measured in Princeton PARSTAT 4000 with an ac amplitude of 5 mV over the frequency range from 50 kHz to 0.05 Hz.

The pore size distribution and the porosity of fresh and aged cells were measured using the mercury intrusion porosimetry (MIP) with PoreMaster 33 type from Quantachrome. The MIP could measure pore diameters from a nanometer to micrometer scale, which matched well with the pore range in the electrode film sample compared to nano-computed tomography (CT) just monitoring the pore diameters above 500 nm [31, 32]. Scanning electron microscopy (SEM) was carried out to observe the surface microscopic morphology

changes of the positive and negative electrodes for fresh and aged cells. SEM images were taken with ULTRA 55 type from Carl Zeiss SMT Corporation. For porosity and SEM analysis, the electrodes were washed with DMC and evaporated at room temperature.

## 3. Results and Discussion

*3.1. Cycle Performance of Cells and Characteristics of Electrodes.* The cycle performance of NCA-based 18650 cells at different discharge rates is shown in Figure 1. Figure 1(a) displays the cycle life of the cells at 2.0 C discharge rate and 1.5 C rate at 25°C, and two cells are tested for either discharge rates. It can be noted that the capacity retention at 2.0 C is better than that at 1.5 C and the former's cycle life is about twice that of the latter. Figure 1(b) demonstrates that the direct current resistance (DCR) has increased by 20% after the cycles of one cell at various discharge rates. When the capacity decreases to 80% of the initial state, the whole output capacity/energy for 2.0 C aged cells is clearly higher than that for 1.5 C aged cells, as listed in Table 2.

The positive and negative electrodes for fresh and aged cells are reassembled into 2032 coin cells with Li metal as counter electrode. The capacity calibration are operated with 0.2 C CC-CV charge mode and 0.2 C CC discharge; the voltage range is 2.5 V~4.2 V for the positive electrodes and 0.005 V~1.5 V for the negative electrodes. The characteristics of different electrodes for fresh and aged cells are shown in Figure 2.

Figure 2(a) presents the discharge curves for the positive and negative electrodes. As can be seen, the capacity of the positive electrodes can remain 86% for 1.5 C aged cells and 87% for 2.0 C aged cells and this difference with cell capacity retention of 80% is derived from the different charge and discharge rates. The capacity ratio of the negative to the positive (N/P) ratio can be calculated as follows:

$$\frac{N}{P} \text{ ratio} = \frac{C_n \times S_n \times r_{\text{active-graphite}}}{C_p \times S_p \times r_{\text{active-NCA}}}, \quad (1)$$

where  $C_n$  and  $C_p$  are the capacity of the negative and positive electrodes, respectively;  $S_n$  and  $S_p$  are the area coating density of the negative and positive electrodes, respectively;  $r_{\text{active-graphite}}$  and  $r_{\text{active-NCA}}$  are the ratio of active material in the electrodes.

According to (1), it can be known that the N/P ratio value for 1.5 C aged cells increases to 1.19, while for 2.0 C aged cells, it decreases to 1.06, and the details are listed in Table 3. These results indicate that the negative electrodes have enough capacity balance even for aged cells so the capacity fading is attributed to the deterioration of the NCA. The above conclusion is essentially consistent with previous reports [23–25]. However, it cannot explain why the 2.0 C discharge rate is better than the 1.5 C discharge rate.

In order to explore the reason for the above phenomena, the intercalation ability of Li<sup>+</sup> for the positive electrodes and deintercalation ability of Li<sup>+</sup> for the negative electrodes had been evaluated based on the discharge rate performance of different electrodes for fresh and aged cells as shown in

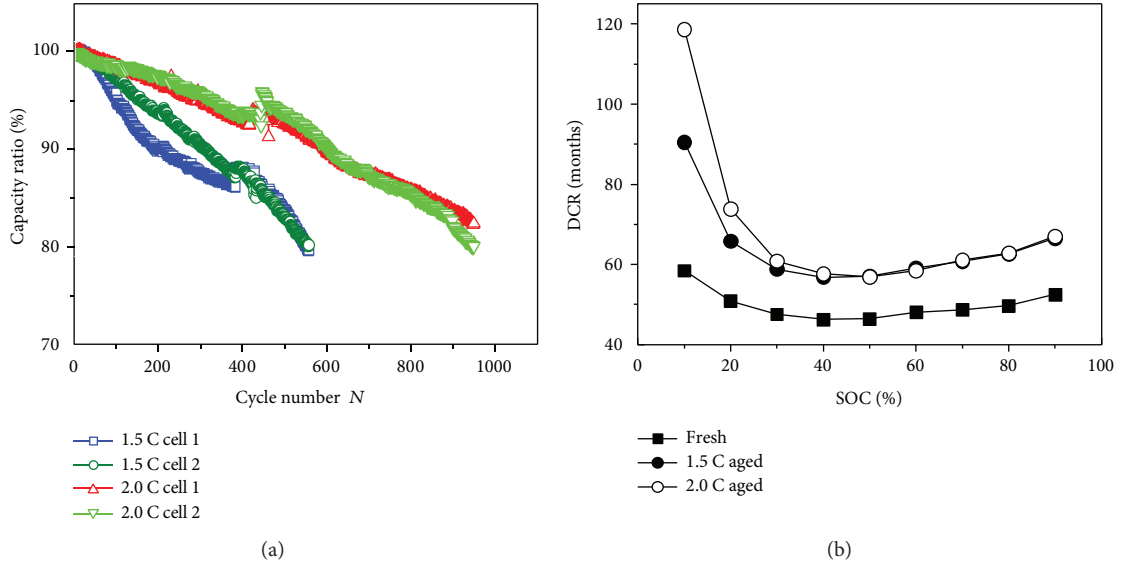


FIGURE 1: Cycle performance of NCA-based 18650 cells cycled at different discharge rates. (a) Cycle life curves; (b) direct current resistance (DCR) curves.

TABLE 2: Whole output capacity/energy for aged cells.

Rate	Total charge capacity (Ah)	Total discharge capacity (Ah)	Total charge energy (Wh)	Total discharge energy (Wh)
0.5 C/1.5 C	1267	1266	4888	4254
0.5 C/2.0 C	2133	2129	8271	6993

Figure 2(b). It can be figured out that the intercalation ability of  $\text{Li}^+$  for the positive electrodes is very similar after 1.5 C or 2.0 C aged and their capacities deteriorate by about 5% at the 1.5 C rate, about 18% at the 2.0 C rate compared with those of fresh cells. However, it can be also seen that the negative electrodes after 2.0 C aged exhibit better rate performance at 1.5 C or 2.0 C rate than those for 1.5 C aged, which implies that there is a great difference in the deintercalation ability of  $\text{Li}^+$  for the negative electrodes after different aging. Consequently, it can be inferred that the capacity fading of NCA/graphite-based LIB is mainly associated with the negative electrodes, which reminds us not only to consider the positive electrode's effect on capacity loss but also to attach more importance to negative electrode's effect on cycle life.

Figure 2(c) displays the incremental capacity analysis (ICA) curves of the positive and negative electrodes for fresh and aged cells at a 0.2C discharge rate, in which each peak involves a phase reaction. For the positive electrodes, there exist six peaks in fresh and aged cells, marked separately as peak (1) to peak (6). The voltage of each peak has increased but the  $dQ/dV$  decreased for aged cells, reflecting that the phase structure do not change during the cycle. This conclusion is also similar to that of other researches analyzed through XRD and Raman methods [25], that is, the NCA crystal structure did not suffer serious damage during the cycle tests. For the negative electrodes, it can be found that there are five phase transition processes, corresponding to peak (1') to peak (5'). The voltage of each peak has decreased and the  $dQ/dV$  increased

for aged cells, especially for peak (5'), while the overall peak heights for 2.0 C aged are lower than those for 1.5 C aged, revealing that the fading of the cells for 1.5 C aged at the lower voltage is obviously induced by the negative electrodes.

The impedance was measured at 50% SOC at 25°C, and the frequency range is 0.05 Hz to 50 kHz. The impedance of the negative electrodes for coin cells is shown in Figure 2(d) and that of the positive electrodes is presented in Figure 3. As seen from Figure 2(d), the impedance of the negative electrodes after 1.5 C aged is larger than that after 2.0 C aged and thus can lead to the faster deterioration of the rate performance, which is in good agreement with experimental results for rate performance in Figure 2(b). Through critical equivalent circuit model (ECM) for LIB from a relevant literature [33], the impedance was composed of ohmic resistance ( $R_o$ ), solid electrolyte interface resistance ( $R_{SEI}$ ), charge transfer resistance ( $R_{ct}$ ), and diffusion resistance ( $R_{diff}$ ). Accordingly, we can conclude that for aged cells,  $R_o$  increases while it is similar for 2.0 C aged and 1.5 C aged and  $R_{SEI}$  and  $R_{ct}$  increase greatly compared to fresh cells but the impedance for 2.0 C aged is smaller than that for 1.5 C aged.

**3.2. Changes in Morphology and Porosity of Disassembled Electrodes.** Figure 4 presents the SEM images of the positive and negative electrodes for fresh and aged cells, and the magnification for the positive electrodes is 20,000 times and 5000 times for the negative electrodes. It can be observed that there

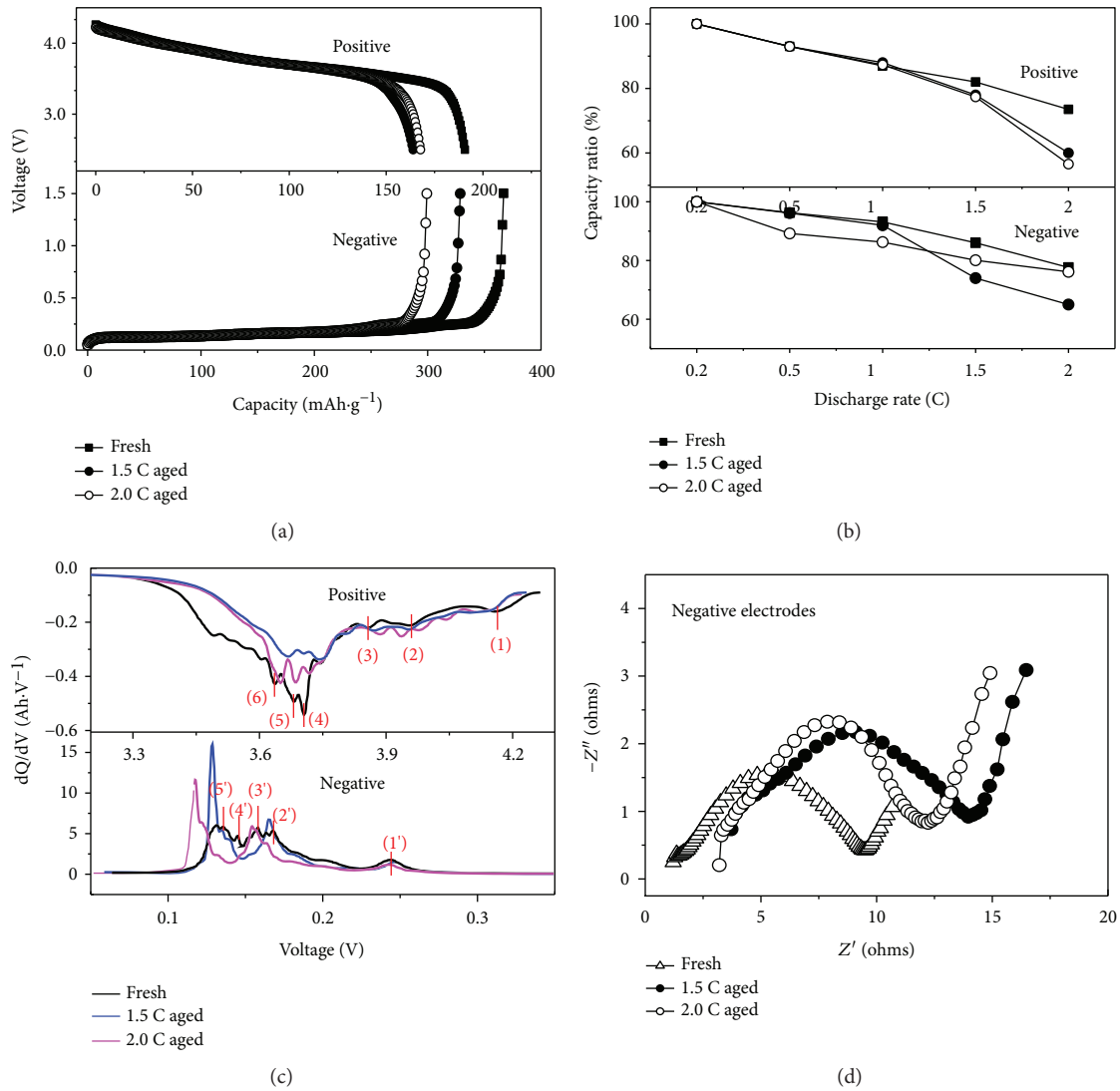


FIGURE 2: Characteristics of different electrodes for fresh and aged cells. (a) Discharge curves of different electrodes at 0.2 C; (b) discharge rate performances of different electrodes; (c) ICA curves of different electrodes; (d) Nyquist plots of the negative electrodes.

TABLE 3: Capacity and N/P ratio of the electrodes for fresh and aged cells.

Information of the electrodes		Capacity at 0.2 C (mAh·g <sup>-1</sup> )	N/P ratio
Fresh	Positive	190	1.09
	Negative	365.5	
1.5 C aged	Positive	164	1.19
	Negative	344	
2.0 C aged	Positive	167	1.06
	Negative	306	

are some special microcracks in the electrodes of aged cells, not only in NCA-positive electrodes but also in graphite-negative electrodes. For the positive electrodes, these microcracks will lead to the capacity loss and resistance increase

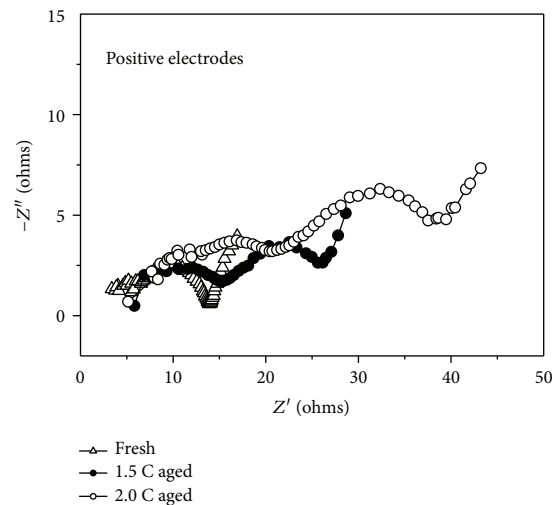


FIGURE 3: Nyquist plots of the positive electrodes for fresh and aged cells.

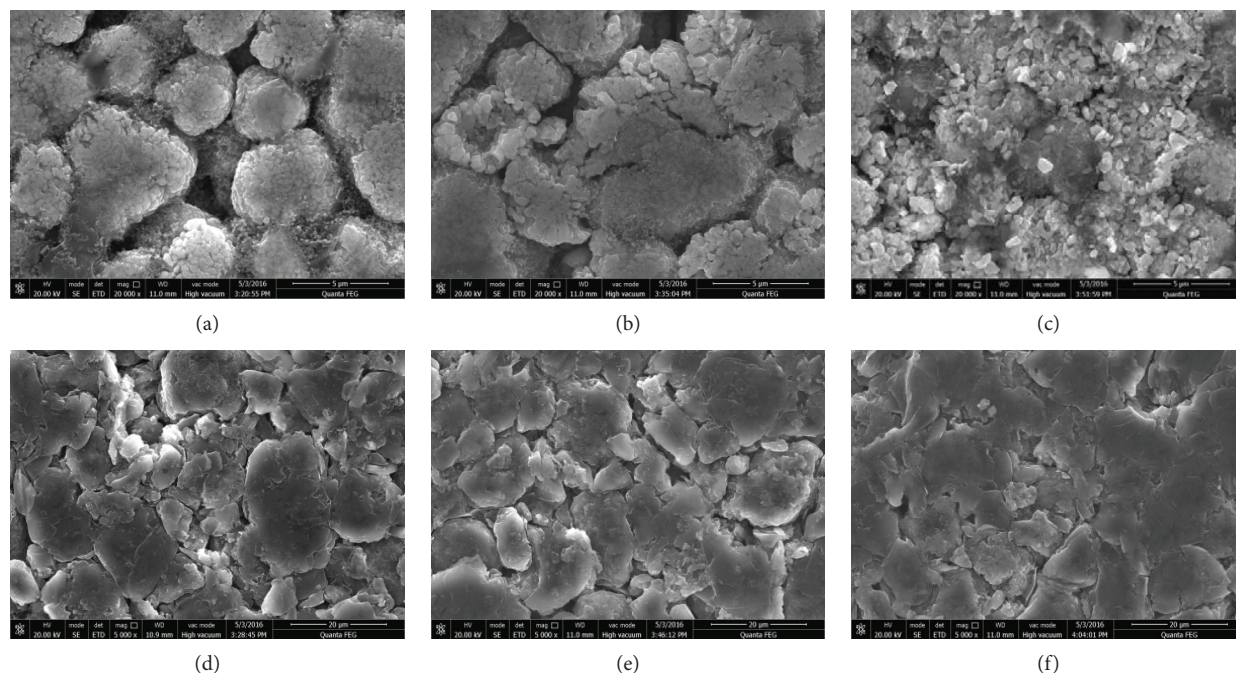


FIGURE 4: SEM images of the positive and negative electrodes for fresh and aged cells. (a) Fresh positive electrode, (b) 1.5 C aged positive electrode, (c) 2.0 C aged positive electrode, (d) fresh negative electrode, (e) 1.5 C aged negative electrode, and (f) 2.0 C aged negative electrode.

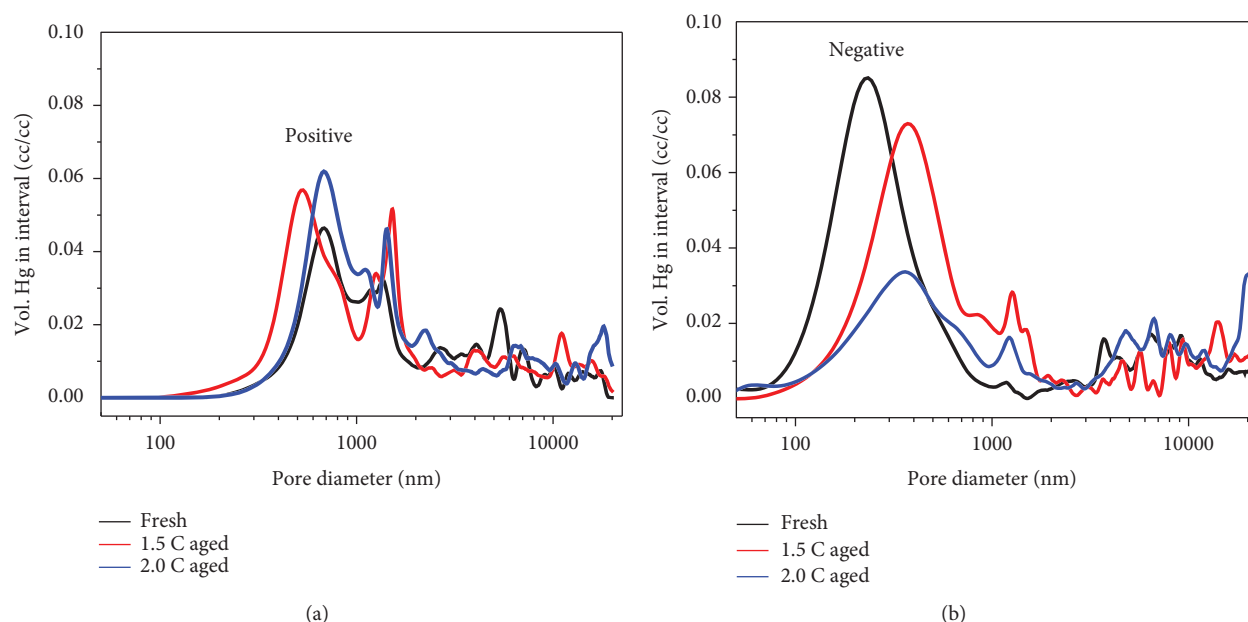


FIGURE 5: Pore distribution of the electrodes for fresh and aged cells. (a) Positive electrodes; (b) negative electrodes.

in the cells, and for negative electrodes, they will bring about the SEI reproduction which can cause the consumption of  $\text{Li}^+$  and resistance to increase [23–25].

The pore distribution of the electrodes for fresh and aged cells is shown in Figure 5, and the average pore size and porosity of the electrodes are listed in Table 4. The porosity

remains basically unchanged for the positive electrodes but decreases remarkably for the negative electrodes. Moreover, the average pore diameters of the negative electrodes are significantly reduced as aged. Combined with Figure 4 and relevant reference [32], it can be deduced that the micro-cracks will accelerate the side reaction between active and

TABLE 4: Average pore size and porosity of the electrodes for fresh and aged cells.

Electrodes	Type	Pore size (nm)	Porosity (%)
	Fresh	312	18.0
Positive	1.5 C aged	399	18.1
	2.0 C aged	313	17.8
	Fresh	911	20.0
Negative	1.5 C aged	574	18.0
	2.0 C aged	589	12.6

electrolyte, which is favourable to form the thicker SEI and other chemicals, and therefore hinder the  $\text{Li}^+$  insertion and reduce the pore diameters. However, this phenomenon is less obvious in the positive electrodes.

It is worth noticing that we have neglected the effect of electrolyte resistance on the capacity fading in the electrode analysis part. Firstly, the electrolyte has been consumed fully when we disassemble the cells and cannot get any droplet for analysis. Secondly, we have adopted the new electrolyte when we assemble the coin cells, which hinder the electrolyte effect resulting in not only the changes of composition but also the changes of ion conductive ability.

As we know, the resistance of the cells is composed of three parts and can be expressed as follows:

$$R_{\text{cell}} = R_{\text{positive/electrolyte}} + R_{\text{negative/electrolyte}} + R_{\text{electrolyte}} \quad (2)$$

where  $R_{\text{positive/electrolyte}}$  is the resistance of the positive electrodes and its interface resistance with electrolyte,  $R_{\text{negative/electrolyte}}$  is the resistance of the negative electrodes and its interface resistance with electrolyte, and  $R_{\text{electrolyte}}$  is only the resistance of the electrolyte.

#### 4. Conclusion

To clarify the fading mechanism about the effect of different discharge rates on NCA-based 18650 cells, two different discharge rates (1.5 C and 2.0 C) were employed and the electrochemical characteristics and morphology changes of the electrodes were investigated during aged process. The capacity losses for aged cells at both discharge rates are monitored by the positive electrodes. When the capacity of the cells deteriorates to 80% of initial capacity, the residual capacity of NCA is similar, about 86% of the initial capacity at the 0.2 C rate. The negative electrodes have enough capacity balance to the positive electrodes from N/P analysis, even at the end of life which was defined as 80% of initial capacity. The difference of capacity fading for aged cells cycled at 1.5 C or 2.0 C is monitored by the negative electrodes through EIS and  $\text{Li}^+$  insertion and deinsertion analysis, showing that the impedance of the negative electrodes after 2.0 C aged is smaller than that after 1.5 C aged. The porosity of the negative electrodes is decreased as aged, which has blocked the  $\text{Li}^+$  insertion and led to the Li metal deposition even though the negative electrodes have enough balance at the end of life. The above analysis gives the initial reasons why the NCA/graphite-based LIB has better cycle life at a 2.0 C

discharge rate than at a 1.5 C discharge rate, and deeper reasons should be explored in future research.

#### Data Availability

The data used to support the findings of this study are available from the corresponding author upon request.

#### Conflicts of Interest

The authors declare that they have no conflicts of interest.

#### Acknowledgments

This work was financially supported by the National Natural Science Foundation of China (no. 51004077), the Distinguished Middle-Aged and Young Scientist Encourage and Reward Foundation of Shandong Province (no. BS2010CL046), and the Natural Science Foundation of Shandong Province (no. ZR2015PE007).

#### References

- [1] B. Scrosati and J. Garche, "Lithium batteries: status, prospects and future," *Journal of Power Sources*, vol. 195, no. 9, pp. 2419–2430, 2010.
- [2] M. Wakihara, "Recent developments in lithium ion batteries," *Materials Science and Engineering R-Reports*, vol. 33, no. 4, pp. 109–134, 2001.
- [3] N. Nitta, F. Wu, J. T. Lee, and G. Yushin, "Li-ion battery materials: present and future," *Materials Today*, vol. 18, no. 5, pp. 252–264, 2015.
- [4] M. A. Hannan, M. S. H. Lipu, A. Hussain, and A. Mohamed, "A review of lithium-ion battery state of charge estimation and management system in electric vehicle applications: challenges and recommendations," *Renewable and Sustainable Energy Reviews*, vol. 78, pp. 834–854, 2017.
- [5] C. Delmas, M. Ménétrier, L. Croguennec et al., "An overview of the  $\text{Li}(\text{Ni},\text{M})\text{O}_2$  systems: syntheses, structures and properties," *Electrochimica Acta*, vol. 45, no. 1-2, pp. 243–253, 1999.
- [6] C. S. Johnson, N. Li, C. Lefief, and M. M. Thackeray, "Anomalous capacity and cycling stability of  $x\text{Li}_2\text{MnO}_3 \cdot (1-x)\text{LiMO}_2$  electrodes (M = Mn, Ni, Co) in lithium batteries at 50°C," *Electrochemistry Communications*, vol. 9, no. 4, pp. 787–795, 2007.
- [7] Z. Lu, X. Tan, Y. Tang, and K. Zhou, "LiNi<sub>0.7</sub>Co<sub>0.15</sub>Mn<sub>0.15</sub>O<sub>2</sub> microspheres as high-performance cathode materials for lithium-ion batteries," *Rare Metals*, vol. 33, no. 5, pp. 608–614, 2014.
- [8] K. K. Lee, W. S. Yoon, K. B. Kim, K. Y. Lee, and S. T. Hong, "Characterization of  $\text{LiNi}_{0.85}\text{Co}_{0.10}\text{M}_{0.05}\text{O}_2$  (M = Al, Fe) as a cathode material for lithium secondary batteries," *Journal of Power Sources*, vol. 97–98, pp. 308–312, 2001.
- [9] Z. Wang, H.-Q. Lu, Y.-P. Yin et al., "FePO<sub>4</sub>-coated  $\text{Li}[\text{Li}_{0.2}\text{Ni}_{0.13}\text{Co}_{0.13}\text{Mn}_{0.54}]\text{O}_2$  with improved cycling performance as cathode material for Li-ion batteries," *Rare Metals*, vol. 36, no. 11, pp. 899–904, 2017.
- [10] M. Jo, M. Noh, P. Oh, Y. Kim, and J. Cho, "A new high power  $\text{LiNi}_{0.81}\text{Co}_{0.1}\text{Al}_{0.09}\text{O}_2$  cathode material for lithium-ion batteries," *Advanced Energy Materials*, vol. 4, no. 13, article 1301583, 2014.

- [11] C. T. Hsieh, H. H. Hsu, J. P. Hsu, Y. F. Chen, and J. K. Chang, "Infrared-assisted synthesis of lithium nickel cobalt alumina oxide powders as electrode material for lithium-ion batteries," *Electrochimica Acta*, vol. 206, pp. 207–216, 2016.
- [12] Y. Makimura, S. Zheng, Y. Ikubara, and Y. Ukyo, "Microstructural observation of  $\text{LiNi}_{0.8}\text{Co}_{0.15}\text{Al}_{0.05}\text{O}_2$  after charge and discharge by scanning transmission electron microscopy," *Journal of the Electrochemical Society*, vol. 159, no. 7, pp. A1070–A1073, 2012.
- [13] H. Xie, G. Hu, K. Du, Z. Peng, and Y. Cao, "An improved continuous co-precipitation method to synthesize  $\text{LiNi}_{0.80}\text{Co}_{0.15}\text{Al}_{0.05}\text{O}_2$  cathode material," *Journal of Alloys and Compounds*, vol. 666, pp. 84–87, 2016.
- [14] C. J. Han, J. H. Yoon, W. I. Cho, and H. Jang, "Electrochemical properties of  $\text{LiNi}_{0.8}\text{Co}_{0.2-x}\text{Al}_x\text{O}_2$  prepared by a sol-gel method," *Journal of Power Sources*, vol. 136, no. 1, pp. 132–138, 2004.
- [15] S. H. Ju, J. H. Kim, and Y. C. Kang, "Electrochemical properties of  $\text{LiNi}_{0.8}\text{Co}_{0.2-x}\text{Al}_x\text{O}_2$  ( $0 \leq x \leq 0.1$ ) cathode particles prepared by spray pyrolysis from the spray solutions with and without organic additives," *Metals and Materials International*, vol. 16, no. 2, pp. 299–303, 2010.
- [16] K. He, Z. Ruan, X. Teng, and Y. Zhu, "Facile synthesis and electrochemical properties of spherical  $\text{LiNi}_{0.85-x}\text{Co}_{0.15}\text{Al}_x\text{O}_2$  with sodium aluminate via co-precipitation," *Materials Research Bulletin*, vol. 90, pp. 131–137, 2017.
- [17] J. Duan, G. Hu, Y. Cao et al., "Enhanced electrochemical performance and storage property of  $\text{LiNi}_{0.815}\text{Co}_{0.15}\text{Al}_{0.035}\text{O}_2$  via Al gradient doping," *Journal of Power Sources*, vol. 326, pp. 322–330, 2016.
- [18] X. Li, W. Ge, H. Wang et al., "Enhancing cycle stability and storage property of  $\text{LiNi}_{0.8}\text{Co}_{0.15}\text{Al}_{0.05}\text{O}_2$  by using fast cooling method," *Electrochimica Acta*, vol. 227, pp. 225–234, 2017.
- [19] H. Y. Tran, C. Täubert, and M. Wohlfahrt-Mehrens, "Influence of the technical process parameters on structural, mechanical and electrochemical properties of  $\text{LiNi}_{0.8}\text{Co}_{0.15}\text{Al}_{0.05}\text{O}_2$  based electrodes—a review," *Progress in Solid State Chemistry*, vol. 42, no. 4, pp. 118–127, 2014.
- [20] Y. Makimura, T. Sasaki, T. Nonaka et al., "Factors affecting cycling life of  $\text{LiNi}_{0.8}\text{Co}_{0.15}\text{Al}_{0.05}\text{O}_2$  for lithium-ion batteries," *Journal of Materials Chemistry A*, vol. 4, no. 21, pp. 8350–8358, 2016.
- [21] X. Yan, L. Chen, S. A. Shah, J. Liang, and Z. Liu, "The effect of  $\text{Co}_3\text{O}_4$  &  $\text{LiCoO}_2$  cladding layer on the high rate and storage property of high nickel material  $\text{LiNi}_{0.8}\text{Co}_{0.15}\text{Al}_{0.05}\text{O}_2$  by simple one-step wet coating method," *Electrochimica Acta*, vol. 249, pp. 179–188, 2017.
- [22] S. Muto, Y. Sasano, K. Tatsumi et al., "Capacity-fading mechanisms of  $\text{LiNiO}_2$ -based lithium-ion batteries II. Diagnostic analysis by electron microscopy and spectroscopy," *Journal of the Electrochemical Society*, vol. 156, no. 5, pp. A371–A377, 2009.
- [23] S. Watanabe, M. Kinoshita, T. Hosokawa, K. Morigaki, and K. Nakura, "Capacity fading of  $\text{LiAl}_y\text{Ni}_{1-x-y}\text{Co}_x\text{O}_2$  cathode for lithium-ion batteries during accelerated calendar and cycle life tests (effect of depth of discharge in charge–discharge cycling on the suppression of the micro-crack generation of  $\text{LiAl}_y\text{Ni}_{1-x-y}\text{Co}_x\text{O}_2$  particle)," *Journal of Power Sources*, vol. 260, pp. 50–56, 2014.
- [24] S. Watanabe, M. Kinoshita, T. Hosokawa, K. Morigaki, and K. Nakura, "Capacity fade of  $\text{LiAl}_y\text{Ni}_{1-x-y}\text{Co}_x\text{O}_2$  cathode for lithium-ion batteries during accelerated calendar and cycle life tests (surface analysis of  $\text{LiAl}_y\text{Ni}_{1-x-y}\text{Co}_x\text{O}_2$  cathode after cycle tests in restricted depth of discharge ranges)," *Journal of Power Sources*, vol. 258, pp. 210–217, 2014.
- [25] S. Watanabe, M. Kinoshita, and K. Nakura, "Capacity fade of  $\text{LiNi}_{(1-x-y)}\text{Co}_x\text{Al}_y\text{O}_2$  cathode for lithium-ion batteries during accelerated calendar and cycle life test. I. Comparison analysis between  $\text{LiNi}_{(1-x-y)}\text{Co}_x\text{Al}_y\text{O}_2$  and  $\text{LiCoO}_2$  cathodes in cylindrical lithium-ion cells during long term storage test," *Journal of Power Sources*, vol. 247, pp. 412–422, 2014.
- [26] M. Wohlfahrt-Mehrens, C. Vogler, and J. Garche, "Aging mechanisms of lithium cathode materials," *Journal of Power Sources*, vol. 127, no. 1-2, pp. 58–64, 2004.
- [27] G. Sarre, P. Blanchard, and M. Broussely, "Aging of lithium-ion batteries," *Journal of Power Sources*, vol. 127, no. 1-2, pp. 65–71, 2004.
- [28] M. Dubarry, C. Truchot, B. Y. Liaw et al., "Evaluation of commercial lithium-ion cells based on composite positive electrode for plug-in hybrid electric vehicle applications. Part II. Degradation mechanism under 2C cycle aging," *Journal of Power Sources*, vol. 196, no. 23, pp. 10336–10343, 2011.
- [29] G. Ning, B. Haran, and B. N. Popov, "Capacity fade study of lithium-ion batteries cycled at high discharge rates," *Journal of Power Sources*, vol. 117, no. 1-2, pp. 160–169, 2003.
- [30] D. Wong, B. Shrestha, D. A. Wetz, and J. M. Heinzel, "Impact of high rate discharge on the aging of lithium nickel cobalt aluminum oxide batteries," *Journal of Power Sources*, vol. 280, pp. 363–372, 2015.
- [31] S. A. Channagiri, S. C. Nagpure, S. S. Babu, G. J. Noble, and R. T. Hart, "Porosity and phase fraction evolution with aging in lithium iron phosphate battery cathodes," *Journal of Power Sources*, vol. 243, pp. 750–757, 2013.
- [32] Y. Sheng, C. R. Fell, Y. K. Son, B. M. Metz, J. Jiang, and B. C. Church, "Effect of calendaring on electrode wettability in lithium-ion batteries," *Frontiers in Energy Research*, vol. 2, 2014.
- [33] Y. Zhang and C. Y. Wang, "Cycle-life characterization of automotive lithium-ion batteries with  $\text{LiNiO}_2$  cathode," *Journal of the Electrochemical Society*, vol. 156, no. 7, p. A527, 2009.

## Research Article

# Surface Characteristic Effect of Ag/TiO<sub>2</sub> Nanoarray Composite Structure on Supercapacitor Electrode Properties

Jie Cui,<sup>1</sup> Lin Cao,<sup>2</sup> Dahai Zeng,<sup>2</sup> Xiaojian Wang,<sup>2</sup> Wei Li,<sup>2</sup> Zhidan Lin<sup>1b</sup>,<sup>2</sup> and Peng Zhang<sup>1b</sup><sup>2</sup>

<sup>1</sup>Analytical and Testing Center of SCUT, South China University of Technology, Guangzhou 510640, China

<sup>2</sup>Institute of Advanced Wear & Corrosion Resistant and Functional Materials, Jinan University, Guangzhou 510632, China

Correspondence should be addressed to Zhidan Lin; [linzd@jnu.edu.cn](mailto:linzd@jnu.edu.cn) and Peng Zhang; [tzhangpeng@jnu.edu.cn](mailto:tzhangpeng@jnu.edu.cn)

Received 30 March 2018; Accepted 28 May 2018; Published 24 July 2018

Academic Editor: Hai-Wen Li

Copyright © 2018 Jie Cui et al. This is an open access article distributed under the Creative Commons Attribution License, which permits unrestricted use, distribution, and reproduction in any medium, provided the original work is properly cited.

Ag-ion-modified titanium nanotube (Ag/TiO<sub>2</sub>-NT) arrays were designed and fabricated as the electrode material of supercapacitors for electrochemical energy storage. TiO<sub>2</sub> nanotube (NT) arrays were prepared by electrochemical anodic oxidation and then treated by Ag metal vapor vacuum arc (MEVVA) implantation. The Ag amount was controlled via adjusting ion implantation parameters. The morphology, crystallinity, and electrochemistry properties of as-obtained Ag/TiO<sub>2</sub>-NT electrodes were distinguished based on various characterizations. Compared with different doses of Ag/TiO<sub>2</sub>-NTs, the electrode with the dose of  $5.0 \times 10^{17}$  ions·cm<sup>-2</sup> exhibited much higher electrode capacity and greatly enhanced activity in comparison to the pure TiO<sub>2</sub>-NTs. The modified electrode showed a high capacitance of 9324.6 mF·cm<sup>-3</sup> (86.9 mF·g, 1.2 mF·cm<sup>-2</sup>), energy density of 82.8 μWh·cm<sup>-3</sup> (0.8 μWh·g, 0.0103 μWh·cm<sup>-2</sup>), and power density of 161.0 mW·cm<sup>-3</sup> (150.4 μW·g, 2.00 μW·cm<sup>-2</sup>) at the current density of 0.05 mA. Therefore, Ag/TiO<sub>2</sub>-NTs could act as a feasible electrode material of supercapacitors.

## 1. Introduction

Nowadays, with the rapid development of science and technology, the depletion of fossil fuels urges a need for efficient, clean, and sustainable sources of energy, as well as with the demand for energy conversion and storage [1–3]. In recent years, supercapacitors have drawn great attention, mainly due to their high power and energy density and long lifecycle, which led to the high-power output and high-energy storage. The electrode material is one of the most important components that govern the overall electrochemical performance of the supercapacitor. Therefore, the development of high-performance electrode material is extremely important [4]. The critical problem is the energy density limitation, which has already hindered its extensive application. Hence, it is pressing to discover new electrode materials for enhancing high capacitance.

Aiming to improve the electrode material capacitance, the design of supercapacitor electrode materials starts with two aspects to solve the problem. One approach is to prepare a nanostructure with suitable pore-size distribution and pore

network, which leads to high specific surface area, more active sites and high rates of ion diffusion, and a low internal electrical resistance for more efficiency at carrying electronic charges [5–7]. It would also bring a better electrochemical and mechanical stability for good cycling performance. It is crucial to match the size of solvated anions and cations by tuning the structure of the nanopores [8–10]. Another way is to design and prepare a composite material, which can combine the high-capacitance materials with large specific surface structure materials.

Among a large number of advanced supercapacitor electrode materials, metal oxides such as titanium oxides are considered as one of the most promising materials for the next generation of supercapacitors [11–14]. In general, metal oxides can provide higher energy density for supercapacitors than conventional carbon materials and better electrochemical stability than polymer materials [15]. They not only store the energy like electrostatic carbon materials but also exhibit the electrochemical faradaic reactions between electrode materials and ions within appropriate potential windows [16–18]. The metal oxides should be electronically

conductive for the supercapacitor application [19–21]. For the electrochemical stability, the metal can exist in two or more oxidation states over a continuous range with no phase changes, which may involve structure changes to reduce the stability of electrodes [22–24]. The oxide lattice also can facilitate the protons intercalating freely into and out of the oxide during the reduction and oxidation processes, respectively [25].

TiO<sub>2</sub>-NTs with vertically oriented nanotube arrays can provide a direct pathway for electron transport along the nanotube's long axis to the substrate [26]. It provides a high surface area, which also shows excellent chemical stability. It also enhances the electrocatalytic activity, cycling stability, and charge rate performance of supercapacitors [27, 28]. Nevertheless, poor capacitive behaviour still limits the use of TiO<sub>2</sub>-NTs. Its large bandgap causes a poor efficiency and low conductivity. Therefore, it is necessary to improve the conductivity of TiO<sub>2</sub>. The electrical conductivity of TiO<sub>2</sub> electrodes can be achieved in a composite electrode material by introducing a conductive substance into the oxide [29, 30].

Ag is considered as one of the prospective modified materials because of its relatively high conductivity. Herein, we report a composite supercapacitor electrode (Ag/TiO<sub>2</sub>-NT arrays) to improve the electric conductivity by introducing Ag into TiO<sub>2</sub>-NTs. Therefore, a modified large specific area and good conductive supercapacitor electrode can be obtained. The conventional anodization process was used to prepare TiO<sub>2</sub>-NTs, and the Ag was induced by ion implantation method. The morphologies, microstructures, and electrochemical performances of the Ag/TiO<sub>2</sub>-NT products were investigated.

## 2. Materials and Methods

**2.1. Materials.** All the chemicals used in this study were analytical reagent grade. Meanwhile, ammonium fluoride (NH<sub>4</sub>F) and ethylene glycol (EG) were obtained from Tianjin Damao Chemical Reagent Factory. Sodium sulfate (Na<sub>2</sub>SO<sub>4</sub>) and ethanol were provided by Guangzhou Chemical Reagent Factory. The pure titanium foil (99.6% pure), with a thickness of about 30 μm, was purchased from Guangzhou Zhongyao Metal Technology Co. Ltd. Pure Ag (99.999% pure) was prepared for ion implantation target.

**2.2. Fabrication of Ag/TiO<sub>2</sub>-NT Arrays.** The TiO<sub>2</sub>-NT arrays were prepared by two-electrode electrochemical anodic oxidation. Before the anodization, the pure titanium foil was ultrasonically washed for 10 minutes in acetone, absolute ethanol, and deionized water. During the anodic oxidation process, the pretreated Ti foil was used as the anode and the stainless steel as the cathode, with an electrolyte which was composed of glycol (98 vol. %), deionized H<sub>2</sub>O (2 vol. %), and NH<sub>4</sub>F (0.3 wt. %). The oxidation voltage was 40 V, and the anodic oxidation time was 1 h. After that, the anodized TiO<sub>2</sub>-NT arrays were treated with Ag-ion implantation with an accelerating voltage of 60 kV and the different ion implantation dose. Then, Ag/TiO<sub>2</sub>-NT samples were obtained by adjusting the implanting doses of 0.5, 1.0, 5.0, and 10.0 × 10<sup>17</sup> ions·cm<sup>-2</sup>.

**2.3. Characterization.** Morphological observations were carried on a field-emission scanning electron microscope (FE-SEM, Zeiss, Oberkochen, Germany) and a field-emission transmission electron microscope (TEM, JEOL 2100F, Japan). Electrochemical measurements, such as galvanostatic charge–discharge (GCD), cyclic voltammetry (CV), and electrochemical impedance spectroscopy (EIS, 100 kHz to 0.01 Hz), were tested by an electrochemical workstation (Princeton PARSTAT 4000). The electrochemical performance of individual electrodes was tested by a three-electrode system with a 0.5 M Na<sub>2</sub>SO<sub>4</sub> solution serving as an electrolyte; a platinum electrode and a saturated calomel electrode (SCE) were used as a counter electrode and reference electrode, respectively.

## 3. Results and Discussion

**3.1. Effect of Ag-Ion Implantation on the Microstructure of TiO<sub>2</sub>-NTs.** Modified surface morphologies of Ti fossil after anodic oxidation and ion implantation with the Ag dose of 0 ions·cm<sup>-2</sup> (pure TiO<sub>2</sub>-NTs), 0.5 × 10<sup>17</sup> ions·cm<sup>-2</sup>, 1.0 × 10<sup>17</sup> ions·cm<sup>-2</sup>, 5.0 × 10<sup>17</sup> ions·cm<sup>-2</sup>, and 10.0 × 10<sup>17</sup> ions·cm<sup>-2</sup> are shown in Figure 1. As shown in Figures 1(a) and 1(b), the surface morphology of TiO<sub>2</sub>-NTs presented as a nanotube array structure. And the average inner diameter of the tube is about 50 nm. After Ag-ion implantation, the surface morphology changed a lot. A net-like surface layer with uniform pores was formed after the Ag-ion implantation dose of 0.5 × 10<sup>17</sup> ions·cm<sup>-2</sup> (as Figures 1(c) and 1(d) showed). The outermost layers of the NT wall were destroyed, and partial NT disconnected and reconnected into a network-like structure. The inside wall of the tube became a little rougher, which may further increase the surface-specific surface area. Although the top surface was changed a lot, it can be seen that the nanotube structure in the whole length is similar with Figure 1(b) as shown in the section view in Figure 1(d). Quite different with the surface of TiO<sub>2</sub>-NT arrays, the pipe orifices were blocked as shown in Figures 1(e) and 1(f), which was caused by the partial TiO<sub>2</sub>-NTs connected during the heat effect in ion implantation while the Ag-ion implantation dose is up to 1 × 10<sup>17</sup> ions·cm<sup>-2</sup>. Besides that, a large number of much finer pores were generated. It can also be found that the length of NTs was reduced obviously as shown in the section view (Figure 1(f)) due to the surface TiO<sub>2</sub> wall being involved in the generation of the new surface. The top nanotubes' lamellar "gap-" like structure is formed by the heat effect increased with the ion bombardment. And the bottom secondary nanotube grew under the action of high temperature. Therefore, the nanotube narrowed into a closed aperture. The surface was fully covered by a nanoisland-like structure as shown in Figure 1(g), when the Ag dose was up to 5.0 × 10<sup>17</sup> ions·cm<sup>-2</sup>. Meanwhile, many nanopores were generated on the wall. Hence, the wall of NTs became much rougher as shown in Figure 1(h). When the Ag-ion implantation dose reached 10.0 × 10<sup>17</sup> ions·cm<sup>-2</sup> (Figures 1(i) and 1(j)), some globular particles appeared and distributed near the top of the nanotubes. It is possible that a part of the nanotube was destroyed; a lot of porous debris formed under the

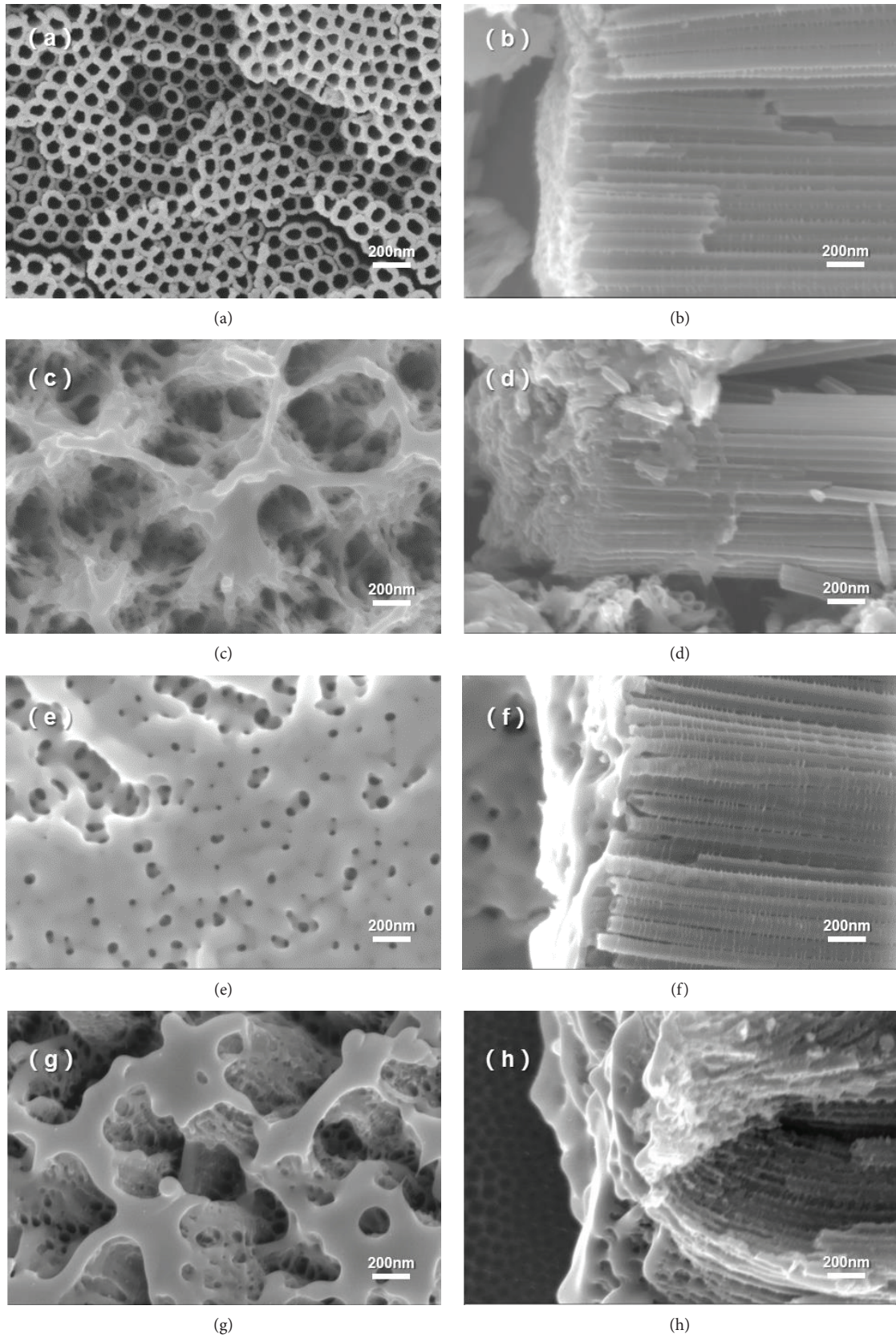


FIGURE 1: Continued.

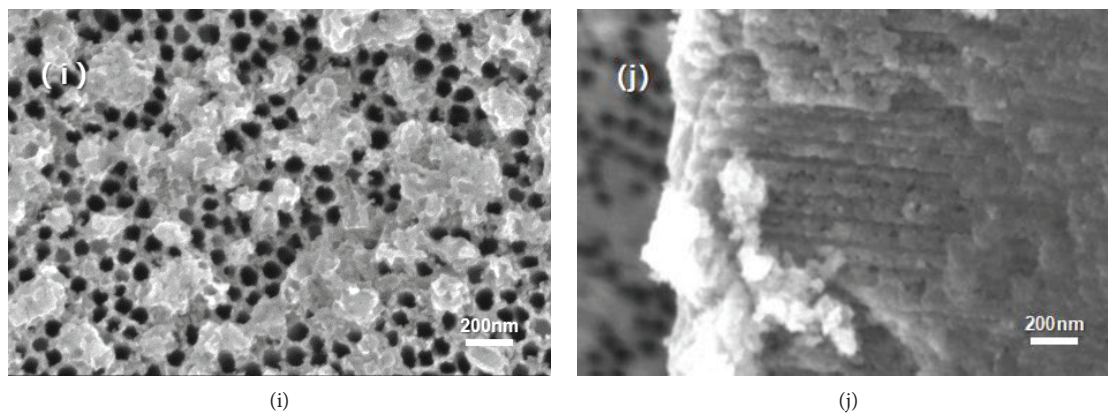


FIGURE 1: SEM images of Ag/TiO<sub>2</sub> electrode at different doses of Ag-ion implantation: top-view of (a) 0 ions·cm<sup>-2</sup>, (c)  $0.5 \times 10^{17}$  ions·cm<sup>-2</sup>, (e)  $1.0 \times 10^{17}$  ions·cm<sup>-2</sup>, (g)  $5.0 \times 10^{17}$  ions·cm<sup>-2</sup>, and (i)  $10.0 \times 10^{17}$  ions·cm<sup>-2</sup>; side-view of (b) 0 ions·cm<sup>-2</sup>, (d)  $0.5 \times 10^{17}$  ions·cm<sup>-2</sup>, (f)  $1.0 \times 10^{17}$  ions·cm<sup>-2</sup>, (h)  $5.0 \times 10^{17}$  ions·cm<sup>-2</sup>, and (j)  $10.0 \times 10^{17}$  ions·cm<sup>-2</sup>.

large number of ion bombardment. The cross-section observation showed that the wall of NTs became much rougher than that of the lower Ag dose. And the wall near the surface almost collapsed under such a high Ag dose. According to the surface and section analysis, it can be inferred that there were two opposite processes, a formation growth process by heat effect and a damage process by high-energy ion bombardment. Therefore, the island-like structure was formed on the surface occurring with the surface layer growth and destruction. At the same time, the nanopores have been created by ion bombardment damage under high Ag dose. And it may lead to higher specific surface area. Meanwhile, the length of the nanotube was further shortened while the Ag dose increased as shown in Figure S3 in the supplementary material. It can be inferred that there is a saturated dose by ion implantation method. When the implantation was lower than the saturated dose, ions were just injected into the surface. Meanwhile, a new phase or new structure was generated by the heat effect and the joining of the new ion. Once the implantation dose was oversaturated, the matrix structure may be damaged due to the overheat effect and excessive ion bombardment.

In order to further investigate the new phase after Ag-ion implantation, the microstructure of the Ag-ion implantation dose under  $5.0 \times 10^{17}$  ions·cm<sup>-2</sup> and  $10.0 \times 10^{17}$  ions·cm<sup>-2</sup> was also observed by transmission electron microscopy (TEM), high-resolution TEM (HRTEM), high-angle annular dark field (HAADF), and energy-dispersive X-ray detector (EDX). It can be proved that Ag nanoparticles were created both in this two samples as shown in Figures 2(a) and 2(b). It can also be found that the spherical particle as marked in red dotted circular areas is found both in these two samples as shown in Figures 2(c) and 2(d), which is consistent with the high-magnification SEM images as shown in Figure S1 in the support information (SI). And the particle sizes in these two samples are 10–15 nm and 20–35 nm, respectively, which supports that particle size of Ag is increased while the implantation dose is up to  $10.0 \times 10^{17}$  ions·cm<sup>-2</sup>. Besides that, it can also be found that the matrix of TiO<sub>2</sub>-NTs shows partial amorphous as shown in Figure 2(b) while the dose is

up to  $10.0 \times 10^{17}$  ions·cm<sup>-2</sup>. This is very different with the crystalline TiO<sub>2</sub> in the sample under the dose of  $5.0 \times 10^{17}$  ions·cm<sup>-2</sup>. Besides that, the EDX of these two samples as shown in Figure 2 in SI shows that the Ag is homogeneously distributed in the TiO<sub>2</sub>-NT matrix.

Hence, it can be briefly summarized that there is a relationship between the structure and Ag implantation as shown in Figure 3. Firstly, TiO<sub>2</sub>-NT array structures were formed on the Ti foil matrix after electrochemical anodization in a two-electrode system. Then a few nano-Ag particles were generated, and the surface was modified under lower Ag dose. While the Ag dose increased continuously, more Ag particles formed on the TiO<sub>2</sub>-NT arrays and the length of the tube was shortened. However, the TiO<sub>2</sub>-NT array matrix was damaged, and the particle size of Ag increased under the oversaturated Ag dose.

**3.2. Effect of Ag/TiO<sub>2</sub> Electrode Conductivity by Ion Implantation.** In order to research the conductive properties of Ag/TiO<sub>2</sub> electrodes, the four-point probe resistance meter method was chosen. Electrode resistivity with different Ag implantation doses was obtained as shown in Figure 4. Compared with the unmodified samples, the resistivity of the sample was decreased significantly with the increase of ion implantation dose. It can be found that resistivity of the Ag/TiO<sub>2</sub> electrode reduced from 523.7 Ω·cm (the unmodified NTs) to 21.6 Ω·cm; the minimum resistivity sample had a corresponding Ag dose of  $5.0 \times 10^{17}$  ions·cm<sup>-2</sup>. Hence, it is no doubt that Ag-ion implantation modification can greatly improve the conductivity especially under the dose of  $5.0 \times 10^{17}$  ions·cm<sup>-2</sup>. In addition, although the resistivity increased a bit more when the dose increased to  $10.0 \times 10^{17}$  ions·cm<sup>-2</sup>, it is still much smaller than that of unmodified samples. Obviously, the slight increased resistivity may be impacted by the almost blocked and damaged tubes under the oversaturated dose. Therefore, the appropriate Ag dose with smaller particle size and integrated array structure may contribute to enhance the conductivity and smoothen the passage of the electronic transmission

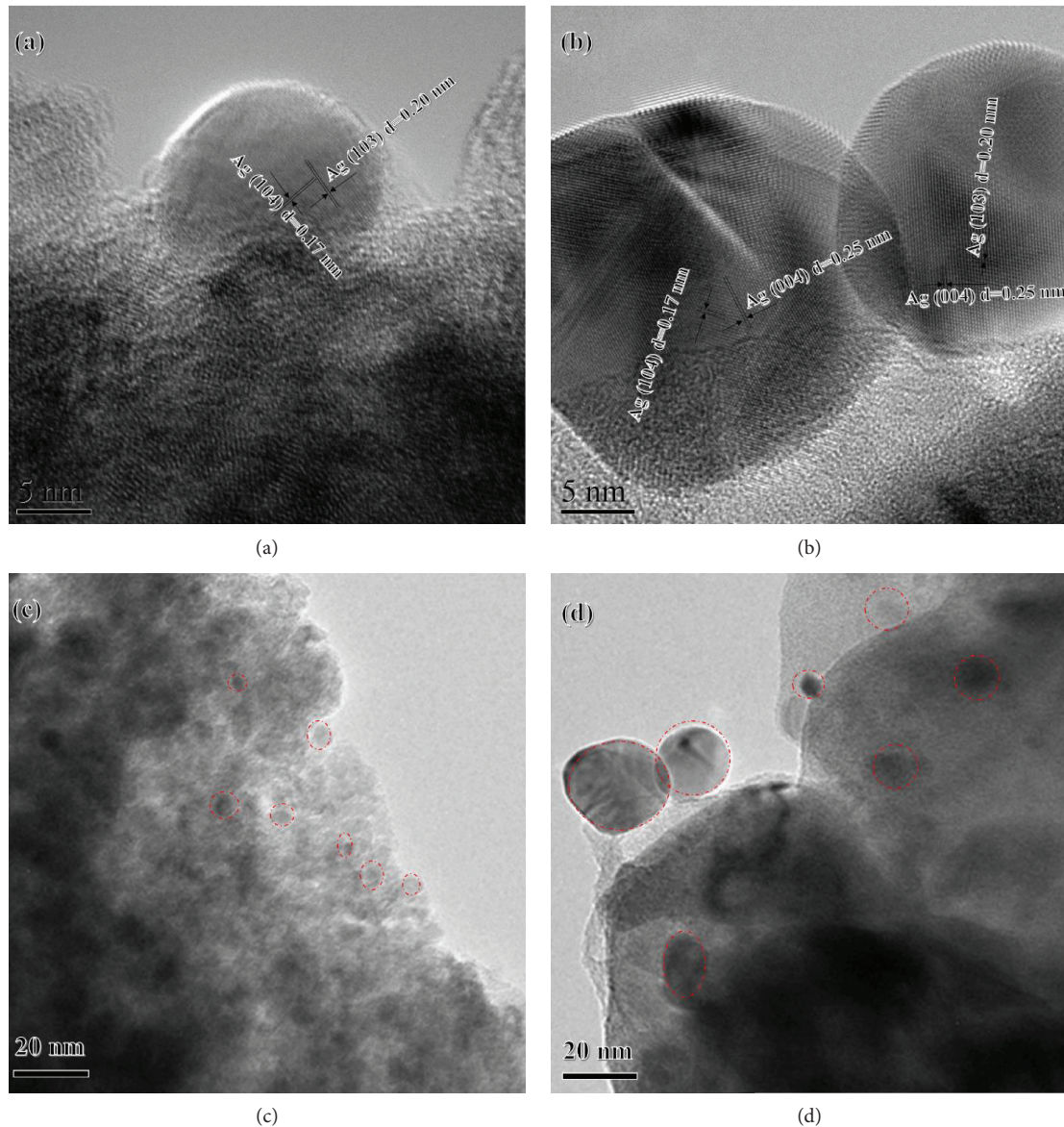


FIGURE 2: HRTEM and TEM bright images of the Ag/TiO<sub>2</sub> electrode at different doses of Ag-ion implantation: (a, c)  $5.0 \times 10^{17}$  ions·cm<sup>-2</sup>; (b, d)  $10.0 \times 10^{17}$  ions·cm<sup>-2</sup>.

channel, which can finally improve the conductivity of the Ag/TiO<sub>2</sub>-NT electrodes.

**3.3. Effect on Ag/TiO<sub>2</sub> Electrode Electrochemical Properties by Ion Implantation.** The CV curves of the Ag/TiO<sub>2</sub> composite electrode with different Ag ions were obtained at the sweep speed of  $100 \text{ mV} \cdot \text{s}^{-1}$  as shown in Figure 5. The CV curve shape of the Ag/TiO<sub>2</sub> electrode is rectangular, which stands for a good capacitor performance. That is because the improved electrical conductivity is beneficial a lot to the electrochemical reaction in the process of rapid transmission and transfer of electric charge. The significantly increased integral area of the CV curves illustrates the significantly enhanced electrode electrochemical activity and the effectively improved capacitance. The specific capacitance was calculated as shown in Figure 6 by CV curves under different Ag-ion implantation dosages. The electrochemical activity of

the Ag/TiO<sub>2</sub> electrode changed with the increase of the Ag-ion implantation dose. And the variation trend is consistent with the change of electrode conductivity, which is also increased with the Ag dose lower than  $5.0 \times 10^{17}$  ions·cm<sup>-2</sup> and then decreased with the reincreased Ag dose. Therefore, the Ag/TiO<sub>2</sub> electrode with a dose of  $5.0 \times 10^{17}$  ions·cm<sup>-2</sup> shows the best electrochemical activity while the resistance rate is the minimum, which is contributed by the appropriate Ag doping with smaller particle size and smooth passage of the electronic transmission channel. It can also be found obviously that the area of the CV curve and the capacitance is decreased when the dose of Ag ions is  $10.0 \times 10^{17}$  ions·cm<sup>-2</sup> which is also consistent with the change of resistivity. This indicates again that the Ag dose of  $5.0 \times 10^{17}$  ions·cm<sup>-2</sup> is the most suitable dose, which leads to an appropriate Ag doping and a relatively complete NT array structure. In short, the above experimental results show that Ag-ion implantation is a

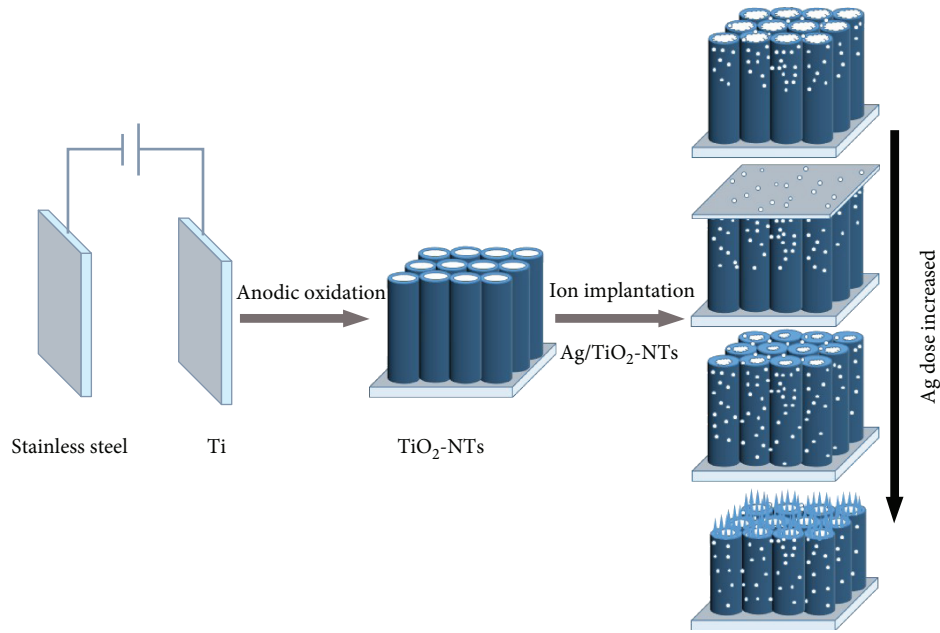


FIGURE 3: Schematic illustration for the synthesis process of the Ag-ion implantation on  $\text{TiO}_2$ -NTs.

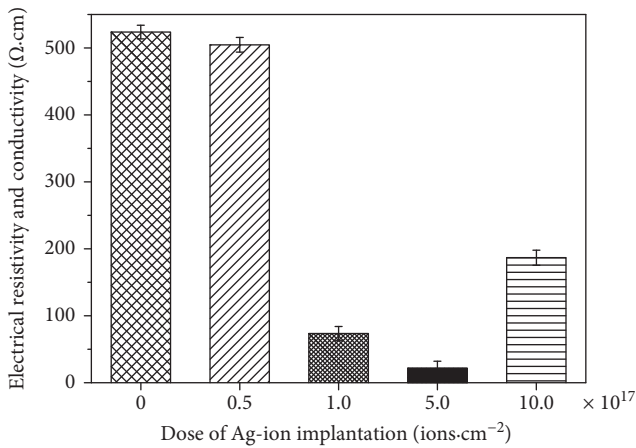


FIGURE 4: The resistivity of  $\text{Ag}/\text{TiO}_2$  electrodes at different doses of Ag-ion implantation.

very effective measure to improve the conductivity and electrochemical activity of  $\text{Ag}/\text{TiO}_2$  electrodes. And the most appropriate Ag dose is  $5.0 \times 10^{17} \text{ ions}\cdot\text{cm}^{-2}$  in the presented study.

The charge-discharge curve (GCD curve) in Figure 7 also shows that the electrochemical activity of the electrode is enhanced with the improvement of electrode conductivity, and the charge and discharge performance is also improved significantly. The  $\text{Ag}/\text{TiO}_2$  electrode GCD curve shows a good triangular shape (Figure 7) under different Ag-ion implantation dosages, when the current density is  $0.05 \text{ mA}\cdot\text{cm}^{-2}$ . The curve also has a good linear relationship between potential and time. It reveals that the electrode materials have a good coulombic efficiency. With the increase of the Ag-ion implantation dose, the electrode material needs a longer discharge time, which indicates that the electrode material shows a larger capacity to store energy. The ratio of capacitance can be calculated by the GCD curve as shown

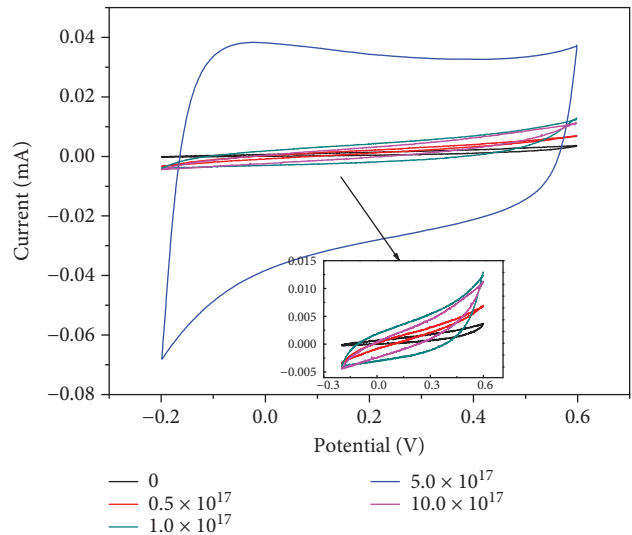


FIGURE 5: CV curves of  $\text{Ag}/\text{TiO}_2$  electrodes at different doses of Ag-ion implantation ( $100 \text{ mV}\cdot\text{s}^{-1}$ ).

in Figure 8. The electrode without Ag-ion implantation is only  $32.9 \text{ mF}\cdot\text{cm}^{-3}$  ( $0.00625 \text{ mF}\cdot\text{cm}^{-2}$ ), while the modified ones are  $378.8$ ,  $2246.7$ ,  $9324.6$ , and  $54.3 \text{ mF}\cdot\text{cm}^{-3}$  ( $0.0625$ ,  $0.344$ ,  $1.156$ , and  $0.00625 \text{ mF}\cdot\text{cm}^{-2}$ , resp.), with the corresponding dose of  $0.5 \times 10^{17} \text{ ions}\cdot\text{cm}^{-2}$ ,  $1.0 \times 10^{17} \text{ ions}\cdot\text{cm}^{-2}$ ,  $5.0 \times 10^{17} \text{ ions}\cdot\text{cm}^{-2}$ , and  $10.0 \times 10^{17} \text{ ions}\cdot\text{cm}^{-2}$ . The specific capacitance of the  $5.0 \times 10^{17} \text{ ions}\cdot\text{cm}^{-2}$  sample is increased about 282.4% much more than the untreated one.

In order to further verify the performance of the  $\text{Ag}/\text{TiO}_2$  electrodes with the dose of  $5.0 \times 10^{17} \text{ ions}\cdot\text{cm}^{-2}$ , the CV test was performed at different scanning rates (Figure 9). During the  $-0.2\sim 0.6 \text{ V}$  voltage range, the shape of the CV curve basically keeps consistent with the increase of the scanning speed. The  $\text{Ag}/\text{TiO}_2$  electrode CV curves still keep a good

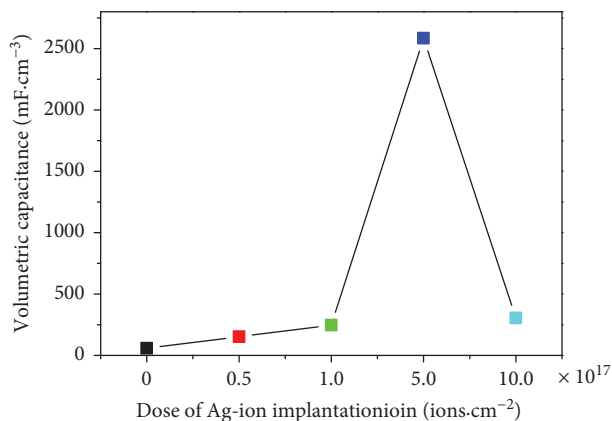


FIGURE 6: Relationship between the dose of Ag-ion implantation and specific capacitance.

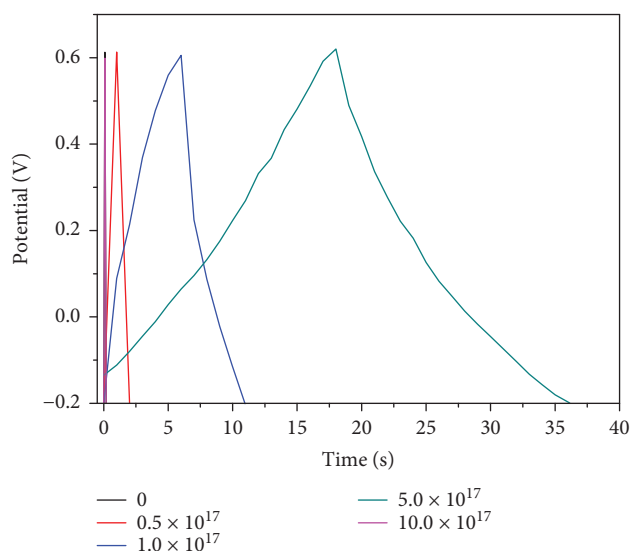


FIGURE 7: GCD curve of Ag/TiO<sub>2</sub> electrodes at different doses of Ag-ion implantation.

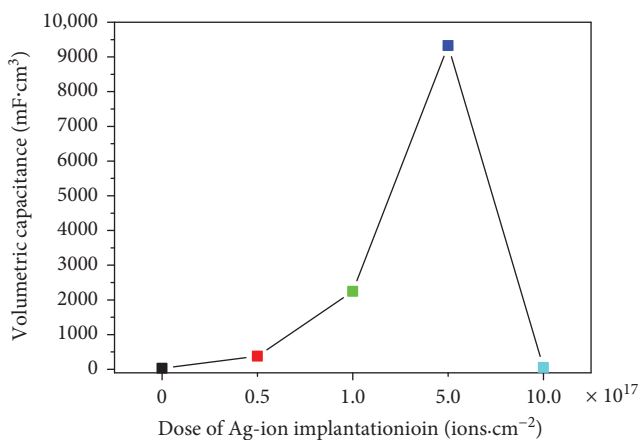


FIGURE 8: Relationship between different doses of Ag-ion implantation and specific capacitance.

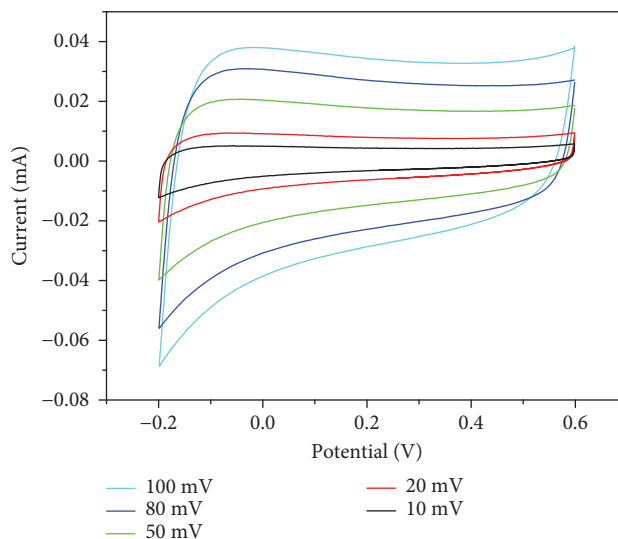


FIGURE 9: CV curves with different scan rates for Ag-ion implantation dose of  $5.0 \times 10^{17}$  ions·cm<sup>-2</sup>.

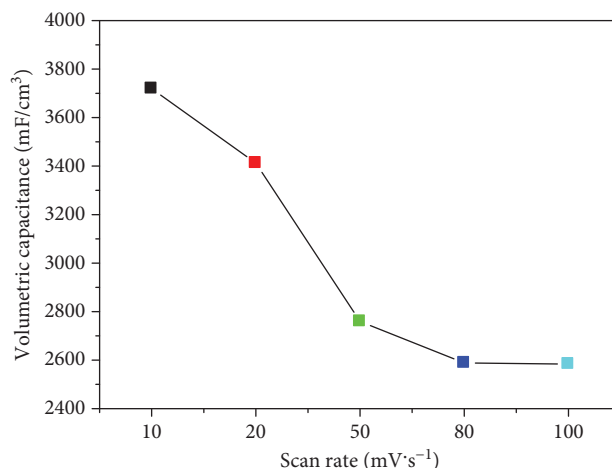


FIGURE 10: Relationship between different scan rates and specific capacitance for Ag-ion implantation dose of  $5.0 \times 10^{17}$  ions·cm<sup>-2</sup>.

rectangular shape with a larger integral area at a high scan speed ( $100 \text{ mV}\cdot\text{s}^{-1}$ ). The large specific capacitance shows that the electrode electrochemical performance is improved obviously after modified ion implantation. With the scanning speed increased, the specific capacitance of electrode materials is also decreased. But the specific capacitance remains at a rate of 69.5% (Figure 10), while the sweep speed from 10 up to  $100 \text{ mV}\cdot\text{s}^{-1}$ . It shows that the electrode response performance to voltage variation is relatively good, and the electrode owns a good ratio performance.

The GCD curves of the Ag/TiO<sub>2</sub> electrode with an Ag dose of  $5.0 \times 10^{17}$  ions·cm<sup>-2</sup> at different current densities are shown in Figure 11. The electrode charge and discharge curves of the electrode show a good symmetry and linear properties under different current densities, which means that the electrode has a high coulombic efficiency. When the electrode under the given current density at 0.05, 0.1, and  $0.5 \text{ mA}\cdot\text{cm}^{-2}$ , the specific capacitance is 9324.6, 7963.7,

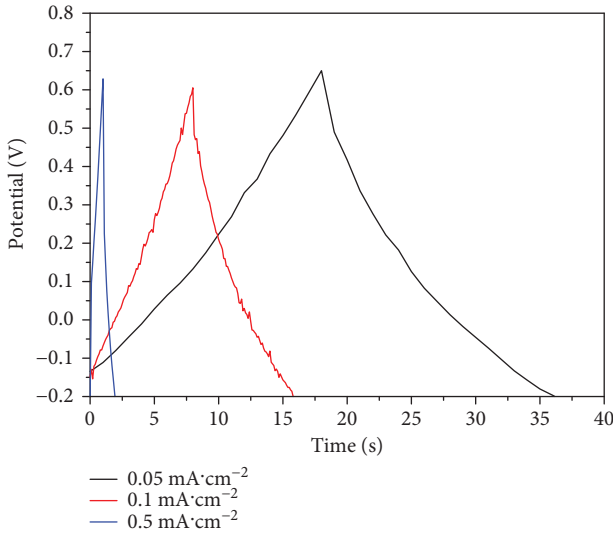


FIGURE 11: GCD curves with different current densities for Ag-ion implantation dose of  $5.0 \times 10^{17}$  ions·cm<sup>-2</sup>.

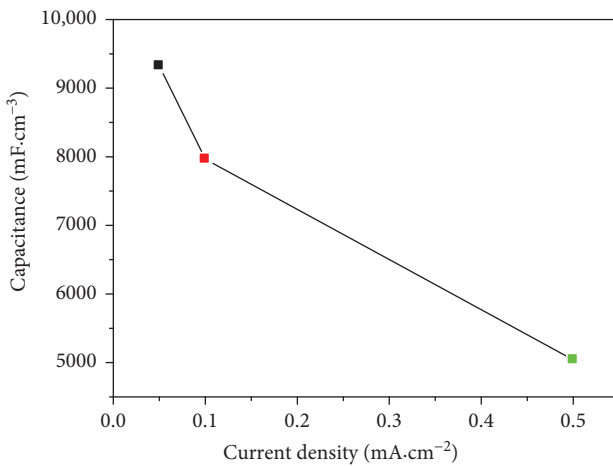


FIGURE 12: Area-based magnification curve for Ag-ion implantation dose of  $5.0 \times 10^{17}$  ions·cm<sup>-2</sup>.

and  $5040.3 \text{ mF}\cdot\text{cm}^{-3}$  (1.156, 0.988, and  $0.625 \text{ mF}\cdot\text{cm}^{-2}$ ) (Figure 12), respectively, which remains at a rate of 54.0%. After the Ag-ion implantation is modified, the conductivity of the electrode was improved. And the electron can be quickly transmitted to the  $\text{TiO}_2$ -NTs at a large current charge and discharge process, in which ratio performance has no sharp attenuation. The modified electrode owns a good capacitance characteristic.

An electrochemical impedance test was used to evaluate the conductivity and ion transfer capacity of the supercapacitor electrode material. The Ag/ $\text{TiO}_2$  electrode impedance diagram with the Ag dose of  $5.0 \times 10^{17}$  ions·cm<sup>-2</sup> is shown in Figure 13. The semicircle diameter of the high-frequency zone is small, which indicates that the internal resistance of the electrode material is very small after the modification of Ag-ion implantation. The straight line is close to  $90^\circ$  of the low-frequency area, which shows a better electrode capacitance performance. Nyquist plots in Figure 13 illustrate the

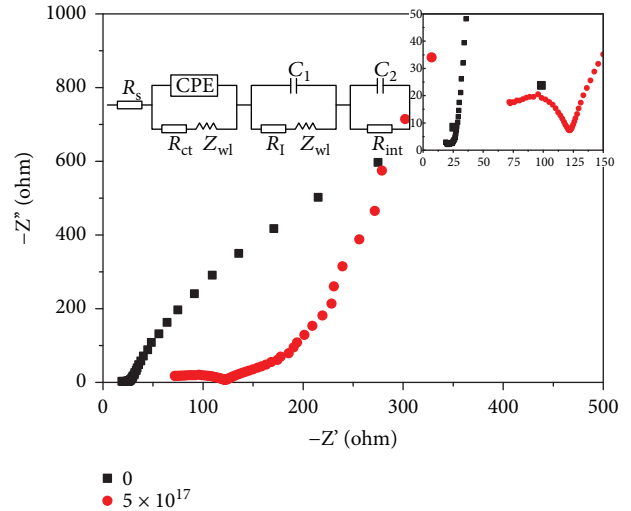


FIGURE 13: Impedance curve of Ag-ion implantation dose of  $5.0 \times 10^{17}$  ions·cm<sup>-2</sup>.

impedance characteristics of the  $\text{TiO}_2/\text{Ti}$  and  $\text{Ag}/\text{TiO}_2/\text{Ti}$  electrodes in  $0.5 \text{ M Na}_2\text{SO}_4$  solution. According to the Randles circuit in Figure 13, the intercept on the real axis represents the series resistance ( $R_s$ ); this impedance is contributed from the contact resistance, bulky electrolyte, and electrode. The arc arises from the charge-transfer resistance ( $R_{ct}$ ) at the electrode/electrolyte interface, whereas  $Z_w$  represents the Nernst diffusion impedance corresponding to the diffusion resistance of the redox species. CPE is a constant phase element, and it is frequently used as a substitute for capacitors in an equivalent circuit to fit the impedance behaviour of the electrical double layer. The  $R_{ct}$  values of the  $\text{TiO}_2/\text{Ti}$  and  $\text{Ag}/\text{TiO}_2/\text{Ti}$  electrodes are  $310,000$  and  $74.79 \Omega\cdot\text{cm}^2$ , respectively, whose values can be employed to assess the charge-transfer ability of the electrodes. A lower  $R_{ct}$  corresponds to facile charge-transfer kinetics within electrodes; therefore, the  $\text{Ag}/\text{TiO}_2/\text{Ti}$  electrode has the highest charge-transfer capacity because of its high electrical conductivity.

## 4. Conclusions

In summary, an Ag-ion implantation modification  $\text{Ag}/\text{TiO}_2$ -NT array composite structure has been successfully synthesized via two steps: anodization and ion implantation. The surface morphology, conductivity, electrochemical properties under different Ag implantation dose was studied. An  $\text{Ag}/\text{TiO}_2$  electrode was prepared, and we got the following conclusions:

- (1) The surface morphology of  $\text{TiO}_2$ -NTs had great changes by Ag-ion-implantation-modifying method. With different Ag-ion implantation doses, the surface morphology of  $\text{Ag}/\text{TiO}_2$  electrodes was affected by the Ag-ion implantation process heating effect on the growth of the surface film layer and the high-energy ion bombardment of surface-coating damage

- (2) Ag-ion implantation has great benefit to the improvement of the Ag/TiO<sub>2</sub> electrode conductivity. When the Ag-ion implantation dose was  $5.0 \times 10^{17}$  ions·cm<sup>-2</sup>, a minimum resistivity (21.6 Ω·cm) was obtained, which had fallen by about 95.8% compared with the sample without ion implantation modification.
- (3) Ag ions were implanted into TiO<sub>2</sub> nanotube array structures; they can enhance the conductivity and smoothen the passage of the electronic transmission channel. When the Ag/TiO<sub>2</sub> electrode was charged at 0.05 mA·cm<sup>-2</sup>, and the implantation dose of Ag ion was  $5.0 \times 10^{17}$  ions·cm<sup>-2</sup>, the specific capacity of the electrode could reach up to 9324.6 mF·cm<sup>-3</sup> (1.156 mF·cm<sup>-2</sup>). The ratio property can reach 54.0% with the current density increased from 0.05 to 0.5 mA·cm<sup>-2</sup>.

Because of the strong synergistic effect between the Ag-NPs and the TiO<sub>2</sub> nanotube array structure in this study, this high-performance Ag/TiO<sub>2</sub> nanotube array structure electrode material is expected to have potential applications in electrochemical energy storage devices.

## Data Availability

All data generated or analysed during this study are included in this article and its supplementary information files.

## Conflicts of Interest

The authors declare that there is no conflict of interest regarding the publication of this paper.

## Acknowledgments

Jie Cui and Peng Zhang designed and conducted the research, collected and analysed the data, and wrote this paper. Lin Cao performed the experiment. Dahai Zeng made the test. Xiaojian Wang guided the experiments. Zhidan Lin, Wei Li, and Peng Zhang offered the materials and instruments. This research was supported by the Guangdong Science and Technology Project Fund (nos. 2014B090915003, 2015B010902005, 2015A030310488, and 2017B090903005) and the scientific cultivation and innovation fund project of Jinan University (no. 21617427). Jie Cui is thankful for the support of the Fundamental Research Funds for the Central Universities (no. 2017BQ046) from SCUT.

## Supplementary Materials

Figure S1: nano-Ag-NPs on the surface of the Ag/TiO<sub>2</sub> electrode with different doses of Ag-ion implantation: (a)  $5 \times 10^{17}$  ions·cm<sup>-2</sup>; (b)  $1 \times 10^{18}$  ions·cm<sup>-2</sup>. Figure S2: elemental mapping by EFTEM analysis for Ag/TiO<sub>2</sub> electrode with different doses of Ag-ion implantation: (a, b)  $5 \times 10^{17}$  ions·cm<sup>-2</sup>; (c, d)  $1 \times 10^{18}$  ions·cm<sup>-2</sup>. Figure S3: section view and nanotube length of Ag/TiO<sub>2</sub> electrode with different doses of Ag-ion implantation: (a) 0 ions·cm<sup>-2</sup>; (b)  $5 \times 10^{16}$  ions·cm<sup>-2</sup>;

(c)  $1 \times 10^{17}$  ions·cm<sup>-2</sup>; (d)  $5 \times 10^{17}$  ions·cm<sup>-2</sup>; (e)  $1 \times 10^{18}$  ions·cm<sup>-2</sup>. (Supplementary Materials)

## References

- [1] H. R. Barai, M. M. Rahman, and S. W. Joo, "Annealing-free synthesis of K-doped mixed-phase TiO<sub>2</sub> nanofibers on Ti foil for electrochemical supercapacitor," *Electrochimica Acta*, vol. 253, pp. 563–571, 2017.
- [2] T. Li, Y. Wu, Q. Wang, D. Zhang, A. Zhang, and M. Miao, "TiO<sub>2</sub> crystalline structure and electrochemical performance in two-ply yarn CNT/TiO<sub>2</sub> asymmetric supercapacitors," *Journal of Materials Science*, vol. 52, no. 13, pp. 7733–7743, 2017.
- [3] J. Zhang, Y. Wang, Y. Qin et al., "A facile one-step synthesis of Mn<sub>3</sub>O<sub>4</sub> nanoparticles-decorated TiO<sub>2</sub> nanotube arrays as high performance electrode for supercapacitors," *Journal of Solid State Chemistry*, vol. 246, pp. 269–277, 2017.
- [4] K. J. Griffith, A. Senyshyn, and C. P. Grey, "Structural stability from crystallographic shear in TiO<sub>2</sub>-Nb<sub>2</sub>O<sub>5</sub> phases: cation ordering and lithiation behavior of TiNb<sub>24</sub>O<sub>62</sub>," *Inorganic Chemistry*, vol. 56, no. 7, pp. 4002–4010, 2017.
- [5] D. Bauer, A. J. Roberts, N. Matsumi, and J. A. Darr, "Nano-sized Mo- and Nb-doped TiO<sub>2</sub> as anode materials for high energy and high power hybrid li-ion capacitors," *Nanotechnology*, vol. 28, no. 19, article 195403, 2017.
- [6] A. Elmouwahidi, E. Bailón-García, J. Castelo-Quibén, A. F. Pérez-Cadenas, F. J. Maldonado-Hódar, and F. Carrasco-Marín, "Carbon-TiO<sub>2</sub> composites as high-performance supercapacitor electrodes: synergistic effect between carbon and metal oxide phases," *Journal of Materials Chemistry A*, vol. 6, no. 2, pp. 633–644, 2018.
- [7] R. Bolagam, R. Boddula, and P. Srinivasan, "Design and synthesis of ternary composite of polyaniline-sulfonated graphene oxide-TiO<sub>2</sub> nanorods: a highly stable electrode material for supercapacitor," *Journal of Solid State Electrochemistry*, vol. 22, no. 1, pp. 129–139, 2018.
- [8] Q. Zhu, K. Liu, J. Zhou, H. Hu, W. Chen, and Y. Yu, "Design of a unique 3D-nanostructure to make MnO<sub>2</sub> work as supercapacitor material in acid environment," *Chemical Engineering Journal*, vol. 321, pp. 554–563, 2017.
- [9] J. H. Lee, J. Y. Lim, C. S. Lee, J. T. Park, and J. H. Kim, "Direct growth of NiO nanosheets on mesoporous TiN film for energy storage devices," *Applied Surface Science*, vol. 420, pp. 849–857, 2017.
- [10] P. Prasannalakshmi, N. Shanmugam, and A. Senthil Kumar, "Electrochemistry of TiO<sub>2</sub>/CdS composite electrodes for supercapacitor applications," *Journal of Applied Electrochemistry*, vol. 47, no. 8, pp. 889–903, 2017.
- [11] J. Xing, W. Zhang, M. Yin, X. Zhu, D. Li, and Y. Song, "Electrodeposition of polyaniline in long TiO<sub>2</sub> nanotube arrays for high-areal capacitance supercapacitor electrodes," *Journal of Solid State Electrochemistry*, vol. 21, no. 8, pp. 2349–2354, 2017.
- [12] A. Massa, S. Hernández, A. Lamberti, C. Galletti, N. Russo, and D. Fino, "Electro-oxidation of phenol over electrodeposited MnO<sub>x</sub> nanostructures and the role of a TiO<sub>2</sub> nanotubes interlayer," *Applied Catalysis B: Environmental*, vol. 203, pp. 270–281, 2017.
- [13] M. Faraji, "Interlaced polyaniline/carbon nanotube nanocomposite co-electrodeposited on TiO<sub>2</sub> nanotubes/Ti for high-performance supercapacitors," *Journal of Solid State Electrochemistry*, vol. 22, no. 3, pp. 677–684, 2018.

- [14] F. Xie, T. Liu, L. Xie, X. Sun, and Y. Luo, "Metallic nickel nitride nanosheet: an efficient catalyst electrode for sensitive and selective non-enzymatic glucose sensing," *Sensors and Actuators B: Chemical*, vol. 255, pp. 2794–2799, 2018.
- [15] L. Wu, F. Li, Y. Xu et al., "Plasmon-induced photoelectrocatalytic activity of Au nanoparticles enhanced TiO<sub>2</sub> nanotube arrays electrodes for environmental remediation," *Applied Catalysis B: Environmental*, vol. 164, pp. 217–224, 2015.
- [16] A. N. Banerjee, V. C. Anitha, and S. W. Joo, "Improved electrochemical properties of morphology-controlled titania/titanate nanostructures prepared by in-situ hydrothermal surface modification of self-source Ti substrate for high-performance supercapacitors," *Scientific Reports*, vol. 7, no. 1, article 13227, 2017.
- [17] M. Y. Rafiq, F. Iqbal, F. Aslam et al., "Fabrication and characterization of ZnO/MnO<sub>2</sub> and ZnO/TiO<sub>2</sub> flexible nanocomposites for energy storage applications," *Journal of Alloys and Compounds*, vol. 729, pp. 1072–1078, 2017.
- [18] Y. Zhao, H. Zhang, A. Liu, Y. Jiao, J. J. Shim, and S. Zhang, "Fabrication of nanoarchitected TiO<sub>2</sub>(B)@C/rGO electrode for 4 V quasi-solid-state nanohybrid supercapacitors," *Electrochimica Acta*, vol. 258, pp. 343–352, 2017.
- [19] P. Nagaraju, A. Alsalmeh, A. Alswieleh, and R. Jayavel, "Facile *in-situ* microwave irradiation synthesis of TiO<sub>2</sub>/graphene nanocomposite for high-performance supercapacitor applications," *Journal of Electroanalytical Chemistry*, vol. 808, pp. 90–100, 2018.
- [20] A. K. Thakur, R. B. Choudhary, M. Majumder, and M. Majhi, "Fairly improved pseudocapacitance of PTP/PANI/TiO<sub>2</sub> nanohybrid composite electrode material for supercapacitor applications," *Ionics*, vol. 24, no. 1, pp. 257–268, 2018.
- [21] Y. E. Zhu, L. Yang, J. Sheng et al., "Fast sodium storage in TiO<sub>2</sub>@CNT@C nanorods for high-performance Na-ion capacitors," *Advanced Energy Materials*, vol. 7, no. 22, article 1701222, 2017.
- [22] P. Agharezaei, H. Abdizadeh, and M. R. Golobostanfard, "Flexible supercapacitor electrodes based on TiO<sub>2</sub>/rGO/TiO<sub>2</sub> sandwich type hybrids," *Ceramics International*, vol. 44, no. 4, pp. 4132–4141, 2018.
- [23] S. Ozkan, N. T. Nguyen, I. Hwang, A. Mazare, and P. Schmuki, "Highly conducting spaced TiO<sub>2</sub> nanotubes enable defined conformal coating with nanocrystalline Nb<sub>2</sub>O<sub>5</sub> and high performance supercapacitor applications," *Small*, vol. 13, no. 14, article 1603821, 2017.
- [24] V. H. Pham, T. D. Nguyen-Phan, X. Tong, B. Rajagopalan, J. S. Chung, and J. H. Dickerson, "Hydrogenated TiO<sub>2</sub>@reduced graphene oxide sandwich-like nanosheets for high voltage supercapacitor applications," *Carbon*, vol. 126, pp. 135–144, 2018.
- [25] D. Mohapatra, S. Parida, B. K. Singh, and D. S. Sutar, "Importance of microstructure and interface in designing metal oxide nanocomposites for supercapacitor electrodes," *Journal of Electroanalytical Chemistry*, vol. 803, pp. 30–39, 2017.
- [26] J. Xu, N. Xu, X. Zhang et al., "*In situ* fabrication of Ni nanoparticles on N-doped TiO<sub>2</sub> nanowire arrays by nitridation of NiTiO<sub>3</sub> for highly sensitive and enzyme-free glucose sensing," *Journal of Materials Chemistry B*, vol. 5, no. 9, pp. 1779–1786, 2017.
- [27] Z. Weng, H. Guo, X. Liu, S. Wu, K. W. K. Yeung, and P. K. Chu, "Nanostructured TiO<sub>2</sub> for energy conversion and storage," *RSC Advances*, vol. 3, no. 47, pp. 24758–24775, 2013.
- [28] Y. Liu, X. Cai, J. Jiang, M. Yan, and W. Shi, "Nitrogen and carbon co-doped Ni-TiO<sub>2</sub> spindles for high performance electrochemical capacitor electrodes," *Applied Surface Science*, vol. 396, pp. 774–779, 2017.
- [29] C. Yu, Y. Wang, J. Zhang et al., "One-step electrodeposition of Co<sub>0.12</sub>Ni<sub>1.88</sub>S<sub>2</sub>@Co<sub>8</sub>S<sub>9</sub> nanoparticles on highly conductive TiO<sub>2</sub> nanotube arrays for battery-type electrodes with enhanced energy storage performance," *Journal of Power Sources*, vol. 364, pp. 400–409, 2017.
- [30] L. Jiang, J. Qi, Y. Sui et al., "Preparation and capacitance properties of Al-doped hierarchical TiO<sub>2</sub> nanostructure by oxidation of Ti-8Al alloy," *Journal of Materials Science: Materials in Electronics*, vol. 28, no. 18, pp. 13770–13779, 2017.

## Review Article

# Advanced SEM and TEM Techniques Applied in Mg-Based Hydrogen Storage Research

Jianding Li,<sup>1</sup> Jincheng Xu,<sup>1</sup> Bo Li,<sup>1</sup> Liqing He ,<sup>2</sup> Huaijun Lin ,<sup>3</sup> Hai-Wen Li ,<sup>4</sup>  
and Huaiyu Shao <sup>1</sup>

<sup>1</sup>*Institute of Applied Physics and Materials Engineering (IAPME), University of Macau, Macau*

<sup>2</sup>*Department of Materials Science and Engineering, Southern University of Science and Technology, Shenzhen 518055, China*

<sup>3</sup>*Institute of Advanced Wear & Corrosion Resistance and Functional Materials, Jinan University, Guangzhou 510632, China*

<sup>4</sup>*Kyushu University Platform of Inter/Transdisciplinary Energy Research (Q-PIT), Kyushu University, Fukuoka 819-0395, Japan*

Correspondence should be addressed to Liqing He; [helq@sustc.edu.cn](mailto:helq@sustc.edu.cn), Huaijun Lin; [hjlin@jnu.edu.cn](mailto:hjlin@jnu.edu.cn), Hai-Wen Li; [li.haiwen.305@m.kyushu-u.ac.jp](mailto:li.haiwen.305@m.kyushu-u.ac.jp), and Huaiyu Shao; [hshao@umac.mo](mailto:hshao@umac.mo)

Received 14 February 2018; Revised 12 May 2018; Accepted 16 May 2018; Published 17 July 2018

Academic Editor: Renato Buzio

Copyright © 2018 Jianding Li et al. This is an open access article distributed under the Creative Commons Attribution License, which permits unrestricted use, distribution, and reproduction in any medium, provided the original work is properly cited.

Mg-based materials are regarded as one of the most promising candidates for hydrogen storage. In order to clarify the relationship between the structures and properties as well as to understand the reaction and formation mechanisms, it is beneficial to obtain useful information about the size, morphology, and microstructure of the studied materials. Herein, the use of scanning electron microscopy (SEM) and transmission electron microscopy (TEM) techniques for the representation of Mg-based hydrogen storage materials is described. The basic principles of SEM and TEM are presented and the characterizations of the size, morphology observation, phase and composition determination, and formation and reaction mechanisms clarification of Mg-based hydrogen storage materials are discussed. The applications of advanced SEM and TEM play significant roles in the research and development of the next-generation hydrogen storage materials.

## 1. Introduction

Mg-based materials are thought to be very promising solid state hydrogen storage systems for mobile or stationary applications due to its low price, abundant resources, and high theoretical hydrogenation capacity [1–10]. However, the challenges of poor kinetics and improper thermodynamics seriously hindered their commercial applications. The situation of the little practical use of Mg-based hydrogen storage materials is mainly attributed to the extremely slow hydrogenation/dehydrogenation reaction, which occurs only at high temperatures (above 523 K). In practice, an activation process of absorption/desorption also requires a high temperature of about 623 K and a hydrogen pressure of 70 atm without any additives [11]. It is reported that there are several reasons which may limit the reaction kinetics. The first one is that the magnesium oxide forms easily on the surface of Mg when the Mg particles are exposed to air. Moreover, the formed MgO layer on the surface of Mg would greatly

prevent the contact of Mg and hydrogen molecules and hamper hydrogen penetration into the Mg-based materials to form a metal hydride. Another one is that the dissociation rate of hydrogen molecules on the metal surface is slow. Numerous efforts are required to improve the kinetics and to tailor the thermodynamics in Mg-based materials. To overcome these drawbacks, different nanoprocessing techniques are adopted to synthesize Mg-based nanomaterials for hydrogen storage development. These techniques include ball milling, hydrogen plasma metal reaction (HPMR), catalyzed solution chemical synthesis, and nanoconfinement [8, 12–27]. Particularly, nanoprocessing for the synthesis of nanosized Mg-based materials has gained more and more interest because of the need to increase the surface contact between Mg and hydrogen and to reduce the diffusion distance for hydrogen in particles and grains [28–30]. Moreover, it is beneficial to represent the microstructures of Mg-based hydrogen storage materials when researchers want to figure out the relationship between the structure and

hydrogen storage performance. Lots of work have been reported on the study of the nanoscale structural characterization of a Mg-based hydrogen storage material by TEM and SEM techniques [31–41]. In some cases, in order to give direct evidence of the operating mechanisms, in situ scanning techniques can be used to directly understand the hydrogen reaction mechanism of  $\text{MgH}_2$  [42–46]. Here, the use of conventional electron microscopies as well as in situ techniques to observe the microstructure information in Mg-based materials and to understand the formation and reaction mechanisms during hydrogen storage processes is described. The main materials discussed in this work include the following:

- (a) Mg and other alloy metal nanoparticles (Ni, Cu, Co, Fe, and Al) synthesized by a hydrogen plasma metal reaction method (size measurements, morphology observation, and correlation study of properties and microstructure)
- (b)  $\text{Mg}_{50}\text{Co}_{50}$  alloy with a body-centered cubic (bcc) structure synthesized by ball milling for 100 h (size measurements and phase and composition determination)
- (c) Mg thin-film sample deposited on a glass substrate by a sputtering method (size measurements)
- (d) Commercial 325 mesh Mg from Alfa Aesar (morphology observation)
- (e)  $\text{Mg}_{50}\text{Co}_{50}$  samples ball milled for various durations (determination of the phase and composition and understanding the formation mechanism)
- (f)  $\text{TiH}_2$  catalyzed a  $\text{MgH}_2$  nanocrystallite sample by a chemical solution synthesis method (phase and composition determination)
- (g)  $\text{MgH}_2$  and  $\text{Mg}_2\text{NiH}_4$  samples from the hydrogenation of Mg and  $\text{Mg}_2\text{Ni}$  (in situ observation of hydrogen reaction mechanism)

## 2. Application of SEM and TEM Techniques for Mg-Based Hydrogen Storage Research

### 2.1. Size Measurements (Particle Size, Crystallite Size, Etc.)

With the emerging of more and more nanotechnologies in the development of Mg-based hydrogen storage materials, it is important to obtain the size information in nanometer and micrometer scales, so that we may understand more about the size effect on hydrogen storage properties in these materials. There have been numerous analytic techniques for size measurements, such as electron microscopy, dynamic light scattering, X-ray diffraction and scattering, field flow fractionation, centrifugal liquid sedimentation, and atomic force microscopy. The TEM technique may provide a two-dimensional picture of sample particles, which can be used for the size distribution evaluation in certain area ranges [47].

Figure 1 shows the TEM images of Mg, Ni, Cu, Co, Fe, and Al nanoparticle samples obtained by a hydrogen plasma metal reaction method. All of these metal nanoparticles after HPMR synthesis show a granular structure. The particle sizes

of these nanoparticle samples for various metals are quite different. Mg particles have a much larger size than the others. The average size of Mg particles is around 300–500 nm, while the ones for Ni, Cu, Co, Fe, and Al are around 30–50 nm. The difference is due to the much faster vaporization rate and higher synthesis rate of Mg than the other metals during the HPMR synthesis process. The evaporation rate depends much on the vaporized metals and it is strongly related to the melting points, boiling points, and saturation vapor pressures of these metals, which influence the size of the synthesized metal nanoparticles [48]. In Figure 1, we can see that the size and distribution of the particles may be easily obtained from TEM observation.

Figure 2 presents the SEM image and dark-field TEM image of the  $\text{Mg}_{50}\text{Co}_{50}$  alloy with a bcc structure. This alloy with a metastable feature and unique microstructure was reported to be able to absorb hydrogen at  $-15^\circ\text{C}$ , which is the lowest temperature reported so far for Mg-based materials to absorb hydrogen [8, 49]. The microstructure information of this sample can be obtained by SEM and TEM observations. From Figure 2(a), we can see that the  $\text{Mg}_{50}\text{Co}_{50}$  alloy after ball milling has a homogenous particle size of around 1–2  $\mu\text{m}$ . From the dark-field TEM in Figure 2(b), we may find some crystallites inside a large particle of the  $\text{Mg}_{50}\text{Co}_{50}$  alloy with a size of just a few nm, which is in agreement with the crystallite size calculated by the broadening of X-ray diffraction peaks [50–52]. The very fine particle size of 1–2  $\mu\text{m}$ , the crystallite size of a few nm, and the bcc nonclose structure are thought to be the main factors of good kinetics at low temperature. In Figures 2(a) and 2(b), we can see that SEM focuses on the surface of the sample, while TEM may see more inside the particle or beyond the surfaces, which makes it possible to measure particle size by SEM observation on the surface and obtain crystallite size inside the particles via transmitted electrons illuminated in the image.

In Figure 3, we use the SEM technique to obtain the thickness size of the thin film. This size is needed for the calculation of thermal diffusivity and thermal conductivity of thin-film samples. From Figure 3, the boundary of the Mg film with the glass substrate is clear and it can be clearly observed that the layer thickness is about 84 nm. With this value, the thermal diffusivity and thermal conductivity of the Pd-capped Mg thin film are calculated to be  $4.62 \times 10^{-5} \text{ m}^2/\text{s}$  and  $82.0 \text{ W/m/K}$ , respectively. When we compare the thermal conductivity and hydrogen absorption kinetics with several other Mg-based materials (325 mesh Mg, Mg single crystal (0001), Mg nanoparticles by HPMR method, and  $\text{Mg}_{50}\text{Co}_{50}$  bcc alloy) the Mg thin-film sample is the optimized sample with superior hydrogen absorption kinetics and good thermal conductivity. By SEM observation, the key thickness size of the Mg thin film is obtained and this makes it possible for the evaluation of thermal physical properties.

2.2. Morphology Observation. Figure 4 compares the observation results from TEM and SEM techniques. The similar information obtained by SEM and TEM methods is the size and shape of the Mg nanoparticles. After hydrogen plasma

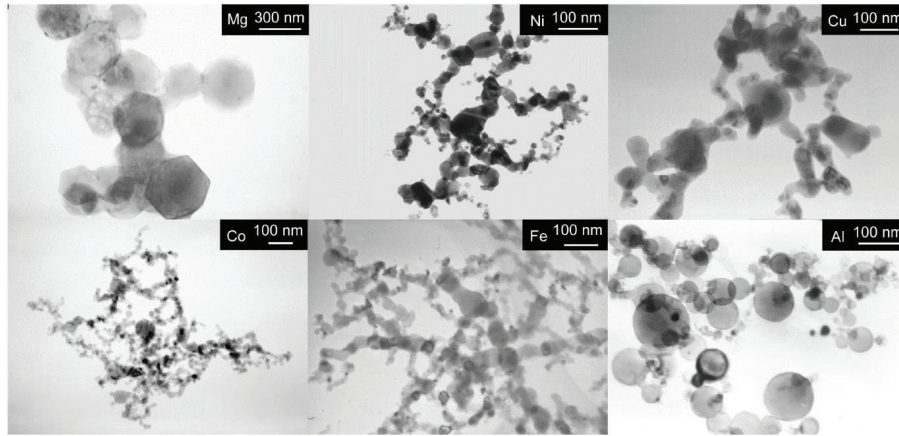


FIGURE 1: TEM images of different metal nanoparticles synthesized by the hydrogen plasma metal reaction method (Mg, Ni, Cu, Co, Fe, and Al) (reproduced with permission from [8]).

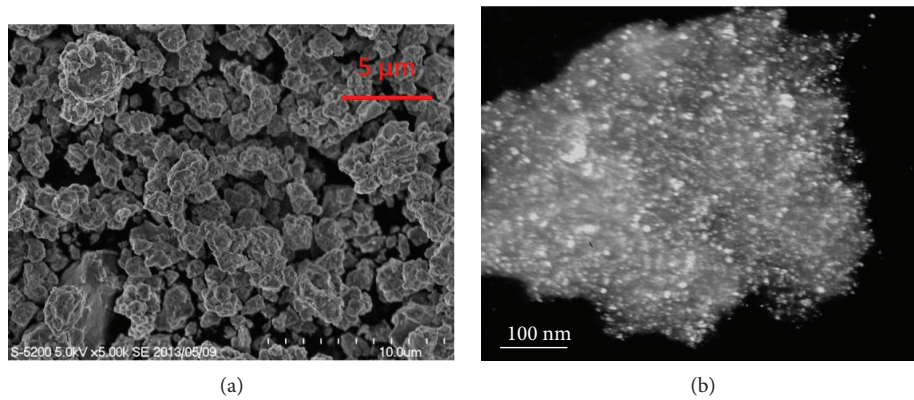


FIGURE 2: (a) SEM image and (b) dark-field TEM image of the  $Mg_{50}Co_{50}$  alloy with a body-centered cubic structure synthesized by ball milling for 100 h (reproduced with permission from [50]).

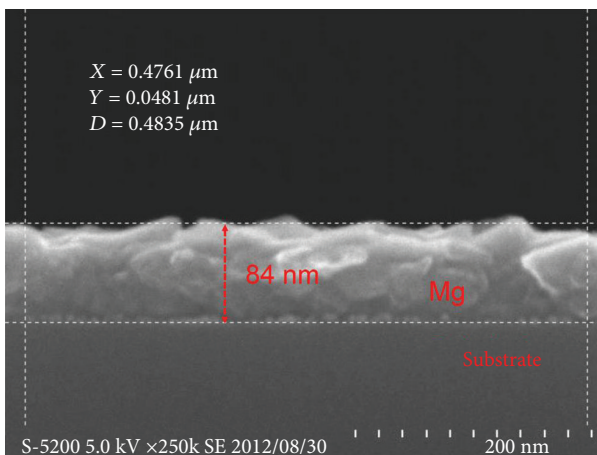


FIGURE 3: SEM image of the cross-sectional observation of the Mg thin film on a glass substrate (reproduced with permission from [50]).

synthesis, the obtained Mg nanoparticles have a size from tens of nm to a few hundred nm and the average size is around 300–500 nm. Most of the Mg particles have a

hexagonal structure. The main difference lies in the dimensional information. TEM provides a 2-dimensional image, while the SEM may provide a 3-dimensional one.

Figure 5 presents the SEM images of two Mg samples. Figure 5(a) shows commercialized Mg particles with a mean size of 40–50  $\mu\text{m}$ . Figure 5(b) shows the Mg thin film deposited on a glass substrate by a direct current magnetron sputtering technique. The crystallite size of Mg on the film surface is around 50–100 nm. From the SEM observation in Figure 5(b), the shape of the small crystal domain is a hexagonal structure, which means that the thin-film synthesis is along the c-axis since the basal plane (0001) of a hexagonal close-packed Mg has the minimum surface energy [54]. Together with the Mg nanoparticles in Figure 4, we may see that the Mg samples by different synthesis methods may present quite a different morphology although both have a hexagonal structure. The SEM technique offers the possibility to observe the surface morphology of the samples.

**2.3. Phase and Composition Determination.** Figure 6 shows the result of the SEM observation and elemental analysis of the  $Mg_{50}Co_{50}$  sample milled for just 0.5 h. Milling the

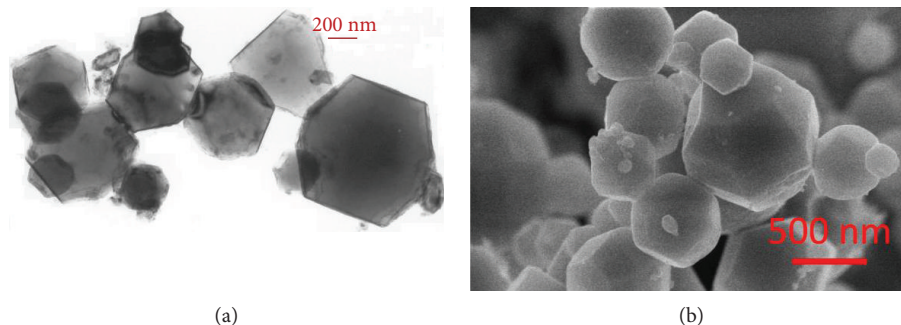


FIGURE 4: (a) TEM image and (b) SEM image of Mg nanoparticles synthesized by the HPMR method (reproduced with permission from [50, 53]).

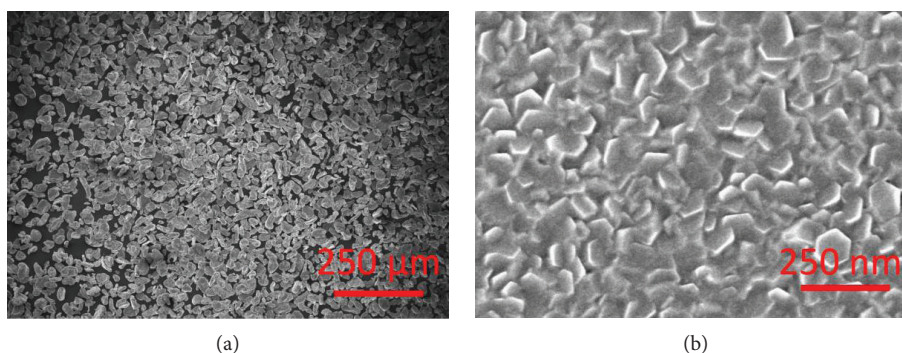


FIGURE 5: SEM images of (a) 325 mesh Mg particles from Alfa Aesar and (b) top view of the Mg thin film on a glass substrate (reproduced with permission from [50]).

mixture sample for 100 h results in the formation of the  $Mg_{50}Co_{50}$  alloy with a bcc structure. After milling for only 0.5 h, it has mainly two Mg and Co phases, which can be confirmed from EDS mapping and X-ray diffraction measurements [49]. When we combine the EDS mapping results with the SEM image, we can see that the small white color particles are Co and the large dark ones are Mg. Here it may demonstrate that through the combination of SE-SEM and BSE-SEM observations as well as EDS elemental analysis mapping and X-ray diffraction techniques, a comprehensive understanding of the phase and composition of the samples may be acquired.

Figure 7 presents the bright-field TEM image and electron diffraction of the bcc-structured  $Mg_{50}Co_{50}$  alloy. In Figure 2, we already discussed that this bcc-structured  $Mg_{50}Co_{50}$  alloy is uniform in size with a particle size of a few  $\mu m$  and a crystallite size of a few nm. The XRD result shows a set of well-broadened reflection peaks [21, 51] and from the broadening, the crystallite size is calculated to be 1–5 nm. In this size, there is no clear boundary between the nanocrystallite and amorphous state, and it is difficult to determine the local lattice structure based on the broadened reflection peaks. However, the electron diffraction characterization attached on the TEM equipment may provide some key information about the lattice structure of the  $Mg_{50}Co_{50}$  alloy after milling for 100 h. After we measured the radii of the electron diffraction rings in Figure 7(b), it was

found that the radii ( $R_1$  to  $R_6$ ) of the diffraction rings from the inside to the outside agree well with the rule of (1).

$$R_1^2 : R_2^2 : R_3^2 : R_4^2 : R_5^2 : R_6^2 = 1 : 2 : 3 : 4 : 5 : 6. \quad (1)$$

This unique accordance indicates that the  $Mg_{50}Co_{50}$  alloy is well indexed as a bcc structure. Here we may see that sometimes, electron diffraction measurements along with SEM may provide a key local lattice structure of the samples, especially when the samples are at a scale of several nm.

Figure 8 presents TEM images of a typical  $MgH_2$  polycrystalline particle in the  $MgH_2$  nanocrystallite sample by a homogeneously catalyzed solution synthesis [20, 55, 56]. This particle has a size of 200–300 nm and some catalyzed Ti with an amorphous-like phase or a crystalline state is confirmed to be located mainly on the rims of the  $MgH_2$  nanocrystals. Figure 8(b) shows one  $MgH_2$  domain with a size of about 50 nm. Since the observation of the TEM images is under a high quality vacuum, it is necessary to prove that the observed area is  $MgH_2$  and not Mg due to evacuation or MgO from oxidization. This key information can be provided from the indexed lattice fringes in Figure 8(c). The three spacings in Figure 8(c) of 0.25, 0.25, and 0.32 nm are in good agreement with the distances of (01-1), (110), and (101) planes of the  $MgH_2$  phase, respectively. This also indicates the electron beam parallel to the (11-1) zone

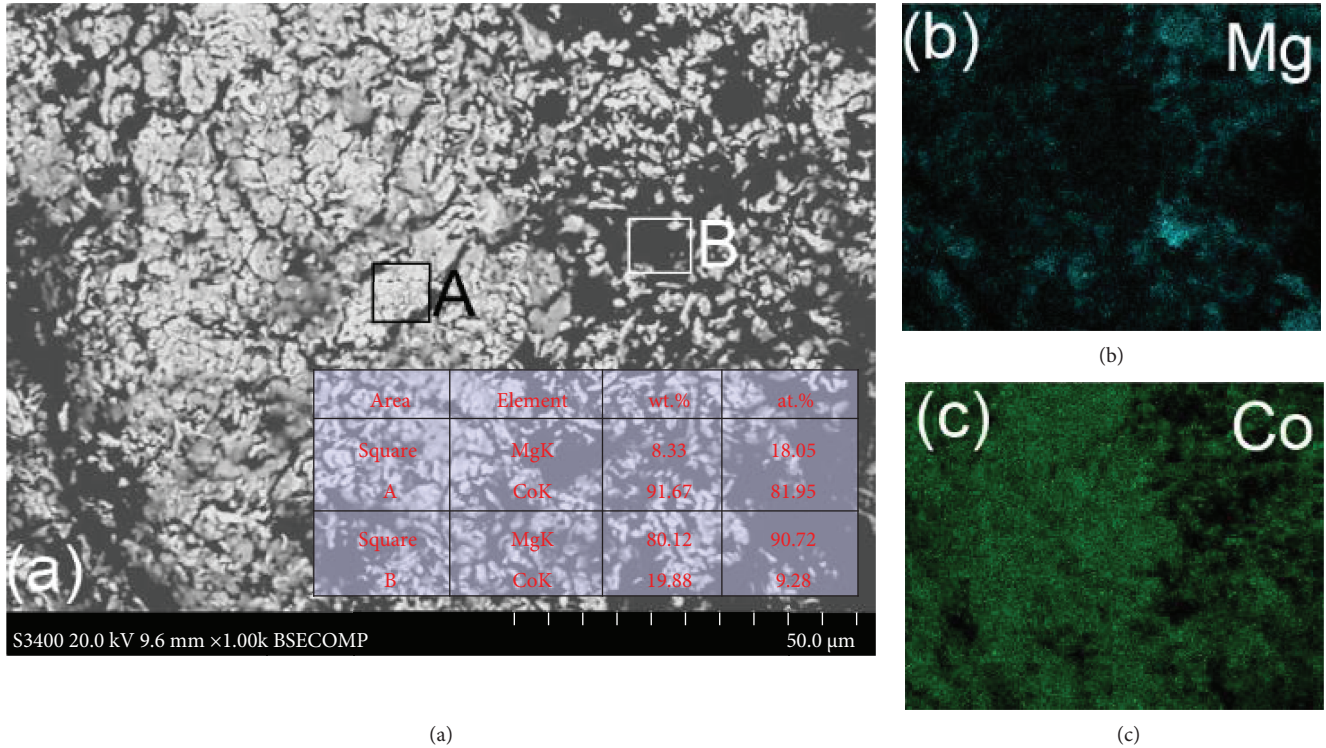


FIGURE 6: (a) BSE-SEM image of the  $Mg_{50}Co_{50}$  sample milled for 0.5 h and the EDS mapping of the Mg element (b) and Co element (c). The inserted table provides the EDS quantitative results of elemental analysis in the selected square areas of A and B in (a) (reproduced with permission from [49]).

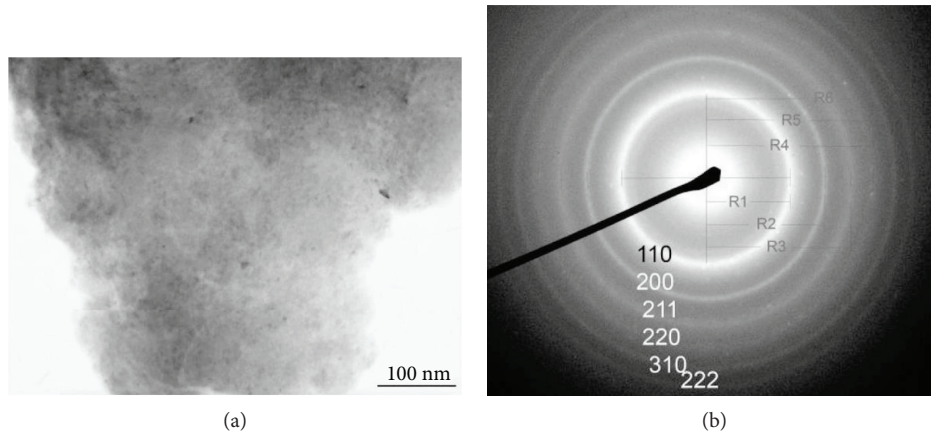
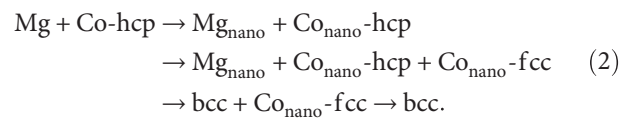


FIGURE 7: (a) Bright-field TEM image and (b) indexed electron diffraction pattern of the  $Mg_{50}Co_{50}$  alloy with a bcc structure synthesized by ball milling for 100 h (reproduced with permission from [51]).

axis. Here we can see that HR-TEM observation and lattice fringe indexation may provide some key information for phase determination in the selected area.

**2.4. Understanding the Formation Mechanism.** XRD may provide the phase and composition of the samples. SEM may present morphology information of the samples, especially on the surface of the particles. The combination of SEM and XRD may be very helpful to the understanding of the evolution mechanism during the synthesis and formation process. Figures 9 and 10 present the BSE-SEM images and

XRD patterns of the  $Mg_{50}Co_{50}$  samples milled for various durations from 0.5 to 400 h [49, 51]. From the XRD curves, we may clarify the formation mechanism of the phases in the  $Mg_{50}Co_{50}$  samples milled from 0.5 to 400 h, as in (2) (hcp means hexagonal close packed and fcc means face-centered cubic).



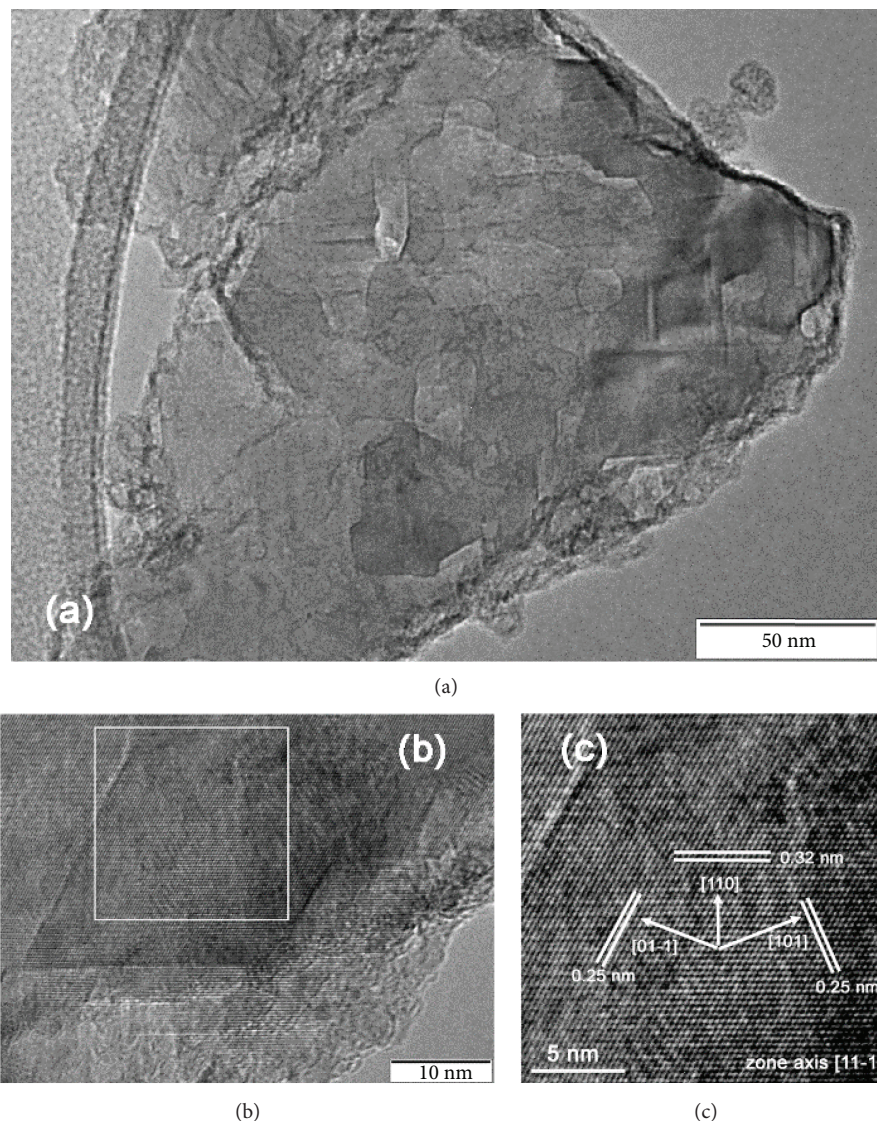


FIGURE 8: TEM images of (a) a typical  $\text{MgH}_2$  particle in the catalyzed  $\text{MgH}_2$  nanocrystallite sample, (b) a typical  $\text{MgH}_2$  nanocrystal area, and (c) a lattice spacing and orientation indexed area marked in (b) (reproduced with permission [20]).

With the combination of the SEM in Figure 9 and the XRD results, the phase and morphology evolution process during the milling of  $\text{Mg}_{50}\text{Co}_{50}$  samples from 0.5 to 400 h can be summarized as follows: firstly, with the beginning of the ball milling, small Co particles are well dispersed on the big Mg particles; secondly, large Mg particles are cracked into small ones and Co particles stick on the surface of Mg particles; thirdly, after around 25 h of milling, the Co phase with an fcc structure is formed and Co particles dissolve into the Mg ones; fourthly, particle sizes continue to decrease and the bcc phase appears after 45 h of milling; and fifthly, after 100 h, only the bcc phase with a crystallite size of only a few nm remains and the particles of the  $\text{Mg}_{50}\text{Co}_{50}$  samples change from irregular shapes to round ones from further welding during the milling. The combination of SEM observation and XRD phase identification may offer an important solution to the understanding of the formation evolution mechanisms.

**2.5. Correlation Study of Properties and Microstructure.** It is well known that the physical and chemical properties of samples can be greatly affected by the microstructure of the samples including shape, particle size, size distribution, and surface morphology, which can be well evaluated by TEM and SEM techniques. Figure 11 presents the TEM images of the Mg nanoparticles before and after hydrogen absorption and desorption processes. Figure 12 demonstrates the first and second cycles of the hydrogen absorption kinetics of Mg nanoparticles. We have already discussed the microstructure of Mg nanoparticles as prepared by the HPMR method [8, 50, 53]. In Figure 11(b), we may see that the hydrogenated sample,  $\text{MgH}_2$  (Mg hydride), has a very light and transparent feature compared to the Mg nanoparticles. This is due to the fact that Mg nanoparticles in Figure 11(a) are in a metal state, while the  $\text{MgH}_2$  nanoparticles have a semiconductor feature. This difference makes the two samples show different optical characteristics under an electron

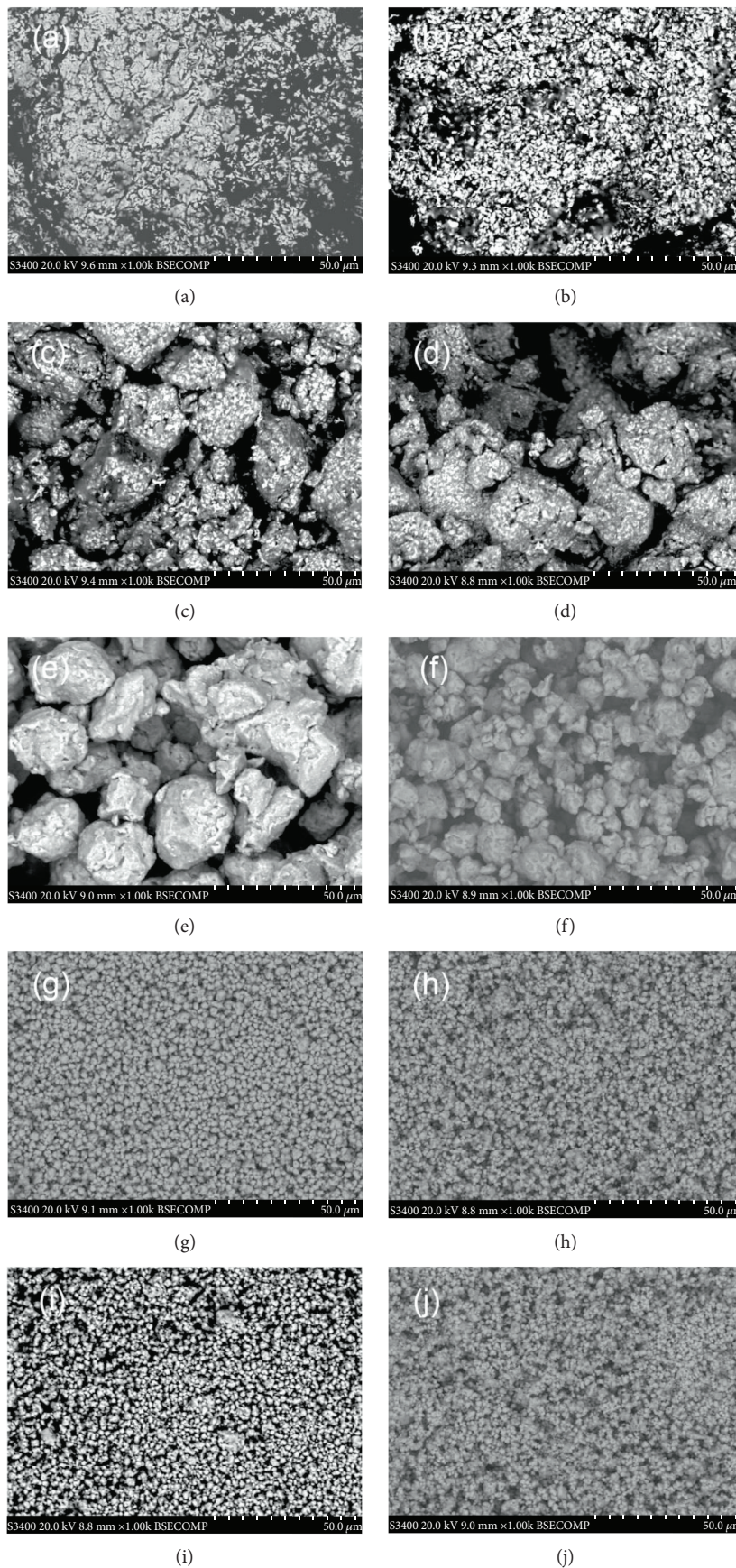


FIGURE 9: Continued.

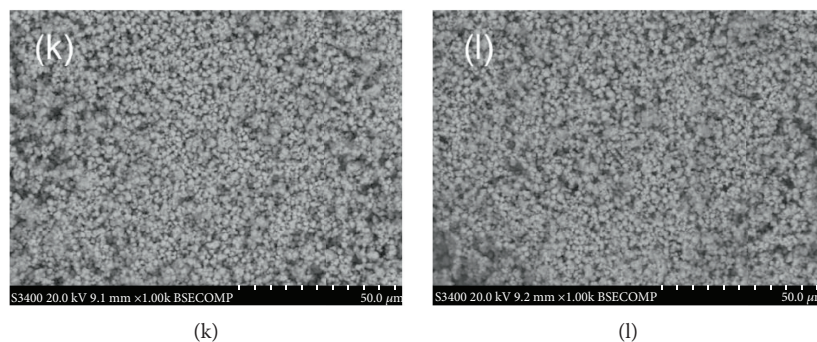


FIGURE 9: BSE-SEM images (at a magnification of 1000) of the  $Mg_{50}Co_{50}$  samples milled at the following durations: (a) 0.5 h, (b) 2 h, (c) 5 h, (d) 10 h, (e) 25 h, (f) 40 h, (g) 50 h, (h) 75 h, (i) 100 h, (j) 200 h, (k) 300 h, and (l) 400 h (reproduced with permission from [49]).

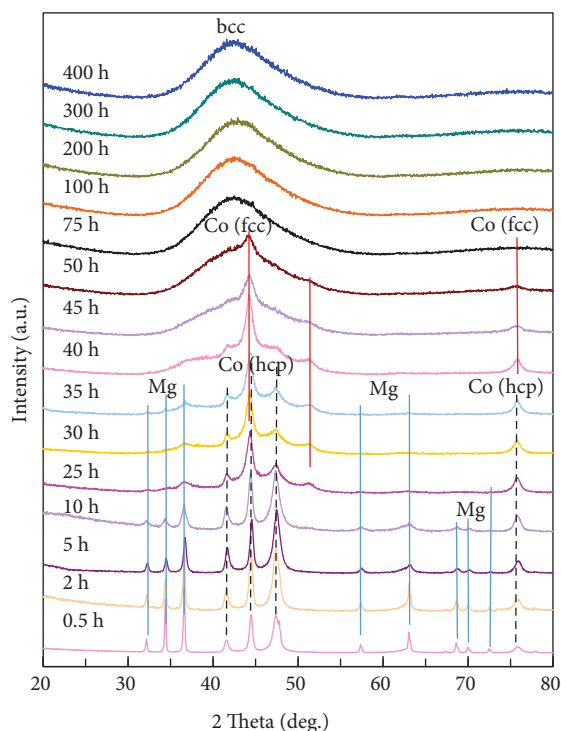


FIGURE 10: XRD patterns of the  $Mg_{50}Co_{50}$  samples ball milled for various durations (0.5 to 400 h) (reproduced with permission from [49]).

beam. Actually, this phenomenon is applied for the research and development of metal hydride-based switchable mirrors [57–60]. Besides this difference, when we compare the as-prepared Mg nanoparticles (Figure 11(a)) with the Mg nanoparticles after hydrogen absorption and desorption cycles (Figure 11(c)), we can see that the sample of Mg nanoparticles after hydrogen storage cycles show broken surfaces and some sponge-like particles. This is because the particle surfaces are cracked due to the entry and exit of hydrogen atoms during the hydrogen absorption and desorption processes. This morphology difference is thought to play an important role in the hydrogen storage properties of the samples.

In Figure 12, we can see from the hydrogen absorption curves that the Mg nanoparticle sample by the HPMR

method at the first cycle absorbs 7.53 wt.% hydrogen in 65 min, while it absorbs almost the same amount of hydrogen at the second and third cycles only after less than 15 min absorption. The Mg nanoparticles had not been subjected to the activation procedure before the three absorption cycles discussed in the previous line: this testifies to the superior hydrogen absorption properties of the nanoparticles prepared by the HPMR method. When we combine the TEM observation results and the ones with the hydrogen absorption kinetics together, we may see that the microstructure change on the surface of the Mg nanoparticles significantly influences the hydrogen absorption properties of the samples. This demonstrates that advanced TEM and SEM microscopy techniques may play essential roles in clarifying relationships between the properties and microstructures of the materials.

**2.6. In Situ Observation of Hydrogen Reaction Mechanism.** In situ scanning techniques are very helpful to understand the hydrogenation and dehydrogenation reactions of Mg-based materials. As a result, direct observations could be obtained to strongly support other experiments such as DSC and TG-MS. Nogita et al. [61] studied the dehydrogenation mechanism of  $MgH_2$  in different sizes by in situ TEM. They reported that the hydrogen release mechanism from bulk  $MgH_2$  with a particle size of  $2 \mu m$  was based on the growth of the multiple preexisting Mg grains (crystallite within the  $MgH_2$  matrix in Figure 13(a)) present, which was due to the difficulty of fully transforming all of the Mg during a hydrogenation cycle. On the other hand, in thin samples analogous to nanopowders, dehydrogenation occurs by a “shrinking core” mechanism as shown in Figure 13(b). In the case of  $Mg_2NiH_x$ , Tran et al. [62] studied the dehydrogenation mechanism of bulk  $Mg_2NiH_4$  using in situ TEM. It was found that the dehydrogenation was based on a mechanism of the nucleation and growth of  $Mg_2NiH_x$  ( $x \sim 0 - 0.3$ ) solid solution grains and was greatly enhanced in the presence of crystal defects occurring as a result of the polymorphic phase transformation as shown in Figure 13(c). Also importantly, with atomic resolution TEM imaging, a high density of stacking faults is identified in the dehydrogenated  $Mg_2NiH_x$  ( $x \sim 0 - 0.3$ ) lattices. Zhu et al. [46] adopted the method of hydriding chemical vapor deposition to synthesize a single-crystal  $MgH_2$  nanofiber. Then, the phase change of

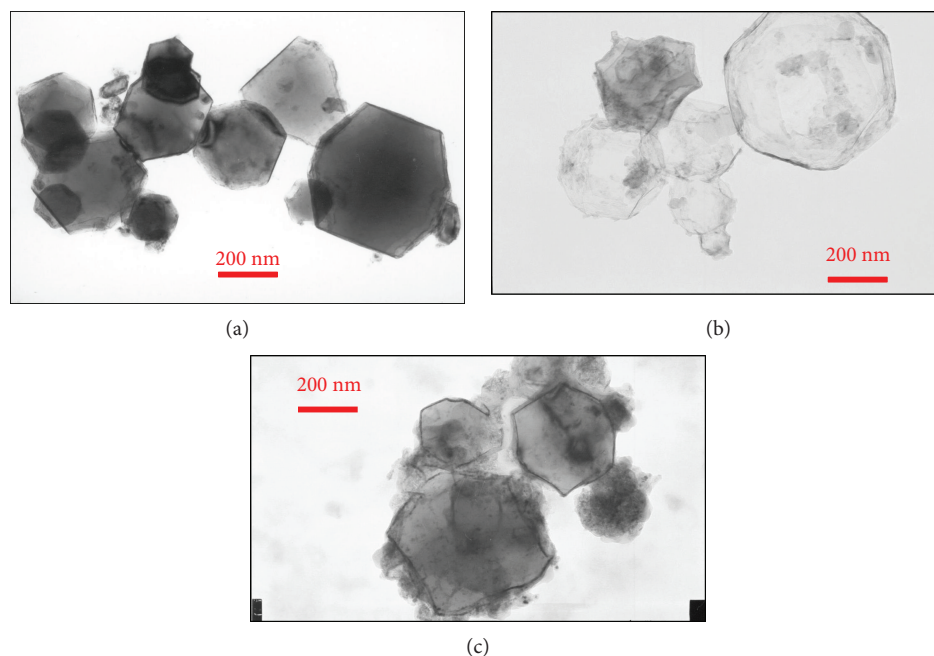


FIGURE 11: TEM images of (a) Mg nanoparticles synthesized by a hydrogen plasma metal reaction method, (b) MgH<sub>2</sub> nanoparticles after hydrogenation of the Mg sample in (a), and (c) the Mg nanoparticle sample after hydrogen absorption and desorption steps (reproduced with permission [53]).

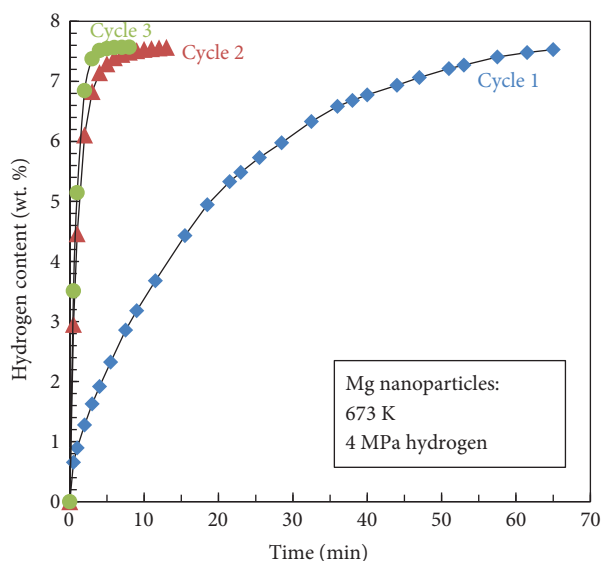


FIGURE 12: The first three hydrogen absorption curves in 4 MPa hydrogen atmosphere and at 673 K for Mg nanoparticles prepared by the HPMR method (reproduced with permission [53]).

the as-obtained MgH<sub>2</sub> nanofiber in the desorption process was observed with the in situ TEM. The results indicated that the orientation relationship between MgH<sub>2</sub> and Mg during the phase change was one of the zone axis of MgH<sub>2</sub> (110) parallel to the Mg (0001) zone axis, or one of the plane (110) of MgH<sub>2</sub> parallel to the basal plane of Mg (0001). Similar results were reported by Paik et al. [43].

Besides the pure MgH<sub>2</sub> and bulk Mg<sub>2</sub>NiH<sub>4</sub>, the catalysts were also introduced into the MgH<sub>2</sub> to investigate the microstructural changes by in situ techniques in the

dehydrogenation process. Isobe et al. [42] ball milled the MgH<sub>2</sub> with different amounts of Nb<sub>2</sub>O<sub>5</sub> to study the effects of Nb<sub>2</sub>O<sub>5</sub> on the desorption of MgH<sub>2</sub> by in situ TEM. It was found that the MgH<sub>2</sub> doped by 1 mol% Nb<sub>2</sub>O<sub>5</sub> started at 150°C and then the nanosized Mg was formed, while the desorption of MgH<sub>2</sub> catalyzed with 10 mol% started at the interface between MgH<sub>2</sub> and Nb<sub>2</sub>O<sub>5</sub> with the temperature increasing, which suggested that hydrogen atoms could diffuse from the MgH<sub>2</sub> phase to the interface between the MgH<sub>2</sub> and Nb<sub>2</sub>O<sub>5</sub>. Similarly, Kim et al. [44] also prepared the NbF<sub>5</sub>-doped MgH<sub>2</sub> by ball milling and then studied the microstructural changes in the desorption process of the as-prepared sample by in situ TEM. Results showed that the amorphous Nb-F thin layer contacted the MgH<sub>2</sub> phase at 25°C, while the amorphous Nb-F layer was transformed to a metallic Nb crystalline layer after complete desorption at 250°C. Based on the above analysis, the in situ technique allows researchers to clearly study the samples in real time under special conditions (such as by heating or at a certain atmosphere), which may strongly support other analyses. In a word, the in situ technique is a powerful strategy to grasp more information from the samples than traditional microscopy.

### 3. Summary and Prospects

The utilization of SEM and TEM techniques for characterizing the size, morphology observation, phase and composition determination, and formation and reaction mechanisms in Mg-based hydrogen storage materials fabricated by different nanoprocessing methods are presented in this paper. Although the information obtained by SEM and TEM about the size and shape of Mg-based materials are similar, TEM

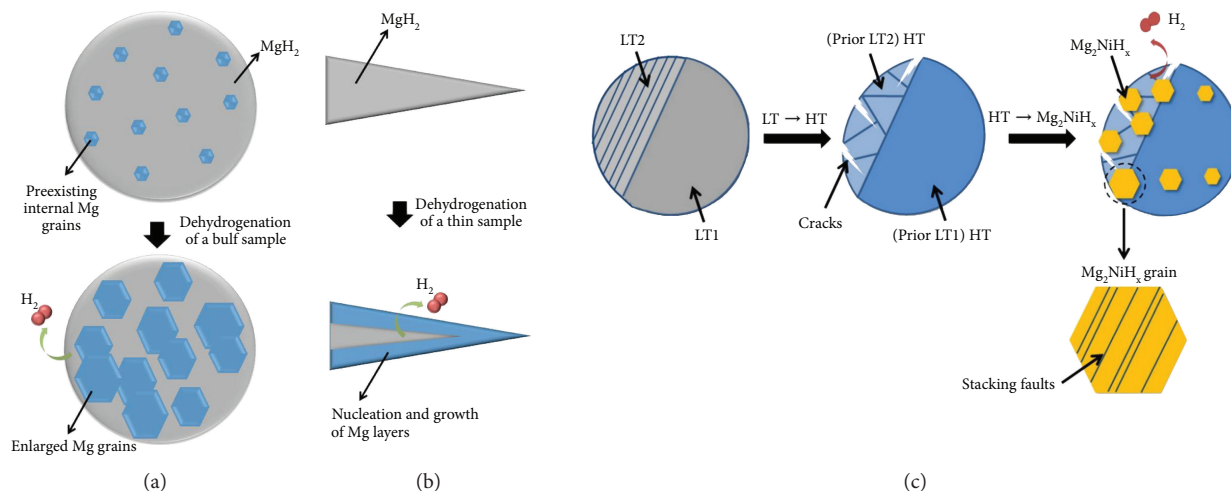


FIGURE 13: Schematic of hydrogen release mechanisms from (a) bulk  $\text{MgH}_2$ , (b) thin  $\text{MgH}_2$ , and (c) bulk  $\text{Mg}_2\text{NiH}_4$  samples (reproduced with permission from [61, 62] (under the Creative Commons Attribution License/public domain)).

provides a 2D image of the particles while SEM may obtain a 3D one. Using the TEM measurement, we could easily obtain the size, size distribution, and average size of various Mg-based samples. The SEM technique also offers the possibility to observe the surface morphology. Additionally, we may well understand the phase, composition, and structure and formation mechanism of Mg-based hydrogen storage materials by the combination of different techniques. However, conventional electron microscopies have challenges compared with in situ scanning techniques when studying the hydrogen reaction mechanism. A special sample holder which may transfer samples from the glove box to the TEM/SEM equipment presents great advantages when it comes to observing sensitive samples. In situ electron microscopy can be allowed to study some changes of the Mg-based materials in real time under special conditions and in turn directly verify the hydrogen reaction mechanism. As modern science moves from studies of structure and ground states to dynamics and functionalities, electron microscopy will clearly experience a revolutionary growth in capabilities in the next decade, from ultrasmall to ultrafast and to multidimensions, which could result in transformative advances in many fields of science and engineering [63].

## Conflicts of Interest

The authors declare no conflict of interest.

## Acknowledgments

Huaiyu Shao acknowledges the Macau Science and Technology Development Fund (FDCT) for funding (project no. 118/2016/A3). This work was also partially supported by a Start-Up Research Fund from the Universidade de Macau (SRG2016-00088-FST). Huaijun Lin thanks the financial support from the National Natural Science Foundation of China (no. 51601090).

## References

- [1] J. Yang, A. Sudik, C. Wolverton, and D. J. Siegel, "High capacity hydrogen storage materials: attributes for automotive applications and techniques for materials discovery," *Chemical Society Reviews*, vol. 39, no. 2, pp. 656–675, 2010.
- [2] M. Zhu, Y. Lu, L. Ouyang, and H. Wang, "Thermodynamic tuning of Mg-based hydrogen storage alloys: a review," *Materials*, vol. 6, no. 10, pp. 4654–4674, 2013.
- [3] H. Zhang, X. Zheng, X. Tian, Y. Liu, and X. Li, "New approaches for rare earth-magnesium based hydrogen storage alloys," *Progress in Natural Science: Materials International*, vol. 27, no. 1, pp. 50–57, 2017.
- [4] T. Sadhasivam, H. T. Kim, S. Jung, S. H. Roh, J. H. Park, and H. Y. Jung, "Dimensional effects of nanostructured Mg/ $\text{MgH}_2$  for hydrogen storage applications: a review," *Renewable & Sustainable Energy Reviews*, vol. 72, pp. 523–534, 2017.
- [5] B. Sakintuna, F. Lamari-Darkrim, and M. Hirscher, "Metal hydride materials for solid hydrogen storage: a review," *International Journal of Hydrogen Energy*, vol. 32, no. 9, pp. 1121–1140, 2007.
- [6] J.-C. Crivello, B. Dam, R. V. Denys et al., "Review of magnesium hydride-based materials: development and optimisation," *Applied Physics A*, vol. 122, no. 2, p. 97, 2016.
- [7] H. Shao, "Heat modeling and material development of Mg-based nanomaterials combined with solid oxide fuel cell for stationary energy storage," *Energies*, vol. 10, no. 11, p. 1767, 2017.
- [8] H. Shao, G. Xin, J. Zheng, X. Li, and E. Akiba, "Nanotechnology in Mg-based materials for hydrogen storage," *Nano Energy*, vol. 1, no. 4, pp. 590–601, 2012.
- [9] H. Shao, L. He, H. Lin, and H.-W. Li, "Progress and trends in magnesium-based materials for energy-storage research: a review," *Energy Technology*, vol. 6, no. 3, pp. 445–458, 2018.
- [10] H. Wang, H. J. Lin, W. T. Cai, L. Z. Ouyang, and M. Zhu, "Tuning kinetics and thermodynamics of hydrogen storage in light metal element based systems—a review of recent progress," *Journal of Alloys and Compounds*, vol. 658, pp. 280–300, 2016.

- [11] C. J. Webb, "A review of catalyst-enhanced magnesium hydride as a hydrogen storage material," *Journal of Physics and Chemistry of Solids*, vol. 84, pp. 96–106, 2015.
- [12] H. Shao, Y. T. Wang, and X. G. Li, "Synthesis and properties of nanostructured Mg<sub>2</sub>Ni-based compounds," *Materials Science Forum*, vol. 475–479, no. 3, pp. 2445–2448, 2005.
- [13] L. Xie, H. Y. Shao, Y. T. Wang, Y. Li, and X. G. Li, "Synthesis and hydrogen storing properties of nanostructured ternary Mg-Ni-Co compounds," *International Journal of Hydrogen Energy*, vol. 32, no. 12, pp. 1949–1953, 2007.
- [14] H. Shao, H. Xu, Y. Wang, and X. Li, "Synthesis and hydrogen storage behavior of Mg-Co-H system at nanometer scale," *Journal of Solid State Chemistry*, vol. 177, no. 10, pp. 3626–3632, 2004.
- [15] H. Shao, T. Liu, and X. Li, "Preparation of the Mg<sub>2</sub>Ni compound from ultrafine particles and its hydrogen storage properties," *Nanotechnology*, vol. 14, no. 3, pp. L1–L3, 2003.
- [16] H. Shao, T. Liu, Y. Wang, H. Xu, and X. Li, "Preparation of Mg-based hydrogen storage materials from metal nanoparticles," *Journal of Alloys and Compounds*, vol. 465, no. 1–2, pp. 527–533, 2008.
- [17] H. Shao, T. Liu, X. Li, and L. Zhang, "Preparation of Mg<sub>2</sub>Ni intermetallic compound from nanoparticles," *Scripta Materialia*, vol. 49, no. 6, pp. 595–599, 2003.
- [18] H. Shao, K. Asano, H. Enoki, and E. Akiba, "Preparation and hydrogen storage properties of nanostructured Mg-Ni BCC alloys," *Journal of Alloys and Compounds*, vol. 477, no. 1–2, pp. 301–306, 2009.
- [19] H. Shao, Y. Wang, H. Xu, and X. Li, "Preparation and hydrogen storage properties of nanostructured Mg<sub>2</sub>Cu alloy," *Journal of Solid State Chemistry*, vol. 178, no. 7, pp. 2211–2217, 2005.
- [20] H. Shao, M. Felderhoff, F. Schuth, and C. Weidenthaler, "Nanostructured Ti-catalyzed MgH<sub>2</sub> for hydrogen storage," *Nanotechnology*, vol. 22, no. 23, article 235401, 2011.
- [21] J. Matsuda, H. Shao, Y. Nakamura, and E. Akiba, "The nanostructure and hydrogenation reaction of Mg<sub>50</sub>Co<sub>50</sub> BCC alloy prepared by ball-milling," *Nanotechnology*, vol. 20, no. 20, article 204015, 2009.
- [22] H. Shao, K. Asano, H. Enoki, and E. Akiba, "Fabrication and hydrogen storage property study of nanostructured Mg-Ni-B ternary alloys," *Journal of Alloys and Compounds*, vol. 479, no. 1–2, pp. 409–413, 2009.
- [23] H. Shao and X. Li, "Effect of nanostructure and partial substitution on gas absorption and electrochemical properties in Mg<sub>2</sub>Ni-based alloys," *Journal of Alloys and Compounds*, vol. 667, pp. 191–197, 2016.
- [24] M. Huang, L. Ouyang, J. Liu, H. Wang, H. Shao, and M. Zhu, "Enhanced hydrogen generation by hydrolysis of Mg doped with flower-like MoS<sub>2</sub> for fuel cell applications," *Journal of Power Sources*, vol. 365, pp. 273–281, 2017.
- [25] H. Shao, C. Chen, T. Liu, and X. Li, "Phase, microstructure and hydrogen storage properties of Mg-Ni materials synthesized from metal nanoparticles," *Nanotechnology*, vol. 25, no. 13, article 135704, 2014.
- [26] T. Liu, H. Shen, Y. Liu et al., "Scaled-up synthesis of nanostructured Mg-based compounds and their hydrogen storage properties," *Journal of Power Sources*, vol. 227, pp. 86–93, 2013.
- [27] J. Zhang, Y. Zhu, H. Lin et al., "Metal hydride nanoparticles with ultrahigh structural stability and hydrogen storage activity derived from microencapsulated nanoconfinement," *Advanced Materials*, vol. 29, no. 24, 2017.
- [28] E. Callini, L. Pasquini, E. Piscopiello, A. Montone, M. V. Antisari, and E. Bonetti, "Hydrogen sorption in Pd-decorated Mg-MgO core-shell nanoparticles," *Applied Physics Letters*, vol. 94, no. 22, article 221905, 2009.
- [29] K. J. Jeon, H. R. Moon, A. M. Ruminski et al., "Air-stable magnesium nanocomposites provide rapid and high-capacity hydrogen storage without using heavy-metal catalysts," *Nature Materials*, vol. 10, no. 4, pp. 286–290, 2011.
- [30] A. Anastasopol, T. V. Pfeiffer, A. Schmidt-Ott, F. M. Mulder, and S. W. H. Eijt, "Fractal disperse hydrogen sorption kinetics in spark discharge generated Mg/NbOx and Mg/Pd nanocomposites," *Applied Physics Letters*, vol. 99, no. 19, article 194103, 2011.
- [31] J. Ditto, D. Krinsley, and K. Langworthy, "Localized grounding, excavation, and dissection using in-situ probe techniques for focused ion beam and scanning electron microscopy: experiments with rock varnish," *Scanning*, vol. 34, no. 5, 283 pages, 2012.
- [32] B. J. Crawford and R. D. Burke, "TEM and SEM methods," *Methods in Cell Biology*, vol. 74, pp. 411–441, 2004.
- [33] L. Reimer, "Electron diffraction methods in TEM, STEM and SEM," *Scanning*, vol. 2, no. 1, 19 pages, 1979.
- [34] B. Bokhonov, E. Ivanov, and V. Boldyrev, "A study of the electron-beam-induced decomposition of magnesium hydride single crystals," *Materials Letters*, vol. 5, no. 5–6, pp. 218–221, 1987.
- [35] O. Friedrichs, J. C. Sánchez-López, C. López-Cartes et al., "Chemical and microstructural study of the oxygen passivation behaviour of nanocrystalline Mg and MgH<sub>2</sub>," *Applied Surface Science*, vol. 252, no. 6, pp. 2334–2345, 2006.
- [36] M. Porcu, A. K. Petford-Long, and J. M. Sykes, "TEM studies of Nb<sub>2</sub>O<sub>5</sub> catalyst in ball-milled MgH<sub>2</sub> for hydrogen storage," *Journal of Alloys and Compounds*, vol. 453, no. 1–2, pp. 341–346, 2008.
- [37] A. Zaluska, L. Zaluski, and J. O. Ström-Olsen, "Nanocrystalline magnesium for hydrogen storage," *Journal of Alloys and Compounds*, vol. 288, no. 1–2, pp. 217–225, 1999.
- [38] M. Zhu, H. Wang, L. Ouyang, and M. Zeng, "Composite structure and hydrogen storage properties in Mg-base alloys," *International Journal of Hydrogen Energy*, vol. 31, no. 2, pp. 251–257, 2006.
- [39] N. Hanada, E. Hirotooshi, T. Ichikawa, E. Akiba, and H. Fujii, "SEM and TEM characterization of magnesium hydride catalyzed with Ni nano-particle or Nb<sub>2</sub>O<sub>5</sub>," *Journal of Alloys and Compounds*, vol. 450, no. 1–2, pp. 395–399, 2008.
- [40] G. Xia, Y. Tan, X. Chen et al., "Monodisperse magnesium hydride nanoparticles uniformly self-assembled on graphene," *Advanced Materials*, vol. 27, no. 39, pp. 5981–5988, 2015.
- [41] M. Danaie and D. Mitlin, "TEM analysis of the microstructure in TiF<sub>3</sub>-catalyzed and pure MgH<sub>2</sub> during the hydrogen storage cycling," *Acta Materialia*, vol. 60, no. 19, pp. 6441–6456, 2012.
- [42] S. Isobe, A. Ono, H. Yao, Y. Wang, N. Hashimoto, and S. Ohnuki, "Study on reaction mechanism of dehydrogenation of magnesium hydride by in situ transmission electron microscopy," *Applied Physics Letters*, vol. 96, no. 22, article 223109, 2010.
- [43] B. Paik, I. P. Jones, A. Walton, V. Mann, D. Book, and I. R. Harris, "MgH<sub>2</sub> → Mg phase transformation driven by a high-energy electron beam: an in situ transmission electron

- microscopy study,” *Philosophical Magazine Letters*, vol. 90, no. 1, pp. 1–7, 2010.
- [44] J. W. Kim, J.-P. Ahn, D. H. Kim et al., “In situ transmission electron microscopy study on microstructural changes in NbF<sub>5</sub>-doped MgH<sub>2</sub> during dehydrogenation,” *Scripta Materialia*, vol. 62, no. 9, pp. 701–704, 2010.
- [45] S. D. Beattie, U. Setthanan, and G. S. McGrady, “Thermal desorption of hydrogen from magnesium hydride (MgH<sub>2</sub>): an in situ microscopy study by environmental SEM and TEM,” *International Journal of Hydrogen Energy*, vol. 36, no. 10, pp. 6014–6021, 2011.
- [46] C. Zhu, N. Sakaguchi, S. Hosokai, S. Watanabe, and T. Akiyama, “In situ transmission electron microscopy observation of the decomposition of MgH<sub>2</sub> nanofiber,” *International Journal of Hydrogen Energy*, vol. 36, no. 5, pp. 3600–3605, 2011.
- [47] S. B. Rice, C. Chan, S. C. Brown et al., “Particle size distributions by transmission electron microscopy: an interlaboratory comparison case study,” *Metrologia*, vol. 50, no. 6, pp. 663–678, 2013.
- [48] S. Ohno and M. Uda, “Generation rate of ultrafine metal particles in “hydrogen plasma-metal” reaction,” *Journal of the Japan Institute of Metals*, vol. 48, no. 6, pp. 640–646, 1984.
- [49] H. Shao, J. Matsuda, H.-W. Li et al., “Phase and morphology evolution study of ball milled Mg-Co hydrogen storage alloys,” *International Journal of Hydrogen Energy*, vol. 38, no. 17, pp. 7070–7076, 2013.
- [50] H. Shao, W. Ma, M. Kohno et al., “Hydrogen storage and thermal conductivity properties of Mg-based materials with different structures,” *International Journal of Hydrogen Energy*, vol. 39, no. 18, pp. 9893–9898, 2014.
- [51] H. Shao, K. Asano, H. Enoki, and E. Akiba, “Fabrication, hydrogen storage properties and mechanistic study of nano-structured Mg<sub>50</sub>Co<sub>50</sub> body-centered cubic alloy,” *Scripta Materialia*, vol. 60, no. 9, pp. 818–821, 2009.
- [52] H. Kim, J. Nakamura, H. Shao et al., “Local structural evolution of mechanically alloyed Mg<sub>50</sub>Co<sub>50</sub> using atomic pair distribution function analysis,” *Journal of Physical Chemistry C*, vol. 115, no. 15, pp. 7723–7728, 2011.
- [53] H. Shao, Y. Wang, H. Xu, and X. Li, “Hydrogen storage properties of magnesium ultrafine particles prepared by hydrogen plasma-metal reaction,” *Materials Science and Engineering: B*, vol. 110, no. 2, pp. 221–226, 2004.
- [54] M. Norek, W. J. Stepniowski, M. Polanski, D. Zasada, Z. Bojar, and J. Bystrzycki, “A comparative study on the hydrogen absorption of thin films at room temperature deposited on non-porous glass substrate and nano-porous anodic aluminum oxide (AAO) template,” *International Journal of Hydrogen Energy*, vol. 36, no. 18, pp. 11777–11784, 2011.
- [55] B. Bogdanović, A. Ritter, and B. Spliethoff, “Active MgH<sub>2</sub>-Mg systems for reversible chemical energy storage,” *Angewandte Chemie International Edition in English*, vol. 29, no. 3, pp. 223–234, 1990.
- [56] B. Bogdanović, S.-t. Liao, M. Schwickardi, P. Sikorsky, and B. Spliethoff, “Catalytic synthesis of magnesium hydride under mild conditions,” *Angewandte Chemie International Edition in English*, vol. 19, no. 10, pp. 818–819, 1980.
- [57] S. J. van der Molen, M. S. Welling, and R. Griessen, “Correlated electromigration of H in the switchable mirror YH<sub>3-δ</sub>,” *Physical Review Letters*, vol. 85, no. 18, pp. 3882–3885, 2000.
- [58] A. T. M. van Gogh, E. S. Kooij, and R. Griessen, “Isotope effects in switchable metal-hydride mirrors,” *Physical Review Letters*, vol. 83, no. 22, pp. 4614–4617, 1999.
- [59] A. Remhof, S. J. van der Molen, A. Antosik, A. Dobrowolska, N. J. Koeman, and R. Griessen, “Switchable mirrors for visualization and control of hydrogen diffusion in transition metals,” *Physical Review B*, vol. 66, no. 2, 2002.
- [60] J. N. Huiberts, R. Griessen, J. H. Rector et al., “Yttrium and lanthanum hydride films with switchable optical properties,” *Nature*, vol. 380, no. 6571, pp. 231–234, 1996.
- [61] K. Nogita, X. Q. Tran, T. Yamamoto et al., “Evidence of the hydrogen release mechanism in bulk MgH<sub>2</sub>,” *Scientific Reports*, vol. 5, no. 1, p. 8450, 2015.
- [62] X. Q. Tran, S. D. McDonald, Q. Gu et al., “In-situ investigation of the hydrogen release mechanism in bulk Mg<sub>2</sub>NiH<sub>4</sub>,” *Journal of Power Sources*, vol. 341, pp. 130–138, 2017.
- [63] Y. Zhu and H. Durr, “The future of electron microscopy,” *Physics Today*, vol. 68, no. 4, pp. 32–38, 2015.

## Research Article

# Effective Removal of Congo Red by Triarrhena Biochar Loading with TiO<sub>2</sub> Nanoparticles

Peng Yu,<sup>1</sup> Tao Hu,<sup>1</sup> Hong Hui Chen,<sup>2</sup> Fangfang Wu,<sup>1</sup> and Hui Liu <sup>1</sup>

<sup>1</sup>College of Science, Hunan Agricultural University, Changsha 410128, China

<sup>2</sup>Changde Xinrui New Material Co. Ltd., Changde 415004, China

Correspondence should be addressed to Hui Liu; [liu.hui@hunau.edu.cn](mailto:liu.hui@hunau.edu.cn)

Received 23 February 2018; Revised 20 April 2018; Accepted 3 May 2018; Published 4 June 2018

Academic Editor: Huaijun Lin

Copyright © 2018 Peng Yu et al. This is an open access article distributed under the Creative Commons Attribution License, which permits unrestricted use, distribution, and reproduction in any medium, provided the original work is properly cited.

A composite of pyrolytic Triarrhena biochar loading with TiO<sub>2</sub> nanoparticles has been synthesized by the sol-gel method. The composite shows a well-developed hollow mesoporous and macropore structure as characterized by XRD, BET, and SEM. When used as an adsorbent to remove Congo red from aqueous solution, it was found that as-prepared composite performed better absorption capacity than single biochar or TiO<sub>2</sub>. The results suggest that biochar loading with TiO<sub>2</sub> could be promisingly implemented as an environmentally friendly and inexpensive adsorbent for Congo red removal from wastewater.

## 1. Introduction

With the rapid development of global printing and dyeing industry (PDI) for decades, a variety of dyes are used in knitting silk, cotton, and so on [1–3]. Considerable industrial wastewater including dyes would have been generated during the processing of PDI [4–8]. Congo red 1-naphthalenesulfonic acid, 3, 3'-(4, 4'-biphenylenebis (azo) bis (4-amino) disodium salt, as one of the most widely used direct dyes in PDI for its high chromaticity, is the critical source contamination of wastewater with high chemical oxygen demand and high biological toxicity [9–14]. Therefore, it is of great significance to remove Congo red from aqueous solution.

It has been reported that physical adsorption is the dominant method for Congo red removal. The materials with a high-specific surface area and an abundant pore structure are explored to absorb Congo red to decontaminate industrial wastewater [15, 16]. For instance, activated carbon (AC), possessing a large specific surface area [17], good environmental friendliness [18], and mechanical stability [19], is a promising material for wastewater treatment [20]. However, its application is limited by high energy consumption and large greenhouse gas emissions during an AC preparation process [21]. Recently, biochar (BC), a precursor of AC, has attracted many researchers' attention [22]. It has a

pore structure with a large surface area and good environmental friendliness as well as AC. In addition, BC could usually be prepared by pyrolysis of biological organic materials under a moderate temperature with low cost. And pyrolytic BC could keep the original structure of the rich organic functional group and could be modified easily [23, 24]. When BC is used as an adsorbent to remove Congo red, its organic functional group would interact weakly with the organic molecule of Congo red. Hence, BC might show better research prospects than AC in terms of waste water purification, heavy metal ion adsorption, and soil restoration [24–28]. However, BC mostly exhibits a micropore and mesoporous structure, which seldom matches Congo red macromolecule. Therefore, it is necessary to enlarge the pore size of BC to enhance its absorption capacity.

In this work, TiO<sub>2</sub> nanoparticles have been loaded to modify BC. Nanosized TiO<sub>2</sub> is also an excellent adsorbent, which has been studied in the aspect of pollution absorption [29]. However, its adsorption capacity is weakened due to the nature of its easy aggregation. Here, OH in the surface of TiO<sub>2</sub> generated via  $\text{Ti-R4} + 4\text{H}_2\text{O} \rightarrow \text{Ti(OH)}_4 + 4\text{R(OH)}$  would interact weakly with C=O of BC. It is predicted that the interaction would introduce TiO<sub>2</sub> to enter the pore structure to enlarge the pore size of BC and avoid aggregation of TiO<sub>2</sub> [30]. Therefore, BC loading with TiO<sub>2</sub> nanoparticles

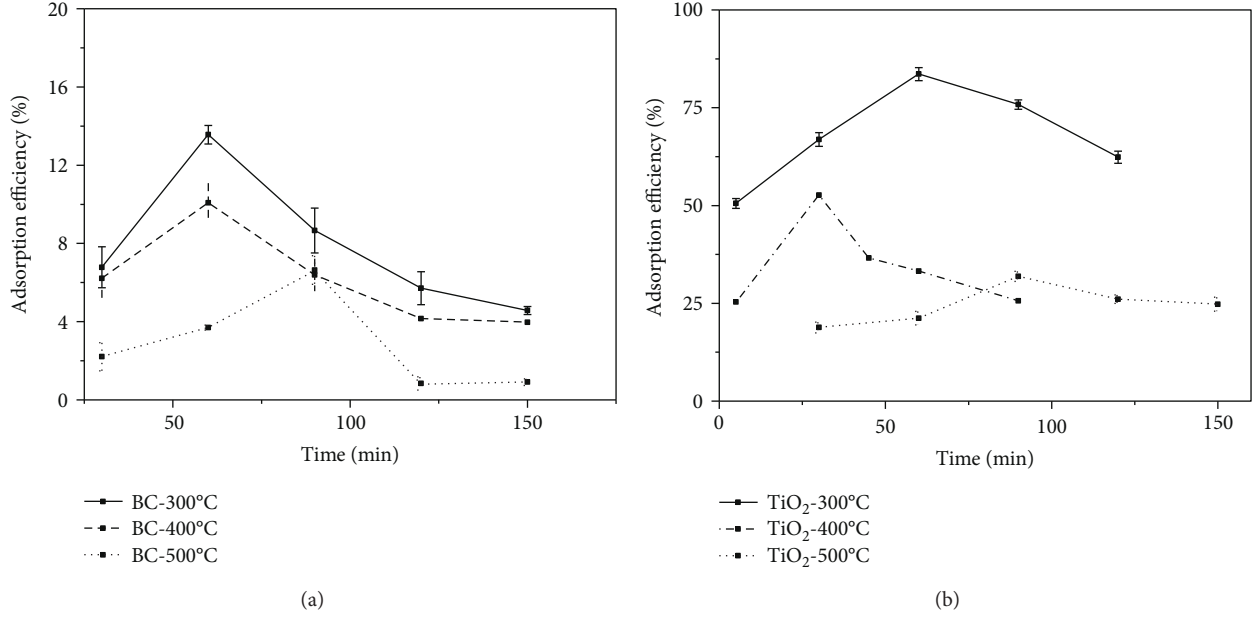


FIGURE 1: The adsorption efficiency of (a) BC and (b) TiO<sub>2</sub> synthesized at 300°C, 400°C, and 500°C.

(BC@TiO<sub>2</sub>) has been synthesized and used as an adsorbent to remove Congo red from aqueous solution. The adsorption performance of BC@TiO<sub>2</sub> composite is expected to be greatly enhanced due to the synergistic adsorption combination of TiO<sub>2</sub> and BC.

## 2. Materials and Methods

**2.1. Material Preparation.** BC was obtained by the pyrolysis of Triarrhena stalks. Triarrhena with a short growth cycle is abundant in the south of the Yangtze River. Triarrhena stalks were collected from Hunan Agricultural University (Changsha, China) miscanthus resources nursery, washed in distilled water to remove adhering impurities, and then chopped into small pieces (1~1.5 cm). Finally, Triarrhena stalk pieces were heated to obtain BC in the nitrogen atmosphere at different temperatures of 300°C, 400°C, and 500°C, named as BC-300°C, BC-400°C, and BC-500°C, respectively.

The composite of BC@TiO<sub>2</sub> was prepared using the following procedure. Firstly, anhydrous ethanol was taken in a beaker, and four n-butyl titanates was dripped dropwise using a burette under magnetic stirring to form yellow clear solution A. Secondly, solution B was prepared by adding acetic acid and distilled water into ethanol in another beaker and then adjust its pH value to 3 by dropping hydrochloric acid. Thirdly, solution A is slowly dripped into solution B under magnetic stirring at a water bath of ambient temperature. Triarrhena BC was added into the mixing solution gel after finishing dropping and continually stirred at a water bath of 80°C for half an hour. And then as-prepared gel was dried at 105°C in an oven for 12h. Lastly, the dried materials were crushed and burned in a nitrogen atmosphere at different temperatures (300°C, 400°C, and 500°C, resp.) to obtain BC@TiO<sub>2</sub> composite, named as BC@TiO<sub>2</sub>-300°C, BC@TiO<sub>2</sub>-400°C, and BC@TiO<sub>2</sub>-500°C, respectively. For comparison,

TiO<sub>2</sub>-300°C, TiO<sub>2</sub>-400°C, and TiO<sub>2</sub>-500°C were prepared in the same procedure without BC.

**2.2. Microstructural Characterization.** The microstructure of samples was characterized by a Shimadzu X-ray 6000 diffractometer (XRD) with Cu K<sub>α</sub> radiation at 40 kV, 30 mA, and a Supra40 Carl Zeiss scanning electron microscopy (SEM) coupled with EDS, determining the mapping distribution of C, O, and Ti. The BET surface area ( $S_{\text{BET}}$ ) and micropore width were analyzed by the specific surface and aperture analyzer (Quadratorb SI series, Quantachrome, USA) using nitrogen adsorption at 77 K.

**2.3. Adsorption Measurements.** As-prepared BC, TiO<sub>2</sub>, and BC@TiO<sub>2</sub> were used as adsorbents for Congo red adsorption study. 0.015 g sample was added into 100 mL Erlenmeyer flasks containing 20 mL Congo red (analytical purity, SSS Reagent Co. Ltd., Shanghai, China), and then Erlenmeyer flasks were placed on a rotary shaker with 150 rpm at 25°C. For the adsorption kinetic study, the suspensions were immediately filtered through a 0.45 μm filter at each sampling time and subjected to analyze. Congo red absolute adsorbed capacity ( $q_e$ ) was calculated by (1) based on mass balance, while the adsorption efficiency was calculated by (2). And then the optimum amount of the optimum adsorbent was determined under the same conditions.

$$q_e = \frac{(C_0 - C_e)V}{m}, \quad (1)$$

$$p = \frac{(C_0 - C_e)V}{C_0} \times 100\%, \quad (2)$$

where  $C_0$  (mg·L<sup>-1</sup>) is referred to the initial Congo red concentration,  $C_e$  (mg·L<sup>-1</sup>) is referred to the Congo red concentration at equilibrium,  $V$  (L) is the solution volume, and  $m$  (g) is concerned to the weight of the adsorbent.

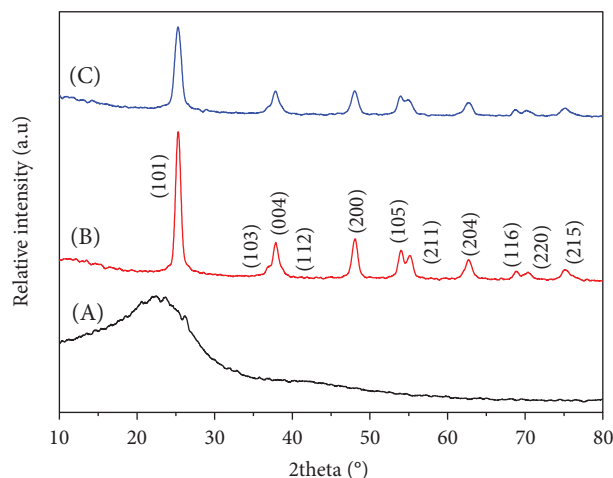


FIGURE 2: XRD patterns of A BC-300°C, B TiO<sub>2</sub>-300°C, and C BC@TiO<sub>2</sub>-300°C.

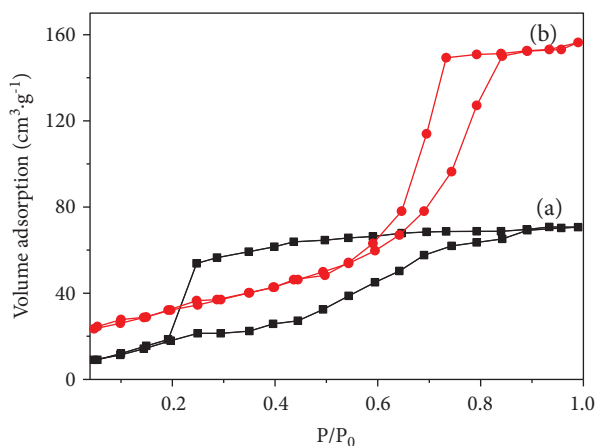


FIGURE 3: N<sub>2</sub> adsorption-desorption isotherms at 77 K on (a) BC-300°C and (b) BC@TiO<sub>2</sub>-300°C.

All adsorption results were calculated from an average of three independent experimental results, and the maximum deviations from the average (error bars) were also indicated.

### 3. Results and Discussion

To determine the optimum temperature of heating treatment, Figure 1 shows the adsorption efficiency of as-prepared BC and TiO<sub>2</sub> prepared at different temperatures of 300°C, 400°C, and 500°C. It could be revealed that a rapid initial sorption could be observed during the first 90 min and the adsorption capacity is basically saturated for all BC and TiO<sub>2</sub> samples. In more detail, BC-300°C performs the largest relative adsorption capacity of 13.56% after about 60 min, while BC-400°C of 10.08% after 60 min and BC-500°C after 90 min as shown in Figure 1(a). TiO<sub>2</sub> performs the same trend that TiO<sub>2</sub>-300°C has the largest relative adsorption efficiency of 83.59%, followed by 52.64% of TiO<sub>2</sub>-400°C and 31.89% of TiO<sub>2</sub>-500°C. Therefore, it is determined that our target material could be prepared at the optimum

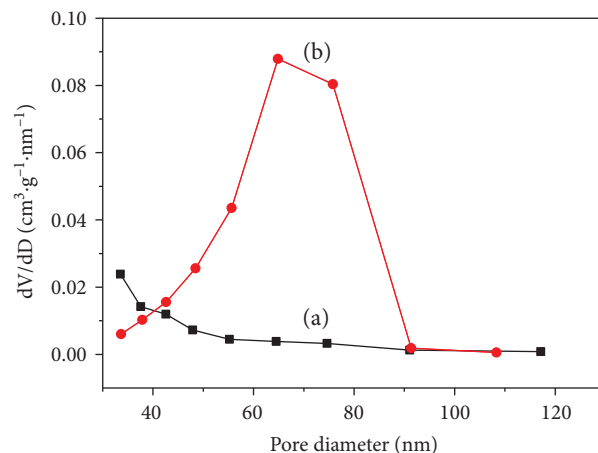


FIGURE 4: The corresponding pore size distribution of (a) BC-300°C and BC@TiO<sub>2</sub>-300°C determined from the desorption branch of the N<sub>2</sub> adsorption-desorption isotherms as shown in Figure 3.

temperature of 300°C with low energy consumption and would have excellent adsorption performance.

Figure 2 shows the XRD patterns of BC-300°C, TiO<sub>2</sub>-300°C, and BC@TiO<sub>2</sub>-300°C. There is a broad diffraction peak ( $2\theta = 20^\circ \sim 27^\circ$ ) which is attributed to disordered structures of BC as shown in Figure 2 A. In Figures 2 B and 2 C, the diffraction peaks at  $2\theta$  of 25.36°, 37.91°, 48.16°, 54.05°, 55.20°, 62.86°, 68.97°, 70.48°, and 75.28° belong to (101), (004), (200), (105), (211), (204), (116), (220), and (215) of anatase TiO<sub>2</sub>, respectively (number 01-084-1286). The broad diffraction peak of C could not be observed because of an overlapping high crystalline TiO<sub>2</sub> peak of (101) in BC@TiO<sub>2</sub>-300°C in Figure 2 C. Compared to Figures 2 B and 2 C, the diffraction peaks of TiO<sub>2</sub> widen and weaken significantly. Based on peak profile analysis using a Voigt function, the grain size of TiO<sub>2</sub> is 71.2 nm in BC@TiO<sub>2</sub>-300°C, which is much finer than 87.5 nm in TiO<sub>2</sub>-300°C.

Figure 3 shows N<sub>2</sub> adsorption-desorption isotherms at 77 K on BC-300°C and BC@TiO<sub>2</sub>-300°C. It could be observed obviously that both BC-300°C and BC@TiO<sub>2</sub>-300°C have a hysteresis loop in Figure 3, indicating that all samples have a pore structure. The hysteresis loop of BC@TiO<sub>2</sub>-300°C is at a higher relative pressure than that of BC-300°C, and the decline in the desorption of BC@TiO<sub>2</sub>-300°C is much sharper than that of BC-300°C. It should be an indication of mesoporous or macropore in BC@TiO<sub>2</sub>-300°C, which would be confirmed in Figure 4. Figure 4 shows the corresponding pore size distribution curve determined from the desorption curve of the N<sub>2</sub> adsorption-desorption isotherms in Figure 3. BC@TiO<sub>2</sub>-300°C exhibits a large average pore diameter of 60 nm and a broad distribution (FWHM = 20 nm). By contrast, BC-300°C shows a pore diameter of less than 40 nm. Correspondingly, the specific surface area of BC@TiO<sub>2</sub>-300°C was calculated to be 161.5 m<sup>2</sup>/g by the BET method, larger than 35.0 m<sup>2</sup>/g of BC-300°C. It could be concluded that the pore size of BC is expanded by loading TiO<sub>2</sub>, for the remaining effect of TiO<sub>2</sub> nanoparticles. Additionally, it is predicted that nanosized TiO<sub>2</sub> could enter a mean pore diameter of 60 nm in BC@TiO<sub>2</sub>-300°C partly.

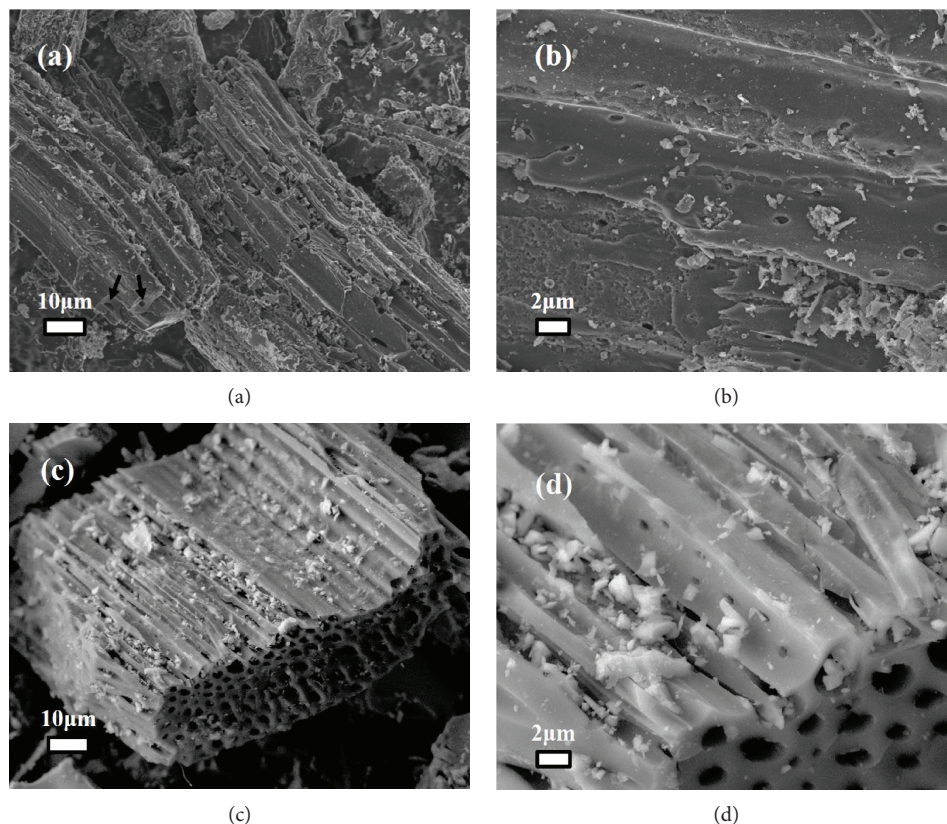


FIGURE 5: SEM images of (a, b) BC-300°C and (c, d) BC@TiO<sub>2</sub>-300°C.

Figure 5 shows the SEM images of BC-300°C and BC@TiO<sub>2</sub>-300°C. Figures 5(a) and 5(c) reveal that both BC-300°C and BC@TiO<sub>2</sub>-300°C have a rod shape of groove. BC@TiO<sub>2</sub>-300°C presents a well-developed hollow rod with dozens of nanometers and TiO<sub>2</sub> nanoparticles filled in the hollow structure partly without obvious aggregation as shown in Figures 5(c) and 5(d). In contrast, BC-300°C mostly shows a micropore rod structure as indicated by arrows in Figure 5(a), and several micropores could be observed randomly on the rod wall in Figure 5(b). It is evidenced that pore enlargement of BC has been induced by TiO<sub>2</sub> loading, consistent with the result of N<sub>2</sub> adsorption-desorption isotherms analysis. Thus, BC@TiO<sub>2</sub>-300°C should perform better adsorption properties of contaminants than BC-300°C.

Figures 6(a)–6(c) show the element mapping images, and Figure 6(d) shows the corresponding SEM images of BC@TiO<sub>2</sub>-300°C. The existence and uniform distribution of Ti and O in BC@TiO<sub>2</sub>-300°C composites are disclosed. Combined with EDS spectrum analysis in Table 1, the loading mass of TiO<sub>2</sub> could be calculated about 21%. In addition, it should be noted that the stoichiometric ratio of O : Ti reaches 5 : 1, much bigger than 2 : 1 in TiO<sub>2</sub>. It is considered that the O of the organic functional group of BC@TiO<sub>2</sub>-300°C would contribute to its extra content. As discussed above, the organic functional group of BC@TiO<sub>2</sub> composite would benefit from Congo red removal.

Figure 7 compares the relative adsorption capacity for BC-300°C, TiO<sub>2</sub>-300°C, and BC@TiO<sub>2</sub>-300°C. The trend of adsorption performance for all samples looks like the same,

rising and reaching saturation in the first 60 min following by declining. The saturated adsorption efficiency for BC@TiO<sub>2</sub>-300°C is enhanced significantly, much more effective than the calculated efficiency of 28.27% by combining with the absorption capacity of 21% TiO<sub>2</sub> (83.59%) and 79% BC (13.56%). It should be attributed to the synergy effects of physical adsorption in pore-enlarging BC and the weak interaction between the organic functional group of BC@TiO<sub>2</sub> and the organic molecule of Congo red. Figure 8 presents the specific adsorption capacity versus the mass of BC@TiO<sub>2</sub>-300°C to remove Congo red. It rises the maximum value of 61.67 mg·g<sup>-1</sup> when the mass is 0.015 g and then falls down sharply.

To investigate the synergistic effect variation along with heating temperature, BC@TiO<sub>2</sub> composites have been prepared at 300°C, 400°C, and 500°C. Figure 9 shows the XRD patterns of BC@TiO<sub>2</sub>-300°C, BC@TiO<sub>2</sub>-400°C, and BC@TiO<sub>2</sub>-500°C. Consistent with Figure 2, all diffraction peaks belong to anatase TiO<sub>2</sub> (number 01-084-1286), while the broad diffraction peak of C could not be observed because of an overlapping high crystalline TiO<sub>2</sub> peak of (101). Along with the temperature increase, the peak intensity increases, and the FWHM narrows, indicating the grain size of TiO<sub>2</sub> gets larger. Calculated by using a Voigt function, the grain size of BC@TiO<sub>2</sub>-300°C, BC@TiO<sub>2</sub>-400°C, and BC@TiO<sub>2</sub>-500°C is 71.2, 74.3, and 84.3 nm, respectively.

Figure 10 presents the adsorption efficiency of BC@TiO<sub>2</sub>-300°C, BC@TiO<sub>2</sub>-400°C, and BC@TiO<sub>2</sub>-500°C. Different from the results in Figure 7, the adsorption saturation of

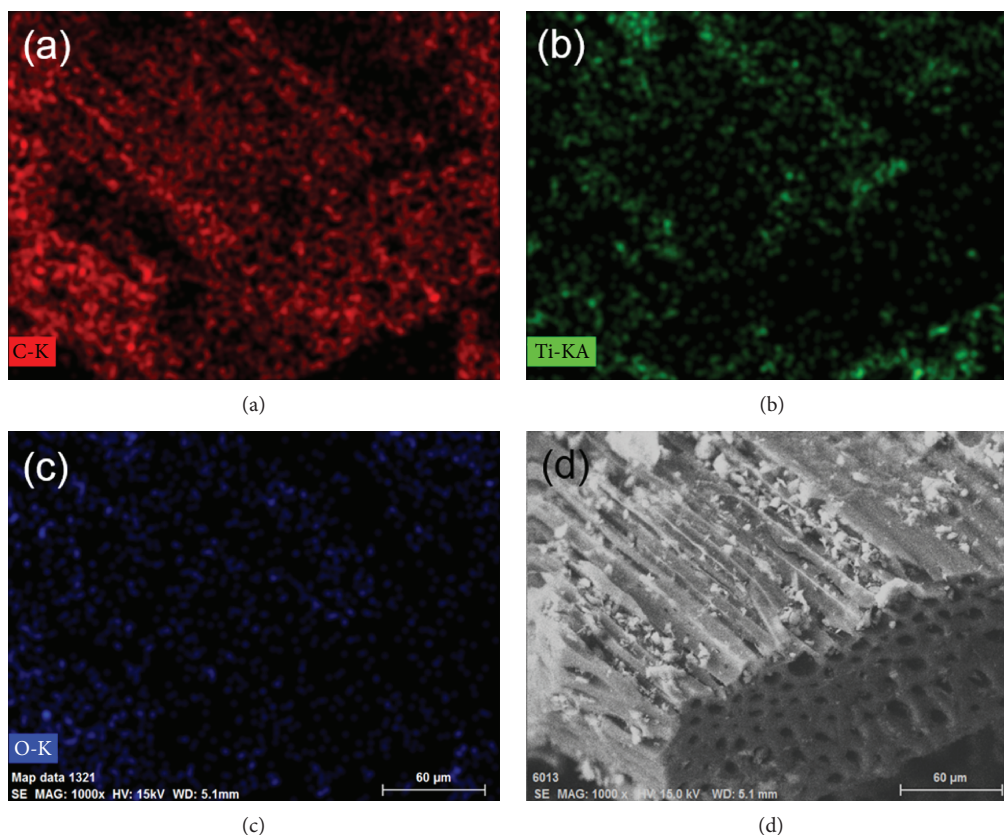


FIGURE 6: (a–c) Element mapping images and (d) the corresponding SEM image of BC@TiO<sub>2</sub>-300°C.

TABLE 1: Element content of BC@TiO<sub>2</sub>-300°C measured by EDS spectrum.

	wt.%	at.%
C	64.44	75.95
O	22.91	20.32
Ti	12.60	3.72

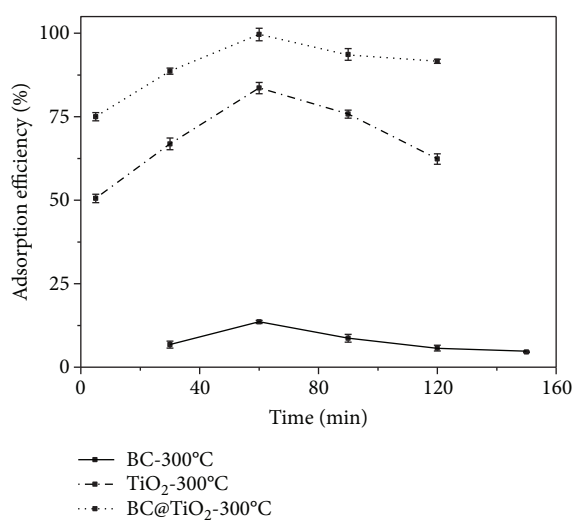


FIGURE 7: Comparison of the adsorption efficiency for BC-300°C, TiO<sub>2</sub>-300°C, and BC@TiO<sub>2</sub>-300°C.

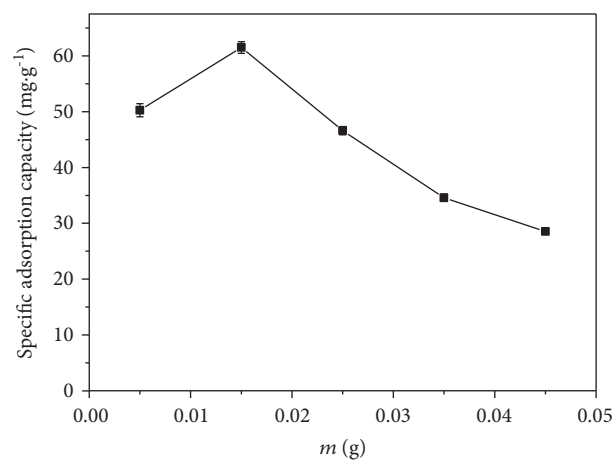


FIGURE 8: The specific adsorption capacity of BC@TiO<sub>2</sub>-300°C.

BC, TiO<sub>2</sub>, and BC@TiO<sub>2</sub> reaches at the same time of 60 min. It would be observed that BC@TiO<sub>2</sub>-300°C, BC@TiO<sub>2</sub>-400°C, and BC@TiO<sub>2</sub>-500°C reach the adsorption saturation at 60, 30, and 90 min, respectively. In the analysis with the results in Figure 1, it would be considered that the grain size of TiO<sub>2</sub> has an impact on the saturated time. Additionally, the saturated value of BC@TiO<sub>2</sub>-300°C, BC@TiO<sub>2</sub>-400°C, and BC@TiO<sub>2</sub>-500°C is larger than the same content of BC and TiO<sub>2</sub>. It indicates the existence of the synergistic adsorption effect of BC and TiO<sub>2</sub> in all BC@TiO<sub>2</sub>-300°C, BC@TiO<sub>2</sub>-

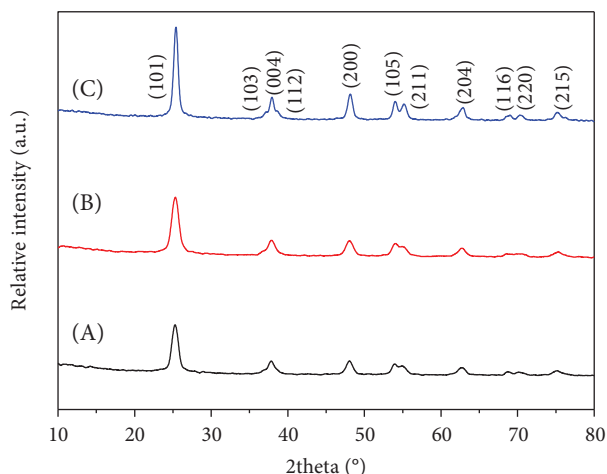


FIGURE 9: XRD patterns of A BC@TiO<sub>2</sub>-300°C, B BC@TiO<sub>2</sub>-400°C, and C BC@TiO<sub>2</sub>-500°C.

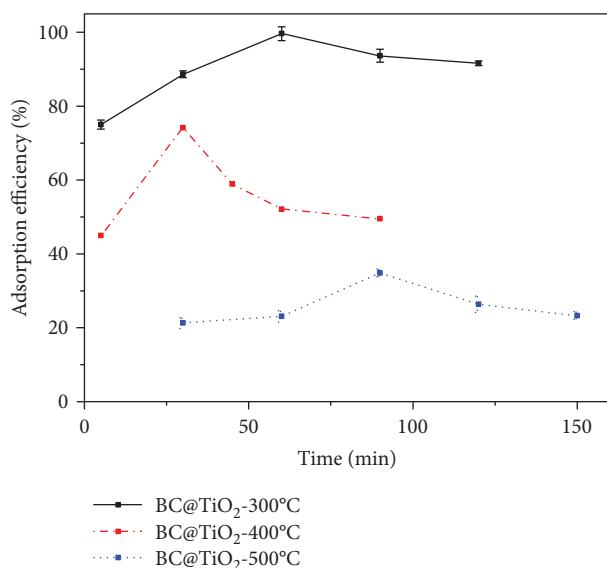


FIGURE 10: The adsorption efficiency of BC@TiO<sub>2</sub>-300°C, BC@TiO<sub>2</sub>-400°C, and BC@TiO<sub>2</sub>-500°C.

400°C, and BC@TiO<sub>2</sub>-500°C. Among them, BC@TiO<sub>2</sub>-300°C shows the best adsorption performance. It would be concluded that the grain size of TiO<sub>2</sub> is smaller, the adsorption efficiency is higher, but adsorption kinetics is not better. The influence mechanism of adsorption kinetics for BC@TiO<sub>2</sub> would be further studied.

#### 4. Conclusion

In this work, an effective absorbent of BC@TiO<sub>2</sub> composite has been successfully explored to apply for Congo red removal from aqueous solution. The well-developed hollow pore size of Triarrhena BC is enlarged at a great extent by loading with TiO<sub>2</sub>. Due to the synergistic adsorption effect of BC and TiO<sub>2</sub>, BC@TiO<sub>2</sub> shows better adsorption capacity. It could be concluded that it is significant to adjust accurately

the pore structure of Triarrhena BC, the grain size of TiO<sub>2</sub>, and the weakly interaction of the functional group between TiO<sub>2</sub> and BC in order to obtain more excellent adsorption capacity of BC@TiO<sub>2</sub> composites.

#### Data Availability

The data used to support the findings of this study are available from the corresponding author upon request.

#### Conflicts of Interest

The authors declare that they have no conflicts of interest.

#### Acknowledgments

This work was supported by the NSFC under Project no. 51701073, the Youth Fund of Hunan Agricultural University no. 16QN13, the Undergraduates' Innovative Project of Hunan Agricultural University no. XCX16007, and the Graduate Innovation Project in Hunan Province no. CX2016B300.

#### References

- [1] K. Y. Chong, C. H. Chia, S. Zakaria, and M. S. Sajab, "Vaterite calcium carbonate for the adsorption of Congo red from aqueous solutions," *Journal of Environmental Chemical Engineering*, vol. 2, no. 4, pp. 2156–2161, 2014.
- [2] N. H. H. Hairom, A. W. Mohammad, and A. A. H. Kadhum, "Nanofiltration of hazardous Congo red dye: performance and flux decline analysis," *Journal of Water Process Engineering*, vol. 4, pp. 99–106, 2014.
- [3] S. Chakraborty, B. Basak, S. Dutta, B. Bhunia, and A. Dey, "Decolorization and biodegradation of congo red dye by a novel white rot fungus *Alternaria alternata* CMERI F6," *Bioresource Technology*, vol. 147, pp. 662–666, 2013.
- [4] K. Hayat, S. Menhas, J. Bundschuh, and H. J. Chaudhary, "Microbial biotechnology as an emerging industrial wastewater treatment process for arsenic mitigation: a critical review," *Journal of Cleaner Production*, vol. 151, pp. 427–438, 2017.
- [5] K. Paździor, J. Wrębiak, A. Klepacz-Smółka et al., "Influence of ozonation and biodegradation on toxicity of industrial textile wastewater," *Journal of Environmental Management*, vol. 195, Part 2, pp. 166–173, 2017.
- [6] A. Đokić and S. Jović, "Evaluation of agriculture and industry effect on economic health by ANFIS approach," *Physica A: Statistical Mechanics and its Applications*, vol. 479, pp. 396–399, 2017.
- [7] M. Kamali and Z. Khodaparast, "Review on recent developments on pulp and paper mill wastewater treatment," *Ecotoxicology and Environmental Safety*, vol. 114, pp. 326–342, 2015.
- [8] H. Y. El-Kassas and L. A. Mohamed, "Bioremediation of the textile waste effluent by *Chlorella vulgaris*," *The Egyptian Journal of Aquatic Research*, vol. 40, no. 3, pp. 301–308, 2014.
- [9] J. Yao, D. Wen, J. Shen, and J. Wang, "Zero discharge process for dyeing wastewater treatment," *Journal of Water Process Engineering*, vol. 11, pp. 98–103, 2016.

- [10] A. K. An, J. Guo, S. Jeong, E.-J. Lee, S. A. A. Tabatabai, and T. O. Leiknes, "High flux and antifouling properties of negatively charged membrane for dyeing wastewater treatment by membrane distillation," *Water Research*, vol. 103, pp. 362–371, 2016.
- [11] T. Robinson, G. McMullan, R. Marchant, and P. Nigam, "Remediation of dyes in textile effluent: a critical review on current treatment technologies with a proposed alternative," *Bioresource Technology*, vol. 77, no. 3, pp. 247–255, 2001.
- [12] X.-A. Ning, J.-Y. Wang, R.-J. Li et al., "Fate of volatile aromatic hydrocarbons in the wastewater from six textile dyeing wastewater treatment plants," *Chemosphere*, vol. 136, pp. 50–55, 2015.
- [13] M. Matouq, N. Jildeh, M. Qtaishat, M. Hindiyeh, and M. Q. Al Syouf, "The adsorption kinetics and modeling for heavy metals removal from wastewater by *Moringa* pods," *Journal of Environmental Chemical Engineering*, vol. 3, no. 2, pp. 775–784, 2015.
- [14] M. Mandegari and H. Fashandi, "Untapped potentials of acrylonitrile-butadiene-styrene/polyurethane (ABS/PU) blend membrane to purify dye wastewater," *Journal of Environmental Management*, vol. 197, pp. 464–475, 2017.
- [15] Y. Yang, G. Wang, B. Wang et al., "Biosorption of Acid Black 172 and Congo red from aqueous solution by nonviable *Penicillium* YW 01: kinetic study, equilibrium isotherm and artificial neural network modeling," *Bioresource Technology*, vol. 102, no. 2, pp. 828–834, 2011.
- [16] S. Kumari, D. Mankotia, and G. S. Chauhan, "Crosslinked cellulose dialdehyde for Congo red removal from its aqueous solutions," *Journal of Environmental Chemical Engineering*, vol. 4, no. 1, pp. 1126–1136, 2016.
- [17] Suhas, P. J. M. Carrott, M. M. L. Ribeiro Carrott, R. Singh, L. P. Singh, and M. Chaudhary, "An innovative approach to develop microporous activated carbons in oxidising atmosphere," *Journal of Cleaner Production*, vol. 156, pp. 549–555, 2017.
- [18] Y. X. Wang, H. H. Ngo, and W. S. Guo, "Preparation of a specific bamboo based activated carbon and its application for ciprofloxacin removal," *Science of the Total Environment*, vol. 533, pp. 32–39, 2015.
- [19] X. Yang, H. Yi, X. Tang et al., "Behaviors and kinetics of toluene adsorption-desorption on activated carbons with varying pore structure," *Journal of Environmental Sciences*, vol. 67, pp. 104–114, 2018.
- [20] M. Olivares-Marín, C. Fernández-González, A. Macías-García, and V. Gómez-Serrano, "Preparation of activated carbon from cherry stones by chemical activation with  $ZnCl_2$ ," *Applied Surface Science*, vol. 252, no. 17, pp. 5967–5971, 2006.
- [21] H. A. Alhashimi and C. B. Aktas, "Life cycle environmental and economic performance of biochar compared with activated carbon: a meta-analysis," *Resources, Conservation and Recycling*, vol. 118, pp. 13–26, 2017.
- [22] Z. Tan, C. S. K. Lin, X. Ji, and T. J. Rainey, "Returning biochar to fields: a review," *Applied Soil Ecology*, vol. 116, pp. 1–11, 2017.
- [23] H. Li, X. Dong, E. B. da Silva, L. M. de Oliveira, Y. Chen, and L. Q. Ma, "Mechanisms of metal sorption by biochars: biochar characteristics and modifications," *Chemosphere*, vol. 178, pp. 466–478, 2017.
- [24] B. de Caprariis, P. de Filippis, A. D. Hernandez et al., "Pyrolysis wastewater treatment by adsorption on biochars produced by poplar biomass," *Journal of Environmental Management*, vol. 197, pp. 231–238, 2017.
- [25] N. Liu, M. Zhu, H. Wang, and H. Ma, "Adsorption characteristics of Direct Red 23 from aqueous solution by biochar," *Journal of Molecular Liquids*, vol. 223, pp. 335–342, 2016.
- [26] X. Zhang, A. K. Sarmah, N. S. Bolan et al., "Effect of aging process on adsorption of diethyl phthalate in soils amended with bamboo biochar," *Chemosphere*, vol. 142, pp. 28–34, 2016.
- [27] Q. Cheng, Q. Huang, S. Khan et al., "Adsorption of Cd by peanut husks and peanut husk biochar from aqueous solutions," *Ecological Engineering*, vol. 87, pp. 240–245, 2016.
- [28] L. Zhou, Y. Liu, S. Liu et al., "Investigation of the adsorption-reduction mechanisms of hexavalent chromium by ramie biochars of different pyrolytic temperatures," *Bioresource Technology*, vol. 218, pp. 351–359, 2016.
- [29] M. Kardanzadeh, I. Kazeminezhad, and S. Mosivand, "Electrosynthesis and characterization of  $TiO_2$  nanoparticles and their application in removal of congo red from water without UV radiation," *Ceramics International*, vol. 44, no. 5, pp. 5652–5659, 2018.
- [30] Y. Yu, J. Wang, and J. F. Parr, "Preparation and properties of  $TiO_2$ /fumed silica composite photocatalytic materials," *Procedia Engineering*, vol. 27, pp. 448–456, 2012.

## Research Article

# Synthesis, Morphology, and Hydrogen Absorption Properties of TiVMn and TiCrMn Nanoalloys with a FCC Structure

Bo Li,<sup>1</sup> Jianding Li,<sup>1</sup> Huaiyu Shao <sup>1</sup>, Wei Li,<sup>2</sup> and Huaijun Lin <sup>2</sup>

<sup>1</sup>Institute of Applied Physics and Materials Engineering (IAPME), University of Macau, Macau

<sup>2</sup>Institute of Advanced Wear & Corrosion Resistance and Functional Materials, Jinan University, Guangzhou 510632, China

Correspondence should be addressed to Huaiyu Shao; hshao@umac.mo and Huaijun Lin; hjlin@jnu.edu.cn

Received 22 January 2018; Revised 30 March 2018; Accepted 19 April 2018; Published 3 June 2018

Academic Editor: Daniele Passeri

Copyright © 2018 Bo Li et al. This is an open access article distributed under the Creative Commons Attribution License, which permits unrestricted use, distribution, and reproduction in any medium, provided the original work is properly cited.

TiVMn and TiCrMn alloys are promising hydrogen storage materials for onboard application due to their high hydrogen absorption content. However, the traditional synthesis method of melting and continuous necessary heat treatment and activation process are energy- and time-consuming. There is rarely any report on kinetics improvement and nanoprocessing in TiVMn- and TiCrMn-based alloys. Here, through ball milling with carbon black as additive, we synthesized face-centered cubic (FCC) structure TiVMn- and TiCrMn-based nanoalloys with mean particle sizes of around a few to tens of  $\mu\text{m}$  and with the crystallite size just 10 to 13 nm. Differential scanning calorimetry (DSC) measurements under hydrogen atmosphere of the two obtained TiVMn and TiCrMn nanoalloys show much enhancement on the hydrogen absorption performance. The mechanism of the property improvement and the difference in the two samples were discussed from microstructure and morphology aspects. The study here demonstrates a new potential methodology for development of next-generation hydrogen absorption materials.

## 1. Introduction

For the realization of hydrogen energy society, it is crucial to develop low-cost and high-energy density hydrogen storage technologies and materials [1–5]. In the last decades, numerous types of hydrogen storage materials have been investigated for solid-state onboard storage of hydrogen [6, 7], for instance, metals and alloys [8–12], complex hydrides [13–16], chemical compounds [17–19], and carbon-based absorbents [20, 21]. However, none of these studied systems could entirely meet the technical requirements set by the US Department of Energy for onboard storage. Novel ideas and technologies are needed to develop future hydrogen storage materials.

Metal-/alloy-based hydrogen storage materials are thought to be promising candidates due to the good properties in capacity, kinetics and cycle ability, and so on, and these materials have presented excellent application performance in Ni-metal hydride (Ni-MH) rechargeable batteries [22–24], with low requirement on hydrogen storage capacity. However, preceding design and development in traditional

interstitial metal-/alloy-based hydrogen storage materials suffer from limited capacity, poor kinetics, and lattice volume expansion. TiVMn- and TiCrMn-based alloys with bcc-Lave phase structure have been widely investigated for onboard hydrogen storage development due to the room temperature working temperature and possibly high hydrogen absorption capacity (3.5–4.2 wt%) [25–33]. However, synthesis of these alloys, normally by melting method, needs quite harsh conditions, which is also highly energy inefficient. Afterwards, the obtained alloys need strict conditions for heat treatment and hydrogen sorption activation processes before it may reversibly absorb and desorb hydrogen. Therefore, the kinetics of the TiVMn- and TiCrMn-based alloys should be enhanced. Ball milling technique is one of the most popular synthesis and downsizing methods to improve the sorption kinetics for hydrogen storage materials. However, we may hardly find any reports on synthesis of these two alloys by ball milling (or mechanical alloying) methods. The reason is that direct ball milling of the mixture of raw metals of Ti, V, and so on will result in sticking of the sample to the vessel wall and milling balls (see Figure S1). Here, we report that TiVMn and

TiCrMn alloys with fine particle size and uniform nanostructured crystallite size were obtained through ball milling with carbon black as additive. Interestingly, these synthesized alloys are with a FCC structure, which is the first time to be reported in TiVMn- and TiCrMn-based alloys. Structure, morphology, and hydrogen storage properties of the TiVMn- and TiCrMn-based nanoalloys are discussed in this work.

## 2. Experimental Details

TiVMn and TiCrMn alloys were synthesized from Ti (-325 mesh, purity > 99.5%, Alfa Aesar), V (-325 mesh, purity > 99.5%, Alfa Aesar), and Mn (-325 mesh, purity > 99.5%, Alfa Aesar) metals and Ti (-325 mesh, purity > 99.5%, Alfa Aesar), Cr (-200 mesh, purity > 99%, Alfa Aesar) and Mn (-325 mesh, purity > 99.5%, Alfa Aesar) metals, respectively, by mechanical alloying method. Another 10 wt% carbon black (Sigma Aldrich) was added as additive during the milling process. The mechanical alloying process of these alloys was carried out with a rotation speed of 600 rpm and a milling duration of 10 h under Ar atmosphere using Fritsch P7 planetary micromill. For a typical milling process, 0.5 g mixture of the raw metals with an atomic ratio of 1 : 1 : 1 and 0.05 g (10 wt%) carbon black was put into a 45 ml stainless steel vessel. Ten stainless steel milling balls with a diameter of 0.7 cm and an average weight of 1.5 g were used. The ball-to-sample ratio was 30 : 1.

The X-ray diffraction (XRD) measurements were carried out using a Rigaku diffractometer (Ultima IV) with  $\text{CuK}\alpha$  radiation at a generator voltage of 40 kV and a current of 40 mA, to obtain the phase information of the samples. The analysis of the microstructure and elemental information was conducted using scanning electron microscope (SEM) (S3400N, Hitachi). It may investigate samples by both secondary electron (SE) and backscattered electron (BSE) signals. The SEM apparatus is attached with an energy-dispersive X-ray spectrometer (EDS). Differential scanning calorimetry (DSC) measurements under hydrogen atmosphere were carried out to study the hydrogen absorption properties of the alloys, through a Rigaku TP-8230 HP apparatus under a constant hydrogen pressure of 1 MPa with a flow rate of 200 ml/min.

## 3. Results and Discussion

From the XRD curves of the ball milled TiVMn-10%C and TiCrMn-10%C alloys which have been normalized to clearly present the phase compositions of each sample, we can see that both of these two reflection patterns are in perfect fitting with a FCC structure (face-centered cubic, space group:  $Fm\bar{3}m$  no. 225), showing 5 reflections of (111), (200), (220), (311), and (222) at around 37°, 43°, 62°, 75°, and 78°, respectively. There is no obvious diffraction peak from the raw materials (Ti, V, Mn, and C or Ti, Cr, Mn, and C), which means the starting metal powders have been transformed into the new phase. The lattice parameter of the TiVMn alloy is  $a = 4.234 \text{ \AA}$ , and the one for the TiCrMn alloy is  $a = 4.270 \text{ \AA}$ . In Figure 1, we can see that the diffraction peaks present severe broadening, which indicates a rather fine

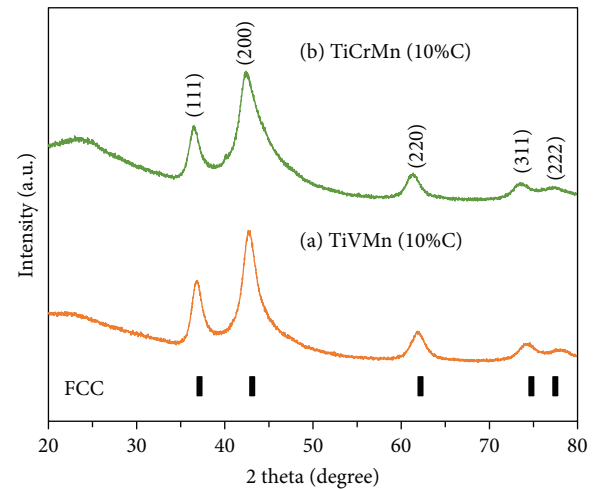


FIGURE 1: X-ray diffraction curves of (a) TiVMn-10%C and (b) TiCrMn-10%C nanoalloys with a FCC structure after 10 h mechanical alloying process.

nanocrystalline microstructure in these two samples. The average crystallite sizes of the TiVMn and TiCrMn nanoalloys were calculated to be 12.6 nm and 10.4 nm. As we discussed above, there is rarely any report on nanoprocessing synthesis of TiVMn- and TiCrMn-based hydrogen storage materials. Ball milling is the most popular synthesis technique applied in various hydrogen storage materials to obtain nanosize samples [34–46]. However, milling of the mixture of Ti-based materials such as Ti and V powders normally results in a melted metal state (see Figure S1) and not any powder sample can be obtained after the milling with a duration of 2 to 24 hours. Here, through addition of 10 wt% carbon black, we successfully synthesized nanostructured TiVMn and TiCrMn alloys with very fine nanocrystallite structures. The specific atomic position of Ti, V, Mn, and C in the TiVMn alloy with FCC structure (or Ti, Cr, Mn, and C in TiCrMn alloy), at this moment, is under study. Recently, we have made some progress and discussion in the  $\text{Ti}_{50}\text{V}_{50}\text{-C}$  alloy sample [47].

Figures 2 and 3 are the SE-SEM and BSE-SEM images of the TiVMn and TiCrMn nanoalloy samples at different magnifications (400x to 10,000x). From these two figures, we may see the size and morphology of the two obtained samples after ball milling synthesis process. From Figures 2(a) and 2(b), we can see that both of the two samples show uniform morphology in a large range (ca.  $300 \mu\text{m} \times 200 \mu\text{m}$ ). Figures 2(c) and 2(d) may be more clearly presenting some difference in the morphology of these two samples. The TiVMn alloy particles are with a larger size range than the TiCrMn ones. The particles of TiVMn in Figures 2(c) and 2(e) show a size from a few hundred nm to a few dozen  $\mu\text{m}$ , while the ones for TiCrMn (Figures 2(d) and 2(f)) are in a size range mainly around 2 to 5  $\mu\text{m}$ . This morphology difference of the synthesized samples in the same milling conditions is thought to be attributed to the raw composition of starting metal materials. Ball milling method is a high-energy operation of repeated welding and fracturing of the raw mixture samples. In our former studies of Mg-Co-

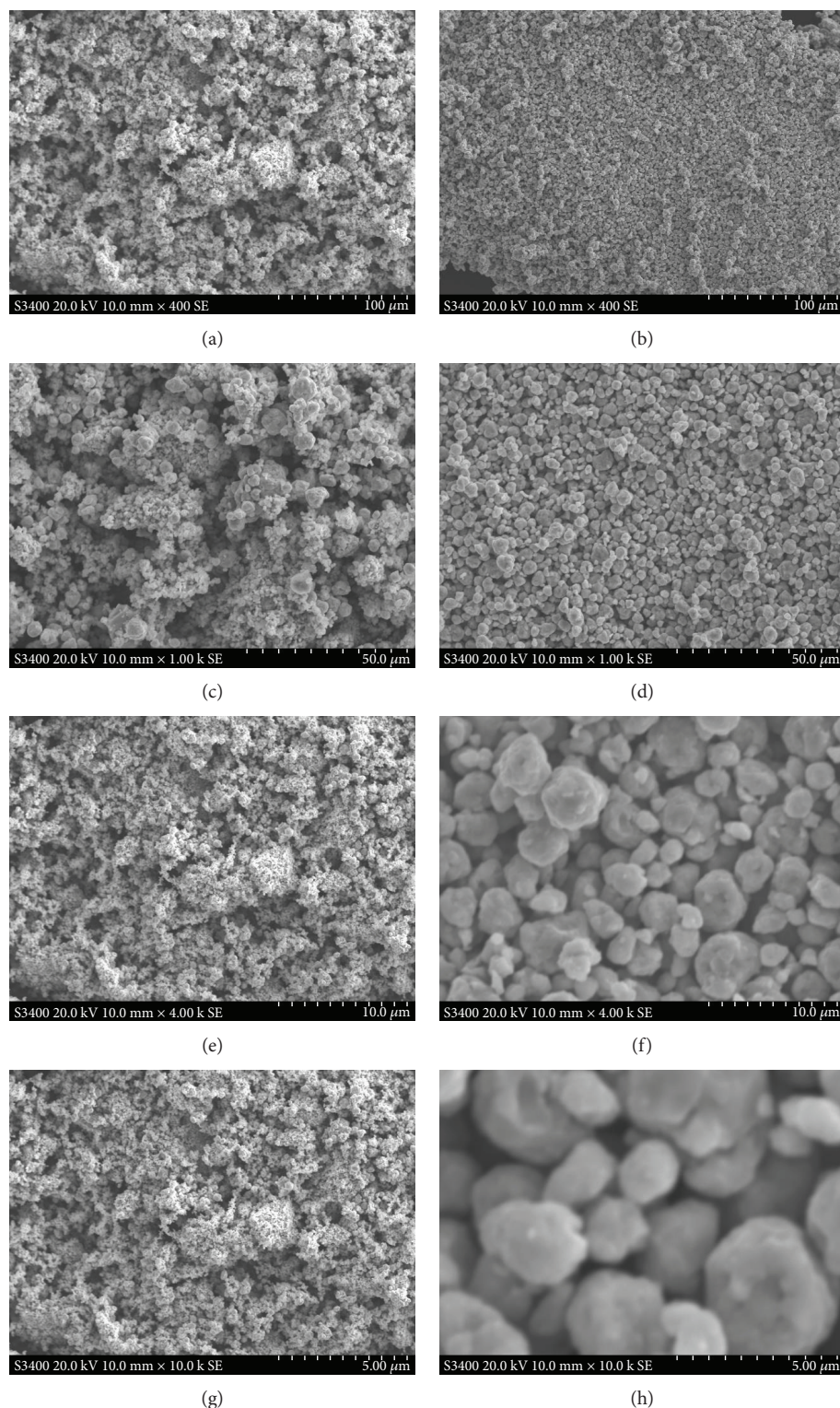


FIGURE 2: SE-SEM images of the synthesized TiVMn nanoalloy (a) 400x, (c) 1000x, (e) 4000x, and (g) 10,000x and TiCrMn nanoalloy (b) 400x, (d) 1000x, (f) 4000x, and (h) 10,000x after 10 h milling.

based materials, no additional composition is needed for the milling process [45]. However, in the milling process of TiVMn and TiCrMn from raw metal mixture, some additives, in this case carbon black, are essential to guarantee that powder samples can be obtained after 10 h milling.

Figures 2(g) and 2(h) present some detailed morphology with high magnification for certain sample areas of the TiVMn and TiCrMn alloys, respectively. Ball milling method has been widely adopted in synthesis of hydrogen storage materials in nanostructure [48]. In our previous work, we have

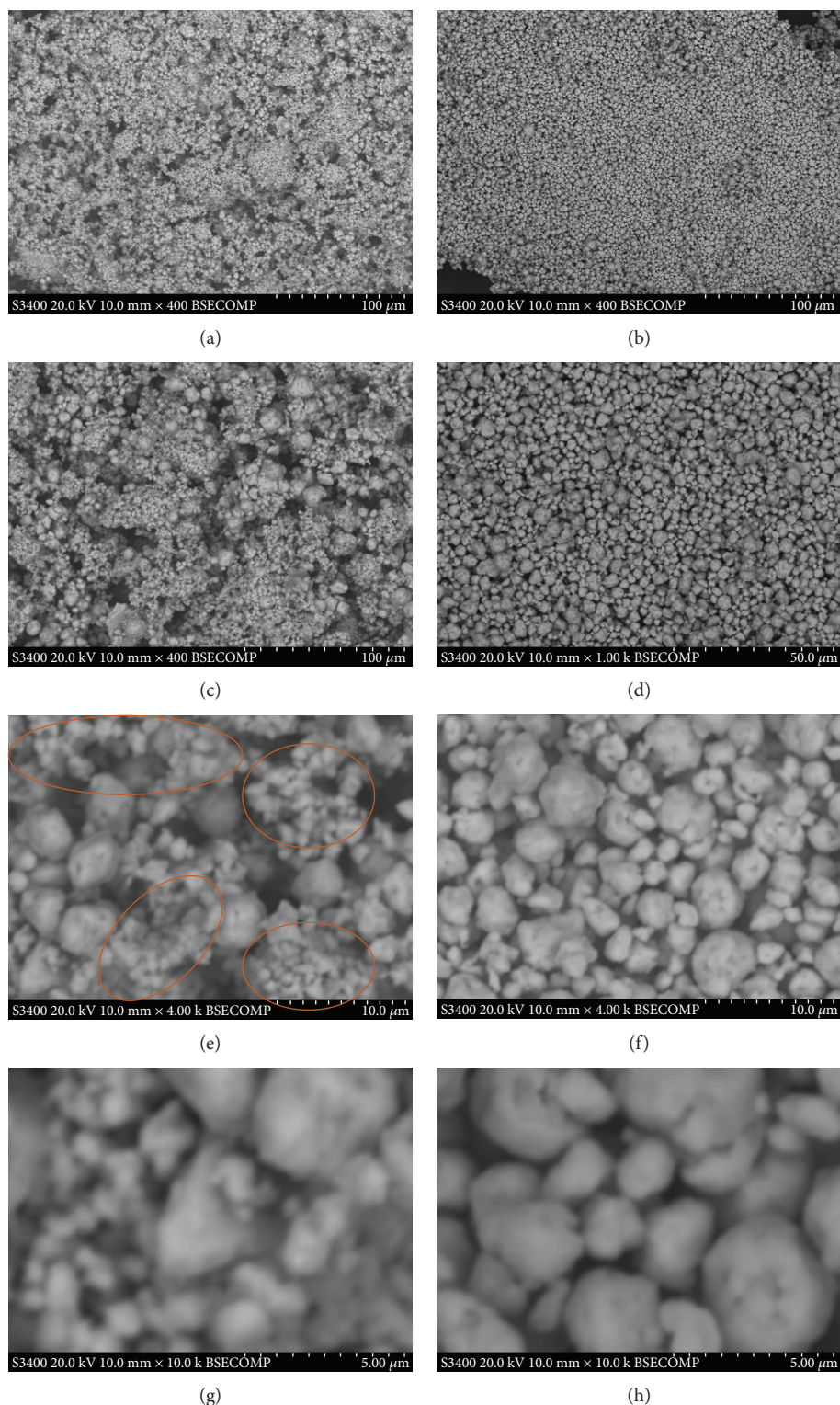


FIGURE 3: BSE-SEM images of the synthesized TiVMn nanoalloy (a) 400x, (c) 1000x, (e) 4000x, and (g) 10,000x and TiCrMn nanoalloy (b) 400x, (d) 1000x, (f) 4000x, and (h) 10,000x after 10 h milling.

used ball milling technique to synthesize Mg-based metastable hydrogen storage alloys and we reported the Mg-Co-based metastable alloy with body-centered cubic structure which may absorb hydrogen at  $-15^{\circ}\text{C}$  which is the lowest temperature reported so far for Mg-based material to absorb

hydrogen [5, 45, 49, 50]. SEM as one scanning technique to obtain morphology of the samples may provide some key information to understand the formation mechanism of the obtained alloy from raw metal mixture. In our previous study [45], we comprehensively investigated the

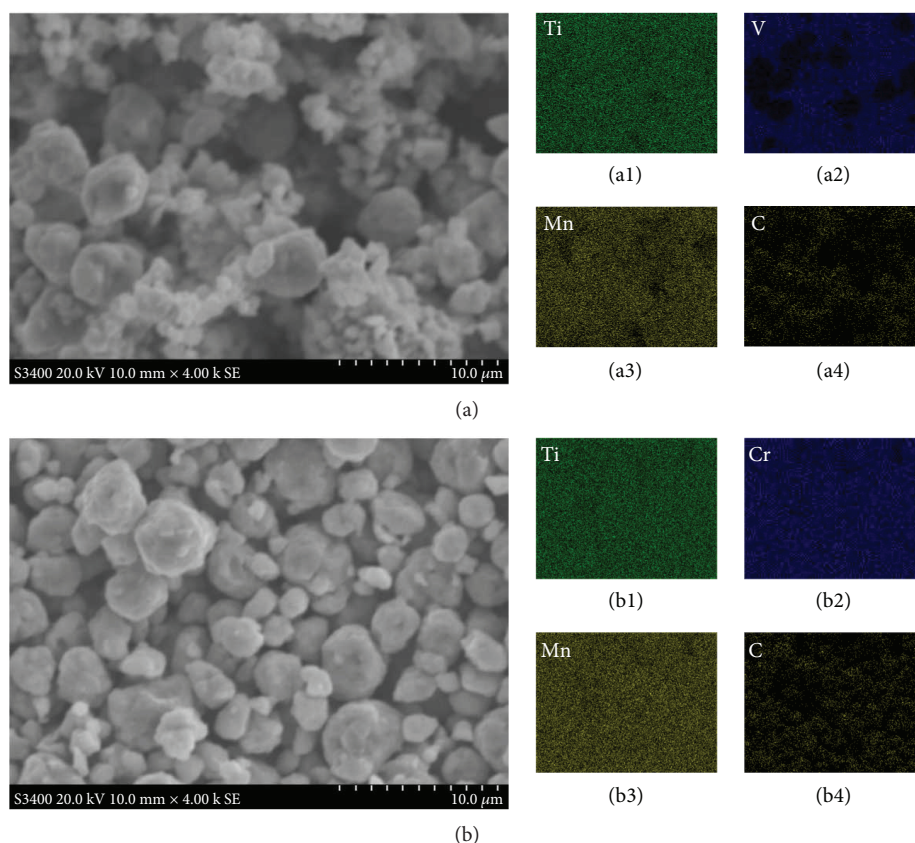


FIGURE 4: SE-SEM images of the (a) TiVMn and (b) TiCrMn nanoalloys. EDS mappings of (a1) Ti, (a2) V, (a3) Mn, and (a4) C for the corresponding TiVMn area in (a) and (b1) Ti, (b2) Cr, (b3) Mn, and (b4) C for the corresponding TiCrMn area in (b).

formation evolution process of Mg-Co nanoalloys milled from 0.5 to 400 h.

When we compare Figure 3 with Figure 2, the SE-SEM images may give us information about the three-dimensional morphology of the two alloy particle samples, while the BSE signal ones may be more sensitive in the composition difference of the particle surface. For the TiCrMn alloy in Figures 3(b), 3(d), 3(f), and 3(h), the BSE-SEM images indicate quite a uniform contrast, which demonstrates that the surface of the TiCrMn alloy is with quite a homogenous composition. For the TiVMn sample in Figures 3(a), 3(c), 3(e), and 3(g), the situation is a little different with that for the TiCrMn alloy sample. We can see that there are two domains with a little different contrast—the gray area and the white one. In Figure 3(e), we can also clearly observe some areas with much smaller particle size compared with the nearby ones (in orange circles). From XRD analysis, there is only one FCC phase in both of these two samples. However, the SE-SEM and BSE-SEM images can tell some obvious difference in particle size and surface composition.

Figure 4 presents the elemental analysis results of the particles in the TiVMn and TiCrMn alloy samples. From Figure 4(b1)–(b4), we may see that after 10 h ball milling, Ti, Cr, and Mn are homogeneously distributed throughout the TiCrMn sample, which demonstrates that a uniform compound is formed after the milling process. Carbon black

is introduced as additive for milling assistance of TiVMn and TiCrMn samples so that it is possible to obtain powder samples after the milling process, while not the entire sample sticks to the inner wall of the milling vessel or surface of the balls. After the milling, C element is also well dispersed in the sample. Since we cannot detect any C reflection peaks or amorphous background from XRD or find obvious isolate C areas by EDS mapping of the sample, we may conclude that C is in the composition of the FCC structure compound. From the EDS mapping of the TiVMn sample, again, we found some difference with the TiCrMn one. Ti and Mn are homogeneously dispersed in the sample, but different with Cr in the TiCrMn sample, V in the TiVMn sample is not that uniformly distributed. From Figure 4(a) and Figure 4(a2), we can see that the smaller particles (less than  $10\ \mu\text{m}$ ) in the TiVMn sample is much more V rich than the larger ones. We believe that this difference may contribute to different hydrogen storage properties of these two samples. It should be pointed out that it is a universal factor that synthesis by ball milling will introduce some contamination from milling vessel/balls to the sample. In our cases, we found that some Fe element from the milling tools is around 3–8 wt%, which was attributed to the long-time milling process between samples and stainless steel vessels and milling balls.

Figure 5 presents the high-pressure DSC curves of the synthesized TiVMn and TiCrMn alloy samples with FCC structure, under a hydrogen atmosphere of 1 MPa. Hydrogen

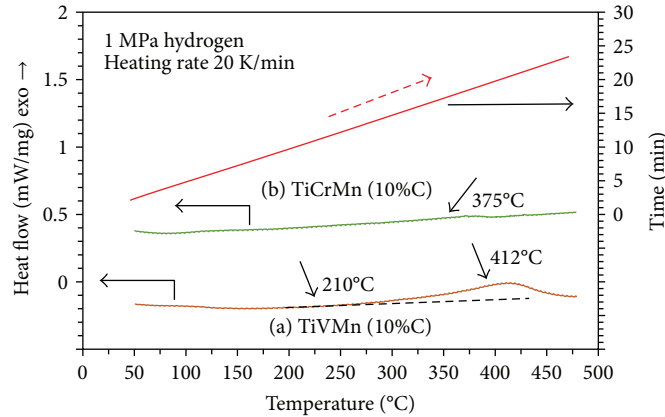


FIGURE 5: High pressure DSC curves of the synthesized TiVMn and TiCrMn nanoalloy samples in 1 MPa hydrogen atmosphere. Red solid line presents the time-heating program information.

pressure DSC is a very simple and essential technique to test the hydrogen absorption and desorption properties of samples. A quite small amount sample is enough (around 10 mg) to obtain some temperature and hydrogen pressure information necessary for the absorption and desorption reactions. The temperature program in Figure 5 was set as from room temperature to 500°C with a heating rate of 20 K/min (red solid line). In Figure 5, we can see that the TiVMn and TiCrMn nanoalloys may show hydrogen absorption (exothermic reaction peaks) before 450°C without any activation process. According to our experiences in study of hydrogen storage alloys for DSC measurements under hydrogen atmosphere, especially for metastable alloys without any phase transfer process in the measurement temperature range, exothermic peaks are attributed to hydrogen absorption reactions [44–46, 51, 52]. The hydrogenation peak temperatures under 1 MPa hydrogen are 412 and 375°C for the TiVMn and TiCrMn nanoalloys, respectively. It is worth noting that although the DSC measurement of samples heated under hydrogen pressure at certain time and temperature point may be similar with the conditions of taking hydrogen absorption measurements, it is still quite different. The reason is that the temperature of the sample at DSC measurement is under heating and the real temperature of the sample is increasing at a very high rate (20 K/min in this case). As a result, the peak temperature derived from the DSC measurements under certain hydrogen pressure actually is much higher than the one needed for hydrogen absorption measurements at the same constant temperature. This means these two alloys may absorb hydrogen at a much lower temperature than 412°C for TiVMn nanoalloy and 375°C for the TiCrMn one without heat treatment and activation. When we compare the hydrogen absorption reaction peaks of these two samples, we can see that although TiCrMn nanoalloy may absorb hydrogen with a peak temperature at around 37°C lower than the TiVMn one, the absorption reaction peak of TiVMn alloy is much larger than the one from TiCrMn alloy. This means a much larger ratio of the TiVMn alloy may start to absorb hydrogen than the TiCrMn one at the corresponding peak temperature. Another essential point is that the TiVMn sample may start to absorb

hydrogen at around 210°C from the DSC measurement. This means that in hydrogen absorption under constant temperature, TiVMn nanoalloy may start the absorption process at a temperature much lower than 210°C. The difference in the hydrogen absorption properties of these two nanoalloy samples is thought to be the V-rich area and partially smaller particle size in the TiVMn nanoalloy sample compared to the TiCrMn one, observed from the SEM characterization techniques.

The TiVMn and TiCrMn alloys synthesized by melting method have been widely investigated as hydrogen storage materials [28, 31, 53–58]. The two alloys after melting are usually with bcc-C14 Lave phase structures, and they may start to absorb hydrogen after a strict heat treatment at a temperature greater than 600°C and an activation process at high temperature and high pressure hydrogen atmosphere, which is quite time- and energy-consuming. So, we may conclude that via ball milling with carbon black, the obtained TiVMn and TiCrMn nanoalloy samples with a FCC structure show much enhanced hydrogen absorption performance than the TiVMn- and TiCrMn-based alloys obtained by melting method, implying a novel development methodology of future hydrogen storage materials.

#### 4. Conclusions

TiVMn and TiCrMn nanoalloys with a FCC structure (face-centered cubic, space group:  $Fm-3m$  no. 225) were synthesized by ball milling with carbon black as additive. The lattice parameter and crystallite size of the TiVMn nanoalloy are  $a = 4.234 \text{ \AA}$  and 12.6 nm, respectively. The ones for the TiCrMn alloy are  $a = 4.270 \text{ \AA}$  and 10.4 nm. The SE- and BSE-SEM observations at different magnifications show that the TiVMn alloy particles (a few hundred nm to a few dozen  $\mu\text{m}$ ) are with a larger size range than the TiCrMn ones (mainly 2 to 5  $\mu\text{m}$ ). In the TiVMn nanoalloy, there are domains with smaller particle size and V-rich composition compared with the other area. The morphology and microstructure differences contribute to the different hydrogen absorption properties by DSC measurements under

hydrogen pressure. The TiVMn nanoalloy and the TiCrMn one show absorption peaks at 412 and 375°C, respectively. But the absorption reaction is much stronger and starts at much lower temperature (210°C) in the TiVMn nanoalloy than that in the TiCrMn one. This work implies a new development methodology of future hydrogen storage materials.

## Data Availability

The data used to support the findings of this study are available from the corresponding author upon request.

## Conflicts of Interest

The authors declare no conflict of interest.

## Acknowledgments

Huaiyu Shao acknowledges the Macau Science and Technology Development Fund (FDCT) for funding (Project no. 118/2016/A3), and this work was also partially supported by a Start-Up Research Fund from the University of Macau (SRG2016-00088-FST). Wei Li thanks the support from Guangdong Science and Technology Department Project (2017B090903005).

## Supplementary Materials

Figure S1: direct ball milling of the mixture of raw metals of Ti, V, and so on will result in sticking of the sample to the vessel wall and milling balls. No powders can be collected after ball milling for 2 to 24 hours. Figure S2: dark-field TEM images of TiVMn (a) and TiCrMn (b). (*Supplementary Materials*)

## References

- [1] L. Schlapbach and A. Züttel, "Hydrogen-storage materials for mobile applications," *Nature*, vol. 414, no. 6861, pp. 353–358, 2001.
- [2] H. Shao, L. He, H. Lin, and H.-W. Li, "Progress and trends in magnesium-based materials for energy-storage research: a review," *Energy Technology*, vol. 6, no. 3, pp. 445–458, 2018.
- [3] D. J. Durbin and C. Malardier-Jugroot, "Review of hydrogen storage techniques for on board vehicle applications," *International Journal of Hydrogen Energy*, vol. 38, no. 34, pp. 14595–14617, 2013.
- [4] R. Mohtadi and S.-i. Orimo, "The renaissance of hydrides as energy materials," *Nature Reviews Materials*, vol. 2, no. 3, article 16091, 2016.
- [5] H. Shao, G. Xin, J. Zheng, X. Li, and E. Akiba, "Nanotechnology in mg-based materials for hydrogen storage," *Nano Energy*, vol. 1, no. 4, pp. 590–601, 2012.
- [6] M. U. Niemann, S. S. Srinivasan, A. R. Phani, A. Kumar, D. Y. Goswami, and E. K. Stefanakos, "Nanomaterials for hydrogen storage applications: a review," *Journal of Nanomaterials*, vol. 2008, Article ID 950967, 9 pages, 2008.
- [7] R. Zacharia and S. U. Rather, "Review of solid state hydrogen storage methods adopting different kinds of novel materials," *Journal of Nanomaterials*, vol. 2015, Article ID 914845, 18 pages, 2015.
- [8] B. Sakintuna, F. Lamari-Darkrim, and M. Hirscher, "Metal hydride materials for solid hydrogen storage: a review," *International Journal of Hydrogen Energy*, vol. 32, no. 9, pp. 1121–1140, 2007.
- [9] V. Berube, G. Radtke, M. Dresselhaus, and G. Chen, "Size effects on the hydrogen storage properties of nanostructured metal hydrides: a review," *International Journal of Energy Research*, vol. 31, no. 6-7, pp. 637–663, 2007.
- [10] H. Wang, H. J. Lin, W. T. Cai, L. Z. Ouyang, and M. Zhu, "Tuning kinetics and thermodynamics of hydrogen storage in light metal element based systems – a review of recent progress," *Journal of Alloys and Compounds*, vol. 658, pp. 280–300, 2016.
- [11] N. Z. A. Khafidz, Z. Yaakob, K. L. Lim, and S. N. Timmiati, "The kinetics of lightweight solid-state hydrogen storage materials: a review," *International Journal of Hydrogen Energy*, vol. 41, no. 30, pp. 13131–13151, 2016.
- [12] S. S. Mohammadshahi, E. M. Gray, and C. J. Webb, "A review of mathematical modelling of metal-hydride systems for hydrogen storage applications," *International Journal of Hydrogen Energy*, vol. 41, no. 5, pp. 3470–3484, 2016.
- [13] L. H. Rude, T. K. Nielsen, D. B. Ravnsbaek et al., "Tailoring properties of borohydrides for hydrogen storage: a review," *Physica Status Solidi a Applications and Materials Science*, vol. 208, no. 8, pp. 1754–1773, 2011.
- [14] E. Fakioglu, Y. Yurum, and T. N. Veziroglu, "A review of hydrogen storage systems based on boron and its compounds," *International Journal of Hydrogen Energy*, vol. 29, no. 13, pp. 1371–1376, 2004.
- [15] I. P. Jain, P. Jain, and A. Jain, "Novel hydrogen storage materials: a review of lightweight complex hydrides," *Journal of Alloys and Compounds*, vol. 503, no. 2, pp. 303–339, 2010.
- [16] S. I. Orimo, Y. Nakamori, J. R. Eliseo, A. Zuttel, and C. M. Jensen, "Complex hydrides for hydrogen storage," *Chemical Reviews*, vol. 107, no. 10, pp. 4111–4132, 2007.
- [17] H. W. Langmi, J. W. Ren, B. North, M. Mathe, and D. Bessarabov, "Hydrogen storage in metal-organic frameworks: a review," *Electrochimica Acta*, vol. 128, pp. 368–392, 2014.
- [18] "Review: Hydrogen storage in metal-organic frameworks," *Chemosuschem*, vol. 3, no. 6, pp. 651–651, 2010.
- [19] D. Ramimoghadam, E. M. Gray, and C. J. Webb, "Review of polymers of intrinsic microporosity for hydrogen storage applications," *International Journal of Hydrogen Energy*, vol. 41, no. 38, pp. 16944–16965, 2016.
- [20] J. Chen and F. Wu, "Review of hydrogen storage in inorganic fullerene-like nanotubes," *Applied Physics A*, vol. 78, no. 7, pp. 989–994, 2004.
- [21] F. Darkrim Lamari, P. Malbrunot, and G. P. Tartaglia, "Review of hydrogen storage by adsorption in carbon nanotubes," *International Journal of Hydrogen Energy*, vol. 27, no. 2, pp. 193–202, 2002.
- [22] H. Y. Shao and X. G. Li, "Effect of nanostructure and partial substitution on gas absorption and electrochemical properties in Mg<sub>2</sub>Ni-based alloys," *Journal of Alloys and Compounds*, vol. 667, pp. 191–197, 2016.
- [23] M. Jurczyk, L. Smardz, and A. Szajek, "Nanocrystalline materials for Ni–MH batteries," *Materials Science and Engineering: B*, vol. 108, no. 1-2, pp. 67–75, 2004.
- [24] W. Hu, L. D. Wang, and L. M. Wang, "Quinary icosahedral quasicrystalline Ti–V–Ni–Mn–Cr alloy: A novel anode material for Ni–MH rechargeable batteries," *Materials Letters*, vol. 65, no. 19-20, pp. 2868–2871, 2011.

- [25] A. G. Aleksanyan, S. K. Dolukhanyan, O. P. Ter-Galstyan, and N. L. Mnatsakanyan, "Hydride cycle formation of ternary alloys in Ti-V-Mn system and their interaction with hydrogen," *International Journal of Hydrogen Energy*, vol. 41, no. 31, pp. 13521-13530, 2016.
- [26] Z. J. Cao, L. Z. Ouyang, H. Wang et al., "Advanced high-pressure metal hydride fabricated via Ti-Cr-Mn alloys for hybrid tank," *International Journal of Hydrogen Energy*, vol. 40, no. 6, pp. 2717-2728, 2015.
- [27] L. Y. Chen, C. H. Li, K. Wang, H. Q. Dong, X. G. Lu, and W. Z. Ding, "Thermodynamic modeling of Ti-Cr-Mn ternary system," *Calphad*, vol. 33, no. 4, pp. 658-663, 2009.
- [28] H. Iba and E. Akiba, "Hydrogen absorption and modulated structure in Ti-V-Mn alloys," *Journal of Alloys and Compounds*, vol. 253-254, pp. 21-24, 1997.
- [29] J. Matsuda, Y. Nakamura, and E. Akiba, "Microstructure of Ti-V-Mn BCC alloys before and after hydrogen absorption-desorption," *Journal of Alloys and Compounds*, vol. 509, no. 11, pp. 4352-4356, 2011.
- [30] Y. Nakamura and E. Akiba, "New hydride phase with a deformed FCC structure in the Ti-V-Mn solid solution-hydrogen system," *Journal of Alloys and Compounds*, vol. 311, no. 2, pp. 317-321, 2000.
- [31] Y. Nakamura, J. Nakamura, K. Sakaki, K. Asano, and E. Akiba, "Hydrogenation properties of Ti-V-Mn alloys with a BCC structure containing high and low oxygen concentrations," *Journal of Alloys and Compounds*, vol. 509, no. 5, pp. 1841-1847, 2011.
- [32] L. Pickering, J. Li, D. Reed, A. I. Bevan, and D. Book, "Ti-V-Mn based metal hydrides for hydrogen storage," *Journal of Alloys and Compounds*, vol. 580, pp. S233-S237, 2013.
- [33] M. Shibuya, J. Nakamura, H. Enoki, and E. Akiba, "High-pressure hydrogenation properties of Ti-V-Mn alloy for hybrid hydrogen storage vessel," *Journal of Alloys and Compounds*, vol. 475, no. 1-2, pp. 543-545, 2009.
- [34] H. Shao, M. Felderhoff, and F. Schuth, "Hydrogen storage properties of nanostructured  $MgH_2/TiH_2$  composite prepared by ball milling under high hydrogen pressure," *International Journal of Hydrogen Energy*, vol. 36, no. 17, pp. 10828-10833, 2011.
- [35] L. Sun, G. X. Wang, H. K. Liu, D. H. Bradhurst, and S. X. Dou, "The effect of Co addition on  $Mg_2Ni$  alloy hydride electrodes prepared by sintering and followed by ball milling," *Journal of New Materials for Electrochemical Systems*, vol. 2, no. 4, pp. 211-214, 1999.
- [36] C. Chen, R. D. Ding, X. M. Feng, and Y. F. Shen, "Fabrication of Ti-Cu-Al coatings with amorphous microstructure on Ti-6Al-4 V alloy substrate via high-energy mechanical alloying method," *Surface and Coatings Technology*, vol. 236, pp. 485-499, 2013.
- [37] L. W. Huang, O. Elkedim, M. Nowak, M. Jurczyk, R. Chassagnon, and D. W. Meng, "Synergistic effects of multi-walled carbon nanotubes and Al on the electrochemical hydrogen storage properties of  $Mg_2Ni$ -type alloy prepared by mechanical alloying," *International Journal of Hydrogen Energy*, vol. 37, no. 2, pp. 1538-1545, 2012.
- [38] F. J. Castro, V. Fuster, and G. Urretavizcaya, " $MgH_2$  synthesis during reactive mechanical alloying studied by *in-situ* pressure monitoring," *International Journal of Hydrogen Energy*, vol. 37, no. 22, pp. 16844-16851, 2012.
- [39] T. Kondo and Y. Sakurai, "Hydrogen absorption-desorption properties of Mg-Ca-V BCC alloy prepared by mechanical alloying," *Journal of Alloys and Compounds*, vol. 417, no. 1-2, pp. 164-168, 2006.
- [40] H. Shao, K. Asano, H. Enoki, and E. Akiba, "Correlation study between hydrogen absorption property and lattice structure of Mg-based BCC alloys," *International Journal of Hydrogen Energy*, vol. 34, no. 5, pp. 2312-2318, 2008.
- [41] H. Shao, K. Asano, H. Enoki, and E. Akiba, "Fabrication and hydrogen storage property study of nanostructured Mg-Ni-B ternary alloys," *Journal of Alloys and Compounds*, vol. 479, no. 1-2, pp. 409-413, 2009.
- [42] H. Kim, J. Nakamura, H. Y. Shao et al., "Insight into the hydrogenation properties of mechanically alloyed  $Mg_{50}Co_{50}$  from the local structure," *The Journal of Physical Chemistry C*, vol. 115, no. 41, pp. 20335-20341, 2011.
- [43] H. Kim, J. Nakamura, H. Y. Shao et al., "Local structural evolution of mechanically alloyed  $Mg_{50}Co_{50}$  using atomic pair distribution function analysis," *The Journal of Physical Chemistry C*, vol. 115, no. 15, pp. 7723-7728, 2011.
- [44] J. Matsuda, H. Shao, Y. Nakamura, and E. Akiba, "The nanostructure and hydrogenation reaction of  $Mg_{50}Co_{50}$  BCC alloy prepared by ball-milling," *Nanotechnology*, vol. 20, no. 20, article 204015, 2009.
- [45] H. Shao, J. Matsuda, H.-W. Li et al., "Phase and morphology evolution study of ball milled Mg-Co hydrogen storage alloys," *International Journal of Hydrogen Energy*, vol. 38, no. 17, pp. 7070-7076, 2013.
- [46] H. Y. Shao, K. Asano, H. Enoki, and E. Akiba, "Preparation and hydrogen storage properties of nanostructured Mg-Ni BCC alloys," *Journal of Alloys and Compounds*, vol. 477, no. 1-2, pp. 301-306, 2009.
- [47] H. Shao, L. He, H. Wu, H.-W. Li, and Z. Lu, "Ti-V based alloy with a NaCl-type structure for hydrogen storage," *Journal of Alloys and Compounds*, 2018, In press.
- [48] F. H. Froes, C. Suryanarayana, K. Russell, and C. G. Li, "Synthesis of intermetallics by mechanical alloying," *Materials Science and Engineering: A*, vol. 192-193, Part 2, pp. 612-623, 1995.
- [49] H. Shao, K. Asano, H. Enoki, and E. Akiba, "Fabrication, hydrogen storage properties and mechanistic study of nanostructured  $Mg_{50}Co_{50}$  body-centered cubic alloy," *Scripta Materialia*, vol. 60, no. 9, pp. 818-821, 2009.
- [50] H. J. Kim, J. Nakamura, H. Y. Shao et al., "Variation in the ratio of  $Mg_2Co$  and  $MgCo_2$  in amorphous-like mechanically alloyed  $Mg_xCo_{100-x}$  using atomic pair distribution function analysis," *Zeitschrift für Kristallographie-Crystalline Materials*, vol. 227, no. 5, pp. 299-303, 2012.
- [51] L. Xie, H. Y. Shao, Y. T. Wang, Y. Li, and X. G. Li, "Synthesis and hydrogen storing properties of nanostructured ternary Mg-Ni-Co compounds," *International Journal of Hydrogen Energy*, vol. 32, no. 12, pp. 1949-1953, 2007.
- [52] H. Shao, G. Xin, X. Li, and E. Akiba, "Thermodynamic property study of nanostructured mg-H, mg-Ni-H, and mg-cu-H systems by high pressure DSC method," *Journal of Nanomaterials*, vol. 2013, Article ID 281841, 7 pages, 2013.
- [53] Z. J. Cao, L. Z. Ouyang, H. Wang, J. W. Liu, L. X. Sun, and M. Zhu, "Composition design of Ti-Cr-Mn-Fe alloys for hybrid high-pressure metal hydride tanks," *Journal of Alloys and Compounds*, vol. 639, pp. 452-457, 2015.

- [54] Z. Dehouche, M. Savard, F. Laurencelle, and J. Goyette, "Ti-V-Mn based alloys for hydrogen compression system," *Journal of Alloys and Compounds*, vol. 400, no. 1-2, pp. 276-280, 2005.
- [55] J. H. Jung, H. H. Lee, D. M. Kim, B. H. Liu, K. Y. Lee, and J. Y. Lee, "New activation process for Zr-Ti-Cr-Mn-V-Ni alloy electrodes: the hot-charging treatment," *Journal of Alloys and Compounds*, vol. 253-254, pp. 652-655, 1997.
- [56] S. M. Lee, S. H. Kim, S. W. Jeon, and J. Y. Lee, "Study on the electrode characteristics of hypostoichiometric Zr-Ti-V-Mn-Ni hydrogen storage alloys," *Journal of the Electrochemical Society*, vol. 147, no. 12, pp. 4464-4469, 2000.
- [57] L. Pickering, D. Reed, A. I. Bevan, and D. Book, "Ti-V-Mn based metal hydrides for hydrogen compression applications," *Journal of Alloys and Compounds*, vol. 645, pp. S400-S403, 2015.
- [58] G. Wojcik, M. Kopczyk, G. Mlynarek, W. Majchrzyckia, and M. BeltowskaBrzezinska, "Electrochemical behaviour of multi-component Zr-Ti-V-Mn-Cr-Ni alloys in alkaline solution," *Journal of Power Sources*, vol. 58, no. 1, pp. 73-78, 1996.

## Research Article

# Structural and Kinetic Hydrogen Sorption Properties of $Zr_{0.8}Ti_{0.2}Co$ Alloy Prepared by Ball Milling

Hui He,<sup>1</sup> Huaqin Kou ,<sup>2,3</sup> Wenhua Luo ,<sup>1</sup> Tao Tang,<sup>2</sup> Zhiyong Huang,<sup>2</sup> Ge Sang,<sup>2</sup> Guanghui Zhang,<sup>2</sup> Jingwen Ba,<sup>2</sup> and Meng Liu<sup>2</sup>

<sup>1</sup>Science and Technology on Surface Physics and Chemistry Laboratory, P.O. Box 9072-35, Mianyang 621908, China

<sup>2</sup>Institute of Materials, China Academy of Engineering Physics, P.O. Box 9071-12, Mianyang 621907, China

<sup>3</sup>State Key Laboratory of Silicon Materials, Zhejiang University, Hangzhou 310027, China

Correspondence should be addressed to Huaqin Kou; kouhuaqin@126.com and Wenhua Luo; luowenhua@caep.cn

Received 27 October 2017; Revised 31 December 2017; Accepted 14 January 2018; Published 12 March 2018

Academic Editor: Huaijun Lin

Copyright © 2018 Hui He et al. This is an open access article distributed under the Creative Commons Attribution License, which permits unrestricted use, distribution, and reproduction in any medium, provided the original work is properly cited.

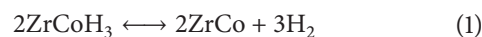
The effects of ball milling on the hydrogen sorption kinetics and microstructure of  $Zr_{0.8}Ti_{0.2}Co$  have been systematically studied. Kinetic measurements show that the hydrogenation rate and amount of  $Zr_{0.8}Ti_{0.2}Co$  decrease with increasing the ball milling time. However, the dehydrogenation rate accelerates as the ball milling time increases. Meanwhile, the disproportionation of  $Zr_{0.8}Ti_{0.2}Co$  speeds up after ball milling and the disproportionation kinetics is clearly inclined to be linear with time at 500°C. It is found from X-ray powder diffraction (XRD) results that the lattice parameter of  $Zr_{0.8}Ti_{0.2}Co$  gradually decreases from 3.164 Å to 3.153 Å when the ball milling time extends from 0 h to 8 h, which is mainly responsible for the hydrogen absorption/desorption behaviors. In addition, scanning electron microscope (SEM) images demonstrate that the morphology of  $Zr_{0.8}Ti_{0.2}Co$  has obviously changed after ball milling, which is closely related to the hydrogen absorption kinetics. Besides, high-resolution transmission electron microscopy (HRTEM) images show that a large number of disordered microstructures including amorphous regions and defects exist after ball milling, which also play an important role in hydrogen sorption performances. This work will provide some insights into the principles of how to further improve the hydrogen sorption kinetics and disproportionation property of  $Zr_{0.8}Ti_{0.2}Co$ .

## 1. Introduction

Because of the rapid decrease of fossil fuels and the increasingly serious environmental pollution in recent years, developing a clean and renewable energy has become an urgent task for mankind [1]. Under the development of ITER (International Thermonuclear Experimental Reactor), fusion energy, by burning the fuel of deuterium (D) and tritium (T) plasma, is regarded as one of the most ideal energy sources due to its huge energy release, abundant fuel resources, and low radioactivity [2–4]. In order to ensure the successful operation of fusion reactors, a viable, highly efficient, safe, and inexpensive hydrogen isotope storage method for D-T fuel is very necessary [5, 6].

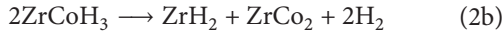
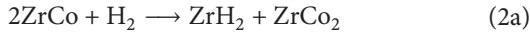
In ITER, the D-T fuel is recommended to be stored as metal deuteride and tritide because solid-state hydrogen isotopes storage offers such advantages as safety, efficiency

(higher bulk hydrogen storage density), and processing convenience over gas and liquid storage methods [7, 8]. Among several alternative hydrogen storage materials, an intermetallic compound of ZrCo is proposed as one of the most suitable candidates for tritium storage according to (1), since it possesses such excellent properties as low equilibrium hydrogen pressure and fast hydrogen absorption rate at room temperature, moderate temperature for hydrogen desorption to 100 kPa, and desirable features of safety like nonradioactivation, low pyrophoricity, and small volume expansion during hydrogen sorption cycles [9–14].



However, its serious degradation of hydrogen storage properties during the hydrogen sorption cycle obstructs its

wide application, resulting from the concomitant hydrogen-induced disproportionation reaction that happened above 573 K during hydrogen sorption process shown as follows [15–18]:



Because of the high thermodynamic stabilities of  $\text{ZrH}_2$  and  $\text{ZrCo}_2$ , the disproportionation of  $\text{ZrCo}$  will cause significant degradation of hydrogen storage properties during the practical hydrogen sorption cycles [19].

Recently, many investigations mainly focused on element substitution have been made to improve the antidisproportionation property of  $\text{ZrCo}$ , which achieved remarkable progress [20–24]. Compared with other elements, Ti has been surprisingly found to be the most effective substitution element for improving the antidisproportionation property so far. Huang et al. [25] found that the equilibrium hydrogen desorption pressure of  $\text{Zr}_{1-x}\text{Ti}_x\text{Co}$  alloy increases along with increasing Ti content. In the meantime, hydrogen sorption cycles do not produce separated  $\text{ZrCo}$ ,  $\text{TiCo}$ , and  $\text{ZrH}_2$ , suggesting that the antidisproportionation property of  $\text{ZrCo}$  alloy is improved by Ti substitution. Zhao et al. also confirmed that partial substitution of Ti for Zr will significantly enhance the antidisproportionation property of  $\text{ZrCo}$  [26, 27]. Zhang et al. [28] systematically compared the effects of Ti substitution on the disproportionation behaviors of  $\text{ZrCo}$  with Sc, Ni, and Fe elements. It was observed that Ti has superior effect on suppressing the disproportionation of  $\text{ZrCo}$ . Similar result was proved by Kou et al. who reported that  $\text{Zr}_{0.8}\text{Ti}_{0.2}\text{Co}$  bed had better durability against disproportionation than  $\text{ZrCo}$  bed and  $\text{Zr}_{0.8}\text{Hf}_{0.2}\text{Co}$  bed [29]. Meanwhile, Jat et al. [30] further investigated the influences of Ti amount on the disproportionation rate of  $\text{Zr}_{1-x}\text{Ti}_x\text{Co}$  alloy and found the disproportionation decreases in order of  $\text{ZrCo} > \text{Zr}_{0.9}\text{Ti}_{0.1}\text{Co} > \text{Zr}_{0.7}\text{Ti}_{0.3}\text{Co} > \text{Zr}_{0.8}\text{Ti}_{0.2}\text{Co}$ .

Although it seems that Ti-substituted  $\text{ZrCo}$  alloy possesses the improved antidisproportionation property, the requirements of practical application still cannot be completely satisfied due to its stagnant hydrogen sorption kinetics. Zhao et al. [26] reported that the hydrogen absorption amount and rate of  $\text{ZrCo}$  decrease with the Ti content increasing. Moreover, Shmayda et al. [31] and Yoo et al. [32] showed that the kinetic response of  $\text{ZrCo}$  for hydrogen sorption is slower than uranium, which restricts the application of  $\text{ZrCo}$  alloy. Therefore, it is of great necessity to further enhance the hydrogen sorption kinetics of Ti-substituted  $\text{ZrCo}$  alloy.

It has extensively shown that mechanical ball milling is an effective technique for improving the kinetic property of hydrogen storage materials [33–36]. However, the effects of ball milling on the hydrogen sorption kinetics and microstructure of  $\text{ZrCo}$ -based alloy have never been investigated. In this paper, we focused on the effects of ball milling on microstructure and kinetic hydrogen sorption properties of  $\text{Zr}_{0.8}\text{Ti}_{0.2}\text{Co}$  alloy. Furthermore, because study of kinetics is clearly beneficial to understanding of mechanism about hydrogen sorption process [20, 37, 38], kinetic analysis has

also been carried out for disproportionation of  $\text{Zr}_{0.8}\text{Ti}_{0.2}\text{Co}$  in this work.

## 2. Experimental

**2.1. Sample Preparation and Kinetic Measurements.**  $\text{Zr}_{0.8}\text{Ti}_{0.2}\text{Co}$  powder with particle size of 2~4 mm was purchased from the General Research Institute for Nonferrous Metals (Beijing, China). The hydrogen sorption behaviors of the samples were investigated by a Sievert type apparatus. The detailed activation procedures of  $\text{Zr}_{0.8}\text{Ti}_{0.2}\text{Co}$  were performed according to [39]. The samples were prepared by ball milling of  $\text{Zr}_{0.8}\text{Ti}_{0.2}\text{Co}$  powder using a planetary mill at 400 rpm for different time. After ball milling, the samples were firstly evacuated at 500°C, and then the hydrogen absorption measurements of samples were conducted at 100°C under 0.8 bar  $\text{H}_2$ . For each time, about 1 g sample was loaded in the reactor of the apparatus, and hydrogen pressure reduction of ~0.2 bar was achieved for hydrogenation. After hydrogenation, the hydrogen in the reactor was evacuated and then the dehydrogenation measurements of samples were carried out from room temperature to 500°C with heating rate of 5°C/min. After that, the isothermal disproportionation kinetics was examined at 500°C for more than 500 min. The change of hydrogen pressure ( $P$ ) as a function of time was recorded from room temperature to the end of the isothermal period. During the whole dehydrogenation process, the initial hydrogen pressure was recorded as  $P_0$  and the maximum addition of hydrogen pressure was denoted as  $P_{\text{max}}$ . As a result, the hydrogen desorption and disproportionation of the sample were quantified by formula as  $(P - P_0)/P_{\text{max}}$ .

**2.2. Structural Characterizations.** X-ray powder diffraction (XRD) method was used to characterize the crystal structures of  $\text{Zr}_{0.8}\text{Ti}_{0.2}\text{Co}$  samples at different states on a DX2700B diffractometer with  $\text{Cu K}_\alpha$  radiation, 40 kV, and 30 mA. The XRD patterns were recorded in steps of 0.02° ( $2\theta$ ) from 20° to 90° with a constant scanning rate of 0.6 s per step. For Rietveld refinement of lattice parameters, special XRD data was obtained by scanning rate of 1.8 s per step.

The morphology of the samples was studied by scanning electron microscope (SEM, Ultra55, CARL ZEISSNTS GmbH) and the compositional analysis on surface was carried out using energy dispersive X-ray spectroscopy (EDS, Inca). Morphological observation inside the particle was carried out by Helios Nanolab 600i Focused Ion Beam (FIB) using beam energy of 20 keV and a beam current of 2.8 nA. The microstructure of the samples was investigated using high-resolution transmission electron microscopy (HRTEM, Libra 200, CARL ZEISS IRTS) with an accelerating voltage of 200 kV.

## 3. Results and Discussion

**3.1. Hydrogen Absorption/Desorption Kinetics.** Figure 1 represents the XRD patterns of activated  $\text{Zr}_{0.8}\text{Ti}_{0.2}\text{Co}$  samples after ball milling for different time. It can be found that  $\text{Zr}_{0.8}\text{Ti}_{0.2}\text{Co}$  samples still keep  $\text{ZrCo}$  phase except for trace

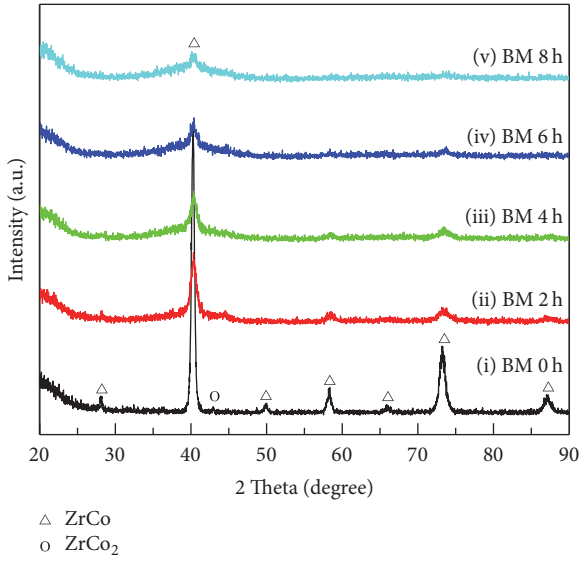


FIGURE 1: XRD patterns of the activated  $Zr_{0.8}Ti_{0.2}Co$  samples after ball milling for different time. (i) 0 h; (ii) 2 h; (iii) 4 h; (iv) 6 h; (v) 8 h.

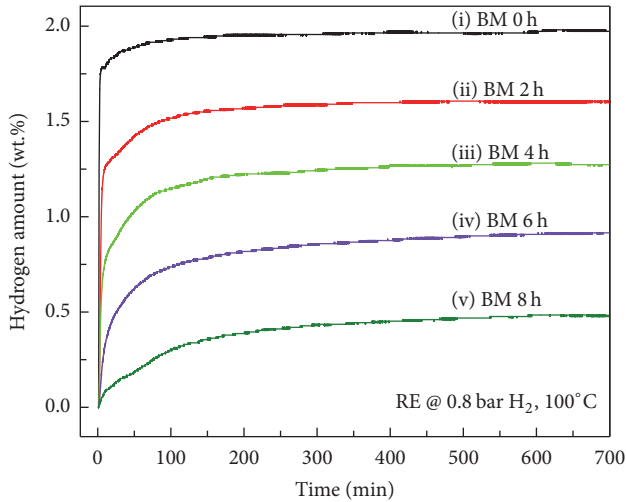


FIGURE 2: Hydrogen absorption curves of  $Zr_{0.8}Ti_{0.2}Co$  samples under 0.8 bar  $H_2$  at  $100^\circ C$  after ball milling for different time. (i) 0 h; (ii) 2 h; (iii) 4 h; (iv) 6 h; (v) 8 h.

amount of  $ZrCo_2$  phase, which is identical with previous researches [26, 27]. Meanwhile, it is clear that the intensities of  $ZrCo$  diffraction peaks decrease and the peaks exhibit broadened characteristics with increasing ball milling time. It is suggested that the crystalline structure of  $ZrCo$  phase may be damaged and the average grain size of samples should decrease during the ball milling process [40].

The hydrogen absorption curves of  $Zr_{0.8}Ti_{0.2}Co$  samples after ball milling for different time are displayed in Figure 2. Since the disproportionation reactions of  $ZrCo$  alloy shown as (2a) and (2b) usually take place at high temperature, the curves in Figure 2 should represent the hydrogenation reaction shown as (1). Obviously, the hydrogen absorption

amount decreases with increasing ball milling time. The hydrogenation amount reaches 1.97 wt.% for the sample without ball milling, whereas the total hydrogen amount of only 0.50 wt.% can be obtained for the sample ball milled for 8 h. Meanwhile, the hydrogen absorption rate also exhibits a tendency to slow down after ball milling.

The dehydrogenation curves of ball milled  $Zr_{0.8}Ti_{0.2}Co$  samples after hydrogenation are shown in Figure 3. According to (2a) and (2b), the disproportionation reaction displayed by (2b) only happens under high hydrogen pressure. However, the hydrogen pressure is lower than 1 bar in this study. Therefore, the disproportionation of  $Zr_{0.8}Ti_{0.2}Co$  sample only takes place according to (2a) in this work, which causes the reduction in hydrogen pressure. As a result, the whole hydrogen desorption curve in Figure 3 can be divided into two stages, respectively, belonging to the temperature programmed dehydrogenation process (Figure 3(b)) and the disproportionation process (Figure 3(c)). It can be observed from the first stage that the hydrogen desorption rate is enhanced with increasing ball milling time, which is beneficial to practical application of  $ZrCo$ -based alloy. The second stage substantially represents an isothermal disproportionation process at  $500^\circ C$ . It can be seen that the disproportionation extent is very slight and the disproportionation rate is slow for all samples at  $500^\circ C$ , which is very close to the result reported by Zhang et al. [28]. Nevertheless, it is readily discernible that the disproportionation rate and extent monotonously grow with increasing ball milling time. These results suggest that not only the dehydrogenation rate but also the disproportionation rate of  $Zr_{0.8}Ti_{0.2}Co$  can be quickened by ball milling, the mechanism of which will be specifically discussed below.

Figure 4 demonstrates XRD patterns of the ball milled  $Zr_{0.8}Ti_{0.2}Co$  samples after disproportionation shown in Figure 3. It can be seen that the diffraction peaks corresponding to  $ZrCo$  phase are clearly present in all samples, though the intensity of  $ZrCo$  peaks decreases slightly with increasing ball milling time. The existence of major phase of  $ZrCo$  illustrates that the dehydrogenation mainly proceeds according to (1). In addition, the weak diffraction peaks of disproportionation products including  $ZrH_2$  and  $ZrCo_2$  can be carefully observed, indicating the disproportionation extent of  $Zr_{0.8}Ti_{0.2}Co$  sample should be small. The intensity of diffraction peaks for  $ZrH_2$  and  $ZrCo_2$  is well in agreement with the disproportionation behaviors displayed in Figure 3, which shows minor reduction in hydrogen pressure.

### 3.2. Structural Characterization and Kinetic Mechanism.

From the results above, it can be found that the hydrogen desorption kinetics and disproportionation kinetics of  $Zr_{0.8}Ti_{0.2}Co$  become faster, while the hydrogenation kinetics is restrained by ball milling. To comprehend these kinetic behaviors, detailed structural characterizations were performed. Firstly, the phase structure variation after ball milling has been investigated. To determine the lattice parameters of  $Zr_{0.8}Ti_{0.2}Co$  samples as accurately as possible, special XRD experiments have been performed to obtain strong diffraction signal by increasing the scanning time. According to the XRD results, the lattice parameters of the samples have been calculated by Rietveld refinement of XRD data via Jade

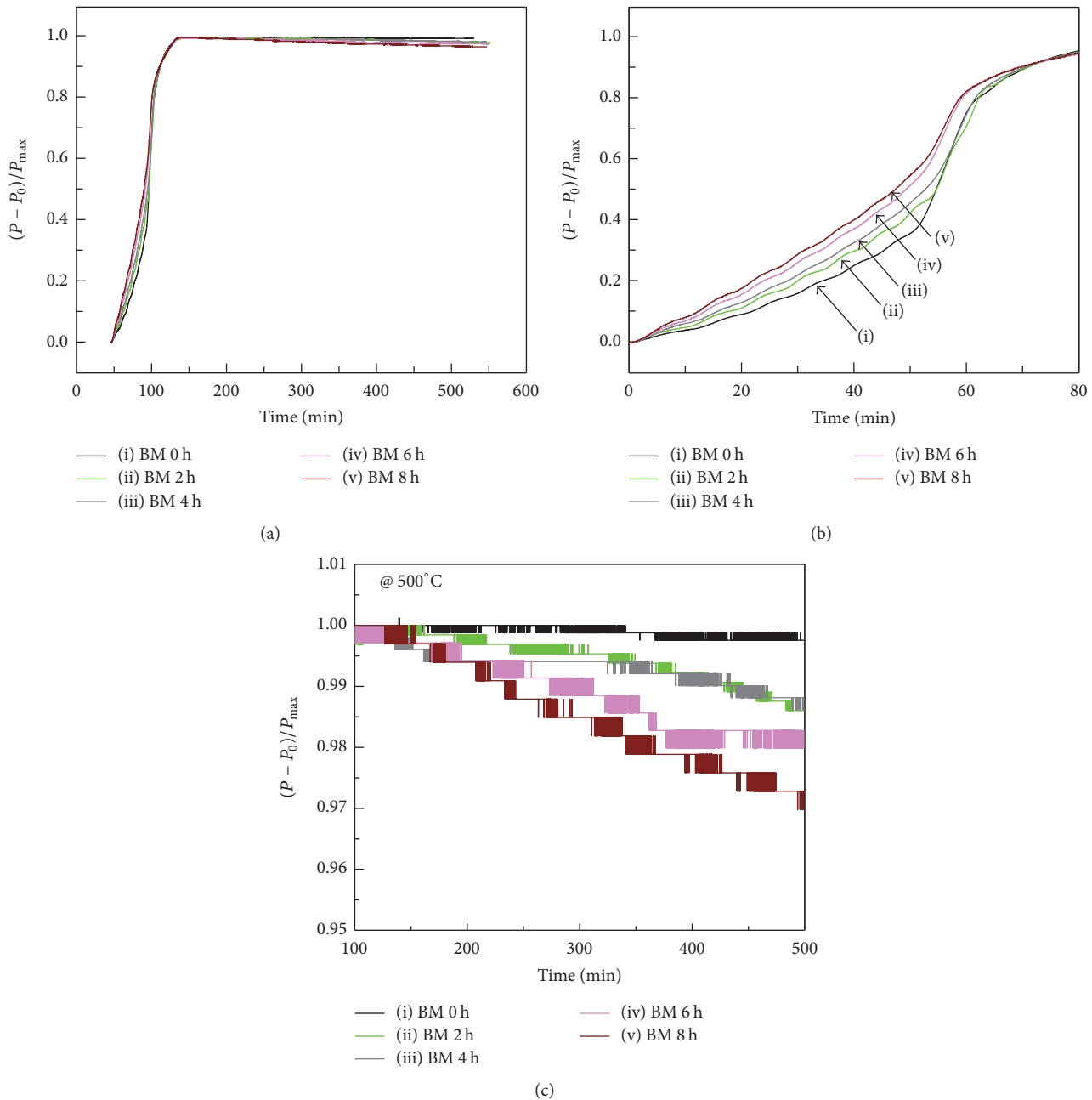


FIGURE 3: Dehydrogenation curves (a), enlarged dehydrogenation curves (b), and enlarged disproportionation curves (c) of  $Zr_{0.8}Ti_{0.2}Co$  samples ball milled for different time. (i) 0 h; (ii) 2 h; (iii) 4 h; (iv) 6 h; (v) 8 h.

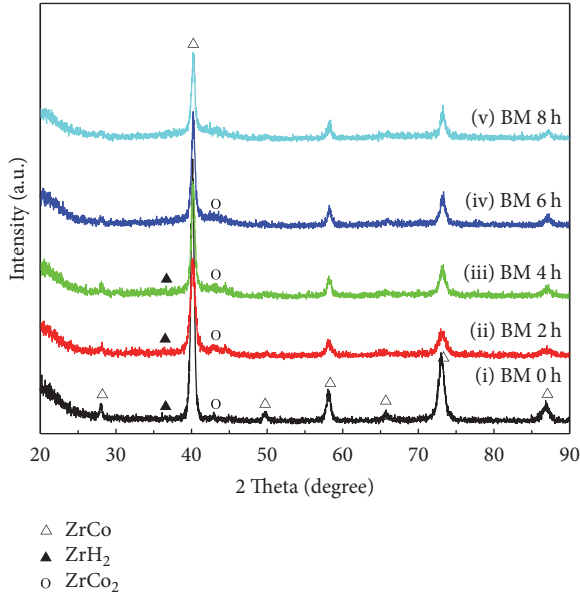
6.0 software. The representative Rietveld refinement pattern of  $Zr_{0.8}Ti_{0.2}Co$  sample is shown in Figure 5. The refinement result shows that the crystal structure of  $Zr_{0.8}Ti_{0.2}Co$  sample without ball milling is CsCl-type cubic (bcc) with lattice parameter  $a = 3.1638 \text{ \AA}$ , which is in good agreement with other study [28]. According to the specific Rietveld refinement results as displayed in Table 1, the lattice parameter and cell volume of  $Zr_{0.8}Ti_{0.2}Co$  sample slightly and continuously decrease with increasing ball milling time, which may be probably attributed to cumulative plastic deformation and microstrain in the crystal lattice during the ball milling

process [33, 40]. In view of the variation of lattice parameter, it is easy to understand the kinetic performances of  $Zr_{0.8}Ti_{0.2}Co$  after ball milling. When the lattice parameter and cell volume become smaller, the occupancy of H atom in interstitial sites will become more difficult but release of H atom from interstitial sites will be easier [41]. Hence, it is observed that hydrogen absorption kinetics decreases but hydrogen desorption kinetics increases for  $Zr_{0.8}Ti_{0.2}Co$  with increasing ball milling time.

To investigate the morphologies of ball milled  $Zr_{0.8}Ti_{0.2}Co$  samples, SEM analysis has been performed and

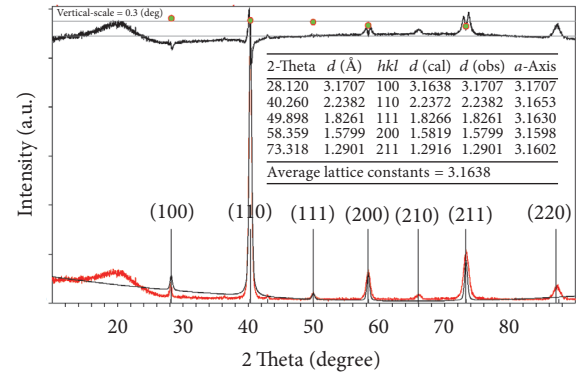
TABLE 1: Rietveld refinement results of XRD patterns of  $Zr_{0.8}Ti_{0.2}Co$  samples after ball milling for different time.

System	Ball milling time/hour	Space group	Lattice parameters of major constituent phase (ZrCo phase)/Å	Cell volume of major constituent phase (ZrCo phase)/Å <sup>3</sup>
ZrCo [13]	0	<i>Pm-3m</i>	3.1957	32.64
	0		3.1638	31.67
	2		3.1587	31.55
$Zr_{0.8}Ti_{0.2}Co$	4	<i>Pm-3m</i>	3.1574	31.48
	6		3.1555	31.42
	8		3.1534	31.35

FIGURE 4: XRD patterns of the ball milled  $Zr_{0.8}Ti_{0.2}Co$  samples after disproportionation. (i) 0 h; (ii) 2 h; (iii) 4 h; (iv) 6 h; (v) 8 h.

the results are shown in Figure 6. After ball milling, the morphologies of  $Zr_{0.8}Ti_{0.2}Co$  sample tend to be small particles from initial chip. Meanwhile, the particle size gradually decreases with increasing the ball milling time. Besides, as the ball milling time increases, the agglomeration of particles is distinctly reduced and the particles become more dispersive.

Furthermore, in order to closely observe the surface of the samples, the SEM images of the ball milled  $Zr_{0.8}Ti_{0.2}Co$  samples at magnification of 10000x were obtained, as shown in Figure 7. A lot of chips and sharp edges are observed for the sample without ball milling. However, the sharp edges can hardly be observed on the surface of ball milled  $Zr_{0.8}Ti_{0.2}Co$  sample, which should be caused by deformation and compaction during the ball milling process. It is well known that the edges are apt to break off and fresh surface will emerge in the process of hydrogenation [42, 43], which is beneficial to enhancement of hydrogen absorption. Moreover, as a direct and fast diffusion path of hydrogen, the edges are also beneficial to fast hydrogen absorption [44]. Hence, the change in morphology is mainly responsible for the decrease

FIGURE 5: Rietveld refinement of X-ray diffraction pattern of  $Zr_{0.8}Ti_{0.2}Co$  sample without ball milling.

of hydrogen absorption kinetics for  $Zr_{0.8}Ti_{0.2}Co$  samples after ball milling.

In order to analyze the composition of the sample surface, two representative EDS spectrums of every sample over the surface were obtained, as shown in Figure 8. The detailed elemental contents for every sample are listed in Table 2. It is interesting to discover that the existence of Fe element on the surface of particles is detected for all ball milled  $Zr_{0.8}Ti_{0.2}Co$  samples. This suggests that the Fe element may be brought by steel milling vessel and balls during the ball milling process [38]. It has been reported that the disproportionation of ZrCo will be accelerated after doping Fe [22, 28]. Hence, it is reasonable to believe that faster disproportionation rate of ball milled  $Zr_{0.8}Ti_{0.2}Co$  samples has direct correlation with the introduced Fe element on the surface of particles. Besides, it can be found that the average atom ratio of  $(Zr + Ti)/(Co + Fe)$  for the selected regions decreases gradually from 0.89 to 0.66 when the ball milling time extends from 0 h to 8 h. As previous studies proved, when the average atom ratio of Zr:Co is much closer to 0.5 (1:2), the elemental recombination of  $ZrCo_2$  phase will be facilitated during the disproportionation process [45, 46]. Consequently, disproportionation of ZrCo is aggravated. Due to the analogical feature of group element, the substitution element of Ti and introduced Fe can, respectively, be included in Zr and Co. As a result, the gradual decrease of  $(Zr + Ti)/(Co + Fe)$  from 0.89 to 0.66 may be another reason that aggravates the disproportionation of  $Zr_{0.8}Ti_{0.2}Co$  sample by increasing ball milling time, as shown in Figure 3.

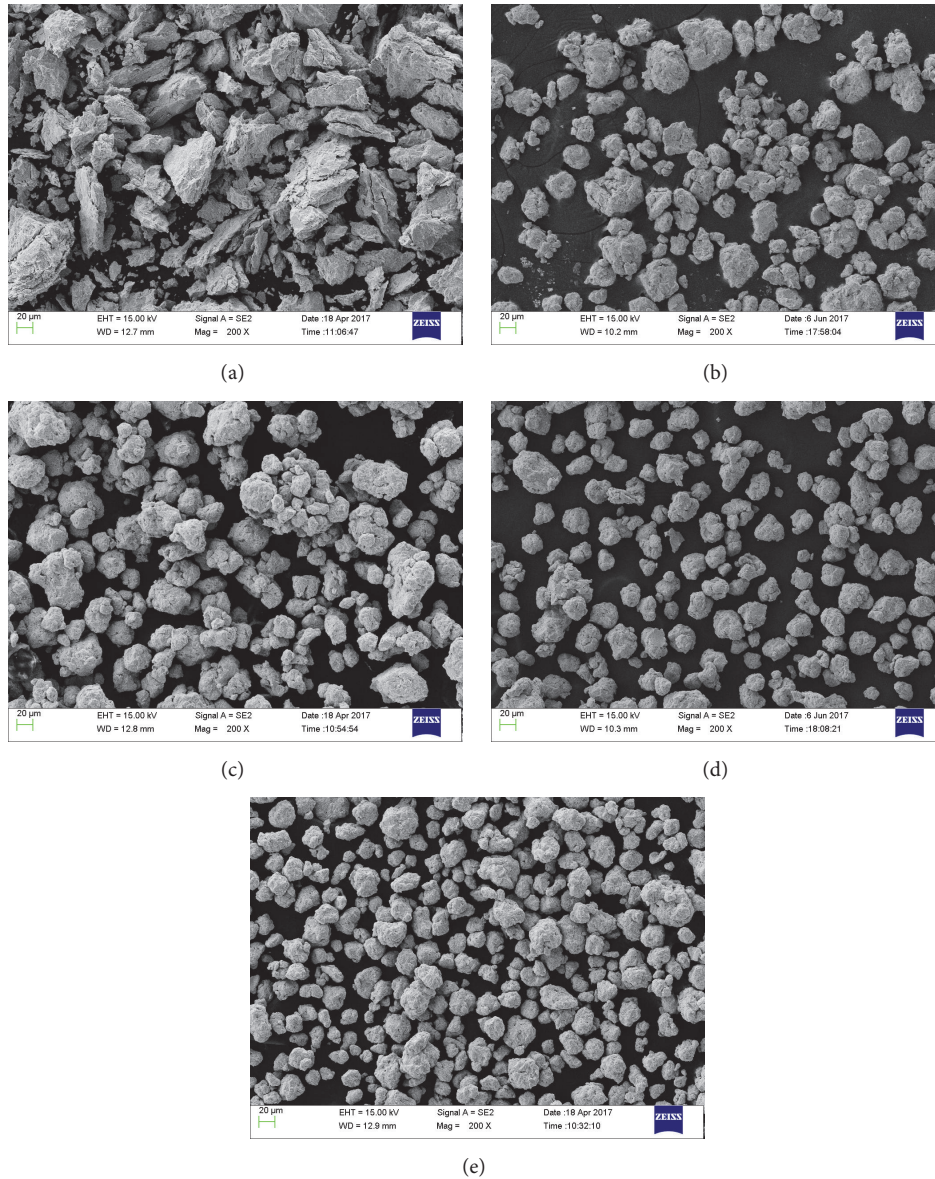


FIGURE 6: SEM images of the  $Zr_{0.8}Ti_{0.2}Co$  samples ball milled for different time. (a) 0 h; (b) 2 h; (c) 4 h; (d) 6 h; (e) 8 h.

In order to further characterize the microstructure, the TEM analysis for  $Zr_{0.8}Ti_{0.2}Co$  samples ball milled for 8 h has been employed and the results are shown in Figure 9. Figures 9(b) and 9(c), respectively, show enlarged TEM images and corresponding SAED patterns of zones 1 and 2 in Figure 9(a). It can be found from the SAED patterns that the  $Zr_{0.8}Ti_{0.2}Co$  particle ball milled for 8 h is comprised of not only polycrystalline regions but also a number of amorphous regions. In accordance with PDF number 030657272, the interplanar distances of 0.218 nm, 0.218 nm, and 0.219 nm in Figure 9(b) all correspond to  $\{110\}$  planes of  $Zr_{0.8}Ti_{0.2}Co$ . According to Figure 5, the interplanar distance of  $\{110\}$  should be 0.224 nm for  $Zr_{0.8}Ti_{0.2}Co$  sample without ball milling. It is clear that the interplanar distance of  $\{110\}$  has been shortened to be about 0.218 nm after ball milling for 8 h. It is suggested that

the lattice parameter of  $Zr_{0.8}Ti_{0.2}Co$  sample was decreased after ball milling, which is in good agreement with the Rietveld refinement results of XRD. Moreover, a number of amorphous regions (over yellow line) are clearly observed in Figure 9(c). Meanwhile, a large number of defects including dislocations and grain boundaries (around green line) are widely observed, which provide a possible explanation for the broadened XRD patterns shown in Figure 1. As well known, these disordered microstructures mentioned above are favorable for H atom diffusion instead of occupation [38, 47]. Therefore, the reduction of the hydrogenation amount and enhancement of the dehydrogenation rate for ball milled  $Zr_{0.8}Ti_{0.2}Co$  samples are probably resulting from the disordered microstructures produced during the ball milling process.

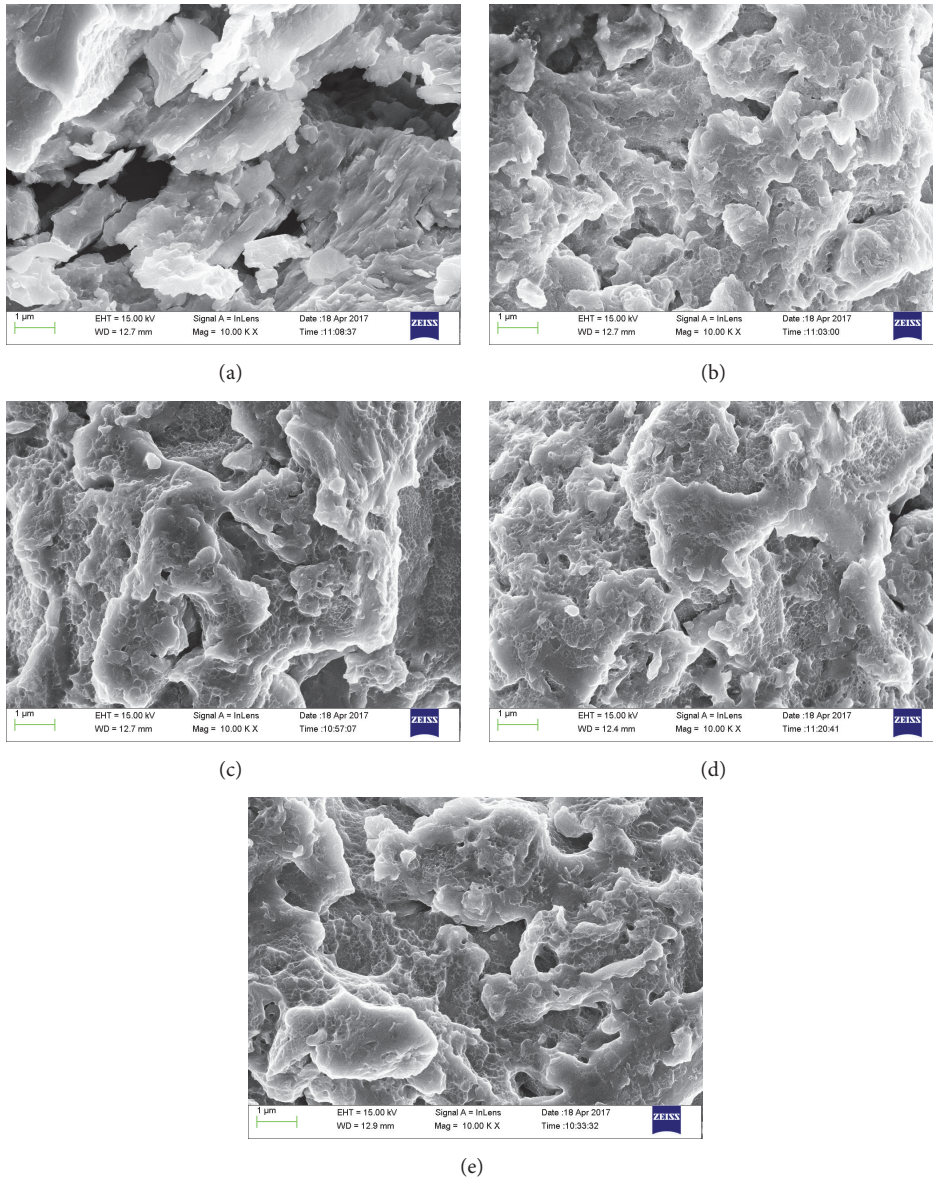
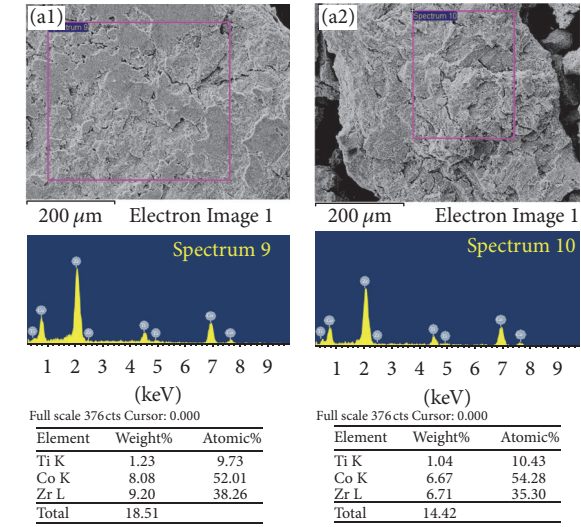


FIGURE 7: SEM images of the  $Zr_{0.8}Ti_{0.2}Co$  samples after ball milling for different time at magnification of 10000x. (a) 0 h; (b) 2 h; (c) 4 h; (d) 6 h; (e) 8 h.

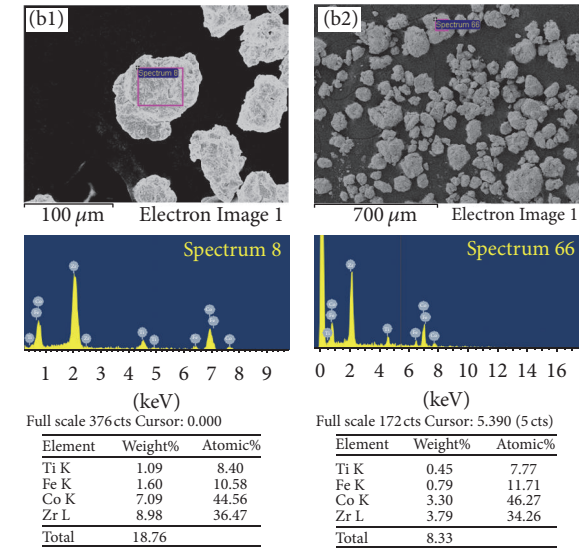
**3.3. Kinetic Model Analysis.** In order to further understand the disproportionation kinetic mechanism, the kinetic analysis of disproportionation has been performed for ball milled  $Zr_{0.8}Ti_{0.2}Co$ . Usually, the relationship between the reacted fraction and reaction time is linear for surface reaction controlled step [48, 49]. According to Figure 3, it can be found that the disproportionation curves of all  $Zr_{0.8}Ti_{0.2}Co$  samples should just represent the initial stage of whole disproportionation and the reaction equilibrium has not been reached within 450 min at  $500^{\circ}C$ . Moreover, the disproportionation kinetics of all  $Zr_{0.8}Ti_{0.2}Co$  samples in this stage is clearly inclined to be linear. Thus, the isothermal disproportionation data of  $Zr_{0.8}Ti_{0.2}Co$  sample after ball milling for different time has been linearly fitted, as shown in Figure 10. It can be seen from the fitting results that the disproportionation kinetics of

$Zr_{0.8}Ti_{0.2}Co$  samples is much closer to linear with increasing the ball milling time. Meanwhile, the slope of fitted line is slightly decreased, corresponding to the slight aggravation of disproportionation rate. The well-fitted linear results suggest that the disproportionation stage of  $Zr_{0.8}Ti_{0.2}Co$  samples curved by Figure 3 should be a surface reaction controlled step.

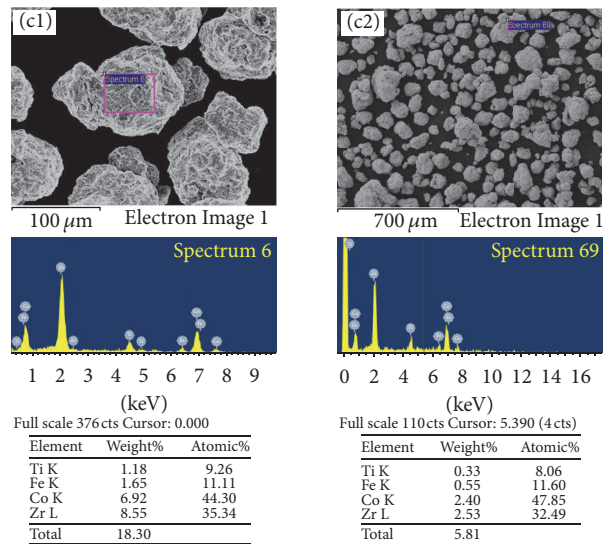
Based on the results of microstructure and kinetic analysis above, some useful insights can be obtained into the mechanism of hydrogen sorption reaction and disproportionation reaction for ball milled  $Zr_{0.8}Ti_{0.2}Co$  samples. The effects of ball milling on the hydrogen sorption and disproportionation behaviors of  $Zr_{0.8}Ti_{0.2}Co$  sample can be deduced from the changed microstructure including lattice parameter, morphology, elemental composition, and crystal defects. For



(a)



(b)



(c)

FIGURE 8: Continued.

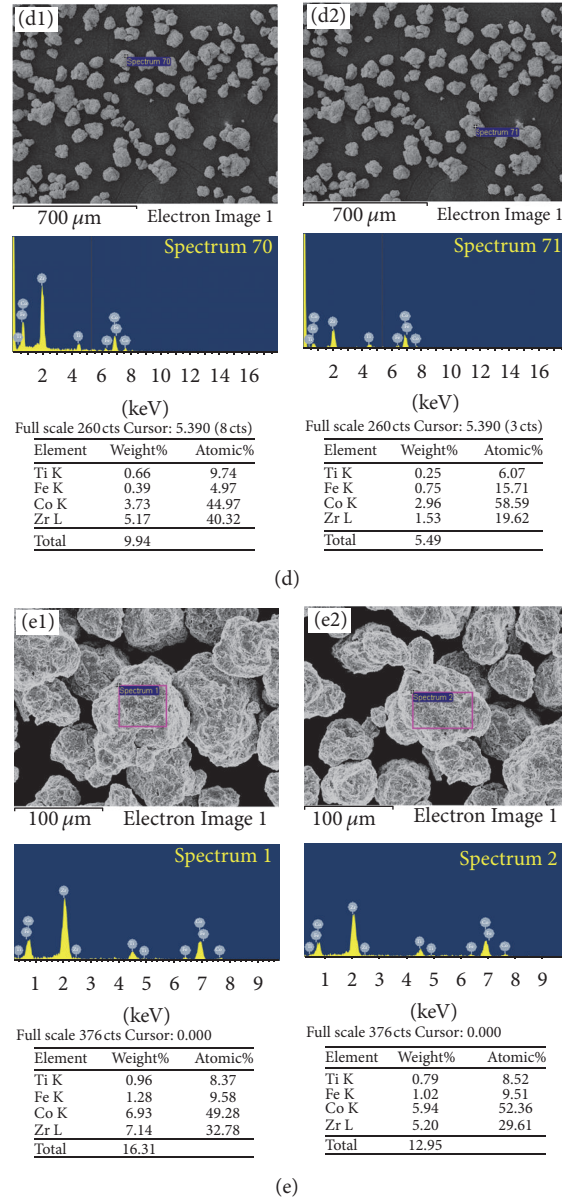


FIGURE 8: EDS results of the  $\text{Zr}_{0.8}\text{Ti}_{0.2}\text{Co}$  samples after ball milling for different time. (a) 0 h; (b) 2 h; (c) 4 h; (d) 6 h; (e) 8 h.

hydrogen sorption reaction, it can be found that ball milling shows negative effect on the hydrogen absorption rate of  $\text{Zr}_{0.8}\text{Ti}_{0.2}\text{Co}$  sample, which is different from the commonly positive effects of ball milling on hydrogen storage materials in many studies. The negative effects of ball milling may be resulting from three aspects: (1) the decreased cell volume makes the entering of hydrogen atom into interstitial site in lattice more difficult; (2) the missing sharp edges of particles cut the paths for fast transfer of hydrogen; (3) the increased disorderliness of microstructure goes against the occupation of hydrogen. As a result, it was observed that the hydrogen absorption rate and amount of  $\text{Zr}_{0.8}\text{Ti}_{0.2}\text{Co}$  sample were decreased by increasing ball milling. On the other hand, it can be found that the ball milling plays a positive role in hydrogen desorption rate. The positive effects of ball milling

may be derived from three points: (1) the decreased cell volume results in the fact that H atoms begin to be less-stable in the crystal lattice and are inclined to leave from crystal interstitial sites; (2) the introduced Fe on the surface may act as catalysts for hydrogen dissociation [50]; (3) the produced lattice defects like dislocations and grain boundaries possibly act as a pathway for hydrogen transportation during dehydrogenation [51, 52]. Consequently, it was seen that the hydrogen desorption rate was increased by ball milling.

For disproportionation reaction, it is found the disproportionation rate of  $\text{Zr}_{0.8}\text{Ti}_{0.2}\text{Co}$  sample was exacerbated by ball milling. According to the kinetic analysis, the disproportionation stage of  $\text{Zr}_{0.8}\text{Ti}_{0.2}\text{Co}$  in this work should be a surface reaction controlled step, indicating that the surface state is very important for the disproportionation.

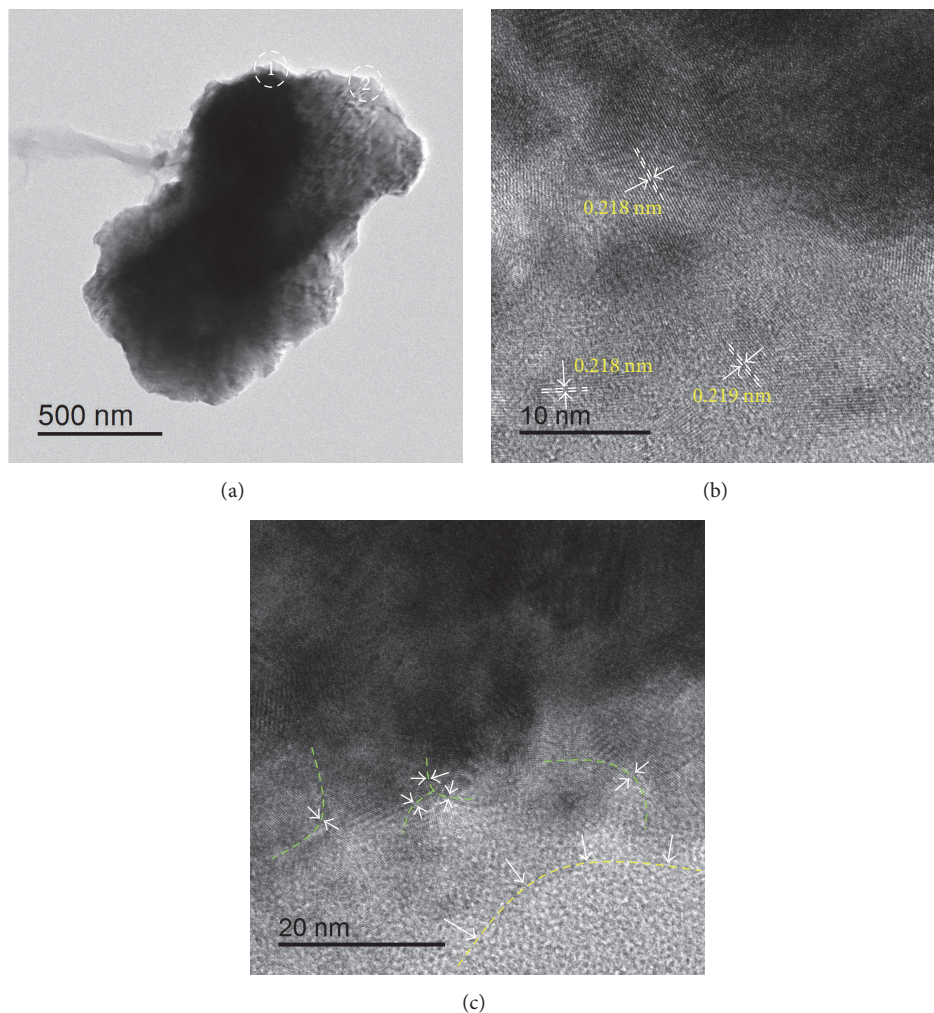


FIGURE 9: TEM analysis of  $Zr_{0.8}Ti_{0.2}Co$  sample for ball milled for 8 h. (a) Low-magnification image of particle; (b) high-resolution image of peripheral zone 1 in (a); (c) high-resolution image of peripheral zone 2 in (a).

TABLE 2: EDS results of elemental composition for selected regions of  $Zr_{0.8}Ti_{0.2}Co$  samples after ball milling for different time.

ZrCo samples	Selected region	Zr (atomic%)	Ti (atomic%)	Co (atomic%)	Fe (atomic%)	(Zr + Ti)/(Co + Fe)
BM 0 h	1#	38.26	9.73	52.01		
	2#	38.49	7.48	54.04		
	Average	38.38	8.61	53.03		0.89
BM 2 h	1#	36.47	8.40	44.56	10.58	
	2#	34.26	7.77	46.27	11.71	
	Average	35.37	8.09	45.42	11.15	0.77
BM 4 h	1#	35.34	9.26	44.3	11.11	
	2#	32.49	8.06	47.85	11.60	
	Average	33.92	8.66	46.08	11.36	0.74
BM 6 h	1#	37.43	8.71	45.97	7.90	
	2#	28.83	7.2	56.89	7.08	
	Average	33.13	7.96	51.43	7.49	0.70
BM 8 h	1#	32.78	8.37	49.28	9.58	
	2#	29.61	8.52	52.36	9.51	
	Average	31.20	8.45	50.82	9.55	0.66

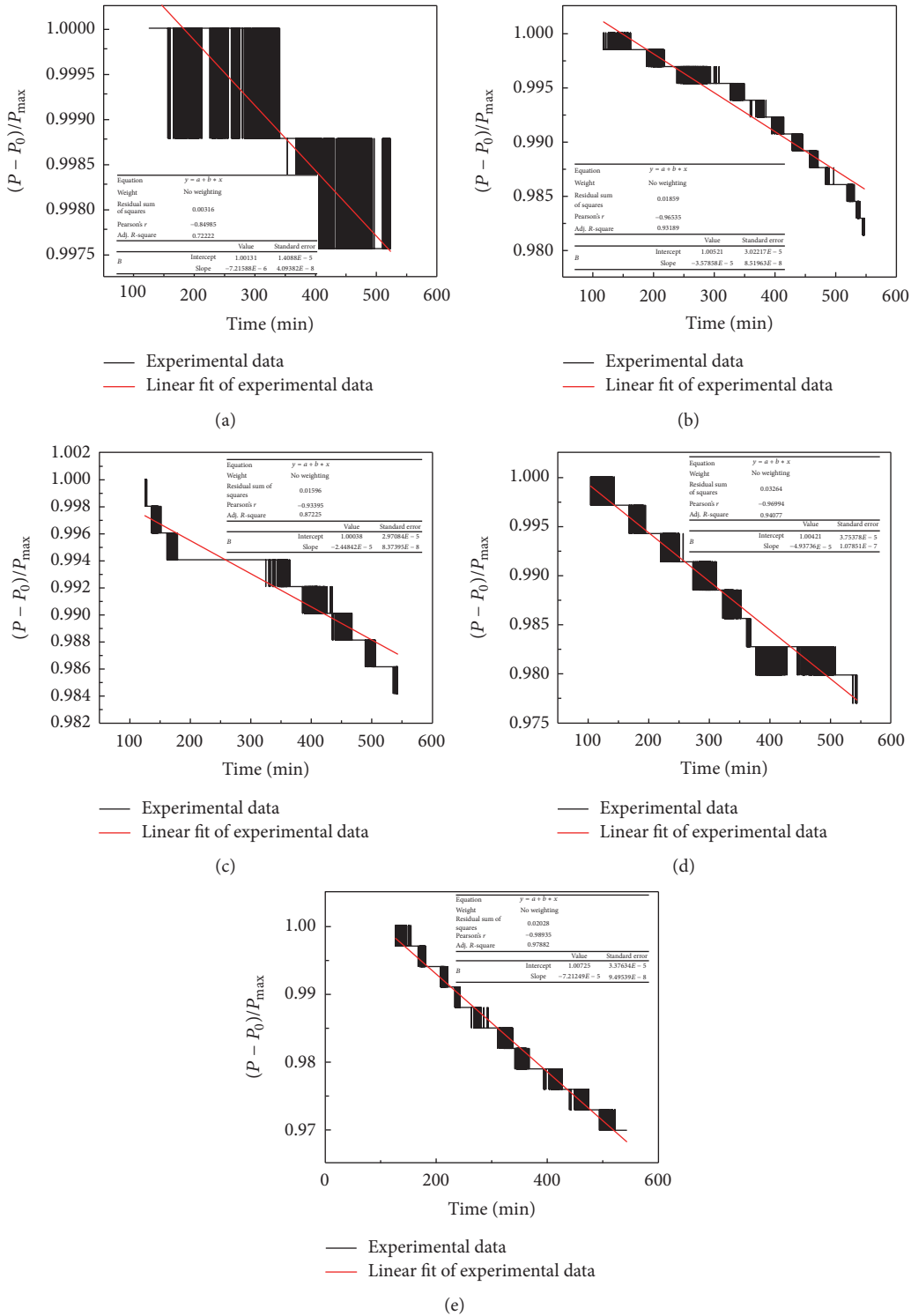


FIGURE 10: The linear fitting results of disproportionation kinetics for  $Zr_{0.8}Ti_{0.2}Co$  samples after ball milling for different time. (a) 0 h; (b) 2 h; (c) 4 h; (d) 6 h; (e) 8 h.

As mentioned in the analysis of EDS results, Fe element was introduced during the ball milling process on the surface of  $Zr_{0.8}Ti_{0.2}Co$  particles, resulting in the gradual decrease of  $(Zr + Ti)/(Co + Fe)$ . This possibly facilitates the elemental recombination of  $ZrCo_2$  phase. So, it is observed that the ball

milled  $Zr_{0.8}Ti_{0.2}Co$  owns faster disproportionation kinetics. On the other hand, it is found from the microstructure that considerable crystal defects and strain energy were formed after ball milling, especially on the surface. It is well known that the crystal defects and strain energy will

facilitate the transfer process of hydrogen atoms during hydrogen sorption reaction, which may be also beneficial for promoting the transfer of hydrogen atom from ZrCo to form ZrH<sub>2</sub>. Consequently, it is observed that the rate of the initial disproportionation stage for Zr<sub>0.8</sub>Ti<sub>0.2</sub>Co is enhanced by ball milling. In conclusion, if Zr<sub>0.8</sub>Ti<sub>0.2</sub>Co is expected to not only own fast hydrogen sorption kinetics but also have good antidisproportionation, it may be a good way to prepare Zr<sub>0.8</sub>Ti<sub>0.2</sub>Co as fine powder with smaller lattice parameter, uniform element distribution, and orderly microstructure and without impurity.

#### 4. Conclusion

In summary, the effects of ball milling on the hydrogen sorption properties and microstructure of Zr<sub>0.8</sub>Ti<sub>0.2</sub>Co have been investigated systematically. Experimental results show that hydrogen absorption kinetics of Zr<sub>0.8</sub>Ti<sub>0.2</sub>Co decreases and the hydrogen desorption kinetics accelerates with increasing the ball milling time. Meanwhile, the disproportionation rate of Zr<sub>0.8</sub>Ti<sub>0.2</sub>Co is aggravated after ball milling. Characterizations of microstructure reveal that the variation of hydrogen sorption kinetics for Zr<sub>0.8</sub>Ti<sub>0.2</sub>Co after ball milling is mainly resulting from the changed microstructure including lattice parameter, morphology, elemental composition, and crystal defects. Kinetic analysis reveals that the initial stage of disproportionation for Zr<sub>0.8</sub>Ti<sub>0.2</sub>Co is a surface step controlled reaction. And the slight aggravation of disproportionation rate may be attributed to the introduced Fe on the surface of particles and the crystal defects together with strain energy after ball milling.

#### Conflicts of Interest

The authors declare that they have no conflicts of interest.

#### Acknowledgments

This work was financially supported by the Foundation of President of China Academy of Engineering Physics (no. YZJJLX2017008), Development Foundation of China Academy of Engineering Physics for Science and Technology (no. 2015B0302067), National Magnetic Confinement Fusion Science Program of China, Open Project of State Key Laboratory of Silicon Materials (SKL2016-10), and National Natural Science Foundation of China (nos. 21573200, 21601165, and 51731002). The authors would like to thank Mr. Weidong Liu and Ms. Ping Zhao for their assistance in experiments and Dr. Huan Wang for fruitful discussions.

#### References

- [1] H. Lund, "Renewable energy strategies for sustainable development," *Energy*, vol. 32, no. 6, pp. 912–919, 2007.
- [2] J. Ongena, R. Koch, R. Wolf, and H. Zohm, "Magnetic-confinement fusion," *Nature Physics*, vol. 12, no. 5, pp. 398–410, 2016.
- [3] D. Clery, "Private fusion machines aim to beat massive global effort," *Science*, vol. 356, no. 6336, pp. 360–361, 2017.
- [4] W. Wayt Gibbs, "Fusion reactor fuels up with bomb ingredient," *Science*, vol. 354, no. 6313, pp. 690–691, 2016.
- [5] N. Holtkamp, "An overview of the ITER project," *Fusion Engineering and Design*, vol. 82, no. 5–14, pp. 427–434, 2007.
- [6] M. Glugla, R. Lässer, L. Dörr, D. K. Murdoch, R. Haange, and H. Yoshida, "The inner deuterium/tritium fuel cycle of ITER," *Fusion Engineering and Design*, vol. 69, no. 1–4, pp. 39–43, 2003.
- [7] R. Bhattacharyya and S. Mohan, "Solid state storage of hydrogen and its isotopes: an engineering overview," *Renewable & Sustainable Energy Reviews*, vol. 41, pp. 872–883, 2015.
- [8] L. Schlapbach and A. Züttel, "Hydrogen-storage materials for mobile applications," *Nature*, vol. 414, no. 6861, pp. 353–358, 2001.
- [9] M. Glugla, D. K. Murdoch, A. Antipenkov et al., "ITER fuel cycle R&D: Consequences for the design," *Fusion Engineering and Design*, vol. 81, pp. 733–744, 2006.
- [10] Z. Zhu, B. Nie, and D. Chen, "A system dynamics model for tritium cycle of pulsed fusion reactor," *Fusion Engineering and Design*, vol. 118, pp. 5–10, 2017.
- [11] F. Wang, R. Li, C. Ding et al., "Recent progress on the hydrogen storage properties of ZrCo-based alloys applied in International Thermonuclear Experimental Reactor (ITER)," *Progress in Natural Science: Materials International*, vol. 27, no. 1, pp. 58–65, 2017.
- [12] R.-D. Penzhorn, M. devillers, and M. Sirch, "Evaluation of ZrCo and other getters for tritium handling and storage," *Journal of Nuclear Materials*, vol. 170, no. 3, pp. 217–231, 1990.
- [13] R. A. Jat, S. C. Parida, J. Nuwad, R. Agarwal, and S. G. Kulkarni, "Hydrogen sorption-desorption studies on ZrCo-hydrogen system," *Journal of Thermal Analysis and Calorimetry*, vol. 112, no. 1, pp. 37–43, 2013.
- [14] M. Devillers, M. Sirch, S. Bredendiek-Kämper, and R.-D. Penzhorn, "Characterization of the ZrCo-hydrogen system in view of its use for tritium storage," *Chemistry of Materials*, vol. 2, no. 3, pp. 255–262, 1990.
- [15] S. Konishi, T. Nagasaki, and K. Okuno, "Reversible disproportionation of ZrCo under high temperature and hydrogen pressure," *Journal of Nuclear Materials*, vol. 223, no. 3, pp. 294–299, 1995.
- [16] N. Bekris, U. Besserer, M. Sirch, and R.-D. Penzhorn, "On the thermal stability of the zirconium/cobalt-hydrogen system," *Fusion Engineering and Design*, vol. 49–50, pp. 781–789, 2000.
- [17] M. Shim, H. Chung, S. Cho, and H. Yoshid, "Disproportionation characteristics of a zirconium-cobalt hydride bed under iter operating conditions," *Fusion Science and Technology*, vol. 53, no. 3, pp. 830–840, 2008.
- [18] M. Hara, R. Hayakawa, Y. Kaneko, and K. Watanabe, "Hydrogen-induced disproportionation of Zr<sub>2</sub>M (M = Fe, Co, Ni) and reproporationation," *Journal of Alloys and Compounds*, vol. 352, no. 1–2, pp. 218–225, 2003.
- [19] M. Devillers, M. Sirch, and R.-D. Penzhorn, "Hydrogen-induced disproportionation of the intermetallic compound ZrCo," *Chemistry of Materials*, vol. 4, no. 3, pp. 631–639, 1992.
- [20] M. Hara, T. Okabe, K. Mori, and K. Watanabe, "Kinetics and mechanism of hydrogen-induced disproportionation of ZrCo," *Fusion Engineering and Design*, vol. 49–50, pp. 831–838, 2000.
- [21] N. Bekris and M. Sirch, "On the mechanism of the disproportionation of ZrCo hydrides," *Fusion Science and Technology*, vol. 62, no. 1, pp. 50–55, 2012.
- [22] R. A. Jat, R. Singh, S. C. Parida et al., "Structural and hydrogen isotope storage properties of Zr-Co-Fe alloy," *International Journal of Hydrogen Energy*, vol. 40, no. 15, pp. 5135–5143, 2015.

- [23] R. A. Jat, S. C. Parida, R. Agarwal, and S. G. Kulkarni, "Effect of Ni content on the hydrogen storage behavior of ZrCo<sub>1-x</sub>Ni<sub>x</sub> alloys," *International Journal of Hydrogen Energy*, vol. 38, no. 3, pp. 1490–1500, 2013.
- [24] J. Wan, R. Li, F. Wang, C. Ding, R. Yu, and Y. Wu, "Effect of Ni substitution on hydrogen storage properties of Zr<sub>0.8</sub>Ti<sub>0.2</sub>Co<sub>1-x</sub>Ni<sub>x</sub> (x = 0, 0.1, 0.2, 0.3) alloys," *International Journal of Hydrogen Energy*, vol. 41, no. 18, pp. 7408–7418, 2016.
- [25] Z. Huang, X. Liu, L. Jiang, and S. Wang, "Hydrogen storage properties of Zr<sub>1-x</sub>Ti<sub>x</sub>Co intermetallic compound," *Rare Metals*, vol. 25, no. 6, pp. 200–203, 2006.
- [26] Y. Zhao, R. Li, R. Tang et al., "Effect of Ti substitution on hydrogen storage properties of Zr<sub>1-x</sub>Ti<sub>x</sub>Co (x = 0, 0.1, 0.2, 0.3) alloys," *Journal of Energy Chemistry*, vol. 23, no. 1, pp. 9–14, 2014.
- [27] R. A. Jat, S. Pati, S. C. Parida, R. Agarwal, and S. K. Mukerjee, "Synthesis, characterization and hydrogen isotope storage properties of Zr–Ti–Co ternary alloys," *International Journal of Hydrogen Energy*, vol. 42, no. 4, pp. 2248–2256, 2017.
- [28] G. Zhang, G. Sang, R. Xiong, H. Kou, K. Liu, and W. Luo, "Effects and mechanism of Ti, Ni, Sc, Fe substitution on the thermal stability of zirconium cobalt-hydrogen system," *International Journal of Hydrogen Energy*, vol. 40, no. 20, pp. 6582–6593, 2015.
- [29] H. Kou, G. Sang, W. Luo et al., "Comparative study of full-scale thin double-layered annulus beds loaded with ZrCo, Zr<sub>0.8</sub>Hf<sub>0.2</sub>Co and Zr<sub>0.8</sub>Ti<sub>0.2</sub>Co for recovery and delivery of hydrogen isotopes," *International Journal of Hydrogen Energy*, vol. 40, no. 34, pp. 10923–10933, 2015.
- [30] R. A. Jat, R. Singh, S. Pati et al., "An analogy of interstitial site occupancy and hydrogen induced disproportionation of Zr<sub>1-x</sub>Ti<sub>x</sub>Co ternary alloys," *International Journal of Hydrogen Energy*, vol. 42, no. 12, pp. 8089–8097, 2017.
- [31] W. T. Shmayda, A. G. Heics, and N. P. Kherani, "Comparison of uranium and zirconium cobalt for tritium storage," *Journal of the Less-Common Metals*, vol. 162, no. 1, pp. 117–127, 1990.
- [32] H. Yoo, W. Kim, and H. Ju, "A numerical comparison of hydrogen absorption behaviors of uranium and zirconium cobalt-based metal hydride beds," *Solid State Ionics*, vol. 262, pp. 241–247, 2014.
- [33] R. Sen, S. Das, and K. Das, "Microstructural characterization of nanosized ceria powders by X-ray diffraction analysis," *Metallurgical and Materials Transactions A: Physical Metallurgy and Materials Science*, vol. 42, no. 5, pp. 1409–1417, 2011.
- [34] B. Joseph and B. Schiavo, "Effects of ball-milling on the hydrogen sorption properties of LaNi<sub>5</sub>," *Journal of Alloys and Compounds*, vol. 480, no. 2, pp. 912–916, 2009.
- [35] A. Calka and D. Wexler, "Mechanical milling assisted by electrical discharge," *Nature*, vol. 419, no. 6903, pp. 147–151, 2002.
- [36] M. H. Enayati, G. R. Aryanpour, and A. Ebnonnasir, "Production of nanostructured WC-Co powder by ball milling," *International Journal of Refractory Metals and Hard Materials*, vol. 27, no. 1, pp. 159–163, 2009.
- [37] V. Batz, I. Jacob, M. H. Mintz, Z. Gavra, and J. Bloch, "The hydriding kinetics of massive ZrCo," *Journal of Alloys and Compounds*, vol. 325, no. 1-2, pp. 137–144, 2001.
- [38] J. Bloch and M. H. Mintz, "Kinetics and mechanisms of metal hydrides formation - A review," *Journal of Alloys and Compounds*, vol. 253-254, pp. 529–541, 1997.
- [39] H. Kou, W. Luo, Z. Huang et al., "Effects of temperature and hydrogen pressure on the activation behavior of ZrCo," *International Journal of Hydrogen Energy*, vol. 41, no. 25, pp. 10811–10818, 2016.
- [40] M. Senna, P. Billik, A. Y. Yermakov et al., "Synthesis and magnetic properties of CuAlO<sub>2</sub> from high-energy ball-milled Cu<sub>2</sub>O[sbnd]Al<sub>2</sub>O<sub>3</sub> mixture," *Journal of Alloys and Compounds*, vol. 695, pp. 2314–2323, 2017.
- [41] Y. Qi, X. Ju, C. Wan et al., "EXAFS and SAXS studies of ZrCo alloy doped with Hf, Sc and Ti atoms," *International Journal of Hydrogen Energy*, vol. 35, no. 7, pp. 2931–2935, 2010.
- [42] M. Aureli, C. C. Doumanidis, I. E. Gunduz et al., "Mechanics and energetics modeling of ball-milled metal foil and particle structures," *Acta Materialia*, vol. 123, pp. 305–316, 2017.
- [43] S. Rousselot, D. Guay, and L. Roué, "Comparative study on the structure and electrochemical hydriding properties of MgTi, Mg<sub>0.5</sub>Ni<sub>0.5</sub>Ti and MgTi<sub>0.5</sub>Ni<sub>0.5</sub> alloys prepared by high energy ball milling," *Journal of Power Sources*, vol. 196, no. 3, pp. 1561–1568, 2011.
- [44] D. Lee, I. Kwon, J.-L. Bobet, and M. Y. Song, "Effects on the H<sub>2</sub>-sorption properties of Mg of Co (with various sizes) and CoO addition by reactive grinding," *Journal of Alloys and Compounds*, vol. 366, no. 1-2, pp. 279–288, 2004.
- [45] J. Ženíšek, E. Kozeschnik, J. Svoboda, and F. D. Fischer, "Modelling the role of compositional fluctuations in nucleation kinetics," *Acta Materialia*, vol. 91, pp. 365–376, 2015.
- [46] H. Zhang, R. Su, D. Chen, and L. Shi, "Thermal desorption behaviors of helium in Zr-Co films prepared by sputtering deposition method," *Vacuum*, vol. 130, pp. 174–178, 2016.
- [47] S.-I. Orimo and H. Fujii, "Effects of nanometer-scale structure on hydriding properties of Mg-Ni alloys: A review," *Intermetallics*, vol. 6, no. 3, pp. 185–192, 1998.
- [48] Y. Zhang, W.-S. Zhang, M.-Q. Fan et al., "Enhanced hydrogen storage performance of LiBH<sub>4</sub>-SiO<sub>2</sub>-TiF<sub>3</sub> composite," *The Journal of Physical Chemistry C*, vol. 112, no. 10, pp. 4005–4010, 2008.
- [49] Q. Li, L.-J. Jiang, K.-C. Chou et al., "Effect of hydrogen pressure on hydriding kinetics in the Mg<sub>2-x</sub>Ag<sub>x</sub>Ni-H (x = 0.05, 0.1) system," *Journal of Alloys and Compounds*, vol. 399, no. 1-2, pp. 101–105, 2005.
- [50] H. Emami, K. Edalati, J. Matsuda, E. Akiba, and Z. Horita, "Hydrogen storage performance of TiFe after processing by ball milling," *Acta Materialia*, vol. 88, pp. 190–195, 2015.
- [51] K. Edalati, J. Matsuda, M. Arita, T. Daio, E. Akiba, and Z. Horita, "Mechanism of activation of TiFe intermetallics for hydrogen storage by severe plastic deformation using high-pressure torsion," *Applied Physics Letters*, vol. 103, no. 14, Article ID 143902, 2013.
- [52] K. Edalati, M. Matsuo, H. Emami et al., "Impact of severe plastic deformation on microstructure and hydrogen storage of titanium-iron-manganese intermetallics," *Scripta Materialia*, vol. 124, pp. 108–111, 2016.

## Research Article

# A Novel Open-Framework Cu-Ge-Based Chalcogenide Anode Material for Sodium-Ion Battery

Quan Sun,<sup>1,2</sup> Lin Fu,<sup>1</sup> and Chaoqun Shang<sup>3</sup>

<sup>1</sup>School of Materials Science and Engineering, Tongji University, Shanghai 201804, China

<sup>2</sup>Key Laboratory of Electrochemical Energy Storage Technology of Jiangsu Province, Taizhou 225500, China

<sup>3</sup>Department of Materials Science and Engineering, Southern University of Science and Technology, Shenzhen 518055, China

Correspondence should be addressed to Lin Fu; fulin.work@foxmail.com and Chaoqun Shang; shangcq@sustc.edu.cn

Received 13 October 2017; Accepted 23 November 2017; Published 27 December 2017

Academic Editor: Huaiyu Shao

Copyright © 2017 Quan Sun et al. This is an open access article distributed under the Creative Commons Attribution License, which permits unrestricted use, distribution, and reproduction in any medium, provided the original work is properly cited.

Open-framework chalcogenides are potential electrode materials for sodium-ion batteries (SIBs) due to their architectures with fast-ion conductivity. Herein, we report on the successful synthesis of open-framework Cu-Ge-based chalcogenides  $[\text{Cu}_8\text{Ge}_6\text{Se}_{19}](\text{C}_5\text{H}_{12}\text{N})_6$  (CGSe) and the research of their energy storage application as SIB anodes for the first time. As a result, the CGSe anode exhibited good electrochemical performances such as high reversible capacity ( $463.3 \text{ mAh g}^{-1}$ ), excellent rate performance, and considerable cycling stability. Our exploration not only develops a promising electrode material for SIBs, but also extends the application of open-framework chalcogenides.

## 1. Introduction

Because of the identical fundamental principles, sodium-ion batteries (SIBs) are considered to be one of the most potential substitutes for lithium-ion batteries (LIBs) [1, 2]. Moreover, SIBs might become competitive with LIBs in large-scale storage applications owing to the abundance of sodium and shortage of lithium in the earth [3]. Unfortunately, compared with lithium ions ( $0.76 \text{ \AA}$ ), the larger ionic radius of sodium ions ( $1.02 \text{ \AA}$ ) is a big hurdle for intercalation reaction with anode materials [4]. For example, the commercial graphite delivers a sodiation capacity of less than  $35 \text{ mAh g}^{-1}$ , which is several times lower than that of lithiation capacity ( $372 \text{ mAh g}^{-1}$ ) [5]. It is worth celebrating that the anode materials with alloying reaction and conversion reaction mechanism exhibit high specific capacity for SIBs, such as Si, Ge, Sn, Sb, P and their compounds [6–9]. Ge has been found to alloy with Na at room temperature to form NaGe with a theoretical capacity of  $369 \text{ mAh g}^{-1}$  [10]. However, due to the sluggish bulk diffusion of Na ions, elemental Ge delivered high specific capacities only in thin film and amorphous structures, and the Na-ion storage properties of coarser structures

remain limited [11–13]. Furthermore, the serious volumetric variation of Ge during the alloying and dealloying process will lead to fast decay of specific capacity. The preparation of compounds has been applied to overcome the above problems and improve the electrochemical performances of Ge-based anode materials. In recent years, the inorganic Ge-based compounds (such as  $\text{GeO}_2$ /reduced graphene oxide (RGO),  $\text{GeP}_5/\text{C}$ ,  $\text{Zn}_2\text{GeO}_4/\text{RGO}$ , and  $\text{ZnGeP}_2/\text{C}$ ) have been proposed as anode materials for SIBs and have shown stable cycle property and high rate capability [14–17]. Nevertheless, the nanosize particles of these materials as well as the introduction of RGO or C in Ge-based compounds usually aggravate the side reaction with electrolyte and decrease the volume energy density of SIBs. Therefore, it is essential to search novel strategies to enhance the bulk Na ions diffusion and suppress the volume expansion during sodiation of Ge-based anode materials.

Open-framework chalcogenides have aroused intensive interest in visible-light photocatalysis over the past few decades because these materials can integrate porosity with semiconductivity [18]. More importantly, the open-framework chalcogenides with characteristics of three dimensional

(3D) ion migration channels, high porosity, and high anionic framework polarizability have long been recognized as potential fast-ion conductors, which can be used as electrodes or electrolytes in secondary batteries [19]. The Ca-Li-In-S quaternary open-framework chalcogenides with the highest specific conductivity of  $0.15 \Omega^{-1} \text{cm}^{-1}$  at  $27^\circ\text{C}$  under 100% relative humidity have been reported by Zheng et al. [20]. Recently, the crystalline chalcogenide  $(\text{H}_3\text{O})(\text{enH}_2)\text{Cu}_8\text{Sn}_3\text{S}_{12}$  with frame structure has been investigated as anode material in lithium-ion batteries and exhibited a high initial reversible capacity of  $870.3 \text{mAh g}^{-1}$  [21]. However, the electrochemical behavior of this family of materials for SIBs has not been reported. Lately, a Cu-Ge-S open-framework chalcogenide with 3D channels has been reported [22]. The cylindrical channel along the *c*-axis showed a diameter of  $16.4 \text{Å}$ , which provided huge space for Na ions diffusion. Furthermore, the large  $\text{Cu}^+$  to  $\text{Ge}^{4+}$  ratio ( $\text{Cu}/\text{Ge} = 1.6$ ) made this chalcogenide show low electronic band gap ( $2.5 \text{eV}$ ). Moreover, the porous nature of open-framework chalcogenides would facilitate the penetration of electrolyte and transportation of ions and buffer the volume expansion during sodiation [23]. On the other hand, the conversion reaction and alloying reaction of  $\text{Cu}^+$  and  $\text{Ge}^{4+}$  with Na ions in this chalcogenide would exhibit high theoretical capacity. Therefore, the open-framework Cu-Ge-based chalcogenides are highly potential anode materials for SIBs.

In this work, we successfully synthesize a novel open-framework chalcogenide  $[\text{Cu}_8\text{Ge}_6\text{Se}_{19}](\text{C}_5\text{H}_{12}\text{N})_6$  (CGSe) and investigate its sodium-ion storage properties for the first time. The CGSe cubic crystals with  $10\text{--}50 \mu\text{m}$  edge length show good electrochemical performance, indicating that CGSe offers an opportunity to anode materials for high performance SIBs in the future.

## 2. Experimental Details

The CGSe samples were synthesized according to the literature methods [24]. In the typical synthesis process, 187 mg of  $\text{Cu}(\text{Ac})_2 \cdot \text{H}_2\text{O}$ , 104 mg of  $\text{GeO}_2$ , and 215 mg of Se were mixed in 2.5 mL of piperidine (17.3 wt%) solution under vigorous stirring for about 30 min. The reaction solution was then transferred to a 23 mL Teflon-lined stainless-steel autoclave and maintained at  $180^\circ\text{C}$  for 10 days. After cooling, the black cubic crystals were harvested by ultrasonic treatment, washed with ethanol, and dried at  $70^\circ\text{C}$  for 1 day.

The structure of as-prepared samples was determined by single-crystal X-ray diffraction (SCXRD, Agilent diffractometers) using graphite monochromated  $\text{Mo K}\alpha$  radiation ( $\lambda = 0.71073 \text{Å}$ ) with SHELXS-97 method. Its phase purity was supported by powder X-ray diffraction (PXRD, Bruker, D8 advance) using  $\text{Cu K}\alpha$  radiation ( $\lambda = 1.5406 \text{Å}$ ) with a step size of  $0.3^\circ$  in the  $2\theta$  range  $5\text{--}30^\circ$ . The lattice structural details were acquired on a FEI Tecnai  $\text{G}^2 \text{F-20}$  high-resolution transmission electron microscope (HRTEM). The morphologies and corresponding elemental mapping images were obtained by field-emission scanning electron microscope (FE-SEM, Hitachi S-4800).

Na-ion storage properties of CGSe were evaluated using CR2032 coin-type half batteries. The working electrodes were

prepared by coating a mixture containing CGSe (80 wt%), super P (10 wt%), and poly(acrylic) acid (PAA) binder (10 wt%) onto copper foil and dried at  $120^\circ\text{C}$  for 1 day. The coin-type cells assembled in recirculating argon glove box by using Na metal as counter electrode, glass microfiber filter as separator, and 1 M  $\text{NaClO}_4$  dissolved in ethylene carbonate (EC) and dimethyl carbonate (DMC) (1:1 by volume) with 5 wt% fluoroethylene carbonate (FEC) additive as electrolyte. Cyclic voltammetry (CV) data were collected on an electrochemical workstation (BioLogic VMP-300) at a scanning rate of  $0.2 \text{mV s}^{-1}$  in the voltage range of  $0.005\text{--}2.5 \text{V}$  versus  $\text{Na}^+/\text{Na}$ . The cycle and rate properties tests were performed on a LAND battery measurement system (LAND CT2001A) between  $0.005 \text{V}$  and  $2.5 \text{V}$ . The mass loading of CGSe was about  $1.5 \text{mg cm}^{-2}$  in the electrode and the specific capacities were calculated based on active materials.

## 3. Results and Discussion

The CGSe crystallizes in the cubic space group *Im-3*. As depicted in Figure 1(a), all diffraction peaks of PXRD are well matched to the simulated ones from SCXRD analysis, indicating the highly pure single-crystal structure of as-prepared CGSe. In the HRTEM image (Figure 1(b)), the marked lattice distance of  $0.304 \text{nm}$  can be assigned to the (0712) crystal plane of CGSe, which is in agreement with the XRD peak located at  $28.8^\circ$ . The HRTEM image further demonstrated that the crystal structure of as-prepared CGSe is well matched with the SCXRD result.

In open-framework CGSe, the 3D interconnected channels are constructed with the anionic selenide framework  $[\text{Cu}_8\text{Ge}_6\text{Se}_{19}]^{6-}$  and disordered charge-balanced species  $(\text{C}_5\text{H}_{12}\text{N})^+$  [21, 24]. The inorganic species  $[\text{Cu}_8\text{Ge}_6\text{Se}_{19}]^{6-}$  forms the porous structure, while the organic species  $(\text{C}_5\text{H}_{12}\text{N})^+$  acts as the structure stabilizer. As displayed in Figure 2(a), the structural feature of 3D CGSe is the presence of icosahedral  $[\text{Cu}_8\text{Se}_{19}]^{24-}$  cluster, consisting of a cubic array of eight  $\text{Cu}^+$  ions bridged by  $\text{Se}^{2-}$  ions. The shape of  $[\text{Cu}_8\text{Se}_{19}]^{24-}$  cluster defined by nineteen  $\text{Se}^{2-}$  sites is icosahedral. To form the infinite lattice (Figure 2(b)), the primitive cubic packing of icosahedral  $[\text{Cu}_8\text{Se}_{19}]^{24-}$  clusters is cross-linked by dimeric  $\text{Ge}_2\text{Se}_2^{4+}$  unit. Most importantly, this extended CGSe open framework contains abundant interconnected microchannels, which is favorable to the sodium-ion intercalation. Furthermore, compared with Cu-Ge-S chalcogenide, the larger size of  $\text{Se}^{2-}$  compared to that of  $\text{S}^{2-}$  ions would make CGSe have much higher anionic framework polarizability, which is helpful to  $\text{Na}^+$  ions migration. The panoramic SEM image (Figure 2(c)) reveals that the CGSe samples are composed of cubic crystals, and the edge length of the single CGSe is about  $10\text{--}50 \mu\text{m}$ . It could be clearly seen from the high-magnification SEM image (inset in Figure 2(c)) that the inside of CGSe contains a great many of microchannels, which will facilitate the electrolyte infiltration and Na-ion diffusion in bulk CGSe. The energy dispersive X-ray spectroscopy (EDS) elemental mappings of Cu, Ge, and Se, as shown in Figures 2(e)–2(g), respectively, matched well with the corresponding SEM image (Figure 2(d)), indicating

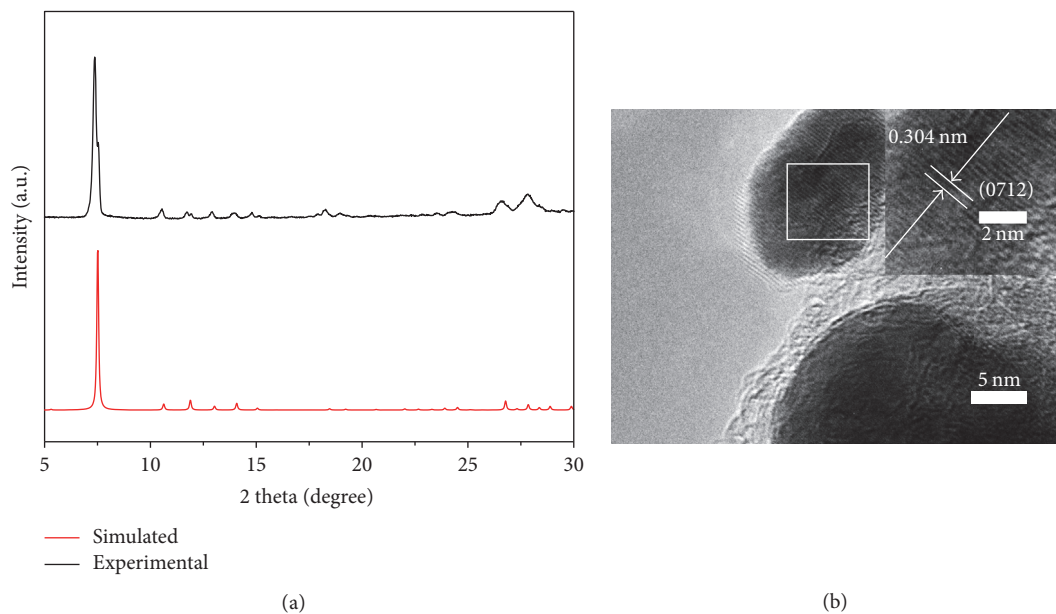


FIGURE 1: (a) XRD patterns and (b) HRTEM image of CGSe.

that these three elements are homogeneously distributed throughout the CGSe mass.

To explore the potential application of CGSe as SIB anode, we evaluated the electrochemical performances with the cyclic voltammetry (CV) and galvanostatic charge/discharge tests. The initial three consecutive CV curves of as-prepared CGSe are shown in Figure 3(a). In the reduction process, a cathodic peak centered at 1.7 V could be attributed to sodium-ion intercalation into the interconnected channels of CGSe and formation of  $\text{Na}_x\text{CGSe}$  [25]. In the first discharge cycle, a weak peak at 0.85 V and a strong peak at 0.56 V were clearly observed, which can be attributed to the decomposition of  $\text{Na}_x\text{CGSe}$  (Cu and Ge are generated) and formation of  $\text{Na}_y\text{Se}$ , respectively [21, 26]. These peaks' shift to about 0.9 (1.1) and 0.4 V in the subsequent cycles is known to represent the activation of electrode materials during the first cycle [27]. Meanwhile, the intensities of peaks of the following two cycles are reduced, indicating the formation of solid electrolyte interface (SEI) film and other some irreversible reactions in the first cycle [28]. The cathodic/anodic couples at voltages of around 0.01/0.21 V might be assigned to signature of the NaGe alloying/dealloying reaction [16]. For the oxidation process, two smooth peaks were located at 1.05 V and 1.32 V in the first scan and disappeared in subsequent cycles because of the decomposition of instability SEI film. Two sharp peaks positioned at 1.61 V and 1.86 V can be associated with the desodiation process of the  $\text{Na}_y\text{Se}$  and regeneration of CGSe, respectively [28–30].

The charge/discharge plateaus are in accordance with the CV results in Figure 3(b). The first charge/discharge curve is obviously different from the following two cycles. Moreover, the initial Coulombic efficiency (CE) is only 72.56% at a current density of  $100 \text{ mA g}^{-1}$ . These abnormal electrochemical

behaviors can be attributed to the SEI formation and other side reactions in the first cycle. In the following two cycles, the almost-overlapped charge/discharge curves as well as the high CE indicate the good reversible properties of CGSe, which should result from the unique morphology and structure of open-framework CGSe. The cycling performance of CGSe electrode was tested at  $100 \text{ mA g}^{-1}$  (Figure 3(c)). The charge capacity is  $463.3 \text{ mAh g}^{-1}$  in the first cycle and  $188 \text{ mAh g}^{-1}$  remains after 50 cycles. In addition, the CE increases to more than 96% (the third cycle) and then keeps stable during cycling. The initial reversible capacity is higher than that of theoretical value of elemental Ge, indicating that CGSe is a promising anode material for high energy density SIB. It is noteworthy that the CGSe anode materials can also exhibit reversible capacity of  $159 \text{ mAh g}^{-1}$  after 50 cycles at the current density of  $200 \text{ mA g}^{-1}$  (Figure 3(d)). The rate capability of CGSe is also investigated. Figure 3(e) shows the third charge/discharge curves of CGSe at different current densities. The excellent rate property is demonstrated by the specific discharge/charge capacities being around  $450/429$ ,  $432/414$ ,  $403/389$ ,  $366/355$ , and  $320/306 \text{ mAh g}^{-1}$  at current density of 50, 100, 200, 500, and  $1000 \text{ mA g}^{-1}$ , respectively. More importantly, although polarization becomes more obvious at the higher current density, the symmetric charge/discharge plateaus are still clearly observed. According to the previous literature, the shorter edge length of 3D channel of open-framework CGSe is about  $6.4 \text{ \AA}$ , which is several times larger than that of ionic radius of sodium ions ( $1.02 \text{ \AA}$ ) [4, 24]. To the best of our knowledge, these large channels are beneficial for the penetration of electrolyte and insertion/extraction of sodium ion, thereby resulting in good electrochemical performance [21, 23].

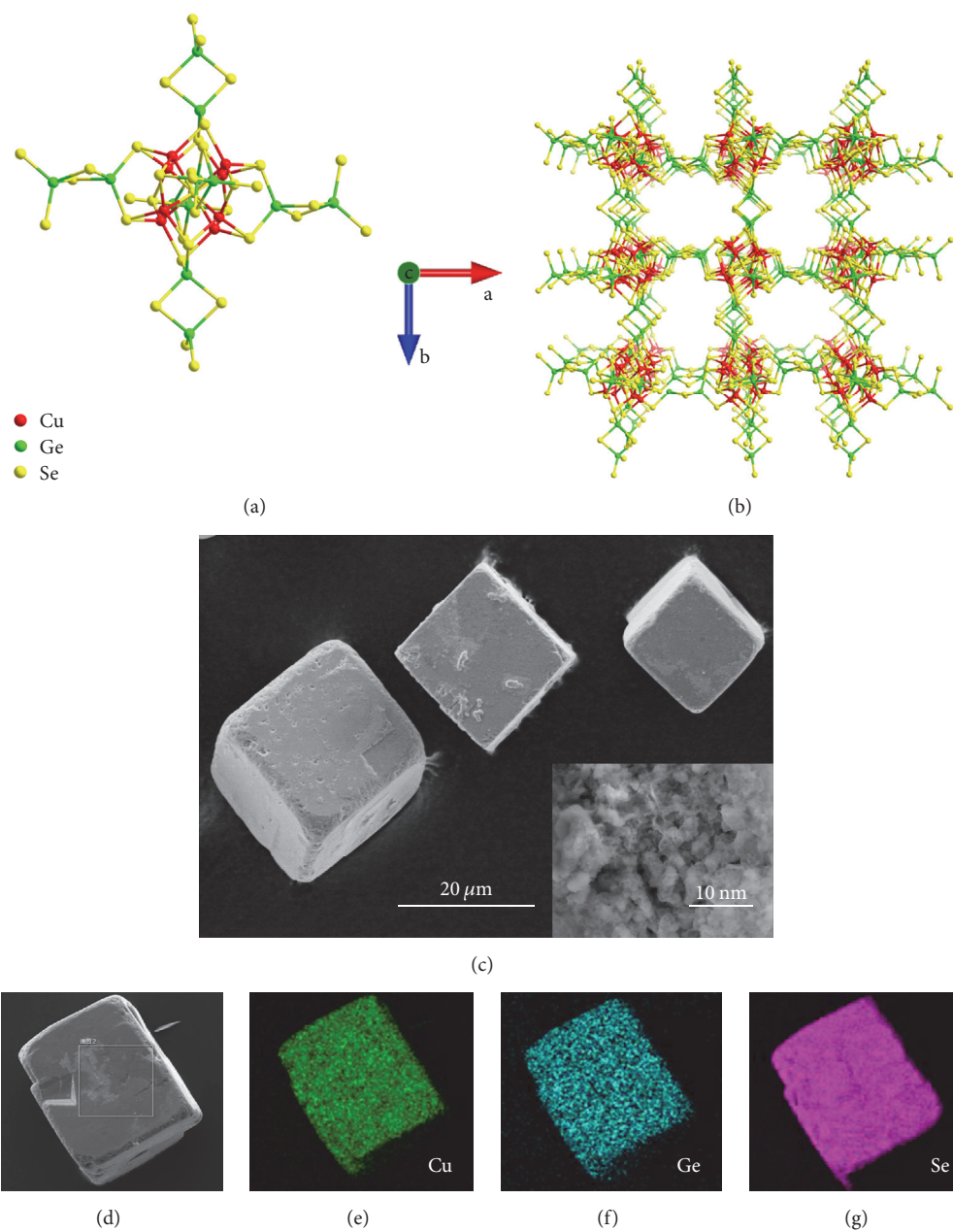


FIGURE 2: (a) The ball and stick mode of icosahedral  $[\text{Cu}_8\text{Se}_{19}]^{24-}$  cluster and its connectivity with twelve  $\text{Ge}^{4+}$  ions. (b) View of the CGSe framework along the  $ab$  direction. (c, d) SEM images and the corresponding EDS mapping of (e) Cu, (f) Ge, and (g) S of CGSe. The high-magnification SEM image inset in Figure 2(c).

#### 4. Conclusions

In conclusion, the crystalline CGSe open-framework material was successfully prepared using a simple solvothermal method. The as-prepared microscale CGSe cubic crystals display high reversible capacity ( $463.3\ \text{mAh g}^{-1}$ ), excellent rate performance, and considerable cycling stability as a novel anode for SIBs because the interconnected channels facilitate penetration of electrolyte and transportation of sodium ions. It is also noteworthy that if the cycling stability of CGSe was improved by further research, it will

become a promising anode in SIB fields. This work not only develops a potential electrode material for SIBs, but also extends the application of open-framework chalcogenides. In the future, it is suggested to pay much attention to the Na-ion storage mechanism as well as the capacity fading mechanism and solutions of the open-framework chalcogenides.

#### Conflicts of Interest

The authors declare no competing financial interest.

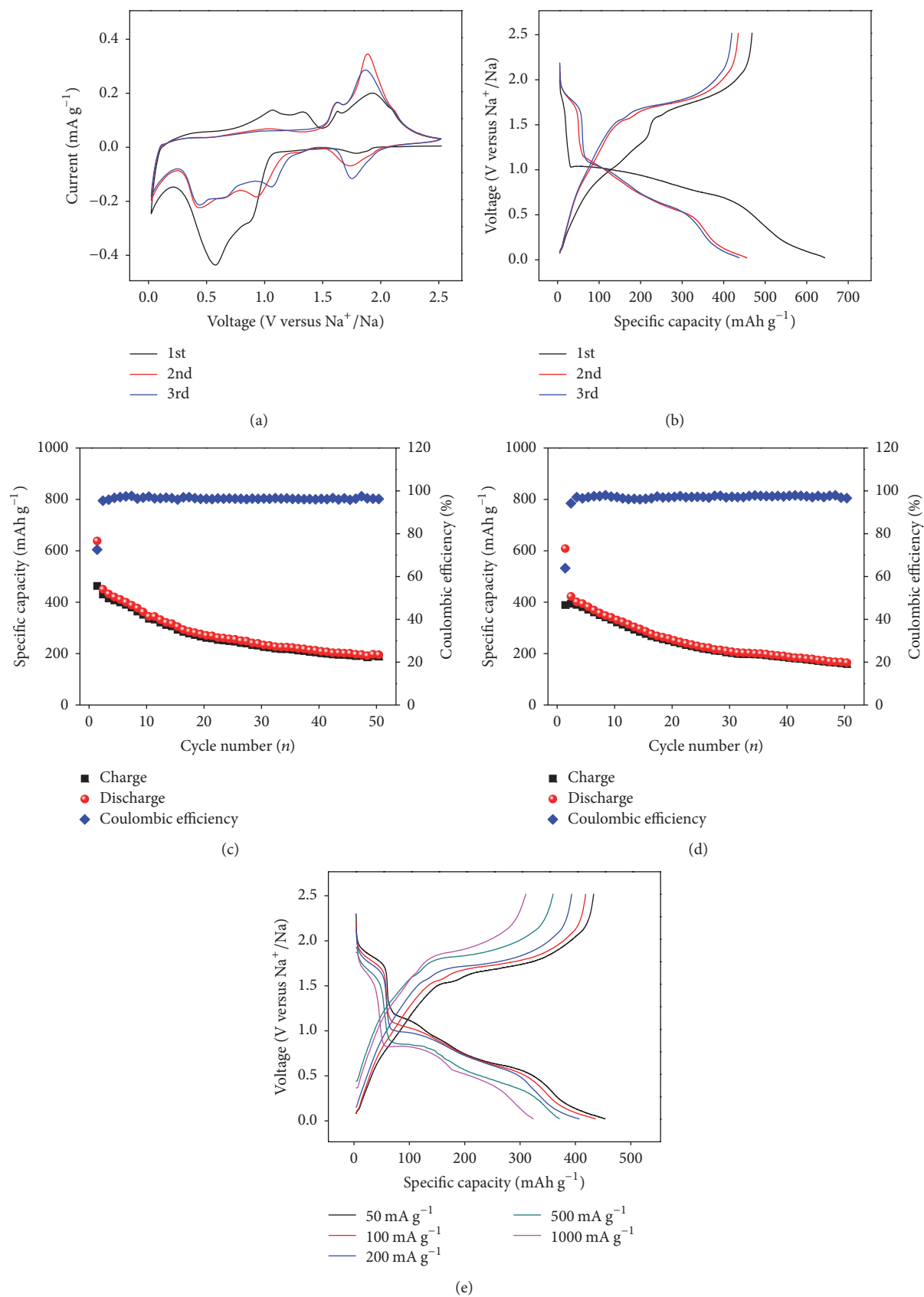


FIGURE 3: (a) The initial three curves of the CGSe at a scanning rate of  $0.2 \text{ mV s}^{-1}$ . (b) The charge/discharge curves and (c) cycling performance of the CGSe at a current density of  $100 \text{ mA g}^{-1}$ . (d) Cycling performance of the CGSe at a current density of  $200 \text{ mA g}^{-1}$ . (e) The rate capability of CGSe under varying current densities (from 50 to  $1000 \text{ mA g}^{-1}$ ), respectively.

## Acknowledgments

This work was supported by the Innovation Capability Construction Program of Jiangsu Province (Grant no. BM2016027) and the Natural Science Foundation of Guangdong Province (Grant no. 2016A030310376).

## References

- [1] N. Yabuuchi, K. Kubota, M. Dahbi, and S. Komaba, "Research development on sodium-ion batteries," *Chemical Reviews*, vol. 114, no. 23, pp. 11636–11682, 2014.
- [2] S. Pat, S. Özen, V. Şenay, and Ş. Korkmaz, "Optical and surface properties of optically transparent  $\text{Li}_3\text{PO}_4$  solid electrolyte layer for transparent solid batteries," *Scanning*, vol. 38, no. 4, pp. 317–321, 2016.
- [3] H. Pan, Y.-S. Hu, and L. Chen, "Room-temperature stationary sodium-ion batteries for large-scale electric energy storage," *Energy & Environmental Science*, vol. 6, no. 8, pp. 2338–2360, 2013.
- [4] H. Kim, H. Kim, Z. Ding et al., "Recent progress in electrode materials for sodium-ion batteries," *Advanced Energy Materials*, vol. 6, no. 19, Article ID 1600943, 2016.
- [5] Y. Wen, K. He, Y. Zhu et al., "Expanded graphite as superior anode for sodium-ion batteries," *Nature Communications*, vol. 5, article no. 4033, 2014.
- [6] J. Hwang, S. Myung, and Y. Sun, "Sodium-ion batteries: present and future," *Chemical Society Reviews*, vol. 46, no. 12, pp. 3529–3614, 2017.
- [7] J. Duan, W. Zhang, C. Wu et al., "Self-wrapped Sb/C nanocomposite as anode material for high-performance sodium-ion batteries," *Nano Energy*, vol. 16, pp. 479–487, 2015.
- [8] W. Luo, F. Shen, C. Bommier, H. Zhu, X. Ji, and L. Hu, "Na-ion battery anodes: materials and electrochemistry," *Accounts of Chemical Research*, vol. 49, no. 2, pp. 231–240, 2016.
- [9] X. Xiao, X. Li, S. Zheng, J. Shao, H. Xue, and H. Pang, "Nanostructured germanium anode materials for advanced rechargeable batteries," *Advanced Materials Interfaces*, vol. 4, no. 6, Article ID 1600798, 2017.
- [10] V. L. Chevrier and G. Ceder, "Challenges for Na-ion negative electrodes," *Journal of The Electrochemical Society*, vol. 158, no. 9, pp. A1011–A1014, 2011.
- [11] A. Kohandehghan, K. Cui, M. Kupsta et al., "Activation with Li enables facile sodium storage in germanium," *Nano Letters*, vol. 14, no. 10, pp. 5873–5882, 2014.
- [12] P. R. Abel, Y.-M. Lin, T. De Souza et al., "Nanocolumnar germanium thin films as a high-rate sodium-ion battery anode material," *The Journal of Physical Chemistry C*, vol. 117, no. 37, pp. 18885–18890, 2013.
- [13] T. Kajita and T. Itoh, "Ether-based solvents significantly improved electrochemical performance for Na-ion batteries with amorphous  $\text{GeO}_x$  anodes," *Physical Chemistry Chemical Physics*, vol. 19, no. 2, pp. 1003–1009, 2017.
- [14] W. Qin, T. Chen, B. Hu, Z. Sun, and L. Pan, " $\text{GeO}_2$  decorated reduced graphene oxide as anode material of sodium ion battery," *Electrochimica Acta*, vol. 173, pp. 193–199, 2015.
- [15] W. Li, L. Ke, Y. Wei et al., "Highly reversible sodium storage in a  $\text{GeP}_5/\text{C}$  composite anode with large capacity and low voltage," *Journal of Materials Chemistry A*, vol. 5, no. 9, pp. 4413–4420, 2017.
- [16] Y. R. Lim, C. S. Jung, H. S. Im et al., " $\text{Zn}_2\text{GeO}_4$  and  $\text{Zn}_2\text{SnO}_4$  nanowires for high-capacity lithium- and sodium-ion batteries," *Journal of Materials Chemistry A*, vol. 4, no. 27, pp. 10691–10699, 2016.
- [17] M. Zhang, R. Hu, J. Liu et al., "A  $\text{ZnGeP}_2/\text{C}$  anode for lithium-ion and sodium-ion batteries," *Electrochemistry Communications*, vol. 77, pp. 85–88, 2017.
- [18] D. Maspoch, D. Ruiz-Molina, and J. Veciana, "Old materials with new tricks: multifunctional open-framework materials," *Chemical Society Reviews*, vol. 36, no. 5, pp. 770–818, 2007.
- [19] N. Zheng, X. Bu, and P. Feng, "Synthetic design of crystalline inorganic chalcogenides exhibiting fast-ion conductivity," *Nature*, vol. 426, no. 6965, pp. 428–432, 2003.
- [20] N. Zheng, X. Bu, and P. Feng, "Pentapertetrahedral clusters as building blocks for a three-dimensional sulfide superlattice," *Angewandte Chemie International Edition*, vol. 43, no. 36, pp. 4753–4755, 2004.
- [21] L. Nie, Y. Zhang, K. Ye et al., "A crystalline Cu-Sn-S framework for high-performance lithium storage," *Journal of Materials Chemistry A*, vol. 3, no. 38, pp. 19410–19416, 2015.
- [22] Z. Zhang, J. Zhang, T. Wu, X. Bu, and P. Feng, "Three-dimensional open framework built from Cu-S icosahedral clusters and its photocatalytic property," *Journal of the American Chemical Society*, vol. 130, no. 46, pp. 15238–15239, 2008.
- [23] Y. Yu, C.-H. Chen, and Y. Shi, "A tin-based amorphous oxide composite with a porous, spherical, multideck-cage morphology as a highly reversible anode material for lithium-ion batteries," *Advanced Materials*, vol. 19, no. 7, pp. 993–997, 2007.
- [24] M. Luo, D. Hu, H. Yang, D. Li, and T. Wu, "PCU-type copper-rich open-framework chalcogenides: pushing up the length limit of the connection mode and the first mixed-metal  $[\text{Cu}_7\text{GeSe}_{13}]$  cluster," *Inorganic Chemistry Frontiers*, vol. 4, no. 2, pp. 387–392, 2017.
- [25] W. Sun, X. Rui, D. Yang et al., "Two-dimensional tin disulfide nanosheets for enhanced sodium storage," *ACS Nano*, vol. 9, no. 11, pp. 11371–11381, 2015.
- [26] Y. Kim, Y. Kim, Y. Park et al., "SnSe alloy as a promising anode material for Na-ion batteries," *Chemical Communications*, vol. 51, no. 1, pp. 50–53, 2015.
- [27] W. Li, M. Zhou, H. Li, K. Wang, S. Cheng, and K. Jiang, "Carbon-coated  $\text{Sb}_2\text{Se}_3$  composite as anode material for sodium ion batteries," *Electrochemistry Communications*, vol. 60, article no. 5519, pp. 74–77, 2015.
- [28] S. Yuan, Y.-H. Zhu, W. Li et al., "Surfactant-free aqueous synthesis of pure single-crystalline SnSe nanosheet clusters as anode for high energy- and power-density sodium-ion batteries," *Advanced Materials*, vol. 29, no. 4, Article ID 1602469, 2017.
- [29] X. Wang, D. Chen, Z. Yang et al., "Novel metal chalcogenide SnSSe as a high-capacity anode for sodium-ion batteries," *Advanced Materials*, vol. 28, no. 39, pp. 8645–8650, 2016.
- [30] S. Yuan, S. Wang, L. Li, Y.-H. Zhu, X.-B. Zhang, and J.-M. Yan, "Integrating 3D flower-like hierarchical  $\text{Cu}_2\text{NiSnS}_4$  with reduced graphene oxide as advanced anode materials for Na-ion batteries," *ACS Applied Materials & Interfaces*, vol. 8, no. 14, pp. 9178–9184, 2016.

## Research Article

# Facile Synthesis of Indium Sulfide/Flexible Electrospun Carbon Nanofiber for Enhanced Photocatalytic Efficiency and Its Application

Liu Han,<sup>1,2</sup> Haohao Dong,<sup>1</sup> Dong Mao,<sup>1,2</sup> Baolv Hua,<sup>1</sup> Qinyu Li,<sup>1</sup> and Dong Fang<sup>1,2</sup>

<sup>1</sup>School of Chemistry and Environmental Engineering, Yancheng Teachers University, Yancheng 224002, China

<sup>2</sup>College of Chemical Engineering, Nanjing Tech University, Nanjing 210009, China

Correspondence should be addressed to Dong Fang; fangd@yctu.edu.cn

Received 25 September 2017; Accepted 26 November 2017; Published 20 December 2017

Academic Editor: Huaiyu Shao

Copyright © 2017 Liu Han et al. This is an open access article distributed under the Creative Commons Attribution License, which permits unrestricted use, distribution, and reproduction in any medium, provided the original work is properly cited.

Heterojunction system has been proved as one of the best architectures for photocatalyst owing to extending specific surface area, expanding spectral response range, and increasing photoinduced charges generation, separation, and transmission, which can provide better light absorption range and higher reaction site. In this paper, Indium Sulfide/Flexible Electrospun Carbon Nanofiber ( $\text{In}_2\text{S}_3/\text{CNF}$ ) heterogeneous systems were synthesized by a facile one-pot hydrothermal method. The results from characterizations of SEM, TEM, XRD, Raman, and UV-visible diffuse reflectance spectroscopy displayed that flower-like  $\text{In}_2\text{S}_3$  was deposited on the hair-like CNF template, forming a one-dimensional nanofibrous network heterojunction photocatalyst. And the newly prepared  $\text{In}_2\text{S}_3/\text{CNF}$  photocatalysts exhibit greatly enhanced photocatalytic activity compared to pure  $\text{In}_2\text{S}_3$ . In addition, the formation mechanism of the one-dimensional heterojunction  $\text{In}_2\text{S}_3/\text{CNF}$  photocatalyst is discussed and a promising approach to degrade Rhodamine B (RB) in the photocatalytic process is processed.

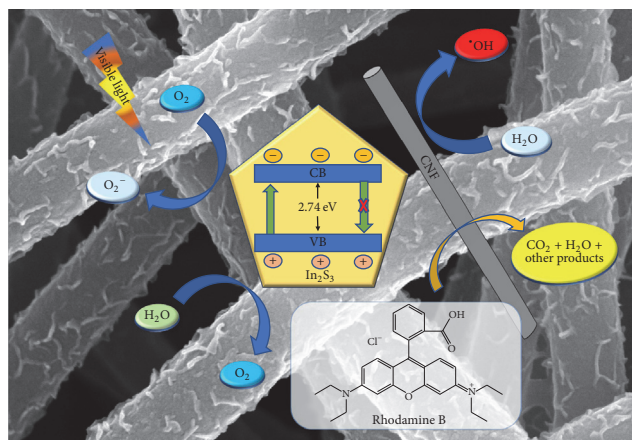
## 1. Introduction

Nowadays, it is a huge challenge for people to deal with the organic pollutant in the energy crisis environment [1–3]. Certainly, photocatalytic as a novel solution has aroused great interest for people. It has been considered as one of the most effective ways for the solar energy conversion and the destruction of organic pollutant [4, 5]. Up to now, numerous experiments of the degradation of organic pollutants by using photocatalysts have been researched. However, the photocatalytic activity of pure photocatalyst is limited by its low efficiency of light absorption, difficult migration, and high recombination probability of photogenerated electron-hole pairs, and the development of photocatalytic technology is still limited for the photocatalyst [6–8]. Therefore, it is urgent and indispensable to find a novel photocatalyst to improve both the photochemical activity and the stability.

$\text{In}_2\text{S}_3$ , as a typical III–VI group sulfide, is an n-type semiconductor with a band gap of 2.0–2.3 eV corresponding to visible light region which attracted intense interest for

optical, photoconductive, and optoelectronic applications. Furthermore,  $\text{In}_2\text{S}_3$  shows property of high photosensitivity and photoconductivity, stable chemical and physical characteristics, and low toxicity; it has great potential for visible-light-driven photodegradation of pollutants [9, 10]. Realistically, the narrow band gap and the rapid recombination of photogenerated electron-hole pairs causing poor quantum yield are similar to other visible light photocatalysts [11–14]. To meet the practical application requirements, it is urgent and important to enhance the photocatalytic efficiency of  $\text{In}_2\text{S}_3$ . Up to now, many attempts have been explored to improve the photocatalytic performance of  $\text{In}_2\text{S}_3$ , such as metal ions doping, coupling with other semiconductors, and carbon materials-based assemblies [15, 16].

As a viable alternative route to boost the efficiency of photocatalysts, CNF-based assemblies have aroused attention [17–19]. CNF is easily synthesized by electrospinning with a large theoretical specific surface area and high intrinsic electron mobility; it possesses physicochemical, superior electronic, mechanical character, and high absorption properties.



SCHEME 1: Postulated mechanism of the visible-light-induced photodegradation of RB with  $\text{In}_2\text{S}_3/\text{CNF}$ .

In particular, compared with traditional carbon nanofibers obtained by other physical and chemical methods, the carbon nanofibers synthesized by electrospinning (CNF) have stronger electronic transport properties [20, 21]. Therefore, it is an ideal method to enhance photocatalytic activity by coupling  $\text{In}_2\text{S}_3$  with CNF to construct  $\text{In}_2\text{S}_3/\text{CNF}$ .

In this work, the CNF was fabricated by electrospinning technique, and  $\text{In}_2\text{S}_3/\text{CNF}$  composites were fabricated through a one-pot hydrothermal reaction as shown in Scheme 1. The photogenerated electrons on the conduction bands (CB) of  $\text{In}_2\text{S}_3$  could easily be transferred to CNF for the positive synergetic effect, in brief, because the formation of interface junction can improve the optical absorption property and simultaneously facilitate the separation of photoinduced electron-hole pairs. In addition, the promising applications of  $\text{In}_2\text{S}_3/\text{CNF}$  composites have excellent performance for the degradation of organic pollutants. This study shows a reliable method to degrade organic pollutants.

## 2. Experimental Section

**2.1. Materials.** All the reagents were of analytical grade and were used as received without further purification.  $\text{InCl}_3 \cdot 5\text{H}_2\text{O}$ , thioacetamide (TAA), and other chemicals were of analytical grade and purchased from Sinopharm Chemical Reagents Co., Ltd. Polyacrylonitrile (PAN) ( $M_w = 150,000 \text{ g mol}^{-1}$ ) was purchased from Sigma-Aldrich.

**2.2. Fabrication of CNF.** According to previous reports [22], PAN nanofiber was synthesized from PAN by a modified electrospinning method. Firstly, 1 g PAN was dissolved completely in 9 mL *N,N*-dimethylformamide (DMF). Then, the mixture was transferred to 5 mL plastic syringe by two times for electrospinning (voltage: 20 kV, injection rate:  $0.2 \text{ mm min}^{-1}$ ). In order to obtain CNF, the PAN was carbonized at  $500^\circ\text{C}$  for 2 h under an inert atmosphere with a heating rate of  $2 \text{ K min}^{-1}$ .

**2.3. Fabrication of  $\text{In}_2\text{S}_3/\text{CNF}$ .**  $\text{In}_2\text{S}_3/\text{CNF}$  with different  $\text{In}_2\text{S}_3$  loadings was then prepared by a facile one-pot hydrothermal method. Briefly, a certain amount of  $\text{InCl}_3 \cdot 5\text{H}_2\text{O}$  (351, 702, or 1053 mg) and thioacetamide (120 mg) was dissolved in ethyl alcohol (40 mL) under ultrasound conditions. The CNF (50 mg) was then immersed in the above solution, which was then transferred to a Teflon-lined autoclave and heated in a homogeneous reactor at  $180^\circ\text{C}$  for 12 h. According to this method, different weight ratios of the  $\text{In}_2\text{S}_3$  to g-CNF samples were synthesized and labeled as  $\text{In}_2\text{S}_3/\text{CNF}$ -1,  $\text{In}_2\text{S}_3/\text{CNF}$ -2, and  $\text{In}_2\text{S}_3/\text{CNF}$ -4, respectively. By controlled trial, the  $\text{In}_2\text{S}_3$  was fabricated by the same method.

**2.4. Characterization.** Scanning electron microscopy (SEM; Hitachi S-4800) coupled with X-ray energy dispersive spectroscopy (SEM-EDS) and transmission electron microscopy (TEM; Hitachi H600) were used to observe the morphology, structure, and size of the  $\text{In}_2\text{S}_3/\text{CNF}$  and its components. The effect of the  $\text{In}_2\text{S}_3$  and CNF contents of  $\text{In}_2\text{S}_3/\text{CNF}$  on its structural properties were investigated by X-ray photoelectron spectroscopy (XPS; Axis Ultra HAS), Raman (Raman; Axis Ultra HAS), and X-ray diffraction (XRD; X' Pert-Pro MPD). The optical properties and the dye concentration were determined by UV-visible diffuse reflectance spectroscopy (UV-vis DRS, Shimadzu UV-3600).

**2.5. Photocatalytic Activity Measurements.** The photocatalytic activities of samples were evaluated by measuring the photodegradation of Rhodamine B (RB) under visible light. In a typical measurement, 40 mg photocatalysts were suspended in 100 mL of 50 ppm aqueous solution of RB. The solution was stirred in the dark for 30 min to obtain a good dispersion and to reach the adsorption-desorption equilibrium between the organic molecules and the catalysts surface [23]. Then the suspension was illuminated with a 250 W xenon lamp. The concentration change of RB was monitored by measuring the UV-vis absorption of the suspensions at regular intervals (take samples every 10 minutes). The suspension was filtered to remove the photocatalysts before

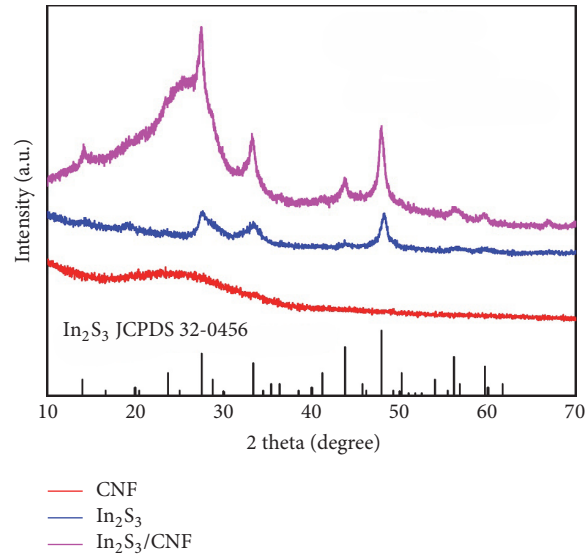


FIGURE 1: XRD patterns of  $\text{In}_2\text{S}_3$ , CNF, and  $\text{In}_2\text{S}_3/\text{CNF}$ -2.

measurement. The concentrations of RB in the reacting solutions were analyzed at  $\lambda = 554 \text{ nm}$  [24]. The photocatalytic activity was analyzed by the time profiles of  $C/C_0$ , where  $C$  is the concentration of RB at the irradiation time  $t$  and  $C_0$  is the concentration in the absorption equilibrium of the photocatalysts before irradiation, respectively. The normalized temporal concentration changes ( $C/C_0$ ) of RB are proportional to the normalized maximum absorbance ( $A/A_0$ ), which can be derived from the change in the RB absorption profile at a given time interval [25].

### 3. Results and Discussion

The X-ray diffraction (XRD) patterns of pure CNF,  $\text{In}_2\text{S}_3$ , and  $\text{In}_2\text{S}_3$  are shown in Figure 1. All of the diffraction peaks can be indexed to that of  $\text{In}_2\text{S}_3$  with a cubic phase structure (JCPDS, number 32-0456). Peaks at  $2\theta$  of 14, 27, 33, 44, 48, 56, and  $60^\circ$  in the XRD patterns of  $\text{In}_2\text{S}_3/\text{CNF}$ -2 and  $\text{In}_2\text{S}_3$  correspond to the (111), (311), (400), (511), (533), and (444) planes of  $\text{In}_2\text{S}_3$ , respectively. The XRD patterns of the  $\text{In}_2\text{S}_3/\text{CNF}$ -2 heterostructures show all the diffraction peaks assigned to hexagonal  $\text{In}_2\text{S}_3$  except the peak at  $25^\circ$  which corresponds to (130) plane of orthorhombic CNF, indicating the existence of  $\text{In}_2\text{S}_3$  and CNF in the  $\text{In}_2\text{S}_3/\text{CNF}$ -2 heterostructures. Moreover, the intensities of the corresponding diffraction peaks of  $\text{In}_2\text{S}_3$  strengthened gradually along with the addition of the CNF in the  $\text{In}_2\text{S}_3/\text{CNF}$ -2 composites; the formation of heterostructures can be demonstrated.

The morphology of the  $\text{In}_2\text{S}_3$  and  $\text{In}_2\text{S}_3/\text{CNF}$ -2 was analyzed by SEM and TEM. The flower-like  $\text{In}_2\text{S}_3$  with an average diameter of  $5 \mu\text{m}$  possesses porous structures due to the aggregation of a certain amount of nanosheets (Figure 2(a)). The TEM image of Figure 2(b) further confirms the result. The SEM image of electrospun CNF is shown in

Figure 2(c), which shows that the average diameter is about  $300 \text{ nm}$  and there is no defect in a smooth surface. As shown in TEM images (Figure 2(d)), it is clear that the surface of  $\text{In}_2\text{S}_3/\text{CNF}$ -2 is uniformly covered by the ultrathin  $\text{In}_2\text{S}_3$  nanosheets after hydrothermal treatment. Further, there is no aggregation found in the surface of  $\text{In}_2\text{S}_3/\text{CNF}$ -2 composites.

The EDX spectrum shown in Figure 2(e) reveals the presence of In and S elements in a mass fraction ratio of 4.47% : 1.61%, which is close to the expected stoichiometry for  $\text{In}_2\text{S}_3$  (Au signal is from FTO substrate).

Figure 3 shows that the different concentration of  $\text{In}_2\text{S}_3$  deposited on the surface of CNF nanofibers. A small amount of nanoplate-like  $\text{In}_2\text{S}_3$  was found on the smooth surface of CNF nanofibers, which correspond to low concentration. As the concentration increases (Figures 3(c) and 3(d)),  $\text{In}_2\text{S}_3$  nanosheets with curled shapes grow vertically on the nanofiber surface and with a uniform distribution. In addition, the surface of nanofiber also turns from smooth to rough. As shown in Figures 3(e) and 3(f), serious aggregation occurred and thick layer  $\text{In}_2\text{S}_3$  nanosheets were observed after further increasing the  $\text{In}_2\text{S}_3$  concentration. The rapid nucleation of  $\text{In}_2\text{S}_3$  at high concentration can be demonstrated.

XPS measurements were carried out to testify the chemical composition and chemical states of elements in  $\text{In}_2\text{S}_3/\text{CNF}$ -2 heterostructure photocatalyst [26]. The full-scale XPS spectrum for  $\text{In}_2\text{S}_3/\text{CNF}$ -2 sample is shown in Figure 4(a), in which the In, S, and C elements could be detected and no other impurities were observed. Figures 4(b), 4(c), and 4(d) show the high-resolution XPS spectra for  $\text{In}_2\text{S}_3/\text{CNF}$  sample. The XPS peaks (Figure 4(b)) at 444.1 and 452.7 eV correspond to the  $\text{In}3d_{5/2}$  and  $\text{In}3d_{3/2}$  states [27], respectively. The peak at 161.9 eV in Figure 4(c) corresponds to the  $\text{S}2p_{3/2}$  state of  $\text{S}_2^{2-}$  moieties. The peak at 284.8 eV in Figure 4(d) corresponds to the C1s state. The above XPS

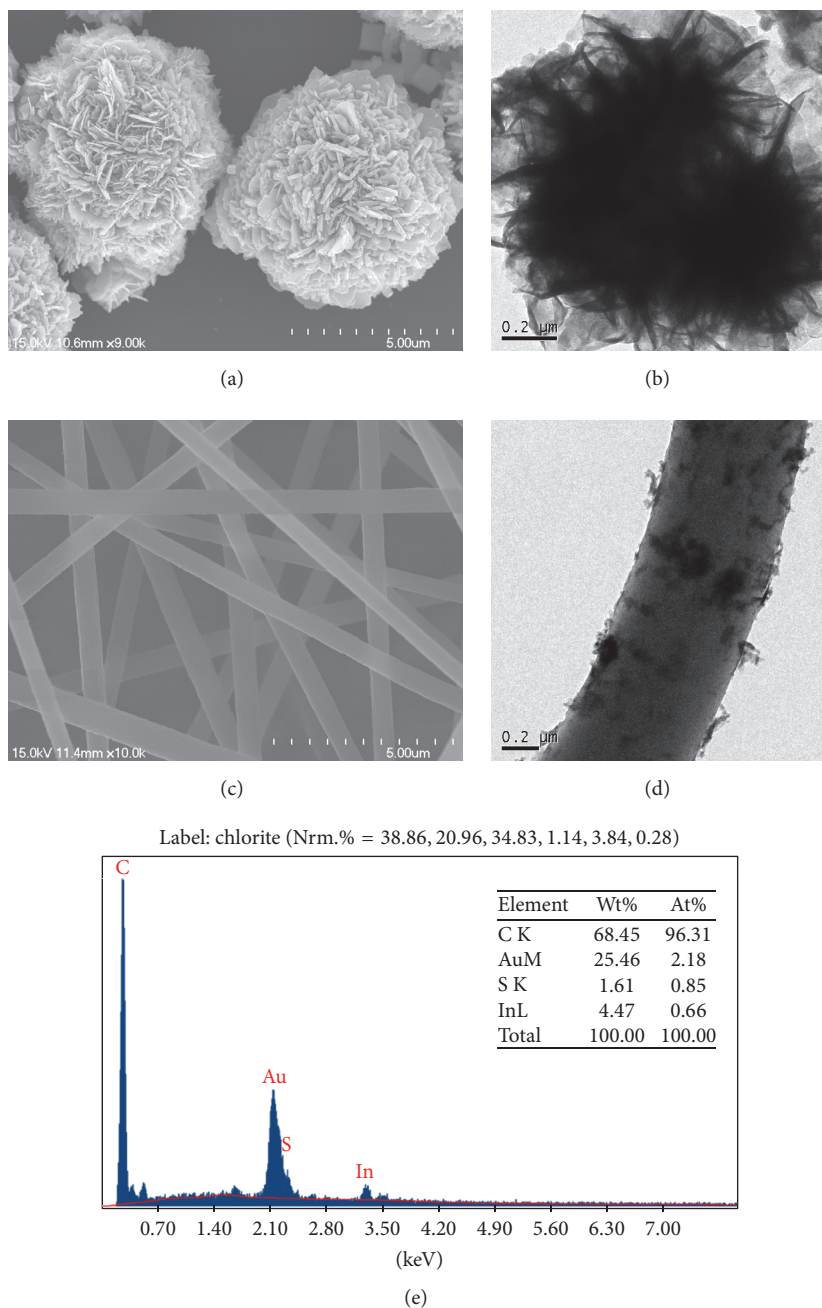


FIGURE 2: SEM images of  $\text{In}_2\text{S}_3$  and CNF ((a) and (c)), TEM images of  $\text{In}_2\text{S}_3$  and  $\text{In}_2\text{S}_3/\text{CNF-2}$  ((b) and (d)), and EDX pattern of  $\text{In}_2\text{S}_3/\text{CNF-2}$  (e).

results confirm that the composites are composed of  $\text{In}_2\text{S}_3$  and CNF.

Raman analysis was explored to confirm the presence of CNF and  $\text{In}_2\text{S}_3$  in  $\text{In}_2\text{S}_3/\text{CNF-2}$  sample (Figure 5). D-peak (D band) represents the defects of C atomic lattice, and G-peak (G band) represents the expansion vibration of the surface of C atom  $\text{sp}^2$  hybridization. And the representative Raman spectrum in a range of Raman shift from 100 to  $2000\text{ cm}^{-1}$  of the CNF shows mainly two peaks centered around  $1369\text{ cm}^{-1}$

(D band) and  $1590\text{ cm}^{-1}$  (G band) for CNF. Furthermore, the degree of fibrosis can be measured by the intensity ratio of the G to D band ( $I_G/I_D$ ) [28–30], where  $I_G/I_D$  is the intensity ratio of D-peak and G-peak. A slight increase in the  $I_G/I_D$  ratio is observed in the spectrum of  $\text{In}_2\text{S}_3/\text{CNF-2}$  composites, the D/G integral intensity ratio ( $I_D/I_G$ ) for CNF in the  $\text{In}_2\text{S}_3/\text{CNF-2}$  sample (1.13) is slightly higher than that of CNF (1.12), it is indicated that a certain amount of  $\text{In}_2\text{S}_3$  deposited on the surface of CNF during the chemical reduction process,

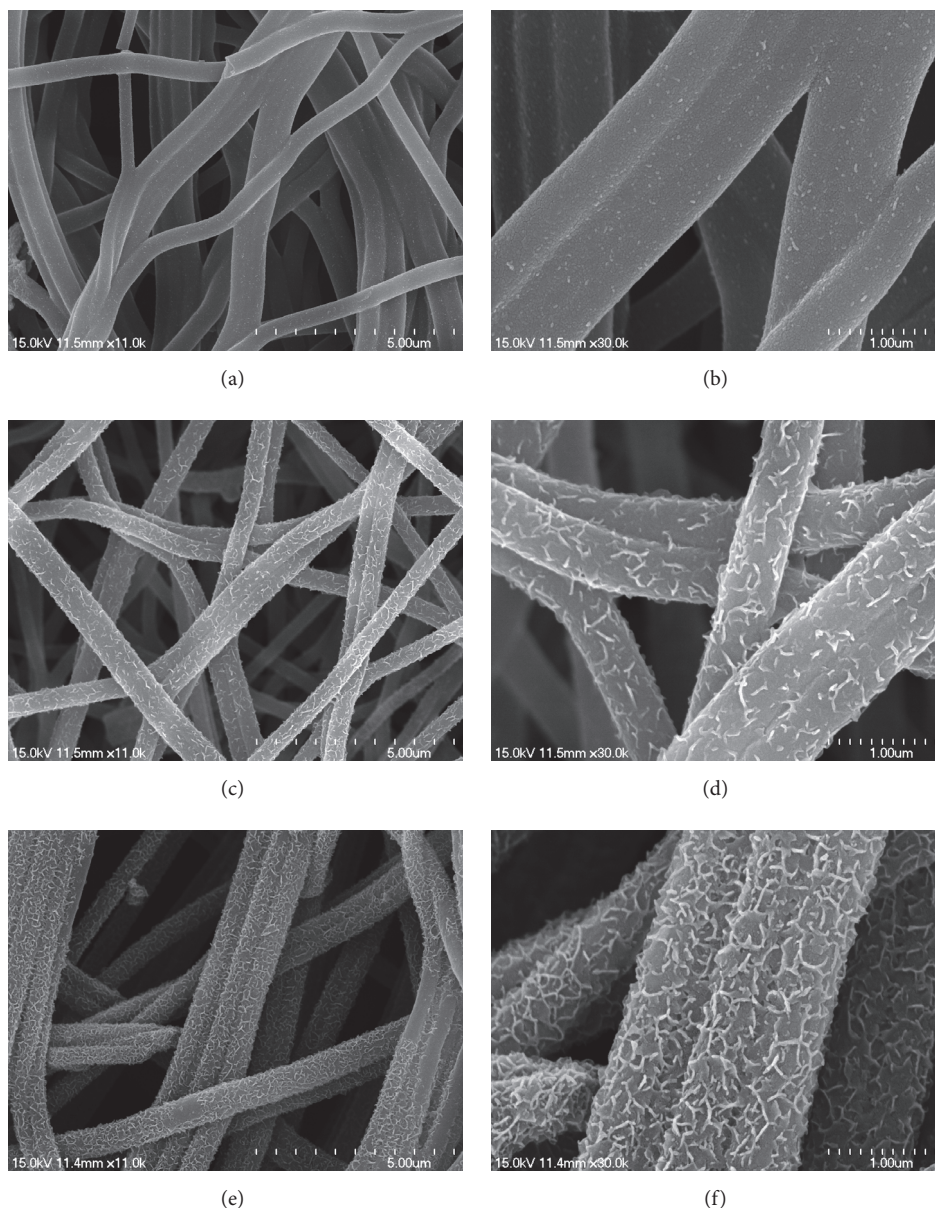


FIGURE 3: Low- (a, c, e) and high- (b, d, f) magnification SEM images of low concentration of  $\text{In}_2\text{S}_3$  loaded on CNF ((a) and (b)), moderate concentration of  $\text{In}_2\text{S}_3$  loaded on CNF ((c) and (d)), and high concentration of  $\text{In}_2\text{S}_3$  loaded on CNF ((e) and (f)).

and the conjugated CNF network was reestablished [31]. The two peaks for D and G band of the composite no shift appears, indicating that only a small amount of  $\text{In}_2\text{S}_3$  deposited on the surface of CNF.

The optical properties of the three samples were detected by UV-vis DRS absorption spectroscopy (Figure 6). Obviously, CNF shows the best performance and its absorption peaks appear in the visible light and UV light regions. It should be noted that  $\text{In}_2\text{S}_3/\text{CNF}-2$  with the addition of CNF showed an increased photocatalytic performance compared to  $\text{In}_2\text{S}_3$  (Figure 6(a)). The band gap energy ( $E_g$ ) of samples was calculated by Tauc's equation

[32, 33] and the result was shown in Figure 6(b); the  $E_g$  values of  $\text{In}_2\text{S}_3$  and  $\text{In}_2\text{S}_3/\text{CNF}-2$  in Figure 6(b) are approximately 2.70 and 3.08 eV. The band gap of  $\text{In}_2\text{S}_3/\text{CNF}-2$  was higher than  $\text{In}_2\text{S}_3$ , which is close to the value of  $\text{In}_2\text{S}_3$  and  $\text{In}_2\text{S}_3/\text{CNF}$  reported in other literatures [10, 34]. Thus, it is indicated that the as-prepared  $\text{In}_2\text{S}_3/\text{CNF}-2$  heterojunction structures have the appropriate  $E_g$  for photodegradation of organic pollutants under visible light irradiation.

In order to detect the ability of photodegradation, different photocatalysts were used to photodegrade organic pollutant under visible light irradiation, then the samples of products were analyzed. The results are shown in Figures 7(a)

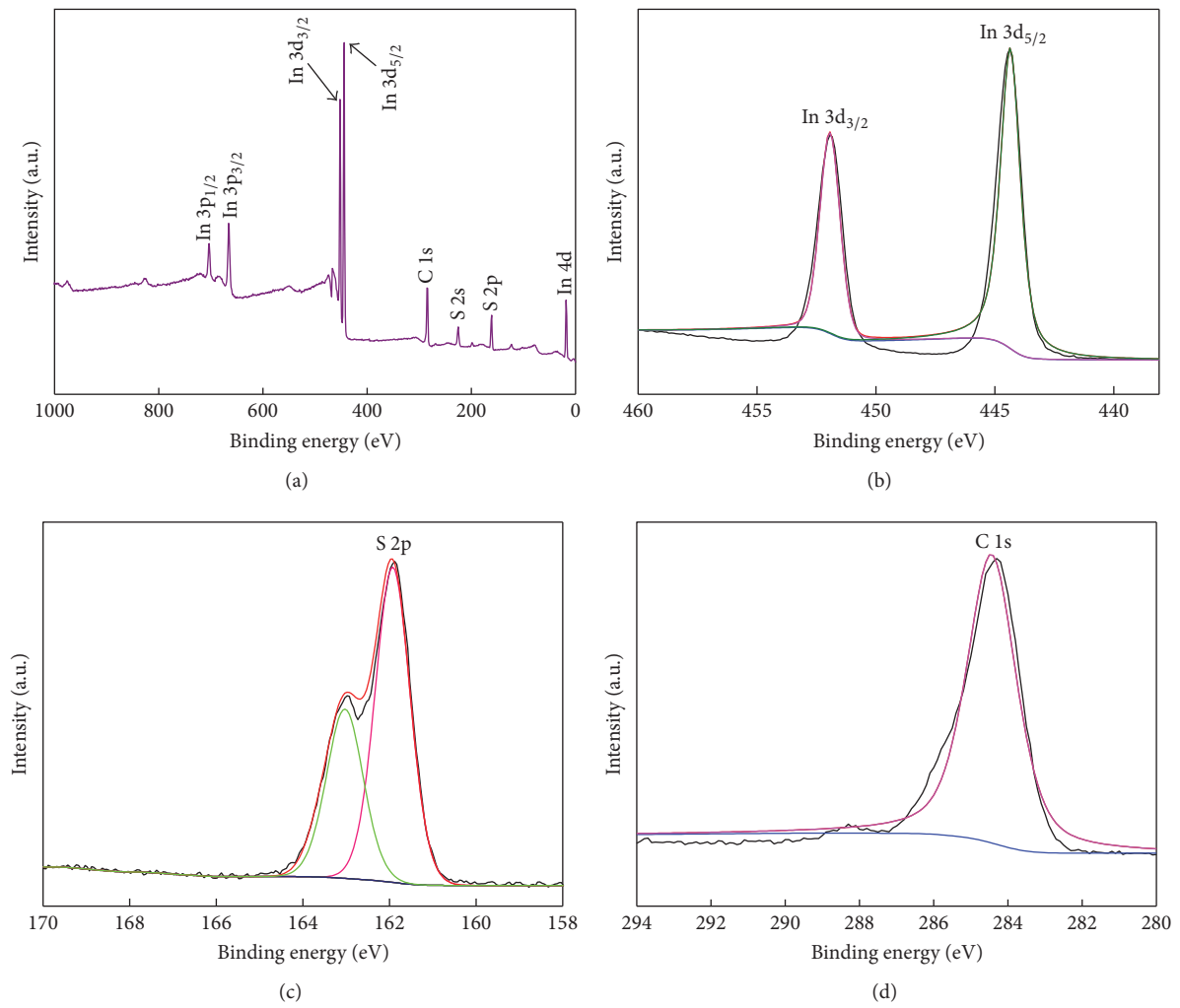


FIGURE 4: XPS spectra of the In<sub>2</sub>S<sub>3</sub>/CNF-2: survey spectrum (a), In 3d (b), S 2p (c), and C 1s (d).

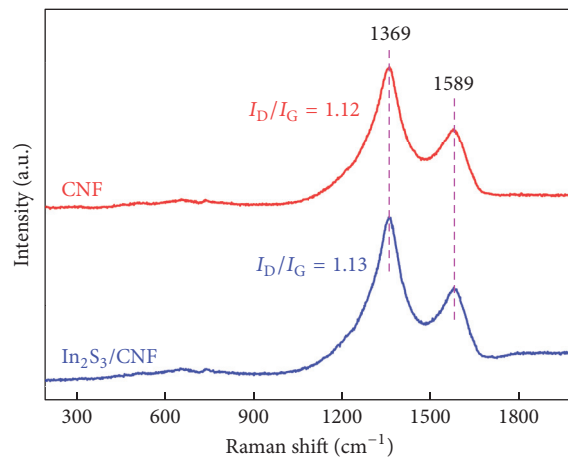


FIGURE 5: Raman spectra of CNF and In<sub>2</sub>S<sub>3</sub>/CNF-2.

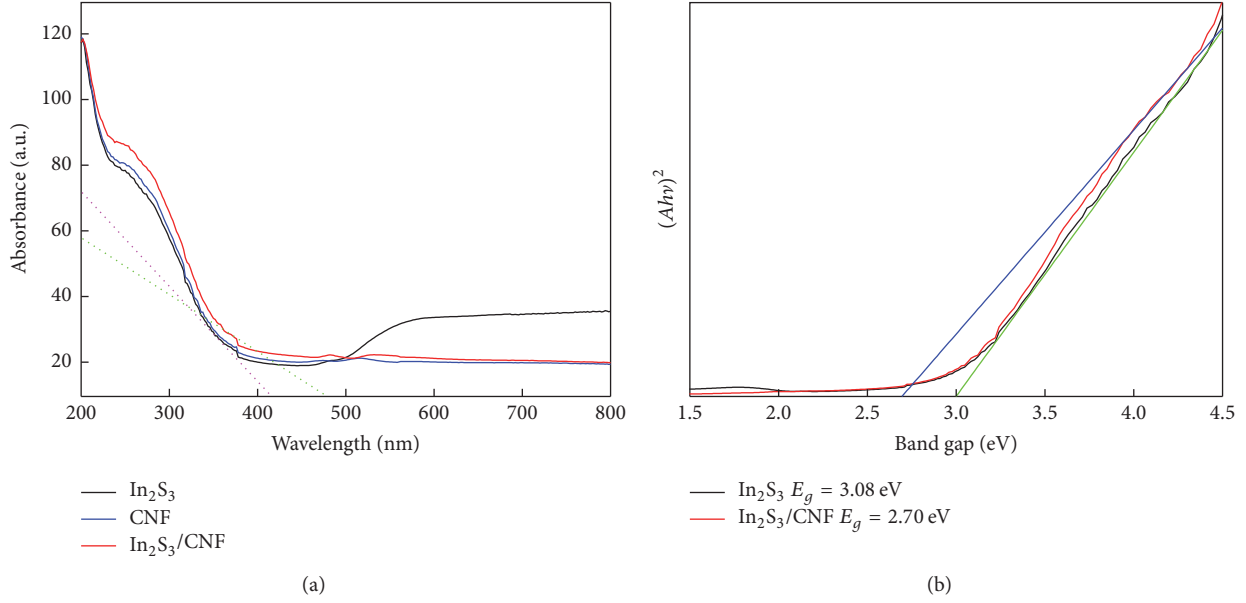


FIGURE 6: UV-vis diffuse reflectance spectrum of In<sub>2</sub>S<sub>3</sub>, CNF, and In<sub>2</sub>S<sub>3</sub>/CNF-2 (a) and the direct band gap determination of In<sub>2</sub>S<sub>3</sub> and In<sub>2</sub>S<sub>3</sub>/CNF-2 (b). The tangent at this point corresponds to the smallest absorption wavelength.

and 7(b); the UV-vis absorption spectra in Figure 7 show the characteristic absorptions of RB at 570 and 580 nm. Owing to the strong absorption ability of CNF, a certain amount of RB was attached to the CNF before irradiation. Furthermore, when the dissociation and adsorption reach equilibrium, the concentration change of Rhodamine B, which is degraded by In<sub>2</sub>S<sub>3</sub> and In<sub>2</sub>S<sub>3</sub>/CNF-2, is the same. The concentration of RB does not significantly change after irradiation as shown in Figure 7(a). The change in the concentration of RB in Figure 7(b) is significantly greater than Figure 7(a), which can be further confirmed through the change of solution color before and after degradation with different photocatalysts.

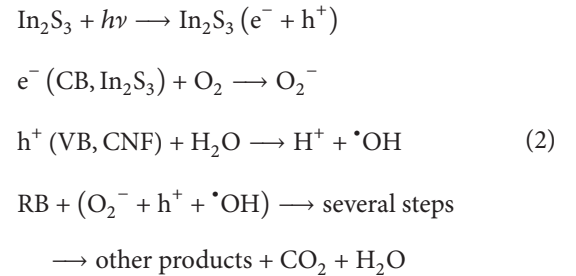
The degradation curves of RB on pure In<sub>2</sub>S<sub>3</sub>, CNF, and In<sub>2</sub>S<sub>3</sub>/CNF-2 composites were shown in Figure 8(a). Obviously, the concentration of CNF almost has no change, indicating that pure CNF has no photocatalytic activity under visible light irradiation. The In<sub>2</sub>S<sub>3</sub>/CNF-2 composites have a better photocatalytic efficiency (78.2%) for RB after visible light irradiation for 60 min than that of pure In<sub>2</sub>S<sub>3</sub>. It is concluded that In<sub>2</sub>S<sub>3</sub>/CNF-2 composites exhibited much higher photocatalytic efficiency compared with the pure In<sub>2</sub>S<sub>3</sub>. For a better comparison of the photocatalytic efficiency of In<sub>2</sub>S<sub>3</sub>/CNF-2 and pure In<sub>2</sub>S<sub>3</sub>, the kinetic analysis of degradation of RB was explored to confirm it. The above degradation reactions followed a Langmuir-Hinshelwood apparent first-order kinetics model [32, 35] when the initial concentrations of the reactants are less than 100 ppm. The Langmuir-Hinshelwood apparent first-order kinetics model is described below:

$$-\ln\left(\frac{C_0}{C}\right) = K_{app}t, \quad (1)$$

where  $K_{app}$  is the apparent first-order rate constant (min<sup>-1</sup>). The determined  $K_{app}$  values for degradation of RB with

different catalysts are presented in Figure 8(b). It is clear that the as-prepared In<sub>2</sub>S<sub>3</sub>/CNF-2 composites show the highest reaction rate among the two catalysts with  $K_{app} = 0.0232 \text{ min}^{-1}$ , while  $K_{app} = 0.0169 \text{ min}^{-1}$  for pure In<sub>2</sub>S<sub>3</sub>. The photocatalytic reactivity order is well consistent with the activity studies above.

It is reasonable to presume that the photogenerated electrons (e<sup>-</sup>) transfer from In<sub>2</sub>S<sub>3</sub> to CNF in the In<sub>2</sub>S<sub>3</sub>/CNF system under visible light irradiation. Therefore, the photogenerated electrons first transfer to CNF and then are trapped by O<sub>2</sub> and H<sub>2</sub>O at the surface of photocatalyst or solution to form the active species such as O<sub>2</sub><sup>-</sup>. These active species could help the degradation of RB dye. At the same time, the photogenerated holes (h<sup>+</sup>) could react with H<sub>2</sub>O to form <sup>•</sup>OH, hydrogen ions (H<sup>+</sup>), and then oxidize RB dye directly [12]. The complete photodegradation process can be summarized by the following reaction steps:



#### 4. Conclusion

In summary, an effective method of preparing In<sub>2</sub>S<sub>3</sub>/CNF photocatalysts was described in this paper. The incorporation

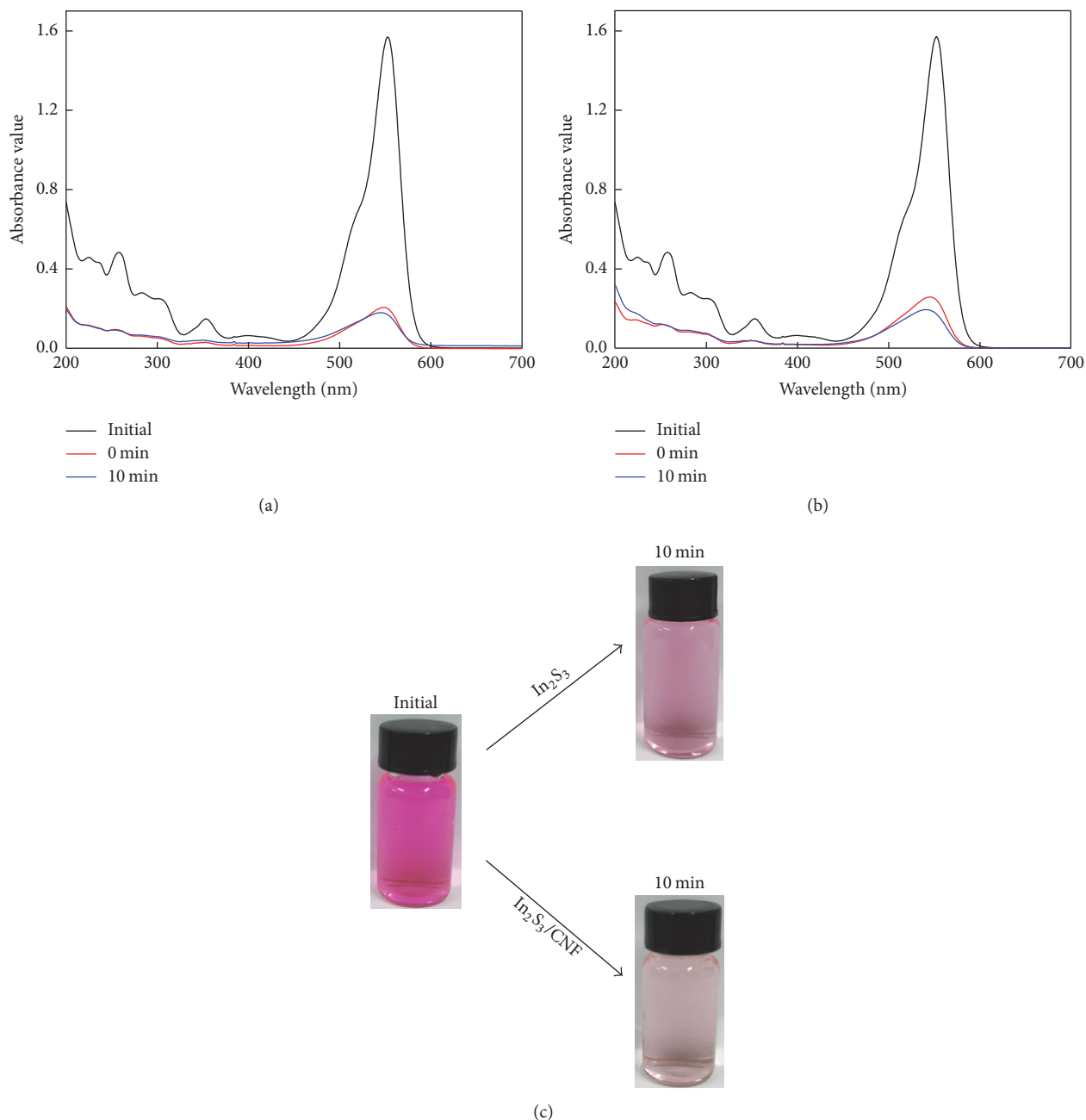


FIGURE 7: Removal efficiency of 50 mg/L RB solution during 10 min of irradiation with  $\text{In}_2\text{S}_3$  (a) and  $\text{In}_2\text{S}_3/\text{CNF}$ -2 (b). The changes of solution color before and after degradation with different photocatalysts under visible light irradiation (c).

of CNF serving as electron collectors realizes a more effective separation of photogenerated electron-hole pairs and greatly boosts the photocatalytic activity of the products compared with the pure  $\text{In}_2\text{S}_3$ . The  $\text{In}_2\text{S}_3/\text{CNF}$ -2 composites show strong adsorption ability towards the RB, they can degrade 50 ppm of RB in 60 minutes under visible lights, and the excellent degradation RB activities of  $\text{In}_2\text{S}_3/\text{CNF}$  are mainly attributed to the large amount of effectively reactive species

like  $\text{h}^+$  and  $\text{O}_2^-$ . Overall, this study provides a new option to construct the semiconductor/CNF composites with high photocatalytic activity, environmental remediation, and energy conversion.

### Conflicts of Interest

The authors declare that they have no conflicts of interest.

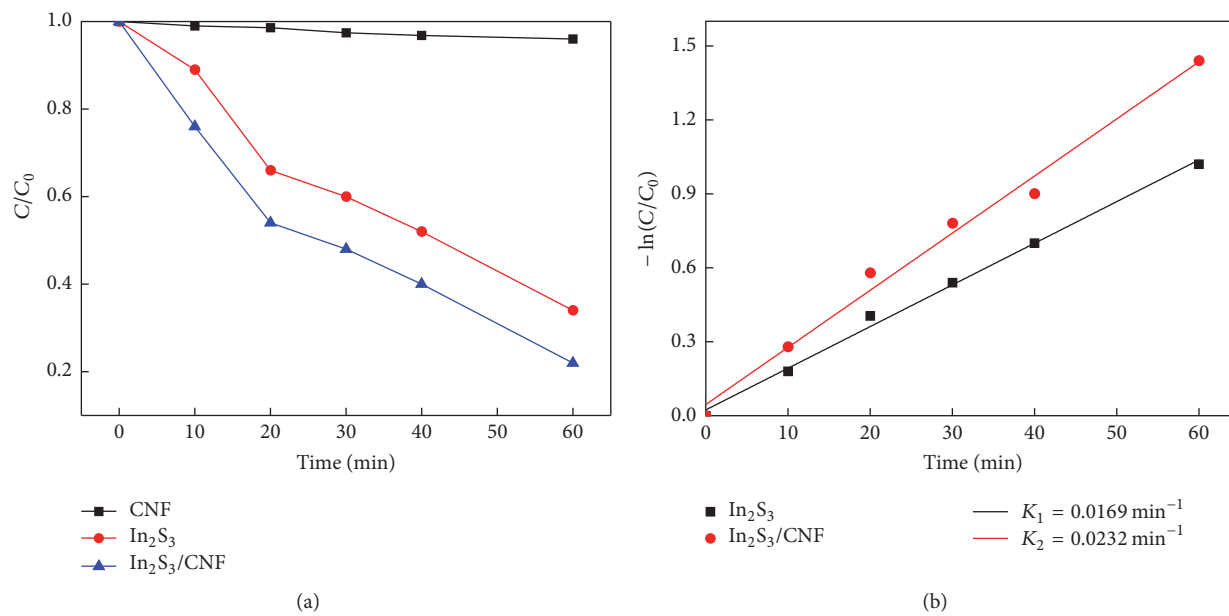


FIGURE 8: Degradation curve of RB over different photocatalysts under visible light (a). Kinetic linear simulation curves of RB degradation over the different photocatalysts under visible light irradiation (b).

## Acknowledgments

The authors are grateful to the Natural Science Foundation of Jiangsu Province (CN) (BK20141257) for financial assistance.

## References

- [1] J. Gong and R. Luque, "Catalysis for production of renewable energy," *Chemical Society Reviews*, vol. 43, no. 22, pp. 7466–7468, 2014.
- [2] S. J. A. Moniz, S. A. Shevlin, D. J. Martin, Z.-X. Guo, and J. Tang, "Visible-light driven heterojunction photocatalysts for water splitting—a critical review," *Energy & Environmental Science*, vol. 8, no. 3, pp. 731–759, 2015.
- [3] T. Phongamwong, W. Donphai, P. Prasitchoke et al., "Novel visible-light-sensitized Chl-Mg/P25 catalysts for photocatalytic degradation of rhodamine B," *Applied Catalysis B: Environmental*, vol. 207, pp. 326–334, 2017.
- [4] K. Kaygusuz, "Energy and environmental issues relating to greenhouse gas emissions for sustainable development in Turkey," *Renewable & Sustainable Energy Reviews*, vol. 13, no. 1, pp. 253–270, 2009.
- [5] Z. Yang, L. Huang, Y. Xie et al., "Controllable synthesis of  $Bi_2WO_6$  nanoplate self-assembled hierarchical erythrocyte microspheres via a one-pot hydrothermal reaction with enhanced visible light photocatalytic activity," *Applied Surface Science*, vol. 403, pp. 326–334, 2017.
- [6] Z. Ai, G. Zhao, Y. Zhong et al., "Phase junction CdS: High efficient and stable photocatalyst for hydrogen generation," *Applied Catalysis B: Environmental*, vol. 221, pp. 179–186, 2018.
- [7] L. He, Z. Tong, Z. Wang, M. Chen, N. Huang, and W. Zhang, "Effects of calcination temperature and heating rate on the photocatalytic properties of ZnO prepared by pyrolysis," *Journal of Colloid and Interface Science*, vol. 509, pp. 448–456, 2018.
- [8] Y. Li, G. Chen, Q. Wang, X. Wang, A. Zhou, and Z. Shen, "Hierarchical ZnS- $In_2S_3$ -CuS nanospheres with nanoporous structure: Facile synthesis, growth mechanism, and excellent photocatalytic activity," *Advanced Functional Materials*, vol. 20, no. 19, pp. 3390–3398, 2010.
- [9] W. Qiu, M. Xu, X. Yang et al., "Biomolecule-assisted hydrothermal synthesis of  $In_2S_3$  porous films and enhanced photocatalytic properties," *Journal of Materials Chemistry*, vol. 21, no. 35, pp. 13327–13333, 2011.
- [10] Y. Xing, H. Zhang, S. Song et al., "Hydrothermal synthesis and photoluminescent properties of stacked indium sulfide superstructures," *Chemical Communications*, no. 12, pp. 1476–1478, 2008.
- [11] Y. Mi, H. Li, Y. Zhang, R. Zhang, and W. Hou, "One-pot synthesis of belt-like  $Bi_2S_3$ /BiOCl hierarchical composites with enhanced visible light photocatalytic activity," *Applied Surface Science*, vol. 423, pp. 1062–1071, 2017.
- [12] C. Yu, K. Wang, P. Yang et al., "One-pot facile synthesis of  $Bi_2S_3/SnS_2/Bi_2O_3$  ternary heterojunction as advanced double Z-scheme photocatalytic system for efficient dye removal under sunlight irradiation," *Applied Surface Science*, vol. 420, pp. 233–242, 2017.
- [13] Y. Yu, L. Yan, J. Cheng, and C. Jing, "Mechanistic insights into TiO<sub>2</sub> thickness in  $Fe_3O_4$ @TiO<sub>2</sub>-GO composites for enrofloxacin photodegradation," *Chemical Engineering Journal*, vol. 325, pp. 647–654, 2017.
- [14] Y. Zhang, J. Chen, L. Hua et al., "High photocatalytic activity of hierarchical  $SiO_2$ @C-doped TiO<sub>2</sub> hollow spheres in UV and visible light towards degradation of rhodamine B," *Journal of Hazardous Materials*, vol. 340, pp. 309–318, 2017.
- [15] X. An, J. C. Yu, F. Wang, C. Li, and Y. Li, "One-pot synthesis of  $In_2S_3$  nanosheets/graphene composites with enhanced visible-light photocatalytic activity," *Applied Catalysis B: Environmental*, vol. 129, pp. 80–88, 2013.

- [16] J. Chen, W. Mei, Q. Huang et al., "Highly efficient three-dimensional flower-like AgI/Bi<sub>2</sub>O<sub>2</sub>CO<sub>3</sub> heterojunction with enhanced photocatalytic performance," *Journal of Alloys and Compounds*, vol. 688, pp. 225–234, 2016.
- [17] Y. K. Kim, S. K. Lim, H. Park, M. R. Hoffmann, and S. Kim, "Trilayer CdS/carbon nanofiber (CNF) mat/Pt-TiO<sub>2</sub> composite structures for solar hydrogen production: Effects of CNF mat thickness," *Applied Catalysis B: Environmental*, vol. 196, pp. 216–222, 2016.
- [18] C. Luo, D. Li, W. Wu, C. Yu, W. Li, and C. Pan, "Preparation of 3D reticulated ZnO/CNF/NiO heteroarchitecture for high-performance photocatalysis," *Applied Catalysis B: Environmental*, vol. 166–167, pp. 217–223, 2015.
- [19] M. Ouzzine, M. A. Lillo-Ródenas, and A. Linares-Solano, "Carbon nanofibres as substrates for the preparation of TiO<sub>2</sub> nanostructured photocatalysts," *Applied Catalysis B: Environmental*, vol. 127, pp. 291–299, 2012.
- [20] W. Li, L. Zeng, Z. Yang et al., "Free-standing and binder-free sodium-ion electrodes with ultralong cycle life and high rate performance based on porous carbon nanofibers," *Nanoscale*, vol. 6, no. 2, pp. 693–698, 2014.
- [21] L. Peng, L. Hu, and X. Fang, "Energy harvesting for nanostructured self-powered photodetectors," *Advanced Functional Materials*, vol. 24, no. 18, pp. 2591–2610, 2014.
- [22] J. S. Im, M. I. Kim, and Y.-S. Lee, "Preparation of PAN-based electrospun nanofiber webs containing TiO<sub>2</sub> for photocatalytic degradation," *Materials Letters*, vol. 62, no. 21–22, pp. 3652–3655, 2008.
- [23] J. Chen, H. Wang, G. Huang et al., "Facile synthesis of urchin-like hierarchical Nb<sub>2</sub>O<sub>5</sub> nanospheres with enhanced visible light photocatalytic activity," *Journal of Alloys and Compounds*, vol. 728, pp. 19–28, 2017.
- [24] L. Zhang, W. Zheng, H. Jiu, W. Zhu, and G. Qi, "Preparation of the anatase/TiO<sub>2</sub>(B) TiO<sub>2</sub> by self-assembly process and the high photodegradable performance on RhB," *Ceramics International*, vol. 42, no. 11, pp. 12726–12734, 2016.
- [25] C. Mendoza, A. Valle, M. Castellote, A. Bahamonde, and M. Faraldos, "TiO<sub>2</sub> and TiO<sub>2</sub>-SiO<sub>2</sub> coated cement: Comparison of mechanic and photocatalytic properties," *Applied Catalysis B: Environmental*, vol. 178, pp. 155–164, 2015.
- [26] Y. Zhong, X. Qiu, D. Chen et al., "Flexible Electrospun Carbon Nanofiber/Tin(IV) Sulfide Core/Sheath Membranes for Photocatalytically Treating Chromium(VI)-Containing Wastewater," *ACS Applied Materials & Interfaces*, vol. 8, no. 42, pp. 28671–28677, 2016.
- [27] J. Li, Y. Ma, Z. Ye et al., "Fast electron transfer and enhanced visible light photocatalytic activity using multi-dimensional components of carbon quantum dots@3D daisy-like In<sub>2</sub>S<sub>3</sub>/single-wall carbon nanotubes," *Applied Catalysis B: Environmental*, vol. 204, pp. 224–238, 2017.
- [28] S. Stankovich, D. A. Dikin, R. D. Piner et al., "Synthesis of graphene-based nanosheets via chemical reduction of exfoliated graphite oxide," *Carbon*, vol. 45, no. 7, pp. 1558–1565, 2007.
- [29] F. Tuinstra and J. L. Koenig, "Raman spectrum of graphite," *The Journal of Chemical Physics*, vol. 53, no. 3, pp. 1126–1130, 1970.
- [30] S. Verma and R. K. Dutta, "Enhanced ROS generation by ZnO-ammonia modified graphene oxide nanocomposites for photocatalytic degradation of trypan blue dye and 4-nitrophenol," *Journal of Environmental Chemical Engineering (JECE)*, vol. 5, no. 5, pp. 4776–4787, 2017.
- [31] S. Kment, Z. Hubicka, H. Kmentova et al., "Photoelectrochemical properties of hierarchical nanocomposite structure: Carbon nanofibers/TiO<sub>2</sub>/ZnO thin films," *Catalysis Today*, vol. 161, no. 1, pp. 8–14, 2011.
- [32] S. Guo, Y. Zhu, Y. Yan, Y. Min, J. Fan, and Q. Xu, "Holey structured graphitic carbon nitride thin sheets with edge oxygen doping via photo-Fenton reaction with enhanced photocatalytic activity," *Applied Catalysis B: Environmental*, vol. 185, pp. 315–321, 2016.
- [33] M. Tahir and N. Saidina Amin, "Photocatalytic reduction of carbon dioxide with water vapors over montmorillonite modified TiO<sub>2</sub> nanocomposites," *Applied Catalysis B: Environmental*, vol. 142–143, pp. 512–522, 2013.
- [34] P. Zhang, C. Shao, Z. Zhang et al., "In situ assembly of well-dispersed Ag nanoparticles (AgNPs) on electrospun carbon nanofibers (CNFs) for catalytic reduction of 4-nitrophenol," *Nanoscale*, vol. 3, no. 8, pp. 3357–3363, 2011.
- [35] L. Han, D. Mao, Y. Huang et al., "Fabrication of unique Tin(IV) Sulfide/Graphene Oxide for photocatalytically treating chromium(VI)-containing wastewater," *Journal of Cleaner Production*, vol. 168, pp. 519–525, 2017.